Experimental investigation of mode I rock fracture toughness

Investigación experimental de la tenacidad de fractura en modo I en rocas

Andrea Muñoz Ibáñez

Doctoral Thesis

2020

SUPERVISORS

Jordi Delgado Martín

Ricardo Juncosa Rivera

Programa de doctorado en Ingeniería Civil

UNIVERSIDADE DA CORUÑA

Jordi Delgado Martín and Ricardo Juncosa Rivera:

DECLARE that the present work, entitled '*Experimental investigation of mode I rock fracture toughness'*, submitted by Andrea Muñoz Ibáñez to obtain the title of Doctor, was carried out under our supervision and fulfils all the requirements for the award of the degree of '*PhD in Civil Engineering with International Mention'*.

Dr. Jordi Delgado Martín	Dr. Ricardo Juncosa Rivera
Advisor	Co-advisor

Conflict of interest

This thesis was written within the scope of a research project funded by Repsol S.A, and has received the support from the MINECO/AEI/FEDER, UE project BIA2017-87066-R.

Acknowledgements

I gratefully acknowledge the financial support granted by the Xunta de Galicia and European Union (European Social Fund - ESF) under a PhD fellowship that allowed me to carry out my research.

First of all, I would like to express my deepest gratitude to my supervisor, Jordi Delgado, for his guidance throughout these years. From the very first moment he awakened my curiosity and interest in research and became the best mentor I could have wished for. He provided me with so many opportunities I would never have imagined and, thanks to him, I lived the most rewarding (and peculiar) adventures around the world. Jordi, I will never be able to thank you enough. A sincere thank you goes also to my co-supervisor, Ricardo Juncosa, whose inspiring questions and suggestions improved the quality of this work.

I appreciate every piece of advice and assistance which came from our colleagues at the Repsol Technology Lab. In particular I would like to express my gratitude towards Jacobo Canal, José Alvarellos, Nubia González and Héctor González, who always followed our research activity with lively interest, providing important advice and useful hints.

I am very grateful to all my former and current colleagues at LaMeRoc for being so supportive and always willing to lend a helping hand when I needed. I would like to thank Juan Rabuñal and the laboratory technicians of the CITEEC for providing technical assistance each time we had a problem. I thank Chiqui and Miguel for offering their time and support with numerical modelling. I also acknowledge the people at Formoso SA for their kindness and their quick response every time we needed them.

I had the most enriching experience during my research stay at the National Oceanography Centre in Southampton. There are few words to describe how grateful I am to Himar, not only for the countless hours of hard work he dedicated to me so unselfishly but specially for pushing me out of my comfort zone. A special thanks to Héctor for introducing me into the world of numerical simulation and all the inspiring discussions we had. Raquel, thank you so much for opening your lovely home to me and welcoming me so warmly. You and your (not so) little Spanish family made this experience unforgettable.

I would like to thank Manika Prasad for giving me the opportunity of completing part of my experimental work in the research facilities of Colorado School of Mines. Thank you to all the people in the Center for Rock Abuse for teaching me new techniques and letting me feel as part of their team. I greatly acknowledge the Engineering Geology and Rock Engineering group at the Ruhr University Bochum for so generously sharing with me their knowledge and expertise in acoustic emission.

Lastly, I would like to thank my friends and family, especially my parents for the unconditional support and for making me the person that I am today. I could not have done it without them. I have saved this last word of acknowledge for Aitor, for being an endless source of patience and love during these years, for always believing in me and pushing me to achieve my goals. Thank you for sharing this journey with me.

Abstract

Mode I fracture toughness (K_{IC}) is one of the most important parameters in rock fracture mechanics. K_{IC} is an intrinsic material property that represents the ability of a material containing a pre-existing defect to resist tensile failure. The International Society for Rock Mechanics (ISRM) has proposed four suggested methods for determining K_{IC}. However, these methods present some drawbacks. The main objective of this thesis is to develop a simple testing approach, called pseudo-compact tension (*p*CT) test, to measure K_{IC} in rocks using cylindrical single edge-notched specimens loaded in pure tension. The study is based on the results of a large set of fracture toughness experiments performed with different rock types, sample sizes, and a range of notch length ratios. The K_{IC} values derived with the *p*CT test are compared with those obtained with one of the suggested methods of the ISRM, the semi-circular bend (SCB) test. Some selected *p*CT and SCB tests were also complemented with the concurrent monitoring of the acoustic emission (AE) activity. With the obtained data, we compare and analyse both testing methods, the effects of specimen size, notch length and lithology, the mechanical evolution along the experiments and the significance of different AE parameters.

Resumen

La tenacidad de fractura en modo I (K_{IC}) es uno de los parámetros más importantes en la mecánica de fractura aplicada a rocas. K_{IC} es una propiedad intrínseca del material que representa su capacidad para resistir su rotura a tracción en la presencia de un defecto preexistente. La Sociedad Internacional para la Mecánica de Rocas (ISRM) ha sugerido cuatro métodos para determinar K_{IC}, pero todos presentan algunos inconvenientes. El principal objetivo de esta tesis es desarrollar un método de ensayo simple, llamado '*pseudo-compact tensión*' (*p*CT), para determinar K_{IC} en rocas mediante muestras cilíndricas ensayadas bajo condiciones de tracción pura. El estudio se basa en los resultados de un número de ensayos llevados a cabo con distintos tipos de roca, tamaños de probeta y longitudes de entalla. Los valores de K_{IC} obtenidos con el ensayo *p*CT se comparan con los obtenidos con el ensayo '*semi-circular bend*' (SCB), uno de los métodos sugeridos por la ISRM. En algunos de estos ensayos también se registró la emisión acústica (AE). Con los datos obtenidos, comparamos y analizamos ambos métodos, los efectos del tamaño de probeta, longitud de entalla y litología, la evolución mecánica y la importancia de diferentes parámetros de AE durante los ensayos.

Resumo

A tenacidade de fractura en modo I (K_{IC}) é un dos parámetros máis importantes na mecánica de fractura aplicada a rochas. K_{IC} é unha propiedade intrínseca do material que representa a súa capacidade para resistir a súa rotura a tracción na presenza dun defecto preexistente. A Sociedade Internacional para a Mecánica de Rochas (ISRM) suxeriu catro métodos para determinar K_{IC}, mais todos presentan algúns inconvenientes. O principal obxectivo desta tese é desenvolver un método de ensaio simple, chamado '*pseudo-compact tensión*' (*p*CT), para determinar K_{IC} en rocha mediante mostras cilíndricas ensaiadas baixo condiciones de tracción pura. O estudo baséase nos resultados dun número de ensaios levados a cabo con distintos tipos de rocha, tamaños de probeta e lonxitudes de entalla. Os valores de K_{IC} obtidos co ensaio *p*CT compáranse cos obtidos co ensaio '*semi-circular bend*' (SCB), un dos métodos suxeridos pola ISRM. Nalgúns destes ensaios tamén se rexistrou a emisión acústica (AE). Cos datos obtidos, comparamos e analizamos ambos métodos, os efectos do tamaño de probeta, lonxitude de entalla e litoloxía, a evolución mecánica e a importancia de diferentes parámetros de AE durante os ensaios.

Extended abstract

Defects such as voids or cracks are inherent in every material. These features can either pre-exist in a component or develop during operation. The simplest failure criteria assume that materials are perfectly homogeneous, isotropic, and free from defects, so that a specimen fails when the stress attains the ultimate strength. However, this is seldom true for real materials, which usually contain discontinuities or defects that may act as stress risers, reducing the overall strength and leading to premature, unexpected failure. The need for in-depth understanding of failure processes triggered the development of fracture mechanics. In contrast to the traditional approach, fracture mechanics assumes the presence of discontinuities in the material, and considers the crack size in failure assessment. The main objective of fracture mechanics is, therefore, to quantify the critical relationship between the applied stress and the size of a defect that would cause catastrophic failure under service. The property that links these two parameters (i.e. stress and crack size), and measures the resistance of a material to crack initiation and propagation is known as the fracture toughness (K_C). Fracture mechanics distinguishes three basic modes of loading that a crack can experience: a) mode I, or opening/tensile mode; b) mode II, or shearing in-plane; and c) mode III, or shearing out-of-plane.

The prediction of failure is one of the main concerns in rock mechanics. However, it is essential to consider that rock materials are discontinuous at all scales. At the micro-scale, rocks contain inherent discontinuities in the form of pores, grain boundaries or microcracks, which can produce high stress concentrations under loading. Since the tensile strength of a rock material is comparatively lower than its compressive and shearing stresses, the mode I fracture toughness (K_{IC}) arises as the most relevant and studied parameter in rock fracture mechanics: the higher the value of K_{IC}, the larger the resistance to

the propagation of tensile cracks. Fracture toughness may have paramount importance in engineering projects involving rock materials, such as thermal (e.g., geothermal and high-level radioactive waste disposal projects), mechanical (e.g., pillar/cave stability in mining), hydraulic/chemical (e.g., hydraulic fracturing, geological storage of CO_2 and underground coal gasification) and process engineering (e.g., drilling, cutting and ore crushing). In recent years, the investigation of crack initiation and propagation in geological materials has become relevant due to the necessity of solving fracture problems in geophysics. In particular, the increasing demand for hydrocarbons has promoted the need for more research on the fracture mechanics of certain lithologies (e.g., tight sands and shales). For this reason, developing appropriate testing methods, with the resulting improvement in accuracy of fracture toughness values, has attracted significant interest. The International Society for Rock Mechanics (ISRM) has proposed four suggested methods for determining K_{IC} using core-based specimens, namely the short rod (SR), chevron bend (CB), cracked chevron notched Brazilian disc (CCNBD), and semi-circular bend (SCB) methods. Some of these methods may be difficult to apply on a routine basis due to a number of issues, such as: a) the small failure initiation and propagation loads require excellent test control; b) a relatively large sample volume is needed (CB); c) cumbersome or difficult sample preparation (SR, CB, and CCNBD); d) imprecisions in the computation of the stress intensity factor (CCNBD); e) the indirect generation of tensile loads via sample compression (especially in SCB and CCNBD); and f) the celerity of crack propagation after the peak strength is attained.

To overcome some of these limitations, the main objective of this thesis is to develop an alternate simple testing approach, referred to as pseudo-compact tension (*p*CT) test, to measure K_{IC} in rocks using cylindrical single edge-notched specimens loaded in pure tension. The *p*CT test is based on a modification of the compact tension (CT) specimen described in the E399-90 ASTM (1997) standard method for testing metals. The *p*CT specimen is a disc-shaped (diameter-to-thickness ratio of ~2) sample that can be cut from rock cores. The two loading holes of the CT specimen are replaced in the *p*CT test by a U-shaped groove. In

addition, a thin radial notch is cut to act as a stress concentrator and provide the location for crack initiation. The geometry of the *p*CT specimen is favourable due to its simplicity, low amount of material needed, and minimal machining requirement. Once the specimen is ready for testing, the test follows a simple and straightforward procedure. The specimen is mounted on a centring cradle and put in contact with a pair of high-strength, high-stiffness steel jaws that fit into the U-shaped groove and transmit the tensile load to the sample. While one of the jaws remains in a static position, the other one is pulled away at a constant displacement rate. The tensile load within the thin notch tends to split the specimen into two symmetrical halves. The crack initiates at the notch tip and propagates along the vertical diameter of the specimen (i.e., the ligament plane).

The K_{IC} values derived with the *p*CT test were validated by comparing the results with those obtained with one of the suggested methods of the ISRM, the SCB test. The SCB specimen geometry is a semi-cylinder with a single thin notch located at the middle of its flat face. We have selected the SCB as benchmark due to its popularity, simplicity (in terms of sample preparation), and straightforward testing configuration. Four different rock types, namely Corvio, Arcera, and Pinacas sandstone and Blanco Mera granite, were used to assess their corresponding K_{IC} using both testing methods. All these rocks are nearly isotropic but differ in strength and mechanical performance. Corvio and Arcera sandstones have a relatively low strength, reduced grain size (< 1mm), high porosity and low elastic moduli. However, the Pinacas sandstone, while having a similar grain size, is significantly tougher and has lower porosity and higher elastic modulus. The Blanco Mera granite is a homogeneous rock of medium grain size (1-6 mm), low porosity and moderate strength.

In the present study, we cored the tested samples from homogeneous rock blocks using diamond drill bits. The plugs obtained were then sliced into discs with a diameter-to-thickness ratio of 2 using a circular diamond blade. For the SCB specimens we diametrically halved the discs with a modified tile saw. In the case of the *p*CT specimens, we carved the U-shaped groove using a 2 mm-thick diamond disc, making several saw-passes while displacing horizontally the

sample after each pass. The vertical position of the disc, which determines the depth of the notch, was set with the aid of a vertical spindle. Good alignment of the sample with respect to the saw was ensured with the aid of reference marks (laser level, set square) and the use of a grip fixed to a horizontal movable stand connected to a horizontal spindle. In both *p*CT and SCB specimens, we used a similar approach to cut the thin straight notch. However, in this case the notch was cut in one single blade pass using a 1 mm-thick disc. Once prepared, the samples were oven dried at 60ºC for a minimum of 24 hours.

A specially- designed experimental device was built to perform the *p*CT tests. The requirements considered in the design include portability (which imposed significant size, weight and robustness constraints), mounting simplicity and mechanical stability of specimens with different sizes during testing, easy installation of the measurement devices and replacement of the failed parts, and quickness of non-testing operations (specimen positioning, cleaning, etc.). The testing device consists of a high-stiffness frame equipped with a 50 kN push/pull load cell, two linear variable differential transducers (LVDTs), and two crack opening displacement (COD) gauges. Electric signals from all the measurement devices are integrated into a dedicated data acquisition system. The movement of the steel jaw is accomplished by means of a 5 mm- lead spindle, which converts the rotatory motion of an electric stepper motor with a step angle of 1.8º (i.e., 200 steps per revolution) into linear displacement. To improve its performance, the motor is connected to a planetary gearhead with a reduction ratio of 1:100. This simple configuration provides a high degree of accuracy in positioning (0.018º/step), equivalent to 0.25 µm/step in terms of linear movement of the shaft, which can be maintained from 0 to 50 kN. The two LVDTs, placed symmetrically on both sides on the specimen, measure the load point displacement (LPD), which corresponds to the displacement of the mobile jaw. Simultaneously, a clip-on gauge mounted on a pair of bolt-on knife-edges attached to the steel jaws measures the same magnitude for redundancy. An additional COD gauge can be mounted directly on the surface of the specimen to measure the crack mount opening displacement (CMOD). Steel knife-edge blades were glued to the samples to make possible this arrangement. While we

have recorded the load vs displacement (*P*-LPD) curves for all the specimens tested with the *p*CT methodology, CMOD has been measured only in 11 of them.

SCB specimens were tested under three-point bending on a stiff servo-electric frame equipped with a 4.448,22 N load cell. In this configuration, we used an upper steel roller to transfer a linear load on the top of the sample, while two additional lower rollers supported the sample. In this case, LPD corresponds to the vertical displacement of the loading roller. To assess CMOD, we have used a pair of LVDTs installed perpendicularly to the notch plane and facing each other along the diametric plane of the specimen. This configuration was selected in order to the problems inherent to the use of clip-on gauges with small size samples. Due to the curved nature of the top surface and the magnification of contact errors associated with the rotation of this surface as the test progresses, we glued 3D printed T-plates to the corresponding edges. For this testing method, we have recorded for all the specimens the load-CMOD (*P*-CMOD) and load-displacement (*P*-LPD) curves.

We analysed the *p*CT and SCB testing methods considering a number of relevant properties, all of them potentially affecting K_{IC}. Although fracture toughness is considered an intrinsic material property and should be reasonably independent of the specimen geometry and loading configuration, experimental K_{IC} values previously reported suggest the contrary. For this reason, *p*CT and SCB specimens 38, 50 and 100 mm in diameter were tested in order to determine size effects. Different notch length ratios were also adopted to explore the effect of notch length on fracture toughness. All the tests were performed at a constant slow displacement rate of 0.1 mm/min (to avoid dynamic effects) under ambient conditions. In this contribution, only Level I (or screening level) tests are reported. Although in this level only the maximum load (P_{max}) needs to be measured to compute K_{IC}, we continuously monitored the load, the load point displacement (LPD) and the crack mouth opening displacement (CMOD) to gain further insight into material behaviour. From the energy balances viewpoint, a crack will propagate when the energy available for crack growth exceeds the resistance of the material. Accordingly, fracture toughness can also be regarded as the energy

release rate needed to create new crack surfaces, and the load-displacement curves for each test were also used to characterize the energy content of the fracturing process. In *p*CT testing, the good control during the experiments even beyond P_{max} allowed splitting the total energy (E_{tot}) into two portions: the pre-peak (E_{pre}, that is the work done on the specimen to induce the initiation of the crack) and the post-peak (E_{post}, that is the work done on the specimen to propagate the crack) energies. To compute K_{IC}, it is necessary to know not only the peak load (P_{max}) and the notch length (a) but also the expression of the dimensionless stress intensity factor (Y') for each particular specimen geometry and loading conditions. For the SCB test, the corresponding expression (Y'_{SCB}) has been previously reported in the literature. However, for our *p*CT configuration no closed-form expression was found. In this case, the finite element method was used to derive a fourth-order polynomial function for each specimen size in terms of various notch length ratios (Y'_{pCT}).

The acoustic emission (AE) technique was used to acquire further insights about the processes of crack initiation, propagation and coalescence. AE is a non-destructive testing technique widely used to monitor the evolution of damage in rocks. When a fracture growths, crack energy is released in the form of elastic waves that travel through the material and can be recorded in real time by AE sensors placed on the specimen surface. In some specimens up to eight AE sensors were located at different distances from the starter notch to monitor the AE activity during testing. The recorded AE parameters (e.g., counts, amplitude, duration, or peak frequency) allowed the assessment of stages and processes, failure advent and cracking modes (e.g., AF:RA ratio and the improved *b*-value). In addition, using the multi-sensor array, we have computed the location of the AE hypocentres as a function of testing time, what was useful to analyse the evolution and propagation of cracks along the ligament length. Based on the AE information, we also explored the relationship between the energy release associated to the fracture process and that captured by AE (E_{AE}). Although the energy magnitudes associated with fracturing and local emission of AE are broadly different (AE can be unevenly scattered and/or attenuated in the sample and interfaces), it may be possible to identify a formal relationship between both

properties so that E_{AE} can be regarded as a proxy for the energy dissipated during the fracture process. In fact, considering that the AE activity is proportional to the number and magnitude of growing cracks, it is reasonable to assume that there might be a relation between AE energy (E_{AE}) and fracture energy.

With the obtained data, we compared the *p*CT and SCB methods from the perspectives of the mechanical evolution along the experiments, and the significance of different AE parameters at different stages of the tests. Our results show that the combination of small displacement (allowing extremely small strain rates), high load capacity and high stiffness of the testing system makes the *p*CT test convenient for the analysis of the toughness of rocks (either fragile or ductile). Moreover, the simpler sample preparation methodology of the *p*CT test compared to other tests makes it an interesting candidate for routine fracture toughness testing. According to our experimental results, it would be advisable to use medium-sized (D = 50 mm) *p*CT specimens with a relatively large notch length ratio (a/b > 0.25) to obtain more consistent K_{IC} values. For the tested rocks, crack growth was slow during the entire duration of the *p*CT experiments, and further crack extension required the continuous movement of the steel jaw. Consequently, the process of crack propagation could be controlled even after the peak strength was reached. The load-displacement (P-d) curves were well defined beyond P_{max}, providing insight into the post-peak behaviour. In general, the loading process could be divided into three major stages: (1) a period during which the curve linearly increased (elastic behaviour); (2) a non-linear period during which new microcracks were formed and the slope of the curve gradually decreased until fracture onset at P_{max}; and (3) a period of softening during which the load decreased as a macroscopic crack propagated along the ligament plane. Contrary, and with the exception of some specimens of Corvio sandstone (that is a soft rock), the loading curves for the SCB tests showed a nearly linear increase path until the specimen abruptly failed at the peak load (P_{max}). This evidences that the SCB methodology does not allow a good control beyond P_{max} and the fracture, once initiated, propagates unstably up to the outer face of the specimen. It can be argued that improving control electronics and system stiffness (to avoid elastic energy storage in the testing device) may improve the quality of the SCB

results. However, in our opinion the key point determining its poorer performance in the post-peak region is that the energy storage in the sample takes place in a volume significantly larger than that surrounding the crack tip (e.g., at the contact point of the rollers and along the ligament up to the starter notch). When load attains P_{max}, all this energy stored in the sample is released suddenly and the crack propagates unstably. However, in the case of the *p*CT test, the load is transferred to the sample along the contact lines of the pulling jaws and from there directly to the starter notch.

Based on the results 146 experiments (81 and 65 *p*CT and SCB tests, respectively), we checked the mutual consistency of the K_{IC} values obtained using both testing methodologies, and assessed the influence of features such as the specimen size or the notch length ratio. With a wide perspective, we observe that for both testing methods the results are broadly compatible in magnitude for each tested rock. Mode I fracture toughness derived from *p*CT testing for Corvio (~0.06-0.12 MPa $m^{1/2}$) and Arcera sandstones (~0.24-0.60 MPa $m^{1/2}$) is low, what is consistent with their condition of weak rocks. However, the K_{IC} values for both Pinacas sandstone and Blanco Mera granite are appreciably higher (~1.05-1.4 MPa $m^{1/2}$). For the same rocks, the SCB testing method results in values slightly larger for the Corvio Sandstone (~0.07-0.18 MPa $m^{1/2}$), but lower for the Arcera sandstone (~0.26-0.46 MPa $m^{1/2}$). In the case of the Pinacas sandstone and the Blanco Mera granite, K_{IC} results are more scattered than for *p*CT testing (~0.69-1.64 and ~0.72-1.51 MPa $m^{1/2}$, respectively). The smaller theoretical fracture process zone (FPZ, that is the microcracked volume located in the neighbourhood of the crack tip) associated with the SCB specimens should led to a potentially lower scatter in the K_{IC} results. However, what we observe is the contrary, what suggests that the FPZ would not be playing a significant role in the *p*CT testing mode. We conjecture that this is associated with the larger ligament length of *p*CT compared with the SCB specimens (~3 times).

For *p*CT tests, the tensile strength and K_{IC} were found to be strongly correlated. Although the values obtained are internally consistent (i.e., small range), K_{IC} was found to be positively related to the specimen size and negatively

related to the notch length in both testing methods. It is interesting to note that lithology seems to magnify the influence of these geometrical features on K_{IC}, and this circumstance can be determinant for the harder (strong cemented) materials (Pinacas sandstone and Blanco Mera granite). In our opinion, in addition to geometric constrains, the characteristics of the rock tested must be considered in order to set up minimum requirements for specimen dimensions in fracture toughness testing. Regarding the testing method, the size effect has a lesser impact in the *p*CT testing methodology, while the SCB test provides less consistent and sensitive information with respect the dependence on notch length.

For the *p*CT test, the good correlation found between LPD and CMOD makes possible the direct assessment of CMOD without employing direct contact transducers such as clip gauges (what is advantageous with small size samples). In turn, this is not possible with the SCB. The relationships among E_{pre} and E_{post} with E_{tot} suggest that, irrespective of lithology, sample size and notch length, the same energy level is required to initiate the fracture or controllably propagate it once initiated. The energy balances obtained have made also possible to support the conjecture of the size-dependent fracture energy value given at a constant notch length. However, our results indicate a more complex dependency, with lithology playing a significant role.

In general, the qualitative evolution of E_{AE} illustrates well the mechanical processes occurring in the tested samples, with net rate changes (acceleration/deceleration) coinciding well with the mechanical transitions. However, the assessment of E_{AE} to try to identify functional relationships with fracture energy has been unsuccessful in the present survey, although we cannot discard eventual relationships with a more comprehensive AE database.

The location of the AE hypocentres was useful to analyse the evolution and propagation of the crack along the ligament length. As expected, at peak load the events were mainly located around the notch tip for both testing methods. In the post-peak region of the *p*CT tests, the distribution conforms a vertical crack, which slightly deviates or increases lateral spread (depending on the material) as

the rock loses cohesion in the later stage of the experiments. These observations are consistent with the macrocracks observed in the specimens after testing. Micro X-ray computed tomography of *p*CT specimens revealed that the macroscopic crack did not always initiate at the notch tip and that the point of generation even varies along the specimen thickness. The semi-circular shape of the notch tip allows crack initiation to occur at any point along the circular geometry of the tip. This factor, together with the particle arrangement of the rock, may determine the deviation of the fracture from the expected propagation path, towards the left or the right side of the specimen. In the SCB tests, the location of the AE hypocentres for the hardest material (Pinacas sandstone) evidence the upwards migration of the AE events from the notch tip up to the top roller at specimen failure. However, for the softest material (Arcera sandstone) we observe a progressive damage in the area next to the loading end that originates an oblique macrocrack. This evidences the potential of the AE technique to better understand the processes associated with fracture toughness testing. In addition, from the location of the AE events it was possible to determine the approximate dimensions of the FPZ.

The analysis of peak frequencies (f_{peak}) revealed apparent inconsistencies with generally accepted behaviour (i.e. high values are expected in connection with microcrack development and low values with fracturing). However, considering the effect of acoustic attenuation it was possible to relate the appearance/disappearance of signals with specific f_{peak} and normalized amplitude (A_{norm}) with the facture processes occurring at different stress levels. In addition, the increased scattering at certain frequency ranges could be linked to the size of the growing defects.

The tensile mode was predominant in the pre-peak and late post-peak stages of the *p*CT tests according to the parametric analysis based in the AF *vs*. RA ratios. Only in the early post-peak region, where the macroscopic cracks grow due to the convergence of micro-mesocracks, a mixed-mode (tensile/shear) appeared in a limited extent. The appearance of a non-tensile cracking mode may be explained by the type or rock and properties (e.g., mineralogy, grain size,

cementation or homogeneity) which determine the orientation of the crack. According to this, if cracking requires less energy to advance through the cement than across grains, the crack plane might not be orthogonal to the tensile load and may conduct to local shearing due to the increase in tortuosity. This is supported by the geometrical features (deviation and branching in the crack plane) observed in the location of the AE events, as well as in the micro X-ray computed tomography. Finally, the analysis of the I*b-values* let us identify a relevant potential to discern the onset separating the stable and unstable crack growth. Anyhow, more specific filtering techniques are required to perform a more detailed analysis.

In summary, and considering the conclusions derived from this work, the *p*CT test presents some advantages over other fracture toughness testing methods: a) reduced rock requirement (disc-shaped specimen with a diameter-to-thickness ratio of 2); b) simpler sample preparation (straight groove and thin starter notch); c) enhanced control of crack propagation (especially beyond peak strength); d) pure tensile loading; and e) more comprehensive and detailed results both in terms of mechanical (e.g., fracture energy evolution) and AE data due to the possibility of capturing the post-peak behaviour. In addition, the testing configuration of the *p*CT test also allows keeping the samples immersed into a fluid bath, and therefore saturated, all along the experiments. This feature makes the *p*CT test suitable for studying the potential impact of saturating fluids on K_{IC}.

From a methodological point of view, a good sample alignment is essential in the SCB method to avoid mixed modes (I / II) in fracture toughness determinations. Furthermore, we also caution about the propensity of this configuration to lateral sliding when applying a linearly distributed force due to the circular nature of the loading surface. None of the two problems is significant with the *p*CT technique.

Contents

List of figures

List of tables

List of symbols and abbreviations

E	Young's modulus
ν.....	Poisson's ratio
σ_c	Compressive strength
σ_t.....	Tensile strength
σ_{yield}...	Yield stress
n_e	Effective porosity
ρ_{bulk} ...	Bulk density
ρ.....	Mass density
V_p	Ultrasonic P-wave velocity
V_s	Ultrasonic S-wave velocity
K_C.....	Fracture toughness
K_{IC}	Mode I fracture toughness
K_I.....	Mode I stress intensity factor
Y'	Dimensionless stress intensity factor
C_i.....	Coefficients of the Y' expression (i = 0 to 4)
SR.....	Short rod
CB.....	Chevron bend
CCNBD	Cracked chevron notched Brazilian disc
SCB ..	Semi-circular bend
CT.....	Compact tension
*p*CT...	pseudo-compact tension
BD.....	Centre-cracked Brazilian disc

BDT ..	Uncracked Brazilian disc test
CCNSCB	Cracked chevron notched semi-circular bend;
WS....	Wedge splitting
MDCT	Modified disk-shaped compact tension
C	Corvio sandstone
AR.....	Arcera sandstone
PN.....	Pinacas sandstone
GR	Blanco Mera granite
R	Specimen radius
B	Specimen thickness
D	Specimen diameter
G_w	U-shaped groove width
G_d.....	U-shaped groove depth
a.....	Notch length
b.....	Distance from the base of the groove to the specimen bottom
a/b.....	Notch length ratio (for pCT specimens)
a/R	Notch length ratio (for SCB specimens)
s.....	Span length
P	Load
P_{max}...	Maximum (peak) load
d.....	Displacement
d_{peak} ..	Displacement at the peak load
σ_{max}...	Applied stress at the maximum load
σ_0	Applied stress
COD..	Crack opening displacement
CMOD	Crack-mouth opening displacement
LPD...	Load point displacement
LVDT.	Linear variable differential transducer
AE.....	Acoustic emission

FE	Finite element
FPZ ...	Fracture process zone
r_{FPZ}	Radius of the fracture process zone
E_{tot}	Total energy from *P*-LPD curves
$E_{tot\text{-}CMOD}$	Total energy from *P*-CMOD curves
E_{pre}	Pre-peak energy
E_{post} ...	Post-peak energy
E_{AE}	AE energy
A	Peak amplitude
A_{norm} ..	Normalized amplitude
AF	Average frequency
RA	Rise angle
FFT ..	Fast Fourier transform
f_{peak} ...	Peak frequency
λ.....	Acoustic wavelength
v.....	Wave propagation velocity
LL	Low peak frequency; low normalized amplitude
LH	Low peak frequency; high normalized amplitude
ML....	Medium peak frequency; low normalized amplitude
HL	High peak frequency; low normalized amplitude
HH	High peak frequency; high normalized amplitude

1. Introduction

1.1. Motivation

The prediction of failure is one of the main concerns in rock mechanics. Since tensile failure is the most common and most important failure mode encountered in brittle materials, the assessment of the tensile strength of rock has attracted special attention. However, performing direct tensile tests in rocks presents some inherent difficulties due to factors such as cumbersome testing arrangements, stress concentration at the loading ends, or tedious sample preparation. As a consequence, the study of tensile failure of rock remains incomplete due to the scarce complete stress-strain curves obtained from direct tensile tests (Tang and Hudson 2010).

The simplest criterion to predict failure is based on the assumption that a material fails when the stress (or strain) reaches its critical value, i.e., the strength of the material. However, this approach disregards the inherent existence of defects such as cracks or voids. Alternatively, the fracture mechanics approach considers the presence of these defects by introducing the crack size as an additional parameter in failure assessment (Anderson 2005). In fact, brittle materials such as rock contain flaws (e.g. voids, pores, microcracks, grain boundaries, etc.) that can increase the stress locally and induce premature failure before the strength of the material is reached. What is more, rock failure is essentially related to the processes of crack initiation and propagation, so the concept of fracture toughness (i.e. the resistance of a material to the propagation of pre-existing defects, K_C) is of special importance in rock mechanics. The study of rock fracture toughness has significant implications in the field of geomechanics and geotechnical engineering, not only in activities like tunnelling or underground excavation but also in energy production.

In the oil and gas industry, fracture toughness has a crucial importance. In recent years, unconventional resources such as shale gas or tight oil have attracted increasing attention due to the downward productivity of conventional reservoirs, which can no longer meet the demand (Taghichian et al. 2018). In unconventional reservoirs, the low permeability of the materials (e.g. tight sandstone or shale) prevents oil and/or gas to flow from the rock formation to the well. A stimulation approach aimed at increasing permeability and enhance extraction consists of injecting fluids under high pressure into the bedrock. This process, known as hydraulic fracturing, induces the creation of new fractures in the rock (in the direction of least resistance) and increases the size and connectivity of the pre-existing cracks. To initiate and propagate tensile fractures under controlled conditions, the fracture toughness of the rock, together with the closure pressure of the formation, have to be overcome (Skomorowski 2016). It is therefore evident that fracture toughness, and in particular mode I (tensile) fracture toughness (K_{IC}), is one of the key parameters that must be considered when designing hydraulic fracturing projects.

In recent years, the contribution of greenhouse gases (e.g., CO_2 emissions associated with burning fossil fuels) to global warming has been a growing concern. Different approaches have been proposed to reduce the levels of CO_2 in the atmosphere and slow down the greenhouse effect. In some of them, such as the use of energy sources with low CO_2 emissions (e.g., geothermal or nuclear energies) or the capture and geological storage of CO_2, the Earth's subsurface plays a major role (Canal-Vila 2016). In order to ensure safe operation and optimize the performance of these technologies, it is essential an in-depth understanding of the processes occurring in the subsurface, as well as the geochemical and mechanical properties of the host rock. For instance, the efficiency of enhanced geothermal systems (EGS), which highly depends on the dimensions of the heat exchange surfaces between the rock and the circulating fluid (Pellet 2018), is conditioned by the precise design and control of hydraulic fractures in the system and therefore, by the proper determination of K_{IC} (Stoeckhert et al. 2016). Similarly, the assessment of fracture toughness is also

essential for safe CO_2 storage in saline aquifers (Xiankai et al. 2018). However, the objective in this case is precisely the opposite, i.e. to avoid the propagation of fractures during fluid injection. In fact, the success of large-scale CO_2 geosequestration and long-term storage highly depends on the capacity of the reservoir to avoid potential leakage of CO_2 along underground pathways such as fractures (Muñoz-Ibáñez et al. 2020). This is also crucial in nuclear energy production, where one of the main concerns is the large levels of hazardous radioactive waste that are disposed in the subsurface (Feng et al. 2019). In order to prevent tensile fracturing of the rock, the geomechanical properties of the reservoirs, including fracture toughness, must be properly defined.

Several experimental studies have been developed in order to gain insight into the fracture behaviour of rocks, including fast brittle fracture, and subcritical (stable) crack growth (Takahashi 1983). A number of experimental procedures have been proposed for the determination of K_{IC} in rocks, and the International Society for Rock Mechanics (ISRM) has endorsed four of them as suggested methods. However, these methods present some drawbacks. In this contribution we propose a new method (*pseudo*-compact tension or *p*CT test) useful to assess the K_{IC} of rocks using disc-shaped specimens loaded under pure tension conditions. In contrast to the methods proposed by the ISRM, the *p*CT method has several advantages like simple sample preparation, small sample requirement, limited size effects, and steady propagation of crack beyond peak load. All of these attributes are valuable to fulfil the necessities of the industry.

1.2. Objectives

The main objectives of the present work are: i) to deepen into the knowledge of the processes that determine the subcritical (i.e. low speed) development of cracks in rock materials; and ii) to develop a new method (*p*CT) for the assessment of mode I fracture toughness (K_{IC}) in rocks.

The previous main objectives can be split into the more specific elements enumerated next: i) based on available information, to design a new experimental device useful to determine K_{IC} by considering simple mechanical concepts and

sufficient performance, simple sample preparation and good reproducibility; ii) to build and to test the functionality of the testing device under prescribed conditions; iii) to develop a methodological framework for the new testing approach, and to compare the obtained results with other recommended techniques aimed at determining K_{IC}; and iv) to apply the new experimental method to different rock-types and to assess the influence of geometrical factors such as specimen size or notch length on K_{IC}.

1.3. Thesis organization

This dissertation is organized around three journal articles (Chapters 3 to 5) which are published or submitted to peer-reviewed journals for publication. The main results of this research are presented in these three chapters. In addition, this thesis includes an introduction, a literature review, conclusions, and future work, and two appendices.

- **Chapter 1** is an introduction to the present dissertation, states the objectives of this thesis, and provides with a list of publications arisen from this work.
- **Chapter 2** encompasses a short literature review of fracture mechanics, focusing on mode I fracture toughness.
- **Chapter 3** presents the new testing approach, called the pseudo-compact tension (*p*CT) method, to measure mode I fracture toughness (K_{IC}) in rock. We present the experimental results of a series of tests performed using four different lithologies, and we provide an expression for the mode I dimensionless stress intensity factor for the particular specimen geometry and loading conditions. We conclude that the *p*CT test is an interesting candidate for routine fracture toughness testing, either in fragile or ductile rocks. This chapter is published in '*Rock Mechanics and Rock Engineering*'.
- In **Chapter 4**, we check the mutual consistency of the K_{IC} values obtained with the *p*CT test and those obtained with one of the methods suggested by the International Society of Rock Mechanics

(ISRM), the semi-circular bend (SCB) method. We discuss the results of 146 tests, while considering a number of relevant properties. We conclude that both specimen size and notch length influence K_{IC}, although the magnitude of their impact is closely related to lithology. In addition to yielding more consistent results that the SCB test, the *p*CT method also provides with a greater wealth of fracture mechanics information, such as the fracture evolution. This chapter has been submitted to '*International Journal on Rock Mechanics and Mining Sciences'*.

- **Chapter 5** extends the work presented in Chapters 3 and 4 by presenting the acoustic emission (AE) data recorded during the *p*CT and SCB tests. We compare the mechanical evolution and the significance of different AE parameters in both testing methods. We also analyse the hypocentre location of AE events and the I*b-value*, and assess the crack modes using a parameter-based strategy. We conclude that the *p*CT test provides more comprehensive and detailed information in terms of AE data. This chapter will be submitted to '*Journal of Petroleum Science and Engineering*'.
- **Chapter 6** summarizes the main conclusions of this study, provides methodological recommendations for performing fracture toughness tests, and suggests future research lines.
- **Appendix A** contains the extended abstract of this thesis in Spanish and Galician languages.
- **Appendix B** provides a detailed description of the specially-designed testing device used to perform *p*CT tests.
- **Appendix C** presents briefly the results of a series of *p*CT tests performed under saturated conditions. We used two different rock types and seven wetting and non-wetting fluids with geological and/or industry related applications. We conclude that fluids have an impact on the K_{IC}, the stiffness, and the energy needed for the generation and propagation of the cracks.

1.4. Publications

A number of publications, including peer-reviewed papers and conference contributions, have arisen from this investigation. These publications, together with other closely related work, are listed below:

1.4.1. Scientific journal papers

- Muñoz-Ibáñez, A., Delgado-Martín, J., Grande-García, E. (2019) Acoustic emission processes occurring during high-pressure sand compaction. *Geophysical Prospecting*, 67: 761-783.
- Muñoz-Ibáñez, A., Falcon-Suarez, I. H., Marín-Moreno, H., Delgado-Martín, J., Mackin, P. (2020) Transport properties of saline CO_2 storage reservoirs with unconnected fractures from brine-CO_2 flow-through tests. *Journal of Petroleum Science and Engineering*, 184: 106551.
- Muñoz-Ibáñez, A., Delgado-Martín, J., Costas, M., Rabuñal-Dopico, J., Alvarellos-Iglesias, J., Canal-Vila, J. (2020) Mode I Fracture Toughness Determination in Rocks Using a Pseudo-Compact Tension (*p*CT) Test Approach. *Rock Mechanics and Rock Engineering*, 53(7): 3267-3285
- Falcon-Suarez, I. H., Papageorgiou, G., Jin, Z., Muñoz-Ibáñez, A., Chapman, M., Best, A.I. (2020) CO_2-brine substitution effects on ultrasonic wave propagation through sandstone with oblique fractures. *Geophysical Research Letters.*
- Muñoz-Ibáñez, A., Delgado-Martín, J., Juncosa-Rivera, J. (*subm*.) Experimental investigation on the size and other effects on mode I fracture toughness in selected rock types using the *p*CT and SCB testing methods. *International Journal of Rock Mechanics and Mining Sciences*.
- Muñoz-Ibáñez, A., Herbón-Penabad, M., Delgado-Martín, J., Alvarellos-Iglesias, J. (*to be subm.*) Acoustic emission monitoring of

mode I fracture toughness tests on sandstone rocks. *Journal of Petroleum Science and Engineering.*

1.4.2. Conference contributions

- Delgado-Martín, J., Muñoz-Ibáñez, A., Grande-García, E., Rodríguez-Cedrún, B. (2016) Phenomenological Description of Acoustic Emission Processes Occurring During High-Pressure Sand Compaction. In: *EGU General Assembly 2016, 17-22 April, Vienna, Austria.* [Poster]
- Muñoz-Ibáñez, A., Grande-García, E., Rodríguez-Cedrún, B., Delgado-Martín, J. (2016) Descripción fenomenológica de procesos de emisión acústica durante la compactación de arena a alta presión. In: Sociedad Española de Mecánica del Suelo e Ingeniería Geotécnica, Sociedade Portuguesa de Geotecnia, Sociedad Española de Mecánica de Rocas (eds.) *Reconocimiento, tratamiento y mejora del terreno: 10º Simposio Nacional de Ingeniería Geotécnica, 19th - 21st October, A Coruña, Spain.* 175-182. [Proceedings & Presentation]
- Muñoz-Ibáñez, A., Delgado-Martín, J., Grande-García, E. (2017) Acoustic emission processes occurring during high-pressure sand compaction. In: *4th International Workshop on Rock Physics, 29th May - 2nd June, Trondheim, Norway.* [Presentation]
- Muñoz-Ibáñez, A., Falcon-Suarez, I. H., Marín-Moreno, H., Delgado-Martín, J. (2018) Transport properties of saline reservoirs with non-connected fractures during CO_2 injection. In: *IEAGHG Summer School 2018, 25th - 29th June, Trondheim, Norway.* [Poster]
- Muñoz-Ibáñez, A., Falcón-Suárez, I. H., Marín-Moreno, H., Delgado-Martín, J. (2018). Experimental insights into the sealing and storage capacity of fractured saline reservoirs during CO_2 injection. In: *AGU Fall Meeting 2018, 10th - 14th December, Washington, EEUU*. [Presentation]

- Falcón-Suárez, I. H., Muñoz-Ibáñez, A. (2018). Pore fluid distribution in saline sandstone CO_2 storage reservoirs with aligned fractures: Experimental geophysical assessment. In: *AGU Fall Meeting 2018, 10th - 14th December, Washington, EEUU*. [Poster]
- Muñoz-Ibáñez, A., Delgado-Martín, J. (2019). Assessment of fracture toughness in rock using a new pseudo-compact tension (*p*CT) test and acoustic emission. In: *5th International Workshop on Rock Physics, 23rd – 26th April, Hong Kong.* [Presentation]
- Muñoz-Ibáñez, A., Delgado-Martín, J., Costas-Piñó, J., Rabuñal-Dopico, J., Alvarellos-Iglesias, J., Canal-Vila, J. (2019). K_{IC} measurement of rocks using a pseudo-compact tension (*p*CT) test. In: Fontoura, S.A.B., Rocca, R.J., Pavón-Mendoza, J.F. *Rock Mechanics for Natural Resources and Infrastructure Development. Proceedings of the 14th International Congress on Rock Mechanics and Rock Engineering (ISRM 2019), 13rd - 18th September, Foz do Iguassu, Brazil. 1005-1013* [Proceedings & Presentation]
- Muñoz-Ibáñez, A., Delgado-Martín, J. (2019). Experimental investigation on the size effects of K_{IC} in selected rock types. In: Fontoura, S.A.B., Rocca, R.J., Pavón-Mendoza, J.F. *Rock Mechanics for Natural Resources and Infrastructure Development. Proceedings of the 14th International Congress on Rock Mechanics and Rock Engineering (ISRM 2019), 13rd - 18th September, Foz do Iguassu, Brazil. 1173-1179* [Proceedings & Presentation]
- Muñoz-Ibáñez, A., Delgado-Martín, J., Juncosa-Rivera, R., Romera-Rodríguez, L., Alejano-Monge, L., Canal-Vila, J., González-Molano, N., Avarellos-Iglesias, J., López-Puiggene, E., Lakshmikantha, M.R. (2019). Development of a true triaxial device for hydraulic fracturing experiments. In: Fontoura, S.A.B., Rocca, R.J., Pavón-Mendoza, J.F. *Rock Mechanics for Natural Resources and Infrastructure Development. Proceedings of the 14th International Congress on Rock Mechanics and Rock Engineering (ISRM 2019), 13rd - 18th*

September, Foz do Iguassu, Brazil. 1195-1202 [Proceedings & Poster]

- Muñoz-Ibáñez, A., Delgado-Martín, J. (2019). Acoustic emmission monitoring of cracking processes in rock using semi-circular bend and pseudo-compact tension tests. In: *12th International Congress on Mechanics, 22nd - 25th September, Thessaloniki, Greece.* [Presentation]
- Muñoz-Ibáñez, A., Herbón-Penabad, M., Delgado-Martín, J. (2019). Impact of Saturating Fluids on Mode-I Fracture Toughness of a Porous Siliceous Sandstone and a Granitic Rock. In: *AGU Fall Meeting 2019, 9th - 13th December, San Francisco, EEUU*. [Poster]

1.5. References

Anderson TL (2005) Fracture mechanics: Fundamentals and applications, Third Edition. CRC Press

Canal-Vila J (2016) Experimental study of effect of CO_2 injection on rocks: coupling hydrodynamic, mechanical and geochemical processesrim. PhD thesis, University of A Coruña, A Coruña, Spain

Feng G, Kang Y, Wang XC (2019) Fracture failure of granite after varied durations of thermal treatment: An experimental study. *Royal Society Open Science* 6:

Muñoz-Ibáñez A, Falcon-Suarez IH, Marín-Moreno H, Delgado-Martín J, Mackin P (2020) Transport properties of saline CO_2 storage reservoirs with unconnected fractures from brine-CO2 flow-through tests. *Journal of Petroleum Science and Engineering* 184:106551

Pellet FL (2018) Rock mechanics and environmental engineering for energy and geo-resources. In: ISRM European Rock Mechanics Symposion Eurock, St. Petersburg, Russia, 22-27 May

Skomorowski N (2016) Modelling of Multistage Hydraulic Fracture Operations in Unconventional Resources – The Application of Geomechanics and Field Data to the Optimization of Fracture Spacing and Production. PhD thesis,

University of Waterloo, Waterloo, Ontario, Canada

Stoeckhert F, Brenne S, Molenda M, Alber M (2016) Mode I fracture toughness of rock under confining pressure. In: Ulusay R, Aydan O, Hasan G, Hindistan MA (eds) Rock Mechanics and Rock Engineering: From the Past to the Future. CRC Press, pp 313–318

Taghichian A, Hashemalhoseini H, Zaman M, Beheshti Zavareh S (2018) Propagation and aperture of staged hydraulic fractures in unconventional resources in toughness-dominated regimes. *Journal of Rock Mechanics and Geotechnical Engineering* 10:249–258

Takahashi H (1983) Fracture Toughness Evaluation of Rocks in the Presence of Pressurized Water at Elevated Temperature. In: Nemat-Nasser S, Abé H, Hirakawa S (eds) Hydraulic fracturing and geothermal energy. Mechanics of elastic and inelastic solids, vol 5. Springer, Dordrecht. pp 291–305

Tang C, Hudson JA (2010) Rock failure mechanisms: Illustrated and explained. CRC Press

Xiankai B, Meng T, Jinchang Z (2018) Study of mixed mode fracture toughness and fracture trajectories in gypsum interlayers in corrosive environment. *Royal Society Open Science* 5:171374

2. State of the art: rock fracture mechanics

2.1. Introduction

Defects such as voids or cracks are inherent in every material. These features can either pre-exist in a component or develop during operation. The traditional failure criteria state that failure occurs when the stress level overcomes the ultimate strength of the material, disregarding the existence of discontinuities (Serrano and Olalla 1998). However, far from being harmless, flaws can act as local stress risers, reducing the overall strength and leading to premature, unexpected failure of a component or structure well below its design stress (Perez 2004). The need for in-depth understanding of failure processes in materials such as glass, metal and engineering ceramics triggered the development of fracture mechanics (Erdogan 2000). In contrast to the traditional approaches, fracture mechanics assumes the presence of discontinuities in the material, and introduces the crack size as an additional parameter in failure assessment (Anderson 2005). The main objective of fracture mechanics is, therefore, to quantify the critical relationship between the applied stress and the size of a defect that would cause catastrophic failure under service. The property that links these two parameters (i.e. stress and crack size), and measures the resistance of a material to crack initiation and propagation is known as the fracture toughness (Anderson 2005).

Irwin (1958) introduced the three different loading modes that a crack can experience (Figure 2.1). In mode I (opening or tensile mode), the crack is subjected to a normal stress (σ) and the crack faces open perpendicular to the crack plane. In mode II (sliding mode), an in-plane shear stress (τ_i) slides the crack faces relative to each other in the crack plane and perpendicular to the

crack front. In mode III (tearing mode), an out-of-plane shear stress (τ_o) moves the crack surfaces in the crack plane but parallel to the crack front. In the case that both normal and shear stresses act over a crack at the same time, the fracture state (i.e. stress and displacement components) can be described as a combination of the three previous basic modes of loading by applying the principle of superposition.

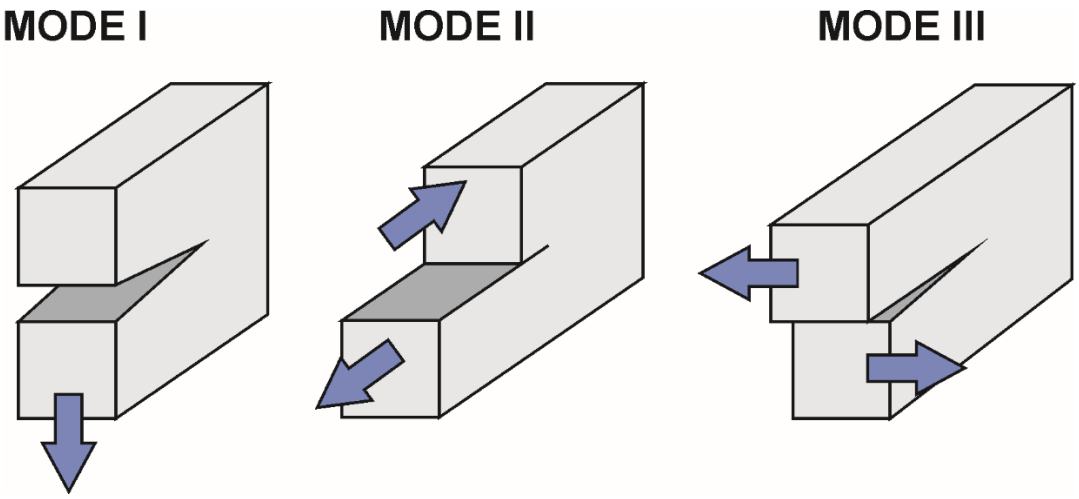

Figure 2.1: Three basic modes of loading. Figure adapted from Anderson (2005).

Rock materials are discontinuous at all scales. At the micro-scale, rocks contain inherent discontinuities in the form of pores, grain boundaries, or microcracks, which can produce high stress concentrations under loading (Whittaker et al. 1992). In recent years, the investigation of crack initiation and propagation in geological materials has become relevant due to the necessity of solving fracture problems in geophysics. In particular, developing appropriate testing methods, with the resulting improvement in accuracy of fracture toughness values, has attracted significant interest. Due to the presence of defects, brittle materials such as rocks are characterized by having lower tensile than compressive or shear strength (Beer et al. 2012). For this reason, one of the main objectives of rock fracture mechanics is to obtain a representative value of the mode I fracture toughness (K_{IC}): the higher the value of K_{IC}, the larger the resistance to the propagation of tensile cracks.

2.2. Fracture toughness

Crack growth can be predicted from two different perspectives that will be discussed in the following: the energy balance criterion, and the stress intensity approach.

2.2.1. The energy-balance approach

The base of fracture mechanics started with the experimental studies of Griffith (1920), who assessed the fracture strength of a brittle solid (glass) containing a pre-existing sharp crack. His work is based on the previous studies of Inglis (1913) focused on determining the stress concentrations around an elliptical hole in a plate. Griffith proposed the first energy criterion for fracture, which is valid for perfectly brittle linear elastic solids and states that fracture occurs when the energy available for crack growth (i.e., for generating two new crack surfaces) is sufficient to overcome the resistance of the material (Lawn 1993). This thermodynamics approach is based on the principle of energy conservation: Griffith's theory assumes that the energy added to and released from the body must be same as the dissipated energy during crack extension (Sun and Jin 2012). For an infinite plate subjected to a tensile stress (σ) which contains a through-thickness crack of length *2a* (Figure 2.2a), the critical stress at failure (σ_f) is given by:

$$\sigma_f = \sqrt{\frac{2\gamma_s E'}{\pi a}} \tag{2.1}$$

where γ_s is the surface energy of the material (and consequently $2\gamma_s$ is the work of fracture), and $E' = E$ for plane stress, and $E' = E/(1-\nu^2)$ for plane strain, being E the Young's modulus, and ν the Poisson's ratio. Equation (2.1) provides a relationship between failure stress and crack length, and gives the criterion for crack growth: the crack will advance if the energy stored in the system is equal or larger to the critical energy (i.e. $\sigma \geq \sigma_f$ in terms of stress).

Irwin (1957) modified Griffith's theory and defined the concept of energy release rate (G), which represents the energy per unit area required for crack propagation:

$$G = 2\gamma_s = \frac{\pi\sigma^2 a}{E'} \tag{2.2}$$

According to the previous expression, crack growth will occur when G reaches the critical energy release rate (G_c), which is considered a material property:

$$G_c = \frac{\pi\sigma_f^2 a}{E'} \tag{2.3}$$

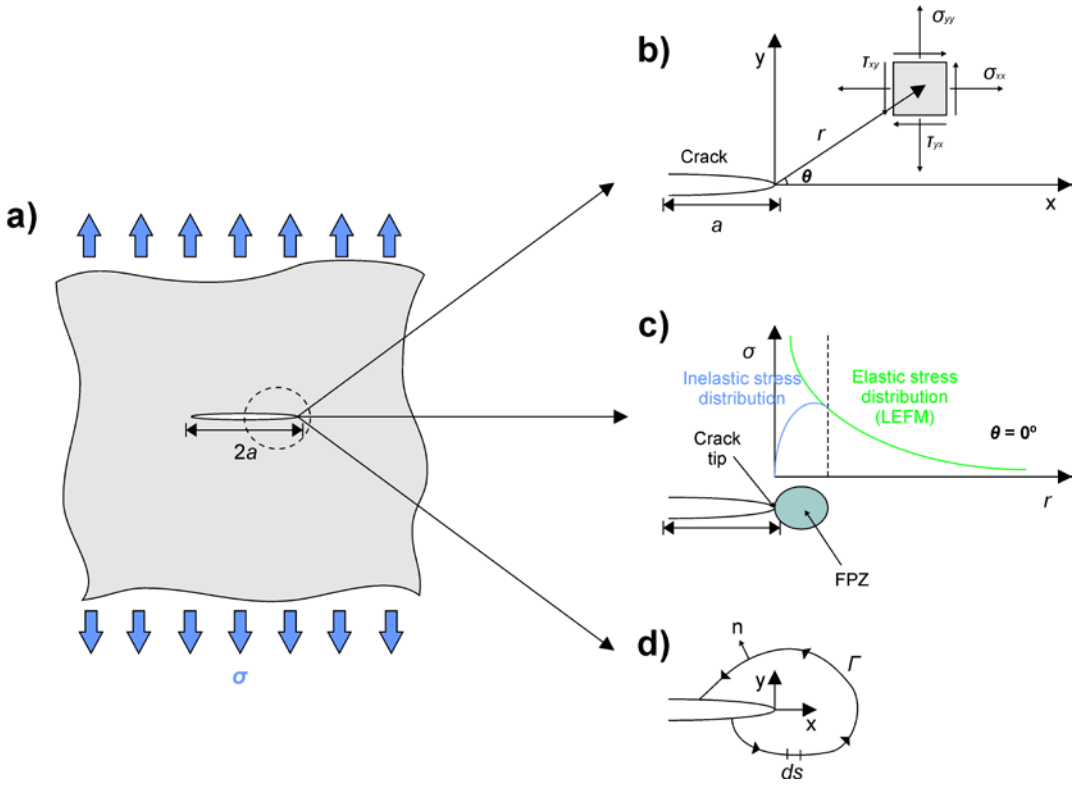

Figure 2.2: (a) Infinite plate subjected to a remote tensile stress (σ) and containing through-thickness crack of length 2a. (b) Definition of the coordinate axes and the stresses near the crack tip. (c) Stress distribution ahead of the crack tip, and location of the fracture process zone (FPZ). (d) Contour around the crack tip. Note: All the figures have been adapted from Anderson (2005).

As previously mentioned, Griffith's theory was limited to linear elastic materials (e.g., glass or ceramics). In order to extended his approach by considering the inelastic deformation at the crack tip observed for ductile (and even brittle) materials, Irwin (1948) and Orowan (1949) added a term representing the plastic energy dissipation (Anderson 2005):

$$G = 2\left(\gamma_e + \gamma_p\right) \tag{2.4}$$

where γ_e is the elastic surface energy, and γ_p is the plastic surface energy.

2.2.2. The stress intensity approach

Linear elastic fracture mechanics (LEFM) is based on the description of the stress field near the crack tip developed by Irwin (1957), who introduced the concept of the stress intensity factor (K). For an infinite plane with a sharp, through-thickness crack of length $2a$ subjected to a tensile stress (σ) acting perpendicular to the crack plane (mode I), the stress distribution ahead of the crack tip is given by:

$$\begin{bmatrix}\sigma_{xx}\\ \sigma_{yy}\\ \tau_{xy}\end{bmatrix} = \frac{K_I}{\sqrt{2\pi r}} cos\left(\frac{\theta}{2}\right)\begin{bmatrix}1 - sin\left(\frac{\theta}{2}\right)sin\left(\frac{3\theta}{2}\right)\\ 1 + sin\left(\frac{\theta}{2}\right)sin\left(\frac{3\theta}{2}\right)\\ sin\left(\frac{\theta}{2}\right)cos\left(\frac{3\theta}{2}\right)\end{bmatrix} \tag{2.5}$$

$$\sigma_{zz} = \nu\left(\sigma_{xx} + \sigma_{yy}\right), \text{for plane strain}$$

$$\sigma_{zz} = 0, f\text{or plane stress}$$

$$\tau_{xz} = \tau_{yz} = 0$$

where σ_{ii} and τ_{ij} are the normal and shear stress components, respectively (the subscripts i and j indicate the x, y and z directions in the Cartesian coordinate system), and r and θ are the cylindrical polar coordinates of a point with respect to the crack tip (Figure 2.2b). K_I is defined as the mode I stress intensity factor, usually expressed in MPa $m^{1/2}$ in the S.I. system. Once K_I is known it is possible to obtain all the components of stress (as well as strain and displacement; see Anderson (2005)) as a function of r and θ. The expression of K_I for an infinite body with a central crack of length $2a$ is shown in Equation (2.6).

$$K_I = \sigma\sqrt{\pi a} \tag{2.6}$$

The stress intensity factor, which describes the stress field at the crack tip region, turns out to be one of the most important concepts in fracture mechanics. However, the expression of K_I given in Equation (2.6) is only valid for an infinite body, and needs to be modified to consider the presence of free finite surfaces. This is accomplished by introducing a correction factor, known as dimensionless stress intensity factor (*Y'*), which accounts for different specimen geometries and loading configurations:

$$K_I = Y'\,\sigma\sqrt{\pi a} \tag{2.7}$$

From the general expression of K_I given in Equation (2.7), it is seen that the stress intensity factor can be computed for any combination of σ and *a* as long as *Y*' is known. *Y'* is usually expressed in the form of an algebraic, trigonometric, or polynomial function. For simple geometries and loading conditions, the expression of *Y'* can be derived analytically, and several closed-form solutions for K_I and *Y'* can be found in the literature for common configurations (Whittaker et al. 1992; Lawn 1993). However, more complex situations require using numerical techniques, such as the finite element method (FEM), to derive *Y'* (Lawn 1993).

Just as the energy balance criterion, the stress intensity approach can be used to assess eventual crack growth or failure of a specimen containing a pre-existing defect: for mode I loading, crack initiation and propagation will occur when K_I reaches its critical value, called mode I fracture toughness (K_{IC}), in the region of the crack tip. K_{IC}, which reflects the ability of a component containing a flaw to resist tensile fracture, is defined as the value of the mode I stress intensity factor at which the crack starts to develop. Taking the expression of the stress intensity factor given in Equation (2.7), K_{IC} can be computed as a function of the external peak load (i.e., the maximum applied stress, σ_{max}), the crack length (*a*), and the specimen geometry and loading configuration (implicit in the expression of *Y'*) as follows:

$$K_{IC} = Y'\sigma_{max}\sqrt{\pi a} \tag{2.8}$$

Fracture mechanics assumes that the fracture toughness is a material property and, therefore, it should be independent of the size and geometry of the specimen tested. However, this assumption is only valid as long as the conditions for LEFM are met (see section 2.2.4 for further discussion).

2.2.3. Equivalence of G and K

As previously discussed, a crack (in mode I loading) will propagate when the stress intensity factor (K_I) or the energy release rate (G_I) exceed their critical value (K_{IC} or G_{IC}, respectively). Therefore, G_I and K_I (and likewise G_{IC} and K_{IC}) cannot be completely independent of each other. As long as the crack extends along its own plane (i.e., no mixed mode conditions) and the material is linear elastic, Irwin (1957) demonstrated that the energy and stress intensity approaches can be related through the following expression:

$$G_I = \frac{K_I^2}{E'} \tag{2.9}$$

The same relationship holds for G_{IC} and K_{IC}.

2.2.4. Non-linear fracture mechanics

According to the linear elastic stress solution (Equation (2.5)), a singularity occurs when $r \rightarrow 0$, or in other words, the stress approaches infinity at the crack tip (Figure 2.2c). However, this situation is physically impossible, and the assumption of linear elasticity might not be valid for the region around the crack tip. This zone of inelastic material behaviour is called the fracture process zone (FPZ), and is characterized for plastic yielding for ductile materials (e.g., metal) or microcracking in brittle (e.g. rock) materials (Hoagland et al. 1973). For the latter, the radius of the inelastic zone (r_{FPZ}) can be determined from the mode I fracture toughness and the tensile strength (σ_t) of the material as follows (Schmidt 1980):

$$r_{FPZ} = \frac{1}{2\pi}\left(\frac{K_{IC}}{\sigma_t}\right)^2 \tag{2.10}$$

Since the stress intensity factor is a linear-elastic concept, it can only be applied if the size of the FPZ is sufficiently small compared to the dimensions of the specimen (Whittaker et al. 1992). Otherwise, LEFM concepts are no longer valid, and other parameters used in elastic-plastic fracture mechanics (EPFM) are needed to describe the stress state at the crack tip (Anderson 2005).

Different approaches have been developed to characterize the nonlinear behaviour of the material ahead of a crack (Zhu and Joyce 2012). Among them, it is worth mention the concept of J-integral (Rice 1968) for computing the energy release rate associated with crack extension. The parameter *J* is equivalent to *G* for linear elastic conditions and, consequently, to the stress intensity factor (*K*). The J-integral, which can therefore be used in both LEFM and EPFM, is path independent: its value remains constant for any continuous path (Γ) within the body that includes the crack tip and connects the bottom and top crack surfaces (Figure 2.2d):

$$J = \int_{\Gamma} \left(W\, dy - \boldsymbol{t} \frac{\partial \boldsymbol{u}}{\partial x} ds \right) \tag{2.11}$$

In Equation (2.11), *W* is the strain energy density, $\boldsymbol{t}$ is the traction vector, $\boldsymbol{u}$ is the prescribed displacement vector, and *s* is the arc length along the arbitrary contour Γ (Anderson 2005). The traction vector is given by $\boldsymbol{t} = \boldsymbol{\sigma n}$, with $\boldsymbol{n}$ being the normal vector on Γ.

2.3. Mode I fracture toughness in rock

Mode I fracture toughness (K_{IC}) is a useful parameter that has been widely applied in many engineering fields related to rock failure, such as slope stability analysis, tunnel boring, rock drilling, blasting and rock fragmentation, hydraulic fracturing, and oil exploration (Whittaker et al. 1992; Feng 2017). In rock mechanics, fracture toughness is used as: (a) a parameter for classification of rock material; (b) a fragmentation index; and (c) a material property in rock modelling and stability analysis (ISRM Testing Commission 1988).

2.3.1. Considerations for K_{IC} testing

K_{IC} can be determined experimentally by testing a rock specimen that contains a pre-existing notch, which can be either straight or chevron-shaped. Straight notches require the fabrication of a sharp notch tip, which can be accomplished either by using a sufficiently thin saw disk or by pre-cracking under cyclic fatigue loading (Anderson 2005). Since none of these two approaches is easy to carry out in practice for materials such as rocks (Ayatollahi et al. 2016; Wei et al. 2016a), chevron notches have emerged as an alternative. The V-shape of the chevron notch allows crack onset at the ligament tip, where the highest tensile stress develops (Newman 1984). As the crack grows along the ligament, the width of the crack front increases so that crack propagation can be initially stable for a relatively long period under increasing load (Guo et al. 1993). Afterwards, when the crack reaches its critical length, sudden failure occurs. The peak load (used to compute K_{IC}) occurs at the transition between the stable and unstable behaviours. The chevron notch can have some advantages over the straight one, such as low loads for crack initiation due to the high stress concentration (Ayatollahi et al. 2016). For the chevron geometry, it is assumed that the crack initiates at the notch tip, and then propagates forming a perfect straight-through, planar symmetric crack front along the ligament plane. If this condition is met, data scattering would be reduced. However, numerical models have revealed that the local stress concentrations in the chevron notch causes the main fracture to grow not only from the notch tip but also from both sides of the notch (Wei et al. 2015). In addition, far from being straight, the actual crack front is considerably curved irrespective of the degree of heterogeneity of the material, inducing errors for fracture toughness measurement.

Although it can be easily accomplished for ductile materials such as metals, the application of pure tensile stresses to materials with a brittle or quasi-brittle behaviour (e.g., ceramics, rocks, and concrete) entails difficulties related to testing arrangements and sample preparation (Perras and Diederichs 2014). For this reason, most of the experimental methods developed to measure K_{IC} in rocks are indirect, that is, the tensile failure is induced by subjecting the

specimens to a compressive load. As a result, there may appear concentrated-load effects as well as shear force components (Li and Wong 2013). The main drawback is that the tensile strength obtained from indirect testing is generally larger than that derived from direct methods (Perras and Diederichs 2014). Since it is expected that K_{IC} is overestimated when derived from indirect testing, there is need of a simple direct method to determine K_{IC} of rock in order to reduce uncertainty in results.

As previously discussed, limitations such as the difficult specimen preparation and the brittle nature of the material have to be considered in rock testing. In the literature, several specimen geometries and testing techniques can be found to determine mode I fracture toughness in rocks. According to the loading configuration, we can group these methods in four major categories: i) compressive tests (e.g., Brazilian disc (Guo et al. 1993), cracked straight through Brazilian disc (Awaji and Sato 1978), flattened Brazilian disc (Wang and Xing 1999), diametral compression (Szendi-Horvath 1980), and modified ring (Thiercelin and Roegiers 1988) tests); ii) three-point bending tests (e.g., chevron notched semi-circular bend (Kuruppu 1997), single edge crack round bar bend (Ouchterlony 1981), single edge notched bending (Tutluoglu and Keles 2011; Ko and Kemeny 2013), straight-notch disc bending (Tutluoglu and Keles 2011) tests; iii) tensile tests (e.g., compact tension (Ouchterlony 1982), round compact tension (Sun and Ouchterlony 1986), or edge notched disc (Donovan and Karfakis 2004) tests); iv) torsion (e.g., double torsion test (Nara et al. 2011)) tests.

2.3.2. ISRM suggested methods

Although there are no standard tests for measuring K_{IC} in rocks, the ISRM has proposed four suggested methods that make use of cylindrical (core-based) specimens: a) chevron bend (CB); b) short rod (SR); c) cracked chevron notched Brazilian disc (CCNBD); d) and semi-circular bend (SCB) tests (Figure 2.3).

Among them, the SR is the only direct testing method. In the CB method, a long cylindrical specimen with a chevron notch perpendicular to the core axis is subjected to three point bending (ISRM Testing Commission 1988). The

CCNBD specimen is a Brazilian disc with a chevron notch in the plane of maximum induced tensile strength which is loaded under compression (ISRM 1995). The SCB method uses semi-circular disc specimens with a straight notch subjected to three point bending (Kuruppu et al. 2014). Finally, the SR is a short cylindrical specimen with a chevron notch cut in the long-axis direction, which leaves a triangular ligament between the two halves (ISRM Testing Commission 1988). In contrast with the three previous testing techniques, in the SR a pure tensile load is applied perpendicularly to the ligament plane. The SR uses the remaining halves of the CB method, enabling to study the effect of anisotropy, and determine K_{IC} parallel and perpendicular to the core axis. While the CCNBD and the SCB methods only offer one level of testing (i.e. level I, which assumes LEFM conditions and only requires the measurement of the peak load), the CB and the SR methods offer an additional testing level (level II). Level II corrects for inelastic effects by considering a degree of nonlinearity and requires the continuous measurement of load and displacement during loading-unloading cycles.

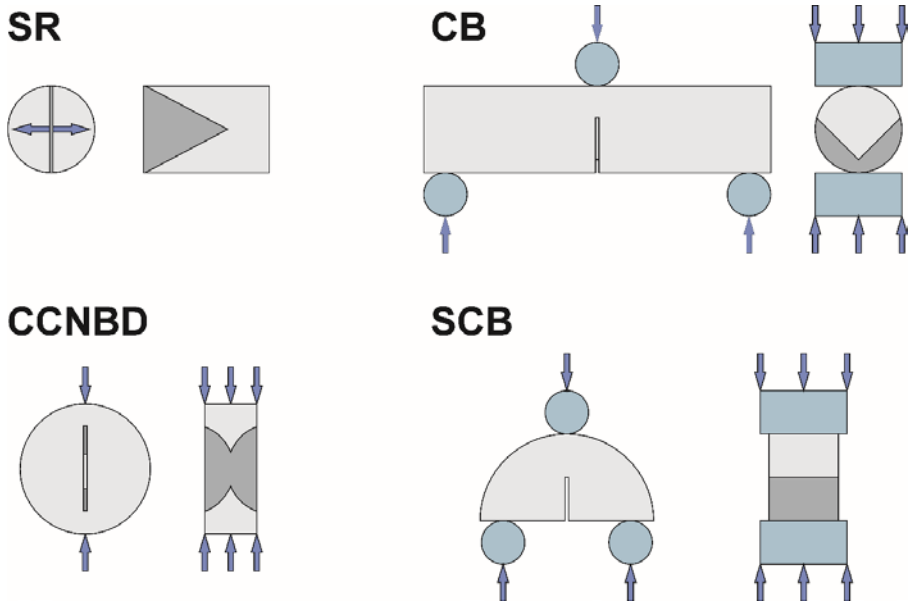

Figure 2.3: ISRM suggested methods: short rod (SR), chevron bend (CB), cracked chevron notched Brazilian disc (CCNBD), and semi-circular bend (SCB).

2.3.3. K_{IC} testing in rock-like materials

Within the realm of concrete and cementitious materials research, a convenient alternative to the bending or tensile tests mentioned previously is the wedge splitting test (WST), which was firstly proposed by Linsbauer and Tschegg (1986) and latter improved by Brühwiler and Wittmann (1990). In the WST, the compressive load applied to the notched sample is transformed into tensile opening via a special testing arrangement based on the wedge mechanism. Among the advantages offered by this method, it is worth mention that an ordinary electromechanical testing machine with a constant actuator displacement rate can be used, and that no sophisticated test stability control apparatus (i.e. closed loop control unit with e.g. crack tip opening displacement as a feedback signal) is necessary.

2.3.4. Factors influencing K_{IC}

As a material property, fracture toughness is expected to be independent of the testing method, specimen geometry, or loading conditions. However, the previous assumption is not valid for inhomogeneous and anisotropic materials such as rock. In fact, a number of researchers have reported different K_{IC} for the same rock type tested under different testing conditions (Khan and Al-Shayea 2000; Iqbal and Mohanty 2007; Kataoka et al. 2015). In addition, factors such as the loading rate (Backers et al. 2003; Ko and Kemeny 2007), the specimen size (Matsuki et al. 1991; Yi et al. 1992; Ayatollahi and Akbardoost 2012; Ueno et al. 2013), confining pressure (Matsuki and Aoki 1990; Stoeckhert et al. 2016; Kataoka et al. 2017), anisotropy (Nasseri and Mohanty 2008; Ghamgosar et al. 2015; Chandler et al. 2016), water content (Nara et al. 2012; Maruvanchery and Kim 2019), or temperature (Funatsu et al. 2004) have been found to influence the values of fracture toughness derived experimentally.

2.3.5. Stable/unstable crack propagation

The process of fracture propagation can be defined from two different perspectives: (i) considering the velocity, so it is possible to distinguish between static and dynamic propagation; or (ii) taking into account the magnitude of the

stress intensity factor, so the distinction is made between stable ($K_I < K_{IC}$) and unstable ($K_I \geq K_{IC}$) propagation (Backers 2004). A stable crack grows slowly under increasing load so it can be controlled and stopped at any moment (i.e. it is necessary an increase in stress for further propagation). This process is called subcritical crack growth (Atkinson 1984), and it is usually observed in the period of non-linear behaviour close to the peak load during which microcracks grow stably. In general, the propagation of an unstable crack is usually fast (dynamic) and uncontrollable due to the energy surplus (the process is no longer governed by the relationship between the applied stress and the crack length (Bieniawski 1967)). In this case, once the maximum strength of the material is reached, there is a sudden drop of load right after P_{max}, and the specimen fails releasing a large amount of energy instantaneously. This is the behaviour, and one of the main drawbacks, observed for the testing methods proposed by the ISRM (i.e. the lack of control on the post-peak region). However, unstable crack propagation can be also slow (static) if the energy needed to produce further crack grow can be controlled by increasing the magnitude of the test control parameter (displacement of the actuator or deformation of the specimen). If the testing conditions are favourable in this respect, a complete load-displacement (*P-d*) curve with a descending branch after peak load can be recorded.

2.3.6. Energy assessment

As discussed by Griffith (1920) and later by Irwin (1948) and Orowan (1949), crack propagation is caused by a transfer into surface energy of the energy delivered from an external load to the specimen, and/or from strain energy. Consequently, fracture toughness can be regarded as a measure of the energy required to create new surface area in a material, that is, to produce crack extension. From this point of view, rock deformation and failure would be irreversible processes in which elastic energy is dissipated and released. During loading, elastic energy is stored both in the specimen and in the testing device. At P_{max}, this energy is released and becomes available for the formation of fracture area in the specimen. After this moment, the possibility of controlling the test in the post-peak region will be determined by factors such as the stiffness of

the testing device, the stiffness of the specimen (i.e. the material properties), and the testing method itself. Uncontrolled fracture propagation will occur when the elastic energy stored in the testing device is larger than the fracture energy necessary to fracture the specimen (Brühwiler and Wittmann 1990). In this case, rock failure will result from the rapid release of the energy stored in the specimen when the critical limit (i.e. K_{IC}) is reached (Liu et al. 2016).

In the field of concrete, the International Union of Laboratories and Experts in Construction Materials, Systems and Structures (RILEM) has suggested using the area below the load-deformation diagram of a three point bending test (TPBT) to determine the specific fracture energy (G_F) (RILEM 1985). In order to do so, it is necessary a controlled (stable) crack propagation beyond P_{max}. i.e., a well-defined descending branch. Similar approaches have also been defined for the compact tension (Wittmann et al. 1988) and the wedge splitting (Brühwiler and Wittmann 1990) tests. In rock fracture toughness testing, the area under the *P-d* curve has also been used to evaluate the fracture energy (Chong et al. 1987). However, if the testing conditions favour dynamic crack growth beyond P_{max} (i.e. no post-peak branch), the assessment of the energy associated to the fracture propagation process is significantly limited. Contrary, if the uncontrolled crack propagation is stable, the complete (i.e. pre- and post-peak) *P-d* diagram can be obtained, making it is possible to compute not only the energy related to the process of crack initiation (i.e. taking the area up to peak load) but also to crack propagation (i.e. the area in the post peak region).

2.4. Acoustic emission

Acoustic emission (AE) is a powerful non-destructive testing (NDT) technique to warn of impeding structural damage. AE can be described as the rapid release of elastic energy occurring inside a material that is being deformed of fractured. AE signals travel from the source in the form of stress waves and can be detected by coupling AE sensors (which convert the mechanical waves into an electrical signals) to the surface of the specimen being tested. AE is frequently used for monitoring structures such as bridges, tunnels, pipes or tanks, but it has also become popular in laboratory testing. AE has some advantages

over other methods used to assess damage. In contrast to optical or scanning electron microscopy, AE analyses the whole volume of interest and it is not only restricted to the inspection of the specimen surface. The simplest approach consists in acquiring AE data using a single channel and counting the number of events generated: the higher the AE rate, the larger the inelastic strain rate. However, if an array of at least four sensors is available and the wave velocity through the material is known, it is possible detect and even locate in real time the growing defects inside the specimen. In order to do this, the relative arrival times and the position of each sensor need to be measured with enough accuracy (Lockner 1993). The attenuation of the signals increases as the distance from the source of the events also increases. The maximum distance at which an AE sensor can detect the acoustic signals depends on factors such as the properties of the material or the geometry of the sample.

AE signals can be classified into two major types: (i) transient (burst) signals with clearly defined starting and ending points, usually associated with growing defects; and (ii) continuous (noise) signals, which never vanish and must be minimized to enhance AE monitoring. When the sources that produce background noise (such as electrical interferences or movements of the testing equipment) cannot be completely removed, it is usual to set a certain detection amplitude threshold (in dB) and frequency bandpass filters (in kHz) in order to eliminate unwanted signals.

2.4.1. AE parameters

Typical parameters of an AE waveform (Figure 2.4) are: (a) counts, or the AE crossing-threshold signals; (b) energy, that is the integral of the squared voltage signal divided by the 10 kΩ reference resistance over the duration of AE waveform (aJ); (c) duration, that is the time interval between the first and the last threshold crossing (μs); (d) peak amplitude, the maximum amplitude of the waveform (dB), which is usually related to the intensity of the source producing the event; (e) rise time, that is the time from the first threshold crossing to the peak amplitude (μs).

Using the previous AE parameters, it is possible to compute additional features such as the average frequency (AF, the ratio between the AE counts and duration, in kHz) or the rise angle (RA, the ratio between the rise time and the amplitude, in ms/V), which are usually used to classify the modes of cracking (tensile, shear, etc.). In addition, the frequency centroid (the frequency of the spectral centroid of the waveform, kHz) and the peak frequency (frequency of maximum power, in kHz) can be reported by applying fast Fourier transforms (FFTs) to the waveforms recorded.

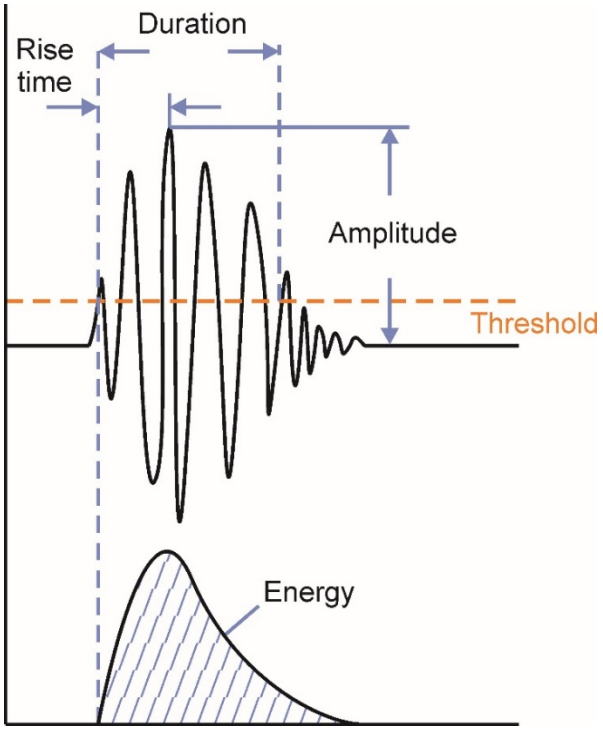

Figure 2.4: AE waveform and related time-domain parameters. Adapted from Shigeishi et al. (2001).

2.4.2. AE in rock mechanics

AE technique has been widely used in rock mechanics studies and engineering applications. In rocks, AE is always a consequence of any type of displacement occurring inside the material (Molenda 2015). Therefore, AE monitoring can provide insight on the brittle rock fracture process, including information about the size and location of the source of events. AE has been

proved to be sensitive to phenomena such as crack initiation and coalesce (Stanchits et al. 2009; Tsangouri et al. 2015). Due to its close relation with specimen failure, special attention has been given to the process of crack growth, which is usually related to acoustic events of high amplitude (He et al. 2010; Molenda 2015). However, less energetic events such as those related to microcracking can even produce transient elastic waves that can be recorded using acoustic emission. This is especially useful for tracking the development (i.e. the size and shape) of the fracture process zone (FPZ) around the notch tip (Xing et al. 2017).

Recently, the ISRM has proposed a suggested method for AE monitoring in laboratory (Ishida et al. 2017). At the lab scale, the sources of the AE events are usually in the order of the grain size (< 1 mm), so the frequency range is usually between 100 kHz and 2 MHz (Lockner 1993). In the rock mechanics field, AE technique has been successfully used to identify fracture propagation and specimen failure in uniaxial compression tests (Zhao et al. 2013; Jie et al. 2015), triaxial tests (Lei et al. 2000; Fortin et al. 2011; Chen et al. 2020), or hydraulic fracturing experiments (Stanchits et al. 2012; Stanchits et al. 2014; Molenda 2015). For the latter, the location of the AE events can be useful to map the orientation of the fracture and infer the propagation rate.

Similarly, different authors have studied the AE signals recorded in fracture toughness tests to provide insight into the fracture process. Nasseri et al. (2006) accurately tracked the development of the FPZ in granitic samples using the CCNBD method. The experimental results reported by Xu et al. (2016) are also illustrative of this process, in which five different stages (from microcracking onset to macrocrack propagation) can be distinguished from the location of the AE events. Using the same testing technique, Kaklis et al. (2017) could identify macrocrack onset and specimen failure of marble samples from the increase in time-based AE parameters such as amplitude or rise time. Also for CCNBD specimens, Wei et al. (2018) observed severe stress concentrations at the loading ends using the experimental distribution of the AE events, which was in agreement with their numerical simulations. In a previous contribution, Wei et al.

(2016) reported a large FPZ at the crack tip of SCB specimens of sandstone. According to these authors, this would be the reason for SCB specimens providing lower values of K_{IC} in comparison with other suggested methods. Taking advantage of the location of events, Yu et al. (2018) identified three different failure modes (i.e. tensile, shear and mixed-mode) around the notch tip during failure of three-point bending tests specimens of granite. Zhou et al. (2018) found that the presence of water not only reduced the K_{IC} of chevron notched semi-circular bend specimens of sandstone, but also the cumulative AE counts, which related with a less energetic and more ductile fracture behaviour. An alternative approach to compute fracture toughness was carried out by Hashida (1993), who used the ratio J-integral/AE energy to identify the onset of macrocrack extension and compute the K_{IC} of granite specimens at this critical point.

2.5. References

Anderson TL (2005) Fracture mechanics: Fundamentals and applications, Third Edition. CRC Press

Atkinson BK (1984) Subcritical crack growth in geological materials. *Journal of Geophysical Research: Solid Earth* 89:4077–4114

Awaji H, Sato S (1978) Combined Mode Fracture Toughness Measurement by the Disk Test. *Journal of Engineering Materials and Technology* 100:175–182

Ayatollahi MR, Akbardoost J (2012) Size effects on fracture toughness of quasi-brittle materials - A new approach. *Engineering Fracture Mechanics* 92:89–100

Ayatollahi MR, Mahdavi E, Alborzi MJ, Obara Y (2016) Stress intensity factors of semi-circular bend specimens with straight-through and chevron notches. *Rock Mechanics and Rock Engineering* 49:1161–1172

Backers T (2004) Fracture toughness determination and micromechanics of rock under mode I and mode II loading. PhD thesis, University of Potsdam,

Potsdam, Germany

Backers T, Fardin N, Dresen G, Stephansson O (2003) Effect of loading rate on Mode I fracture toughness, roughness and micromechanics of sandstone. *International Journal of Rock Mechanics and Mining Sciences* 40:425–433

Beer FP, Johnston ER, DeWolf JT, Mazurek DF (2012) Mechanics of Materials. Sixth edition.

Bieniawski ZT (1967) Mechanism of brittle fracture of rock. *International Journal of Rock Mechanics and Mining Sciences & Geomechanics Abstracts* 4:395–406

Brühwiler E, Wittmann FH (1990) The wedge splitting test, a new method of performing stable fracture mechanics tests. *Engineering Fracture Mechanics* 35:117–125

Chandler MR, Meredith PG, Brantut N, Crawford BR (2016) Fracture toughness anisotropy in shale. *Journal of Geophysical Research: Solid Earth* 121:1706–1729

Chen G, Sun X, Wang J, Wang D, Zhu Z (2020) Detection of cracking behaviors in granite with open precut cracks by acoustic emission frequency spectrum analysis. *Arabian Journal of Geosciences* 13:258

Chong KP, Kuruppu MD, Kuszmaul JS (1987) Fracture toughness determination of layered materials. *Engineering Fracture Mechanics* 258:43–54

Donovan JG, Karfakis MG (2004) Adaptation of a simple wedge test for the rapid determination of mode I fracture toughness and the assessment of relative fracture resistance. *International Journal of Rock Mechanics and Mining Sciences* 41:695–701

Erdogan F (2000) Fracture mechanics. *International Journal of Solids and Structures* 37:171–183

Feng XT (2017) Rock Mechanics and Engineering Volume 2. CRC Press

Fortin J, Stanchits S, Vinciguerra S, Guéguen Y (2011) Influence of thermal and

mechanical cracks on permeability and elastic wave velocities in a basalt from Mt. Etna volcano subjected to elevated pressure. *Tectonophysics* 503:60–74

Funatsu T, Seto M, Shimada H, Matsui K, Kuruppu M (2004) Combined effects of increasing temperature and confining pressure on the fracture toughness of clay bearing rocks. *International Journal of Rock Mechanics and Mining Sciences* 41:927–938

Ghamgosar M, Williams DJ, Erarslan N (2015) Effect of anisotropy on fracture toughness and fracturing of rocks. In: 49th US Rock Mechanics/Geomechanics Symposium, San Francisco, USA, 28 June - 1 July

Griffith AA (1920) The phenomena of rupture and flow in solids. *Philosophical Transactions Royal Society London* 221:163–198

Guo H, Aziz NI, L.C S (1993) Rock fracture toughness determination by the Brazilian test. *Engineering Geology* 33:177–181

Hashida T (1993) Fracture toughness testing of core-based specimens by acoustic emission. *International Journal of Rock Mechanics and Mining Sciences and* 30:61–69

He MC, Miao JL, Feng JL (2010) Rock burst process of limestone and its acoustic emission characteristics under true-triaxial unloading conditions. *International Journal of Rock Mechanics and Mining Sciences* 47:286–298

Hoagland RG, Hahn GT, Rosenfield AR (1973) Influence of microstructure on fracture propagation in rock

Inglis CE (1913) Stresses in a plate due to the presence of cracks and sharp corners. *Transactions of the Institute of Naval Architects* 55:219–241

Iqbal MJ, Mohanty B (2007) Experimental calibration of ISRM suggested fracture toughness measurement techniques in selected brittle rocks. *Rock Mechanics and Rock Engineering* 40:453–475

Irwin GR (1958) Fracture. In: Handbook on physics. Springer Verlag, Berlin, pp 551–590

Irwin GR (1957) Analysis of stresses and strains near the end of a crack traversing a plate. *Journal of Applied Mechanics* 24:361–364

Irwin GR (1948) Fracture Dynamics. *Fracturing of Metals, American Society of Metals* 147–166

Ishida T, Labuz JF, Manthei G, Meredith PG, Nasseri MHB, Shin K, Yokoyama T, Zang A (2017) ISRM Suggested Method for Laboratory Acoustic Emission Monitoring. *Rock Mechanics and Rock Engineering* 50:665–674

ISRM (1995) Suggested method for determining mode I fracture toughness using Cracked Chevron Notched Brazilian Disc (CCNBD) specimens. *International Journal of Rock Mechanics and Mining Sciences & Geomechanics Abstracts* 32:57–64

ISRM Testing Commission (1988) Suggested methods for determining the fracture toughness of rock. *International Journal of Rock Mechanics and Mining Science & Geomechanics Abstracts* 25:71–96

Jie C, Junwei Z, Song R, Lin L, Liming Y (2015) Determination of Damage Constitutive Behavior for Rock Salt Under Uniaxial Compression Condition with Acoustic Emission. *The Open Civil Engineering Journal* 9:75–81

Kaklis K, Mavrigiannakis S, Saltas V, Vallianatos F, Agioutantis Z (2017) Using acoustic emissions to enhance fracture toughness calculations for CCNBD marble specimens. *Frattura ed Integrità Strutturale* 11:1–17

Kataoka M, Mahdavi E, Funatsu T, Takehara T, Obara Y, Fukui K, Hashiba K (2017) Estimation of Mode I Fracture Toughness of Rock by Semi-Circular Bend Test under Confining Pressure Condition. *Procedia Engineering* 191:886–893

Kataoka M, Yoshioka S, Cho S-H, Soucek K, Vavro L, Obara Y (2015) Estimation of Fracture Toughness of Sandstone by Three Testing Methods. In:

Vietrock2015: an ISRM specialized conference, Hanoi, Vietnam, 12-13 March

Khan K, Al-Shayea NA (2000) Effect of specimen geometry and testing method on mixed Mode I-II fracture toughness of a limestone rock from Saudi Arabia. *Rock Mechanics and Rock Engineering* 33:179–206

Ko T, Kemeny J (2007) Effect of confining stress and loading rate on fracture toughness of rocks. In: Rock Mechanics: Meeting Society's Challenges and Demands. pp 625–629

Ko TY, Kemeny J (2013) Determination of the subcritical crack growth parameters in rocks using the constant stress-rate test. *International Journal of Rock Mechanics and Mining Sciences* 59:166–178

Kuruppu MD (1997) Fracture toughness measurement using chevron notched semi-circular bend specimen. *International Journal of Fracture* 86:

Kuruppu MD, Obara Y, Ayatollahi MR, Chong KP, Funatsu T (2014) ISRM-suggested method for determining the mode I static fracture toughness using semi-circular bend specimen. *Rock Mechanics and Rock Engineering* 47:267–274

Lawn B (1993) Fracture of brittle solids. Cambridge University Press, Cambridge

Lei X, Kusunose K, Rao MVMS, Nishizawa O, Satoh T (2000) Quasi-static fault growth and cracking in homogeneous brittle rock under triaxial compression using acoustic emission monitoring. *Journal of Geophysical Research: Solid Earth* 105:6127–6139

Li D, Wong LNY (2013) The Brazilian Disc Test for Rock Mechanics Applications: Review and New Insights. *Rock Mechanics and Rock Engineering* 46:269–287

Linsbauer HN, Tschegg EK (1986) Fracture energy determination of concrete with cube shaped specimens. *Zement und Beton* 31:38–40

Liu XS, Ning JG, Tan YL, Gu QH (2016) Damage constitutive model based on

energy dissipation for intact rock subjected to cyclic loading. *International Journal of Rock Mechanics and Mining Sciences* 85:27–32

Lockner D (1993) The role of acoustic emission in the study of rock fracture. *International Journal of Rock Mechanics and Mining Sciences & Geomechanics Abstracts* 30:883–899

Maruvanchery V, Kim E (2019) Effects of water on rock fracture properties: Studies of mode I fracture toughness, crack propagation velocity, and consumed energy in calcite-cemented sandstone. *Geomechanics and Engineering* 1:57–67

Matsuki K, Aoki T (1990) The effect of confining and pore pressures on fracture toughness of rocks. *Shigen-to-Sozai* 106:713–718

Matsuki K, Hasibuan SS, Takahashi H (1991) Specimen size requirements for determining the inherent fracture toughness of rocks according to the ISRM suggested methods. *International Journal of Rock Mechanics and Mining Sciences and* 28:365–374

Molenda M (2015) Acoustic Emission monitoring of laboratory scale hydraulic fracturing experiments. PhD thesis, Ruhr-University Bochum, Bochum, Germany

Nara Y, Morimoto K, Hiroyoshi N, Yoneda T, Kaneko K, Benson PM (2012) Influence of relative humidity on fracture toughness of rock: Implications for subcritical crack growth. *International Journal of Solids and Structures* 49:2471–2481

Nara Y, Morimoto K, Yoneda T, Hiroyoshi N, Kaneko K (2011) Effects of humidity and temperature on subcritical crack growth in sandstone. *International Journal of Solids and Structures* 48:1130–1140

Nasseri MHB, Mohanty B (2008) Fracture toughness anisotropy in granitic rocks. *International Journal of Rock Mechanics and Mining Sciences* 45:167–193

Nasseri MHB, Mohanty B, Young RP (2006) Fracture toughness measurements

and acoustic emission activity in brittle rocks. *Pure and Applied Geophysics* 163:917–945

Newman JCJ (1984) A review of chevron-notched fracture specimens. Langley Research Center, Virginia

Orowan E (1949) Fracture strength of solids. *Reports on Progress in Physics, Vol XII* 185–232

Ouchterlony F (1981) Extension of the Compliance and Stress Intensity Formulas for the Single Edge Crack Round Bar in Bending. In: Fracture Mechanics for Ceramics, Rocks, and Concrete. ASTM International, 100 Barr Harbor Drive, PO Box C700, West Conshohocken, PA 19428-2959, pp 237–256

Ouchterlony F (1982) Review of fracture toughness testing of rock. *SM Archives* 7:131–211

Perez N (2004) Fracture mechanics. Kluwer Academic Publishers, Boston, MA, USA

Perras MA, Diederichs MS (2014) A Review of the Tensile Strength of Rock: Concepts and Testing. *Geotechnical and Geological Engineering* 32:525–546

RILEM (1985) Determination of the fracture energy of mortar and concrete by means of three-point bend tests on notched beams. *Materials and Structures* 18:287–290

Schmidt RA (1980) A Microcrack Model And Its Significance to Hydraulic Fracturing And Fracture Toughness Testing. In: The 21st U.S. Symposium on Rock Mechanics (USRMS), 27-30 May, Rolla, Missouri

Serrano A, Olalla C (1998) Ultimate bearing capacity of an anisotropic discontinuous rock mass. Part I: Basic modes of failure. *International Journal of Rock Mechanics and Mining Sciences* 35:301–324

Shigeishi M, Colombo S, Broughton KJ, Rutledge H, Batchelor AJ, Forde MC (2001) Acoustic emission to assess and monitor the integrity of bridges.

Construction and Building Materials 15:35–49

Stanchits S, Fortin J, Gueguen Y, Dresen G (2009) Initiation and propagation of compaction bands in dry and wet bentheim sandstone. *Pure and Applied Geophysics* 166:843–868

Stanchits S, Surdi A, Edelman E, Suarez-rivera R (2012) Acoustic Emission and Ultrasonic Transmission Monitoring of Hydraulic Fracture Initiation and Growth in Rock Samples. In: 30th European Conference on Acoustic Emission Testing & 7th International Conference on Acoustic Emission, University of Granada, Spain 12-15 September

Stanchits S, Surdi A, Gathogo P, Edelman E, Suarez-Rivera R (2014) Onset of hydraulic fracture initiation monitored by acoustic emission and volumetric deformation measurements. *Rock Mechanics and Rock Engineering* 47:1521–1532

Stoeckhert F, Brenne S, Molenda M, Alber M (2016) Mode I fracture toughness of rock under confining pressure. In: Ulusay R, Aydan O, Hasan G, Hindistan MA (eds) Rock Mechanics and Rock Engineering: From the Past to the Future. CRC Press, pp 313–318

Sun CT, Jin ZH (2012) Chapter 2 -Griffith Theory of Fracture. In: Fracture Mechanics. Academic Press, pp 11–24

Sun Z, Ouchterlony F (1986) Fracture toughness of stripa granite cores. *International Journal of Rock Mechanics and Mining Sciences & Geomechanics Abstracts* 23:399–409

Szendi-Horvath G (1980) Fracture toughness determination of brittle materials using small to extremely small specimens. *Engineering Fracture Mechanics* 13:955–961

Thiercelin M, Roegiers J-C (1988) Fracture toughness determination with the modified ring test. In: Proceedings of the International Symposium on Engineering in Complex Rock Formations. Elsevier, pp 284–290

Tsangouri E, Aggelis D, Matikas T, Mpalaskas A (2015) Acoustic Emission Activity for Characterizing Fracture of Marble under Bending. *Applied Sciences* 6:6

Tutluoglu L, Keles C (2011) Mode I fracture toughness determination with straight notched disk bending method. *International Journal of Rock Mechanics and Mining Sciences* 48:1248–1261

Ueno K, Funatsu T, Shimada H, Sasaoka T, Matsui K (2013) Effect of Specimen Size on Mode I Fracture Toughness by SCB Test. In: The 11th International conference on Mining, Materials and Petroleum Engineering; the 7th International Conference on Mining, Materials and Petroleum Engineering. Chiang Mai, Thailand, 11-13 November

Wang Q-Z, Xing L (1999) Determination of fracture toughness KIC by using the flattened Brazilian disk specimen for rocks. *Engineering Fracture Mechanics* 64:193–201

Wei MD, Dai F, Xu NW, Liu JF, Xu Y (2016a) Experimental and numerical study on the cracked chevron notched semi-circular bend method for characterizing the mode I fracture toughness of rocks. *Rock Mechanics and Rock Engineering* 49:1595–1609

Wei MD, Dai F, Xu NW, Xu Y, Xia K (2015) Three-dimensional numerical evaluation of the progressive fracture mechanism of cracked chevron notched semi-circular bend rock specimens. *Engineering Fracture Mechanics* 134:286–303

Wei MD, Dai F, Xu NW, Zhao T (2018) Experimental and numerical investigation of cracked chevron notched Brazilian disc specimen for fracture toughness testing of rock. *Fatigue & Fracture of Engineering Materials & Structures* 41:197–211

Wei MD, Dai F, Xu NW, Zhao T, Xia KW (2016b) Experimental and numerical study on the fracture process zone and fracture toughness determination for ISRM-suggested semi-circular bend rock specimen. *Engineering Fracture*

Mechanics 154:43–56

Whittaker BN, Singh RN, Sun G (1992) Rock fracture mechanics: Principles, design, and applications. Elsevier, Amsterdam

Wittmann FH, Rokugo K, Brühwiler E, Mihashi H, Simonin P (1988) Fracture energy and strain softening of concrete as determined by means of compact tension specimens. *Materials and Structures* 21:21–32

Xing YK, Zhang GQ, Lin Q, Bu XQ, Da YP, Qi Y (2017) Subcritical fracture process of sandstone with AE energy analysis. In: 51st US Rock Mechanics / Geomechanics Symposium, San Francisco, California, USA, 25-28 June

Xu Y, Dai F, Zhao T, Xu N wen, Liu Y (2016) Fracture Toughness Determination of Cracked Chevron Notched Brazilian Disc Rock Specimen via Griffith Energy Criterion Incorporating Realistic Fracture Profiles. *Rock Mechanics and Rock Engineering* 49:3083–3093

Yi X, Sun Z, Ouchterlony F, Stephansson O (1992) Specimen size effect of the fracture toughness of Kallax gabbro. In: Wawersik T& (ed) Rock Mechanics. American Rock Mechanics Association, Balkema, Rotterdam, pp 847–856

Yu M, Wei C, Niu L, Li S, Yu Y (2018) Calculation for tensile strength and fracture toughness of granite with three kinds of grain sizes using three-point-bending test. *PLOS ONE* 13:e0180880

Zhao XG, Cai M, Wang J, Ma LK (2013) Damage stress and acoustic emission characteristics of the Beishan granite. *International Journal of Rock Mechanics and Mining Sciences* 64:258–269

Zhou Z, Cai X, Ma D, Cao W, Chen L, Zhou J (2018) Effects of water content on fracture and mechanical behavior of sandstone with a low clay mineral content. *Engineering Fracture Mechanics* 193:47–65

Zhu XK, Joyce JA (2012) Review of fracture toughness (G, K, J, CTOD, CTOA) testing and standardization. *Engineering Fracture Mechanics* 85:1–46

3. Pure mode I fracture toughness determination in rocks using a pseudo-compact tension (*p*CT) test approach

This chapter has been published in '*Rock Mechanics and Rock Engineering*'

Andrea Muñoz-Ibáñez[1], Jordi Delgado-Martín[1], Miguel Costas[2], Juan Rabuñal-Dopico[3], Jose Alvarellos-Iglesias[4], and Jacobo Canal-Vila[4]

3.1. Abstract

Mode I fracture toughness (K_{IC}) quantifies the ability of a material to withstand crack initiation and propagation due to tensile loads. The International Society for Rock Mechanics (ISRM) has proposed four suggested methods for determining K_{IC}. However, these methods present some drawbacks such as insufficient post-peak control, complex sample preparation, and considerable material requirements. Here we present an alternative approach, the called pseudo-compact tension (*p*CT) method, to measure K_{IC} in rocks using disc-shaped specimens loaded in pure tension. The *p*CT specimen has favourable features such as a simple geometry, small sample volume, and minimal machining requirement. The tensile load is transmitted to the specimen through two high-strength, high-stiffness steel jaws that fit into a U-shaped groove cut in the specimen. An additional thin straight notch is introduced to act as a stress concentrator. The crack propagates from the notch tip along the ligament plane, splitting the specimen into two halves. The effects of specimen size and notch length on K_{IC} are determined by testing specimens 100, 50 and 38 mm in

[1] School of Civil Engineering, University of A Coruña, Campus de Elviña s/n, 15071 A Coruña, Spain
[2] Structural Impact Laboratory (SIMLab) and Centre for Advanced Structural Analysis (CASA), Department of Structural Engineering, Norwegian University of Science and Technology (NTNU), Trondheim, NO-7491, Norway
[3] Faculty of Informatics, University of A Coruña, Campus de Elviña s/n, 15071 A Coruña, Spain
[4] Centro de Tecnología de Repsol, Ctra. Extremadura, N-V Km 18, 28935 Móstoles, Spain

diameter with different notch length ratios ($0.1 \leq a/b \leq 0.4$). Tests were performed under ambient conditions and a slow loading rate (0.1 mm/min). Our results show that the *p*CT method is convenient for the assessment of K_{IC} of both fragile and ductile rocks. The method offers good control even beyond the maximum load, making it possible to study the post-peak behaviour of the material.

3.2. Introduction

Most static failure theories assume that materials are perfectly homogeneous, isotropic, and free from defects that can increase stress (Perez 2004). This is seldom true for real materials, which usually contain geometrical discontinuities (i.e., indentations, scratches or gouges) or defects (i.e. voids, cracks or inclusions) that may grow in size and result in global failure of the specimen (Jameel and Harmain 2015). Since these features produce a change in the inherent properties of materials, their presence must be taken into account (Khayal 2017; Sato and Takahashi 2018; Takahashi et al. 2018). By accepting that defects are unavoidable, fracture mechanics deals with the behaviour of cracked materials and structures subjected to stress (Anderson 2005).

Fracture toughness (K_C) quantifies the capability of a material to resist the stresses causing the propagation and growth of pre-existing cracks or flaws (Whittaker et al. 1992). Fracture toughness may have paramount importance in engineering projects involving rock materials, in which cracks are omnipresent (Funatsu et al. 2004; Nasseri et al. 2007; Ko and Kemeny 2013; Major et al. 2014; Erarslan 2016; Talukdar et al. 2018), such as thermal (e.g., geothermal and high-level radioactive waste disposal projects), mechanical (e.g., pillar/cave stability in mining), hydraulic/chemical (e.g., hydraulic fracturing, geological storage of CO_2, and underground coal gasification) and process engineering (e.g., drilling, cutting, and ore crushing). Fracture mechanics distinguishes three basic modes of loading that a crack can experience: a) mode I, or opening/tensile mode; b) mode II, or shearing in-plane; and c) mode III, or shearing out-of-plane (Irwin 1958). Since the tensile strength of a rock material is comparatively lower than its compressive and shearing stresses, the mode I fracture toughness (K_{IC}) arises

as the most relevant and studied parameter in rock fracture mechanics (Whittaker et al. 1992).

In recent years, the increasing demand for hydrocarbons has promoted the need for more research on the fracture mechanics of certain lithologies (tight sands, shales, etc.). For this reason, several methods have been proposed to determine K_{IC} using core-based specimens. The International Society for Rock Mechanics (ISRM) endorses four suggested methods, namely the short rod (SR), chevron bend (CB), cracked chevron notched Brazilian disc (CCNBD), and semi-circular bend (SCB) methods (ISRM Testing Commission 1988; Fowell et al. 1995; Kuruppu et al. 2014). Some of these methods may be difficult to apply on a routine basis due to a number of issues, such as: a) the small failure initiation and propagation loads require excellent test control; b) a relatively large sample volume is needed (CB); c) cumbersome or difficult sample preparation (SR, CB, and CCNBD); d) imprecisions in the computation of the stress intensity factor (CCNBD; Wang, 1998); e) the indirect generation of tensile loads via sample compression (especially in SCB and CCNBD); and e) the celerity of crack propagation after peak strength is attained. To overcome some of these limitations, in this contribution we present an alternate simple approach, referred to as pseudo-compact tension (*p*CT), to measure K_{IC} in rocks using cylindrical single edge-notched specimens loaded in pure tension.

3.3. Materials and methods

3.3.1. Materials

Four different rock types, namely Corvio sandstone (C), Arcera sandstone (AR), Pinacas sandstone (PN), and Blanco Mera granite (GR), were used to assess their corresponding K_{IC}. Arcera sandstone is a medium- to coarse-grained rock whose mineralogy is dominated by quartz (~92%) with lesser kaolinite (~5%) (Canal-Vila 2016). Pinacas sandstone is a grey sandstone with lower quartz content (~54%). Corvio sandstone can be classified as a grain-supported quartzarenite with microcrystalline silica cement (Falcon-Suarez et al. 2017). Blanco Mera granite is a bright white coarse-grained (1-6 mm) rock of moderate

strength (Arzúa and Alejano 2013). The porosity, ultrasonic velocities, uniaxial compressive strength (UCS), and indirect tensile strength were determined for AR, PN and GR under ambient conditions. Data for Corvio sandstone were reported by Falcon-Suarez et al. (2017). The average values of the rock properties obtained from the non-destructive and destructive tests are listed in Table 3.1 and 3.2, respectively.

Table 3.1: Rock properties obtained from non-destructive tests: effective porosity (n_e), bulk density (ρ_{bulk}), and ultrasonic velocities (V_p and V_s).

Rock type	n_e (%)	ρ_{bulk} (g/cm^3)	V_p (m/s)	V_s (m/s)
C*	18.4 - 23.5	2.0 - 2.1	2920	1510
AR	17.3 -18.2	2.2	2634 ± 186	1818 ± 324
PN	5.5 - 6.5	2.5	3686 ± 253	2563 ± 453
GR	1.2 - 1.3	2.6	4100 ± 215	2562 ± 438

* Data reported in Falcon-Suarez *et al.* (2017).

Table 3.2: Rock properties obtained from destructive tests: compressive strength (σ_c), tensile strength (σ_t), Young's modulus (E), and Poisson's ratio (v). σ_c and σ_t were normalized with respect to diameter, length, and thickness according to Thuro et al. (2001) and Yu et al. (2006), respectively.

Rock type	σ_c (MPa)	σ_t (MPa)	E (GPa)	v
C*	35.4 - 44.4	1.9 - 3.1	9.7 - 19.7	0.3 - 0.4
AR	40.2	4.1 - 4.9	12.2	0.4
PN	129.5	11.2 - 11.9	35.0	0.2
GR	60.4 – 83.5	9.7	33.0	0.3

* Data reported in Falcon-Suarez *et al.* (2017).

3.3.2. Experimental concept

The pseudo-compact tension (*p*CT) test is based on a modification of the compact tension (CT) specimen described in the E399-90 ASTM (1997) standard method for testing metallic materials. The testing principle is outlined in Figure 3.1. The *p*CT specimen is a cylindrical, disc-shaped sample that can be cut from rock cores. The two loading holes of the CT specimen are replaced in the *p*CT test by a U-shaped groove. In addition, a thin radial notch is cut to act as a stress concentrator and provide the location for crack initiation. Once the specimen is ready for testing, the test follows a simple and straightforward procedure. The specimen is mounted on a centring cradle and put in contact with a pair of high-strength, high-stiffness steel jaws that fit into the U-shaped groove and transmit the tensile load to the sample. While one of the jaws remains in a static position, the other one is pulled away at a constant displacement rate. The tensile load within the thin notch tends to split the specimen into two symmetrical halves. The crack initiates at the notch tip and propagates along the vertical diameter of the specimen (i.e., the ligament plane). With this basic configuration, the bottom of the sample is not affected by loads other that its own self-weight and that of the sensors used (in our case, acoustic emission sensors and a crack opening displacement gauge).

At this point, it is worth considering that in our research, we have focused on the methods currently in use by rock mechanics practitioners. In concrete research, there exist two methods worth considering due to their geometrical similarity with the method proposed here: the wedge-splitting (WS) test (Linsbauer and Tschegg 1986; Guan et al. 2018) and the modified disk-shaped compact tension (MDCT) test (Cifuentes et al. 2017). The WS test cannot be considered a pure-tension test because it induces significant compressive loads at the bottom side of the tested specimens. The MDCT test geometry is similar to the geometry of the *p*CT approach, but the pulling action is provided by a cemented steel bar, which would be very difficult to install in rock.

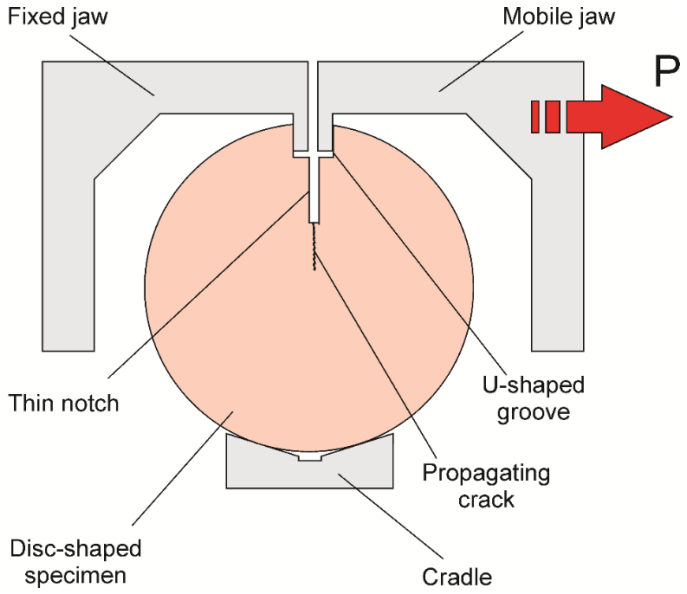

Figure 3.1: Experimental setup of the pseudo-compact tension (*p*CT) test. The *p*CT specimen is placed on the cradle; while the left jaw remains still, the right jaw is pulled away. When the stress intensity factor, K_I, reaches its critical value K_{IC} (i.e., mode I fracture toughness), crack initiates at the notch tip and propagates along the ligament length.

3.3.3. Sample preparation and conditioning

The *p*CT specimen may be obtained from a slice of core that has a thickness to diameter ratio (*B/D*) of 0.5. This value was set by taking into account the recommendations for indirect tensile ("Brazilian") strength tests (ISRM 1978; ASTM D3967-05 2008). The geometry of the *p*CT specimen is favourable due to simplicity, low amount of material needed, and minimal machining requirement.

Since fracture toughness represents a material property, K_{IC} should be reasonably independent of the size of the specimen. However, it has been found that it decreases significantly when the diameter of the specimen decreases below 50 mm (ISRM Testing Commission 1988). For sufficiently large specimens, fracture toughness is expected to remain constant. The minimum specimen diameter that provides consistent K_{IC} results may be identified by testing samples of different sizes (Kuruppu et al., 2014). To determine size effects on K_{IC}, *p*CT specimens 100, 50 and 38 mm in diameter were tested in this study. The

dimensions of the steel jaws that transfer the pulling action to the specimen determine the width (G_w) of the U-shaped groove. For this reason, G_w was set to 10 mm irrespective of specimen size. However, the depth (G_d) of the groove was set to 10 mm for 100 mm diameter samples and reduced to 5 mm for the smaller samples (50 and 38 mm diameters). For crack initiation and propagation, an additional thin (~1 mm), radial, straight notch (*a*) is also cut from the middle of the bottom of the U-shaped groove. The effect of notch length on fracture toughness was accounted for by testing specimens with different notch length ratios ($0.1 \leq a/b \leq 0.4$). In this case, *b* is the distance from the base of the groove to the bottom of the specimen. A schematic diagram of the *p*CT specimen is illustrated in Figure 3.2, and the corresponding dimensions are listed in Table 3.3.

Core plugs 100, 50 and 38 mm in diameter were cut with the aid of a Weka DK32 drill (WEKA Elektrowerkzeuge e.K.) associated with a DM 350 BC mast. Disc-shaped specimens were then sliced using a circular diamond blade. Sample preparation included the careful carving of the groove and the thin notch. Both features were prepared with a customized tile saw using different diamond saw discs (2 mm- thick for the groove, and 1 mm- thick for the notch) and fixtures to control the precise displacement of the disc in the horizontal and vertical directions. A positioning laser helps to align the rotating plane of the saw disc with the vertical diameter of the specimen. Cuts were made by moving the rotating disc through the complete thickness of the specimen. Cutting the groove required several passes of the disc while keeping its depth of cut constant. In contrast, the thin notch was cut in one single blade pass. Once prepared, the samples were oven dried at 60ºC for 24 hours. Then, a couple of knife- edges were epoxy-glued to the specimen surface to attach a clip-on gauge at the level of the notch tip during testing to measure the crack-mouth opening displacement (CMOD). In addition, four magnets with 6 mm- diameter, 3 mm- thickness were glued on the surface of the specimen to hold the same number of acoustic emission (AE) sensors (VS700-D, Vallen).

Table 3.3: pseudo-compact tension (*p*CT) specimen dimensions: *D* = diameter; *B* = thickness; G_d = U-shaped groove depth; G_w = U-shaped groove width; *a/b* = notch length ratio.

D (mm)	*B* (mm)	G_d (mm)	G_w (mm)	*a/b*
100	50	10	10	0.1-0.4
50	25	5	10	0.1-0.4
38	19	5	10	0.1-0.4

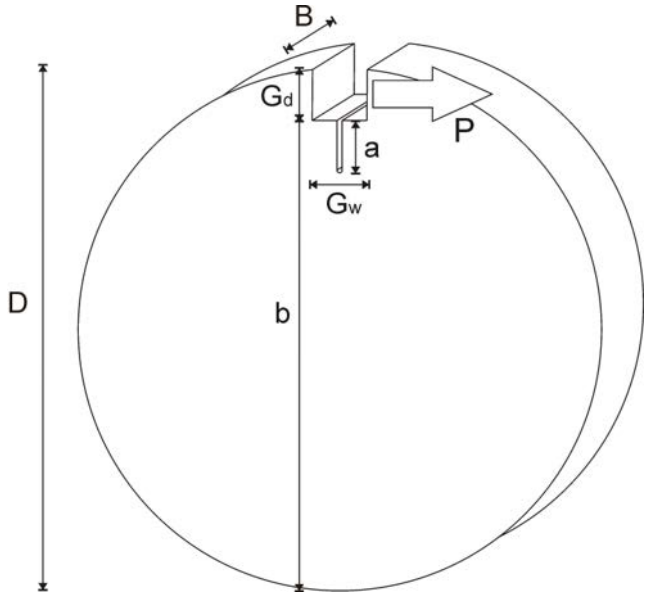

Figure 3.2: Schematic illustration of the geometry and loading configuration of the pseudo-compact tension (*p*CT) specimen: *D* and *B* are the diameter and the thickness of the specimen, respectively; *a* is the notch length; G_d and G_w are the depth and width of the U-shaped groove, respectively; *b* is the distance from the base of the groove to the bottom of the specimen; and *P* is the applied tensile load.

3.3.4. Testing equipment

A specially- designed experimental device was built to perform the *p*CT tests. The requirements considered in the design include portability (which imposed significant size, weight and robustness constraints), mounting simplicity and mechanical stability of the specimens of different sizes during testing, ease

of installation of the measurement devices and replacement of the failed parts, and the quickness of non-testing operations (specimen positioning, cleaning, etc.).

The testing device consists of a high-stiffness frame (AA7075-T6; E = 71.7 GPa, v = 0.33, σ_{yield} = 503 MPa) equipped with a 50 kN push/pull load cell, two linear variable differential transducers (LVDTs), and two crack-opening displacement (COD) gauges (Figure 3.3). Electric signals from all the measurement devices are integrated into a dedicated data acquisition system (GW Inst. instruNet 3.6). The two LVDTs, placed symmetrically on both sides on the specimen, measure the load point displacement (LPD). Simultaneously, a clip-on gauge mounted on a pair of bolt-on knife-edges attached to the steel jaws measures the same magnitude for redundancy. An additional COD gauge can be mounted directly on the surface of the specimen to measure the CMOD.

The movement of the steel jaw is accomplished by means of a 5 mm- lead spindle (VFU 40005 DIN 69051 FORM B, NBS), which converts the rotatory motion of an electric stepper motor (DST56EL61A, Teco Electro Devices Co.) with a step angle of 1.8º (i.e., 200 steps per revolution) into linear displacement (Figure 3.4).

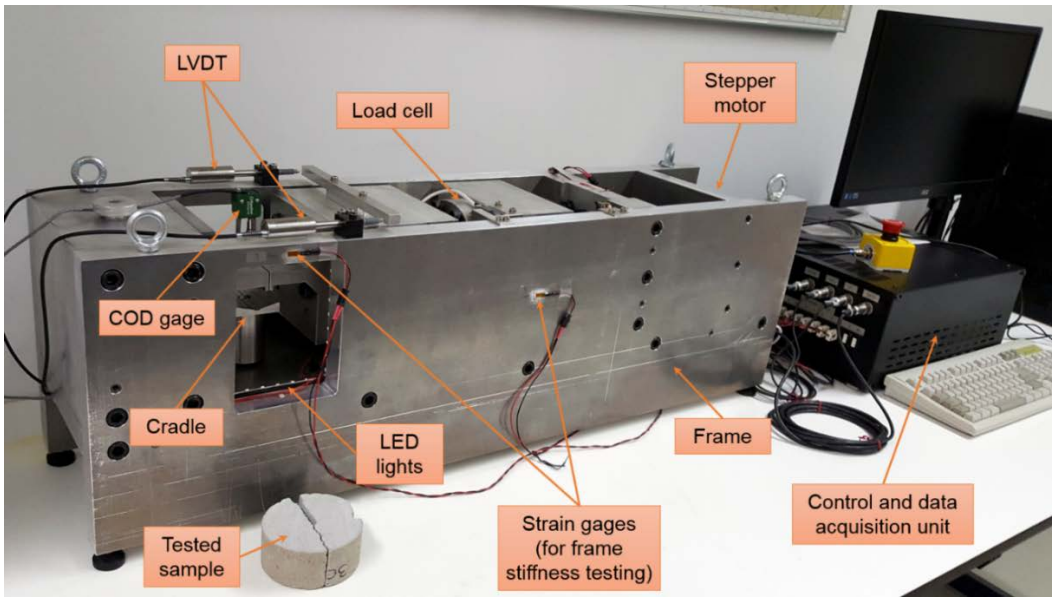

Figure 3.3: Testing equipment designed and built to perform *p*CT tests.

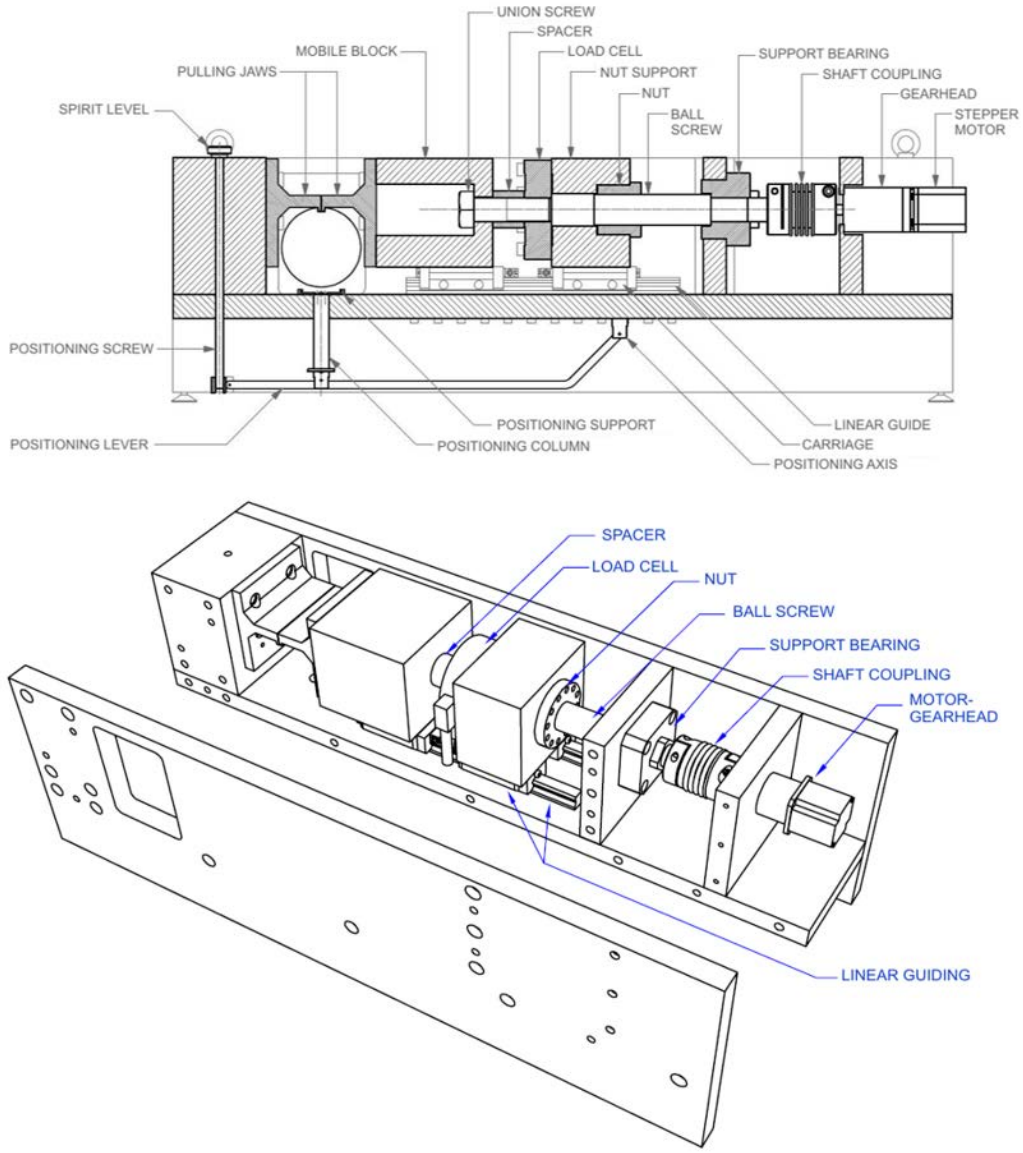

Figure 3.4: Main elements associated with the fracture toughness experimental device.

To improve its performance, the motor is connected to a planetary gearhead (IP-57-M2-100, McLennan Servo Supplies) with a reduction ratio of 1:100. This simple configuration provides a high degree of accuracy in positioning (0.018º/step), equivalent to 0.25 µm/step in terms of linear movement of the shaft, which can be maintained from 0 to 50 kN. The control system consists of: (i) an Arduino-based microcontroller (which commands the motor with a specific program, and keeps track of the displacements and safety signals delivered by

the endstops) and (ii) dedicated software (that makes it possible to set up a testing path). Control commands are transmitted in real time to the microcontroller, which executes them and returns state and displacement data. A stainless steel bellow coupling with a clamping hub (WK4/60-89-SX 49/15, StS Coupling) connects the motor and the spindle. A fixed-side round type support bearing (FK30-C5, Hiwin) provides both axial and rotational support for the spindle.

The stiffness of the loading frame was investigated to assess its elastic energy storage during operation. To this aim, a neoprene layer was compressed between the two steel jaws to a load far above the usual working loads (~25 kN). A total of eight 350 ohm strain gauges were glued with epoxy onto the frame at critical points regarding its geometry (Figure 3.3). For the load applied, the maximum stress recorded at any point of the frame was 10.36 MPa, well below the endurance limit stress (100-150 MPa) provided by the fatigue design curves of AA7075-T6 (Zalnezhad et al. 2012). To further investigate the performance of the device, a 3D finite element model was created in Abaqus/Standard version 6.14 (ABAQUS 2014) to simulate the previous test. The system was modelled as ten separate parts, including the frame, the two steel jaws, and the spindle. The bolted connections in the device were modelled by applying rigid body constraints in the holes, assuming that no relative displacement arises between the parts at the connecting points. The two materials in the machine, namely F1270 steel and AA7075-T6 aluminium, were modelled with a hypoelastic– perfectly plastic constitutive model, assuming elastic moduli of 210 and 71.7 GPa, and Poisson's ratios of 0.3 and 0.33, respectively. The von Mises yield surface was adopted in both cases with associated plastic flow, and the initial yield stresses were 503 MPa for AA7075-T6 aluminium and 700 MPa for F1270 steel. Notice that this rather simple plasticity model was adopted only to verify that no plastic deformation took place in the machine during normal operation; therefore, a detailed description of the work- hardening and the plastic flow was not necessary. The mechanical properties are summarized in Table 3.4. The frame and the jaws were meshed with 10-node quadratic tetrahedrons, while the spindle was modelled with hexahedral elements with 8 nodes and reduced integration,

with the customary hourglass control. The displacement and stress distributions are presented in Figure 3.5. Due to the high stiffness of the device, we observe that the displacement in any of the three principal directions is very small. The largest displacement (~56 µm) appears in the mobile block where the right jaw is attached. The maximum stress (~160 MPa) is found at the steel jaws, and is well below the yield stress of the material (700 MPa).

Table 3.4: Material properties for the FE model of the *p*CT testing equipment. Mass density (ρ), Young's modulus (E), Poisson's ratio (v), and yield stress (σ_{yield}).

ID	Material	ρ (g/cm^3)	E (MPa)	v	σ_{yield} (MPa)
AA7075-T6	Aluminium	2.81	71700	0.33	503
F1270	Steel	7.85	210000	0.3	700

3.3.5. Experimental setup

Figure 3.6 shows a typical loading fixture. The specimen is placed on the positioning cradle and then lifted until the steel jaws fit into the groove. The height of the cradle is manually controlled using a positioning spindle. The verticality of the specimen is checked using a self-levelling cross-line laser. Once the specimen is correctly positioned, the clip-on gauge and the AE sensors are mounted on the specimen surface. In addition, a digital camera is placed in front of the specimen to films crack growth during testing.

3.3.6. Testing procedure

For fracture toughness investigations in rocks, two testing levels are commonly reported in the literature (Ouchterlony, 1988). Level I (or screening level) provides fast and relatively simple access to material properties. In this level, only the maximum load (P_{max}) needs to be measured. Level II (or advanced level) takes into account the non-linear behaviour of typical rocks, allowing a more detailed insight of material behaviour by continuously monitoring both the load and displacement beyond P_{max}. Although the features and characteristics of the

testing equipment developed here are also compatible with level II, for the sake of brevity, only level I tests are reported in this contribution.

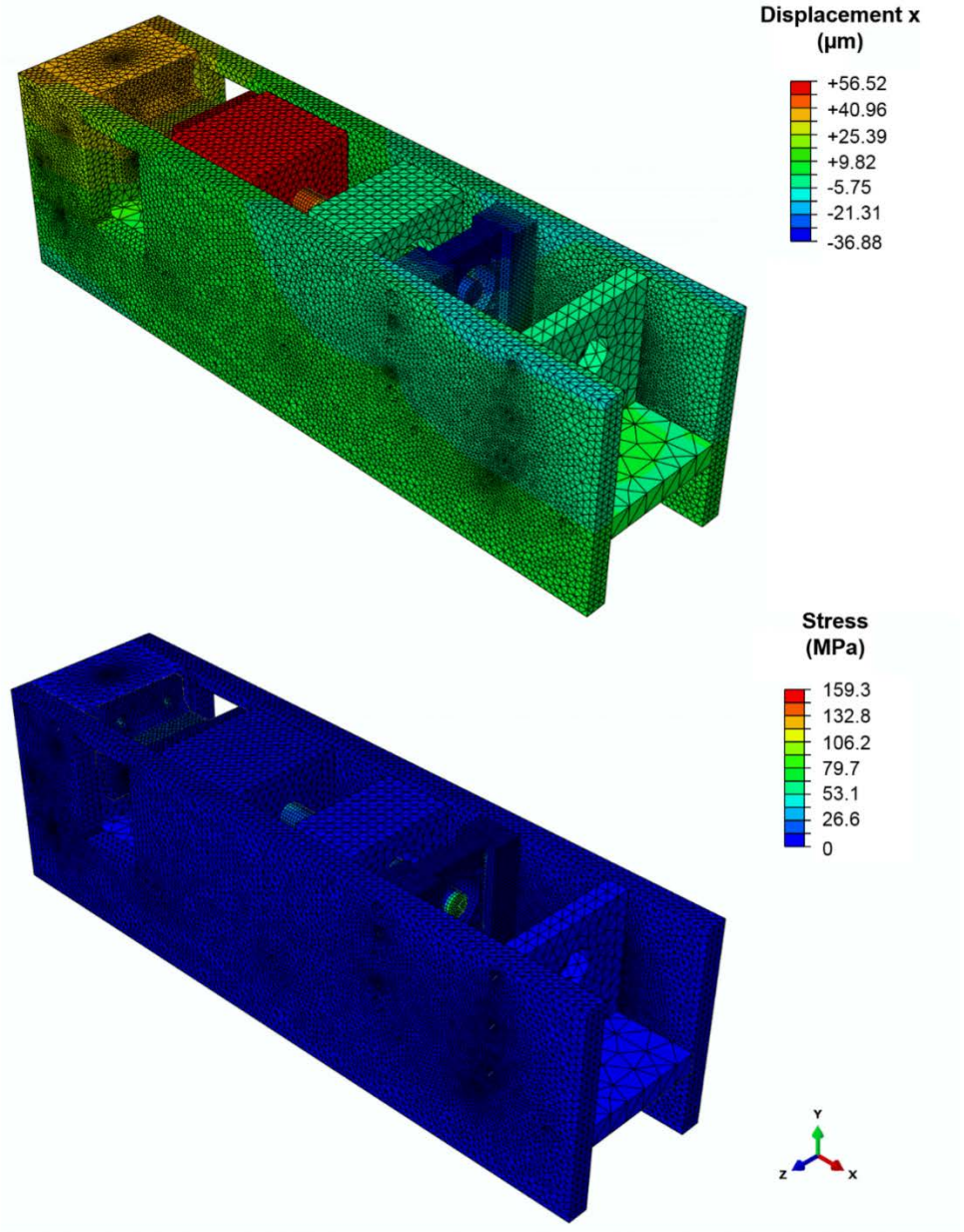

Figure 3.5: Displacement (top) and von Mises stress (bottom) distributions at the maximum compressive load (25 kN) applied during the stiffness assessment of the experimental device.

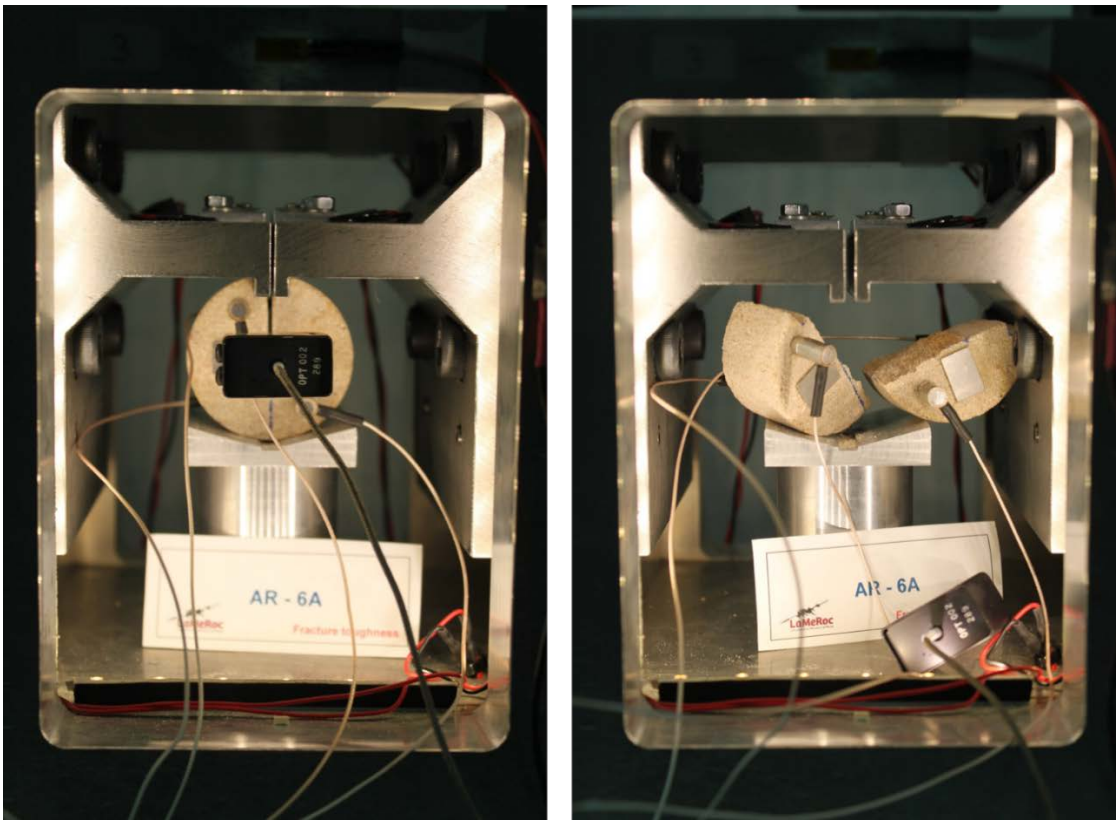

Figure 3.6: Experimental setup of a *p*CT test for a 50 mm in diameter specimen before (left) and after (right) testing. An additional support is required to lift the sample between the steel jaws. Four AE sensors (two on each side) are glued to the specimen surface. A COD gauge is also placed at the level of the crack tip.

Load-displacement graphs can be used to determine the success of a test: a continuous and strength-increasing curve should be observed until specimen failure, when the applied load is expected to drop as the crack propagates through the sample (Kuruppu et al. 2014). Here, the magnitudes of the load (P), LPD and, in some experiments, also CMOD were recorded continuously. Testing was continued beyond P_{max} (i.e., specimen failure) to investigate the post-peak behaviour.

Loading rate affects fracture toughness (Backers et al. 2003). However, at low rates, dynamic effects are negligible and K_{IC} barely changes according to reported evidence (Khan and Al-Shayea 2000; Backers 2004). For this reason, the use of a slow displacement rate (< 0.2 mm/min) is advisable (Backers and Stephansson 2012; Kuruppu et al. 2014). In this study, all the tests were

performed at a constant displacement rate of 0.1 mm/min under ambient conditions. At this loading rate, fracture occurs after a couple of minutes.

A valid fracture toughness test should result in failure of the specimen along the ligament length. The crack is expected to propagate vertically from the notch tip towards the bottom of the sample, splitting the specimen into two similar halves. However, planes of weakness within the sample or highly stressed areas far from the notch tip may cause premature failure in unexpected locations (Veselý et al. 2012). Here, we considered a *p*CT test as valid if the crack started at the notch tip and deviated from the ligament plane by less than 10º. This angle is in accordance with the maximum allowable deviation of 5 mm (~9.1º) proposed by Chandler et al. (2016) for the SR method.

3.3.7. Calculations

The general expression of mode I fracture toughness (K_{IC}) is given in Equation (3.1), where σ_{max} is the applied stress at the critical load ($\sigma_{max} = P_{max}/bB$) and *Y'* is the dimensionless stress intensity factor (Anderson 2005).

$$K_{IC} = Y'\sigma_{max}\sqrt{\pi a} \tag{3.1}$$

For simple specimen geometries and loading configurations, several authors have proposed different analytical solutions of *Y'* (Liu 1996; Fett and Munz 1997; FITNET 2006). Most of these expressions are polynomial equations that extend to the third or fourth order. However, more complex geometries require the use of numerical methods to derive an expression of *Y'* (Ingraffea 2007). The finite element (FE) method is one of the most popular approaches used for this purpose (Wang et al. 2003; Wang et al. 2013; Han et al. 2015; Qian et al. 2016; Wei et al. 2016a). A number of FE packages can perform an analysis of fracture behaviour (Iesulauro 2009; ANSYS 2012; ABAQUS 2014). Since no closed-form expression was found in the literature for our *p*CT geometry, Abaqus/Standard version 6.14 was used to derive *Y'*. Abaqus computes the mode I stress intensity factor (K_I) by using the J-integral method around the crack tip in a region known as the contour integral region (Qian et al. 2016). Although K_I should be independent of the radius of the contour domain where it is

calculated, the high stress concentrations at the crack tip produce large variations in K_I for the first contours (Levén and Rickert 2012). As the number of contours increases, the K_I values tend to converge, and the associated error decreases (Oliveira 2013). The size of the contour integral region (i.e., the number of contours) should be sufficient to allow K_I convergence at a certain distance from the crack tip (Alkiliçgil 2010). Once a consistent K_I value is obtained from the finite element analysis, *Y'* is derived as follows:

$$Y' = \frac{K_I}{\sigma_0\sqrt{\pi a}} \tag{3.2}$$

where σ_0 is the nominal stress acting over the ligament plane for an applied unitary load (*P)*:

$$\sigma_0 = \frac{P}{bB} \tag{3.3}$$

*p*CT specimens 100, 50 and 38 mm in diameter and with diverse notch length ratios were modelled in 2D and 3D. 2D modelling offers the advantage of obtaining an optimized solution within a short computational time. However, 2D modelling requires assuming the state of stress that controls the specimen: the plane stress state prevails in the case of very thin specimens, while the plane strain state is valid for only thick “structures” (Perez 2004). Here, a plane strain condition was assumed for 2D modelling. For specimens with intermediate thickness, 3D finite elements are usually required (Kozak et al. 2003). Although 3D modelling requires a major computation effort to obtain any fracture parameter, the results obtained are generally more accurate. Furthermore, for the 2D models, a single value of K_I is obtained, whereas in 3D modelling, the stress intensity factor varies along the crack front (Ayatollahi et al. 2016). Here, its average value was taken as K_I.

For geometries with one or more planes of symmetry, the partial analysis of a portion of the model reduces the computational burden. The geometrical symmetry of the *p*CT specimen allows the modelling of only one half of the sample. However, we preferred to model the whole specimen due to the asymmetry of both the loading and boundary conditions. The thin notch was

introduced into the 2D and 3D models as a seam and an embedded face, respectively. During mesh generation, the nodes along this edge are duplicated and are allowed to open in the analysis, following the crack extension direction specified by the q-vector (Simulia 2007; Simulia 2009). The contour integral region was defined by a circular mesh centred around the crack tip. In this region, the stress and strain fields become singular, and the mesh density needs to be refined to obtain accurate results. Following Tutluoglu and Keles (2011), the ratio of the contour integral region radius over the specimen radius was set to 0.1 for all the specimen sizes. To account for the $r^{-1/2}$ strain singularity, the region adjacent to the crack front was meshed with special elements with nodes displaced at quarter-point positions (Anderson 2005; Schreurs 2012). As the distance from the crack boundary increases, stress and strain distributions become less crucial. To reduce the computational cost, a coarser mesh was used in the rest of the FE model. 2D and 3D models were meshed with 8-node plane strain elements and 20-node 3D elements, respectively. In the region defining the crack front, these elements were collapsed and transformed into triangular (2D models) or wedge-shaped (3D models) elements to consider the abovementioned stress singularity (ABAQUS 2014; Ayatollahi et al. 2016). Details of the 2D and 3D model meshes are illustrated in Figure 3.7.

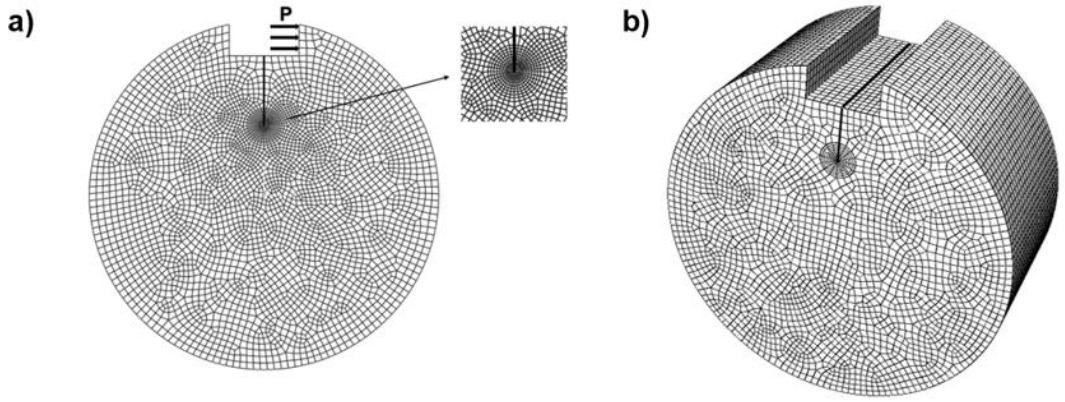

Figure 3.7: Finite element meshes for 2D (left) and 3D (right) used for simulating the pCT specimen in K_I calculations, and detail of the refined mesh around the crack tip.

Contour integral output was requested for eight concentric contours surrounding the crack tip. Constant values were obtained after the fourth contour.

The variation in material characteristics had a slight effect on K_I, but these differences were found to be irrelevant for computing *Y'*, as also reported by Tutluoglu and Keles (2011). K_I values obtained from 2D models were slightly lower than those from 3D models, where the plane strain condition is not totally realized along the crack front due to constraint loss (Qian et al. 2016). The sensitivity of *Y'* to different specimen thicknesses was evaluated by considering different *B*- values (~±50% of the nominal recommended thickness of $B = 0.5D$) while keeping the diameter and notch length constant. The results show that within the range indicated, *B* has no significant impact on *Y'*. This allows us to simplify Equation (3.3) by ignoring *B*. However, it is important to stress that this simplification applies only to the particular *p*CT geometry and loading conditions described in the paper. Based on the previous assumptions, K_I was obtained for each specimen size and a wide range of notch length (*a/b*) ratios. *Y'* was then derived using Equations (3.2) and (3.3). The results derived from the 2D models are plotted as a function of the *a/b* ratio in Figure 3.8. An expression for Y'_{pCT} was then obtained for each specimen size by fitting the results with a fourth-order polynomial function in terms of various *a/b* ratios (Equation (3.4)). The coefficients C_i (i = 0 to 4) are listed in Table 3.5.

$$Y'_{pCT} = C_0 + C_1\left(\frac{a}{b}\right) + C_2\left(\frac{a}{b}\right)^2 + C_3\left(\frac{a}{b}\right)^3 + +C_4\left(\frac{a}{b}\right)^4 \quad (3.4)$$

Table 3.5: Coefficients (C_i) of the dimensionless stress intensity factor (Y'_{pCT}) expression (Equation (3.4)) derived for the *p*CT specimen. Coefficients are given for each specimen diameter (*D*).

D (mm)	C_0	C_1	C_2	C_3	C_4
38	10.278	-24.069	82.329	-136.67	127.89
50	12.651	-47.054	158.72	-247.17	185.22
100	15.341	-74.551	260.03	-404.52	273.19

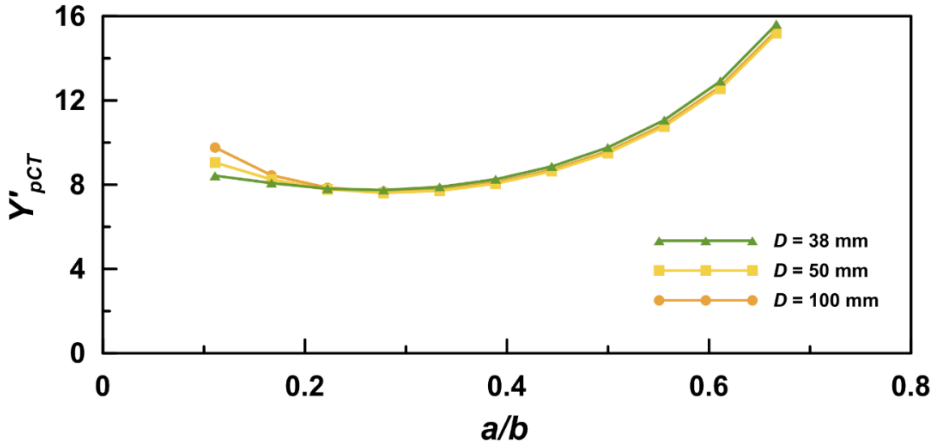

Figure 3.8: Variation of dimensionless stress intensity factor (Y'_{pCT}) as a function of notch length ratio (*a*/*b*) and specimen diameter (*D*).

3.4. Results

3.4.1. Test validity

A total of 81 pseudo-compact tension (*p*CT) tests were performed in this study. Tensile splitting was the dominant failure mode in most of the *p*CT specimens tested. As a result, a macroscopic crack grew along the ligament plane (Figure 3.6). However, a number of tests were considered invalid for one of the following reasons: (1) the crack significantly deviated from the ligament plane (>10º), causing asymmetric specimen failure; (2) failure occurred at a different (highly stressed) location than the notch tip, such as at the contact between the specimen and the steel jaws; (3) the data acquisition system failed during testing.

3.4.2. Load-displacement and load-CMOD curves

The testing results show that the two LVDTs, the clip-on gauge attached to the steel jaws, and the stepper motor offer redundant displacement control. To compute the magnitude of the displacement (*d*), the values recorded by the two LVDTs and the clip-on gauge were normalised and then averaged. A few typical load-displacement (*P*-*d*) curves obtained during the *p*CT testing are plotted in Figure 3.9. The curves are well defined far after the peak load is attained. We

observe that the loading process can be divided into three major stages: (1) a period during which the curve linearly increases (elastic behaviour); (2) a non-linear period during which new microcracks are formed and the slope of the curve gradually decreases until fracture onset at P_{max}; and (3) a period of softening during which the load decreases as a macroscopic crack propagates along the ligament plane. For the tested rocks, crack growth is stable during the entire duration of the experiment, and further crack extension requires the continuous movement of the steel jaw. The load at the critical turning point (P_{max}, d_{peak}) between stages (2) and (3) can be used to compute K_{IC}. For the hardest materials (i.e., Pinacas sandstone and Blanco Mera granite), the curves show a sharper increase to P_{max} than that of the weakest materials (i.e., Corvio and Arcera sandstones). The post-failure branch also decreases more abruptly for harder materials. In general, the curves of PN and GR are characterized by higher maximum loads when than those of AR or C (~70-80% lower).

As seen in Figure 3.10, the slopes of the *P*-CMOD curves are higher than those of the *P-d* curves during loading. At the peak load, the CMOD is comparatively smaller than *d*, especially for harder materials such as Pinacas sandstone.

3.4.3. Mode I fracture toughness results

K_{IC} was computed using Equation (3.1), where *Y'* is the expression derived for the dimensionless stress intensity factor (Y'_{pCT}) given in Equation (3.4). A summary of K_{IC} values obtained in this study for each rock type and specimen size is given in Table 3.6. The magnitude of K_{IC} is larger for Pinacas sandstone and Blanco Mera granite (~1.0-1.4 MPa $m^{1/2}$) than for the Corvio (~0.06-0.12 MPa $m^{1/2}$) and Arcera (~0.2-0.6 MPa $m^{1/2}$) sandstones. The K_{IC} results obtained from valid and invalid (crack deviation > 10º) tests are plotted in Figure 3.11 as a function of the notch length ratio (*a/b*) and specimen diameter (*D*). As seen from this plot, K_{IC} decreases with decreasing specimen size at a given notch length ratio *a/b*. Larger *a/b* ratios also result in lower K_{IC} results for the same specimen diameter.

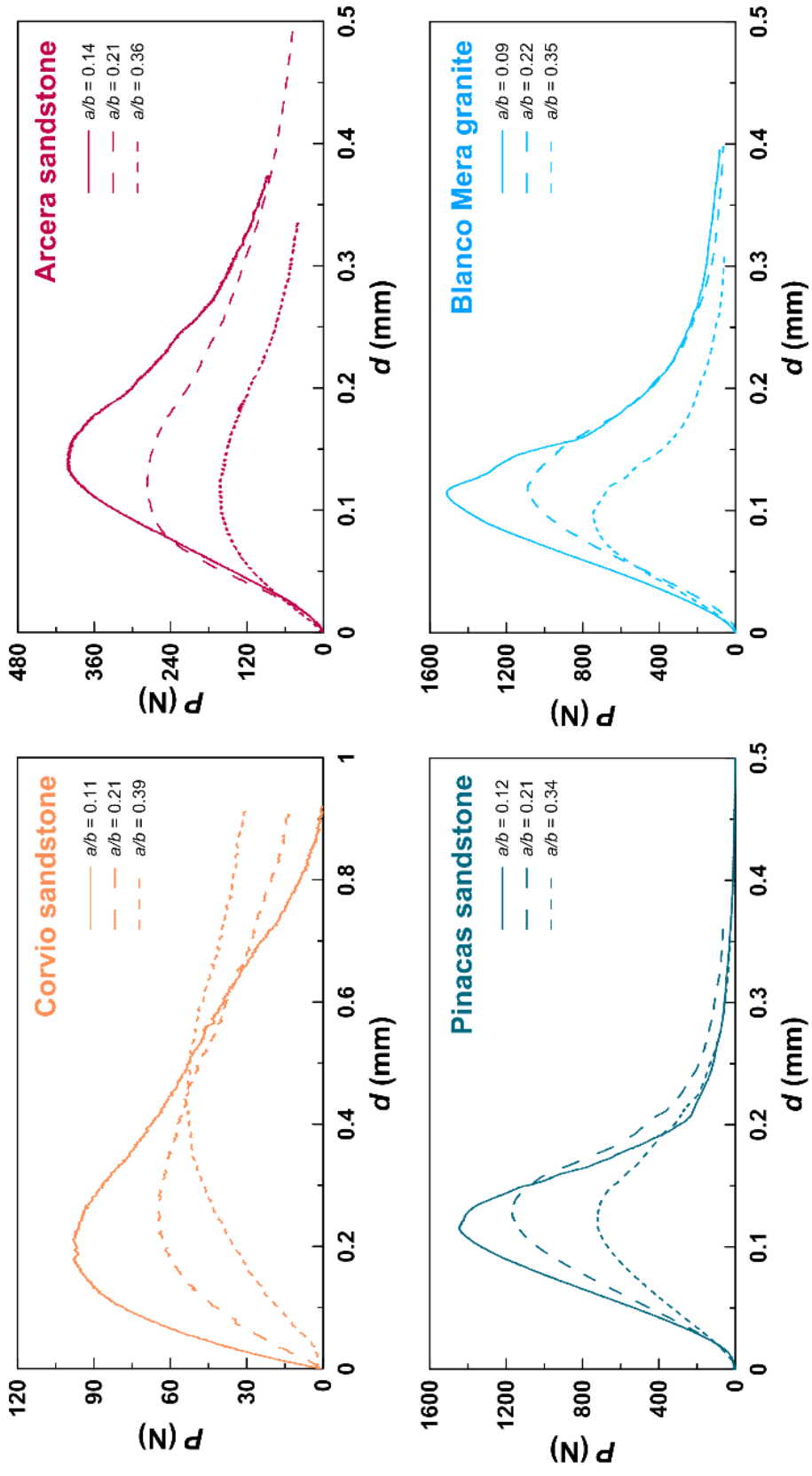

Figure 3.9: Load (*P*) versus displacement (*d*) curves obtained from *p*CT tests performed using 50 mm diameter specimens with different notch length ratios (*a*/*b*): Corvio sandstone (top left); Arcera sandstone (top right); Pinacas sandstone (bottom left); Blanco Mera granite (bottom right).

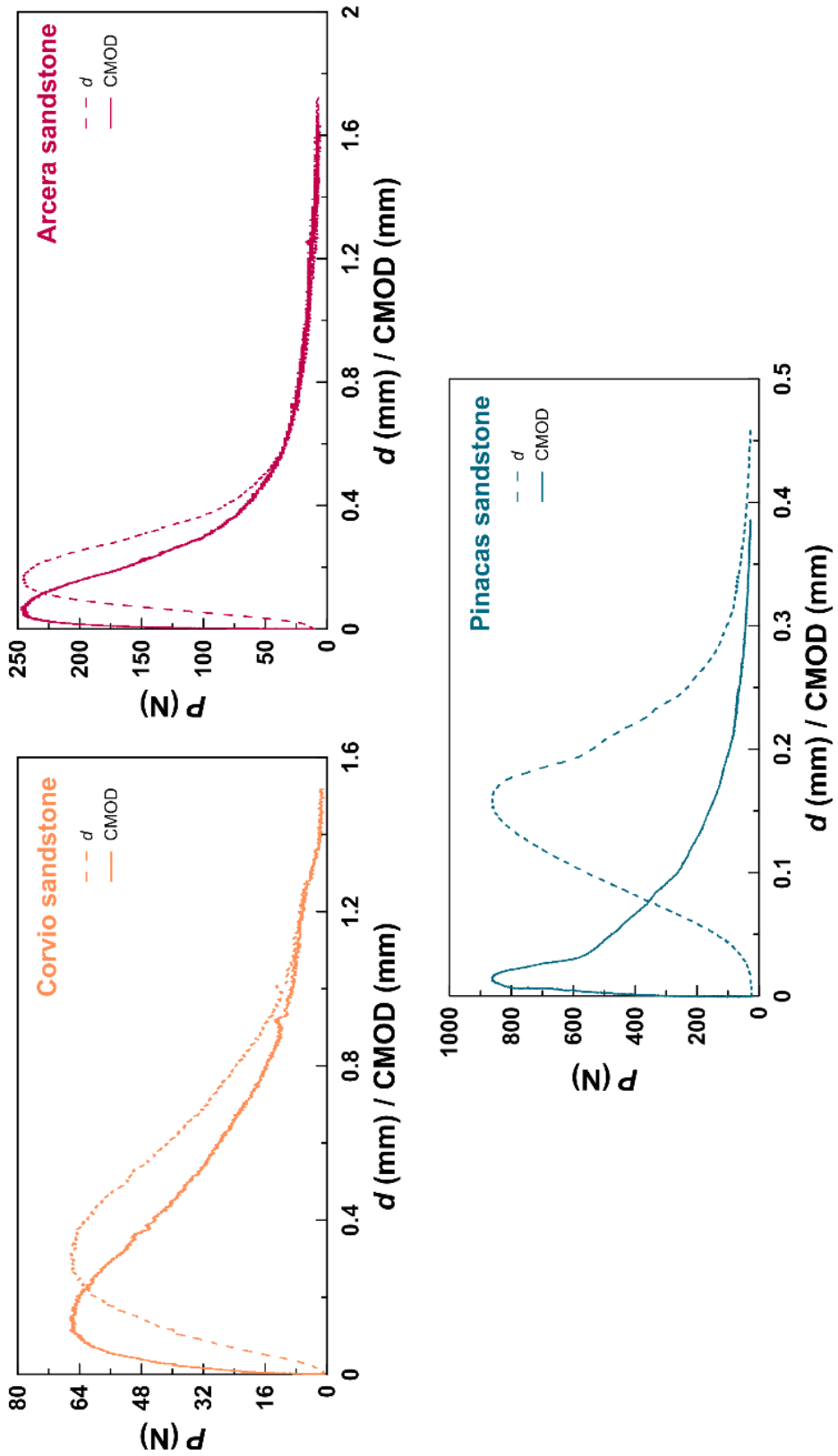

Figure 3.10: Load (*P*) versus displacement (*d*) curves, and load (P) versus crack mouth opening displacement (CMOD) curves obtained from *p*CT tests performed using 50 mm diameter specimens: Corvio sandstone (top left); Arcera sandstone (top right); Pinacas sandstone (bottom).

Table 3.6: Mode I fracture toughness (K_{IC}) results as a function of *p*CT specimen diameter *(D*). Number of valid tests is given into brackets.

Rock type	K_{IC} (MPa m$^{1/2}$)		
	D = 38 mm	*D* = 50 mm	*D* = 100 mm
Corvio sandstone (C)	0.06 – 0.08 (5)	0.07 – 0.12 (8)	-
Arcera sandstone (AR)	0.24 – 0.28 (3)	0.28 – 0.40 (8)	0.26 – 0.60 (9)
Pinacas sandstone (PN)	1.05 – 1.43 (4)	1.13 – 1.46 (9)	1.21 – 1.36 (4)
Blanco Mera granite (GR)	1.05 – 1.09 (2)	1.06 – 1.34 (6)	1.19 – 1.42 (3)

3.5. Discussion

3.5.1. Test validity

From the total of 81 *p*CT tests performed in this study, 61 (~75%) were considered valid in a first approximation. The main reason for considering a test as non-valid was excessive crack deviation from the ligament plane (55% of the non-accepted tests). However, as seen in Figure 3.11, most of the K_{IC} results discarded for this reason are reasonably close to those considered valid, and some of them even fall into the confidence intervals plotted for the 50 mm-diameter specimens. In view of these results, the criterion of validity imposed here (crack deviation < 10º) may be too restrictive, at least for level I testing where only P_{max} is taken into account. Apparently, the deviation of the crack planes towards one side of the samples tested did not follow any discernible pattern, with approximately half of the specimens presenting cracks deviating to each side. Figure 3.12 shows the relation between the notch length ratio (*a/b*) and the angle of deviation of the macrocrack with respect to the ligament plane. Regarding specimen size, 50 mm-diameter specimens have the most reduced angle of spread. This is interesting because these specimens also exhibit the highest rate of success (~89% of tests were valid). In contrast, ~38% of the tests performed with specimens 100 mm in diameter were discarded according to the given criterion. With respect to notch length, no marked trend in deviation angle can be distinguished. However, the majority of non-valid tests (75%) occurred with

samples with *a/b* ≤ 0.25. Taking into account the previous observations, we recommend using medium-sized (*D* = 50 mm) *p*CT specimens with large notch length ratios (*a/b* > 0.25) to improve the success of a test. In addition, we should expect that using *p*CT specimens with *a/b* ratios larger than those tested here would result in a higher rate of success of the experiments. Further testing is necessary in this regard.

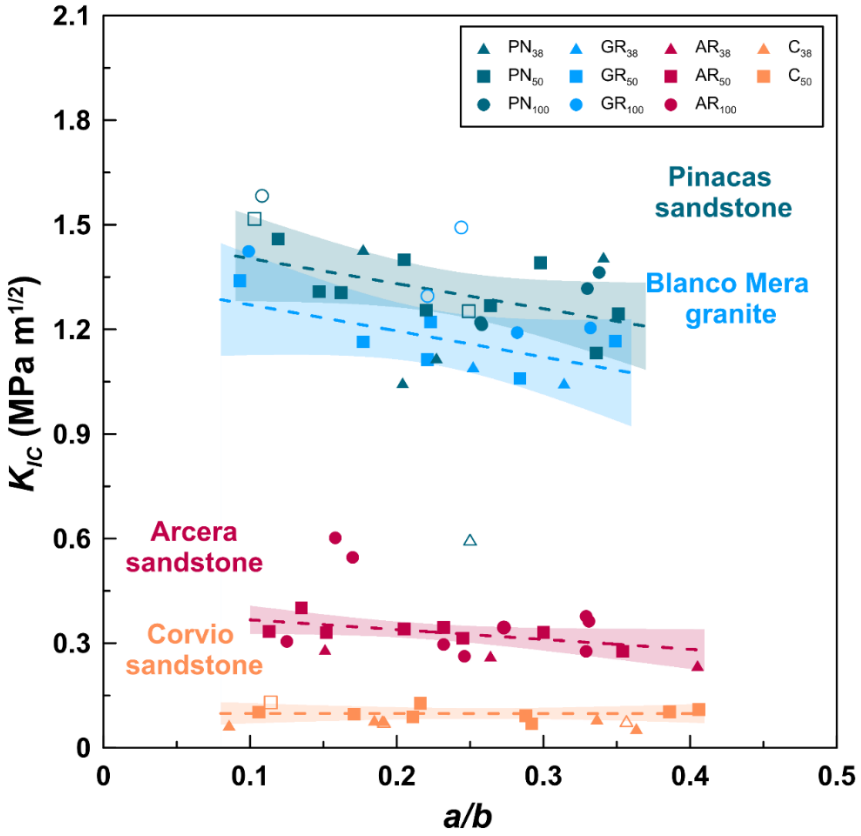

Figure 3.11: Mode I fracture toughness (K_{IC}) results from *p*CT testing as a function of notch length ratio (*a/b*) and specimen diameter (*D*): 38 mm (triangles), 50 mm (squares), and 100 mm (circles). Valid results are shown with filled symbols and invalid results (crack deviation > 10º) are shown with unfilled symbols. Dashed lines represent the linear fits for the valid results (n = 8 for Corvio and Arcera sandstones, n = 9 for Pinacas sandstone, and n = 6 for Blanco Mera granite) obtained from 50 mm-diameter specimens. The shaded areas show the confidence intervals (95%) in each case.

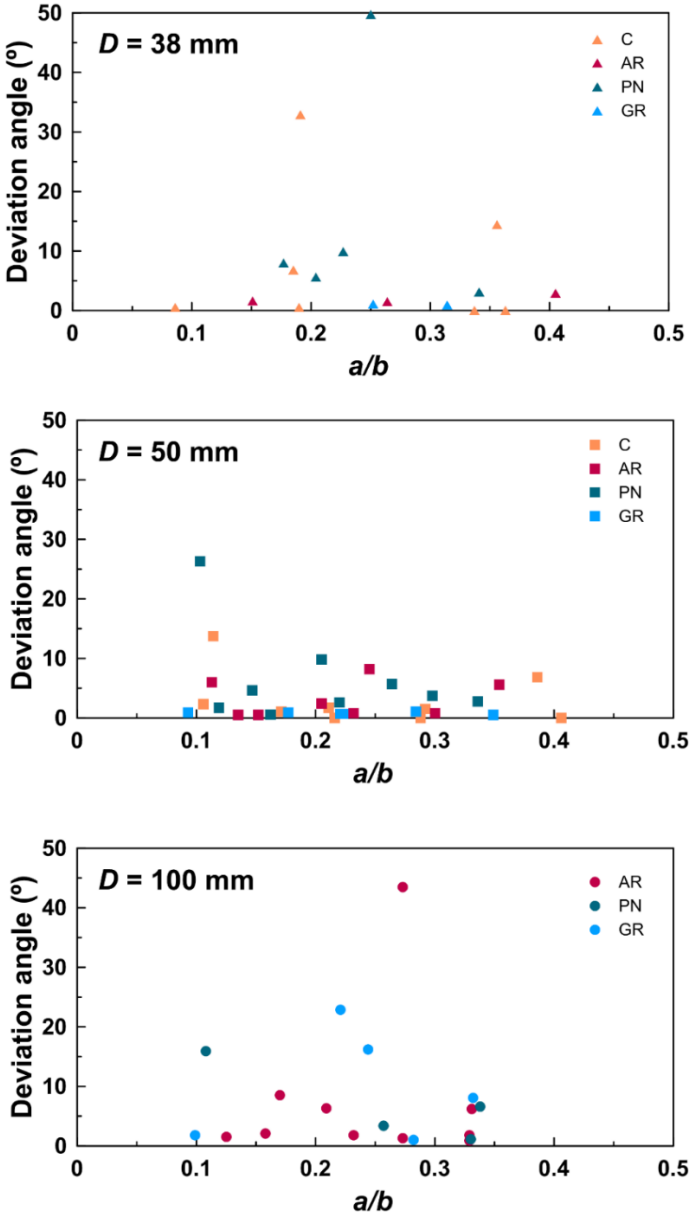

Figure 3.12: Notch length ratio (*a/b*) vs crack deviation angle of 38 (top), 50 (centre), and 100 (bottom) mm diameter *p*CT specimens.

On the other hand, 40% of non-valid tests were produced by specimen failure at highly stressed areas located in points away from the notch tip. This could be related to some inaccuracy in the alignment of the specimen in the loading fixture or to defects within the specimen (such as pre-existing discontinuities or even imperfections arising from the sample preparation process) that could act as stress riser. To reduce the stress concentration in the contact between the flat side of the steel jaws and the specimen, a simple

modification may be performed to include a pair of thin high-strength steel rollers along the jaws. With this configuration, the applied load would be distributed linearly along the U-shaped groove throughout the test.

3.5.2. Mode I fracture toughness

Fracture toughness is considered an intrinsic material property and should be independent of the specimen geometry and loading configuration. However, experimental K_{IC} values derived by a number of authors do not support this statement. Indeed, notable discrepancies in K_{IC} were found when using the same rock type but different testing methods (Alkiliçgil 2010; Aliha et al. 2012; Kataoka et al. 2015). For the sake of standardization, the ISRM has endorsed four suggested methods (SR, CB, CCNBD, and SCB). However, experimental K_{IC} results obtained using these recommendations are not consistent (Iqbal and Mohanty 2007; Aliha et al. 2017).

The K_{IC} results obtained using *p*CT testing for the Corvio and Arcera sandstones are of the same magnitude as published values for similar lithologies but different testing methods, such as CCNBD (Dwivedi et al. 2000), SCB (Singh and Sun 1990), and CB (Brown and Reddish 1997). The results of the Pinacas sandstone compare well with the available data for the Flechtinger (Backers 2004) and Ruhr sandstones (Müller and Rummel 1984) using the CB test. For the Blanco Mera granite, the magnitude of K_{IC} is in agreement with reported data of different granites using the CCNBD (Chang et al., 2002) and CB (Müller and Rummel, 1984) tests. It is worth emphasizing that the experimental values for the same material, specimen geometry and testing method are scattered, both in the literature and in our experiments. This is likely related to the heterogeneous nature of rocks.

3.5.3. Influence of specimen diameter

Mechanical properties of rock, such as its compressive and tensile strength, vary with specimen size (Thuro et al. 2001; Al-Rkaby and Alafandi 2015). Rock strength tends to decrease with increasing specimen size because the larger the specimen is, the higher the probability of including flaws such as

pores, microcracks, or grain boundaries (Hoek and Brown 1997). A number of authors have reported a size effect on K_{IC} in quasi-brittle materials such as rock and concrete (Iqbal and Mohanty 2007; Ueno et al. 2013; Brevik 2016). However, the tendency observed in this case is opposite. Ueno et al. (2013) found that K_{IC} increased with increasing SCB specimen radius for both the Isahaya and Kimachi sandstones. For the latter material, Kataoka and Obara (2015) also reported a positive relation between K_{IC} and the SCB specimen diameter up to D = 140 mm, although fracture toughness tended to converge beyond this value. Similarly, Jeong et al. (2017) observed an increase in K_{IC} with increasing specimen size for SCB samples of Iksan granite.

In this study, *p*CT specimens of different sizes (38, 50, and 100 mm in diameter) were tested. Although the values obtained are internally consistent (i.e., small range), K_{IC} seems to increase with increasing specimen diameter at a given notch length ratio (a/b). The size effect is stronger for the smaller (D = 38 mm) and intermediate-sized (D = 50 mm) samples (Figure 3.13). Regarding lithology, the impact of specimen size on K_{IC} is more notable for weaker materials (Corvio and Arcera sandstones) than for stronger materials (Pinacas sandstone and Blanco Mera granite).

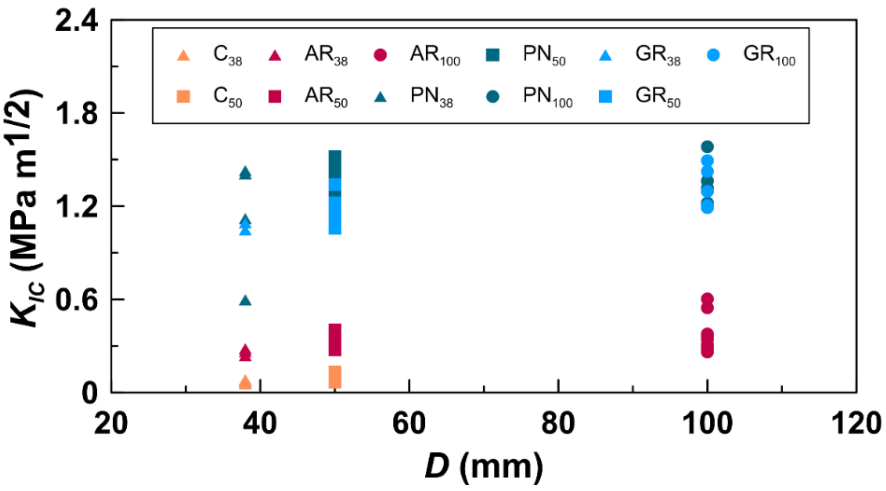

Figure 3.13: Mode I fracture toughness (K_{IC}) as a function of specimen diameter (D) for pCT testing. The subscripts in the legend indicate the specimen diameter (38, 50, and 100 mm).

One reason for larger specimens yielding higher fracture toughness values could be related to the presence of the fracture process zone (FPZ) (Wei et al. 2016b). If the FPZ around the crack tip is sufficiently small compared to the specimen size, the K_{IC} values may be expected to be independent of this feature (Brevik 2016). In addition, flaws within the rock are comparatively larger for smaller specimens, reducing crack resistance. In sufficiently large specimens, the resistance would not be affected by the size of the flaws, and K_{IC} should converge to a constant value (Kataoka and Obara 2015a). In this regard, the ISRM recommends using cores with a diameter much greater than 50 mm to avoid size effects on fracture toughness assessment (ISRM Testing Commission 1988). In the case of the SCB test, Kuruppu et al. (2014) proposed a minimum diameter of 76 mm, or 10 times the grain size. Our experimental results suggest that testing specimens with a diameter of 50 mm could result in underestimation of K_{IC}. In addition, the differences in the mineral species and grain arrangements among different rock types also seem to influence the magnitude of the size effect. Since the K_{IC} results did not converge in the range studied, it cannot be concluded which is the minimum specimen size that provides consistent K_{IC} results. Further investigation is required in this sense.

3.5.4. Influence of notch length

Previous studies indicate that the length of the notch affects K_{IC}. Zhang et al. (2017) found that K_{IC} tends to decrease with increasing notch length for SCB specimens of stabilized soils. Similarly, Chang et al. (2002) also reported this effect using SCB specimens of Keochang granite and Yeosan marble. Conversely, Lim et al. (1994) conducted three-point bending on semi-circular specimens of a synthetic mudstone but did not report an appreciable effect of specimen size or notch length on fracture toughness. Similarly, Funatsu et al. (2015) obtained K_{IC} values that were independent of the notch length (a/R = 0.3-0.5) for SCB specimens of Kimachi sandstone.

Our results show that there is some dependency of mode I fracture toughness on notch length, and we observe that K_{IC} slightly decreases with increasing notch length ratio in *p*CT specimens. Sun and Ouchterlony (1986)

attributed this behaviour to the reduction in the ligament area available for fracture propagation. Our results also suggest that there may be some lithology- or fabric-dependence: the stronger the degree of cementation of the rock (as in the case of the Blanco Mera granite or Pinacas sandstone), the stronger the dependency of K_{IC} is on the notch length.

3.5.5. Grain size effect

The formation of a fracture is closely related to the grain size and particle arrangement of the rock. Consequently, fracture toughness can be expected to depend on the mineral composition and porous structure (Gao et al. 2018). In our work, grain size data are only available for Corvio sandstone (0.15 - 0.3 mm) and Blanco Mera granite (1 - 6 mm). With this limitation, our experimental results suggest that K_{IC} would increase with increasing grain size, as observed by Backers (2004). Conversely, Huang and Wang (1985) reported the opposite behaviour, which they attributed to the effect of the grain boundary contact on the stress intensity factor at the notch tip.

Micro X-ray computed tomography was used for visual observation of the fractures produced in one 38 mm-diameter *p*CT specimen of each rock type after testing. Micro-CT imaging was performed with the MicroXCT-400 apparatus from XRadia at the Petroleum Engineering Department of Colorado School of Mines. As an example, grey-level computed tomography images of the Pinacas sandstone and Blanco Mera granite specimens are shown in Figure 3.14. In the figure, two images are given for each sample: at 1/3 and 2/3 of the thickness of the specimen. The attenuation contrast allows us to visually distinguish the straight notch from the background on the left. The grain boundaries and the macroscopic fracture that initiated from the notch tip can also be identified in the rock matrix. For the specimen of Blanco Mera granite, the geometry of the crack is irregular, predominantly following the grain boundaries. Although the crack also fractures some grains, it tends to avoid those with higher density. This behaviour was also observed by Kataoka and Obara (2015), who attributed this effect to the high resistance to fracture initiation of high density grains, compared to the resistance of grain boundaries. On the other hand, the crack propagation in the

specimen of Pinacas sandstone is comparatively straighter, probably due to its smaller grain size.

From the set of images obtained for each sample, it can be seen that the macroscopic crack did not always initiate at the notch tip and that the point of generation even varies along the specimen thickness. In a first approximation, this behaviour may be attributed to the shape of the notch tip, which is not sharp but semi-circular. Tutluoglu and Keles (2011) reported that the sharpness of the notch tip is not a crucial factor in crack propagation for rock-like materials and that a certain roundness may even be favourable. However, under these circumstances, crack initiation is allowed to occur at any point along the circular geometry of the tip. This factor, together with the particle arrangement of the rock, may determine the deviation of the fracture from the expected path, towards the left or the right side of the specimen.

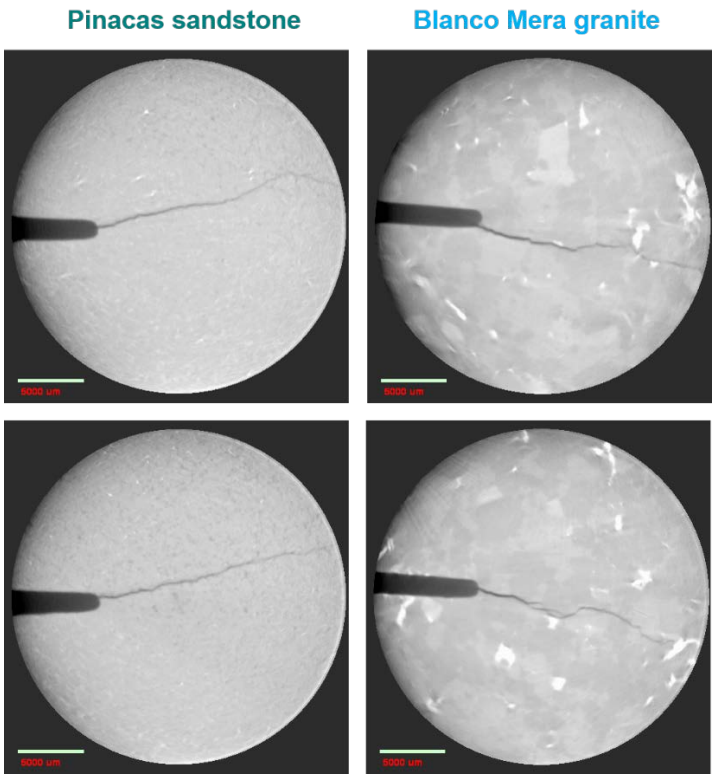

Figure 3.14: Micro X-ray computed tomography images of fractured 38 mm-diameter specimens of Pinacas sandstone (left) and Blanco Mera granite (right) at two different planes along the specimen thickness.

3.5.6. Correlation with tensile strength

Fracture toughness has been correlated with various rock properties, such as density, porosity, Young's modulus, compressive strength, and ultrasonic velocity (Jian-An and Sijing 1985; Chang et al. 2002; Alber and Brardt 2003; Backers 2004; Zhang et al. 2016). In particular, tensile strength and fracture toughness seem to be strongly linked. Backers (2004) argue that tensile strength controls fracture toughness, irrespective of the failure mode, because crack extension first occurs in the plane perpendicular to the highest tension. In Figure 3.15, the K_{IC} values experimentally obtained from the *p*CT testing are plotted as a function of the tensile strength (σ_t). We performed a linear fit to the experimental data, forcing the result to pass through the origin, as suggested by Backers (2004). The regressions proposed by Chandler et al. (2019) for shale and non-shale materials are also plotted in the same graph for comparison. Tensile strength and K_{IC} are found to be linearly correlated ($K_{IC}^{pCT} = 0.11\sigma_t$, $R^2 = 0.95$), in agreement with the behaviour observed by Whittaker et al. (1992) and Zhang (2002) at room temperature.

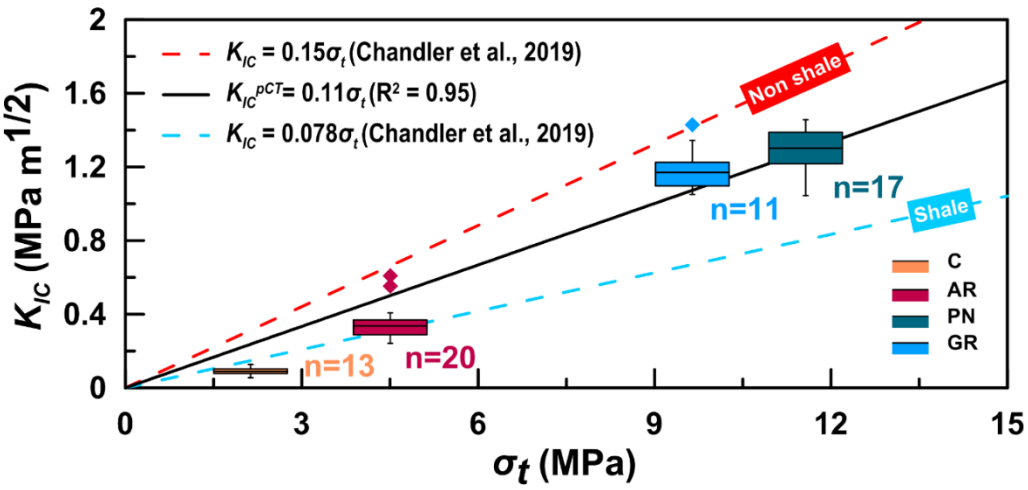

Figure 3.15: Mode I fracture toughness (K_{IC}) as a function of tensile strength (σ_t) for *p*CT testing. The dashed lines are least square fits for shale (blue) and non-shale materials (red) from Chandler et al. (2019). The solid line is the fitting for our experimental data, which is forced to intercept the origin.

3.6. Conclusions

A new method and experimental device designed for measuring the mode I fracture toughness (K_{IC}) of rocks were proposed and described. The testing method, pseudo-compact tension (*p*CT), was used to determine K_{IC} for four different lithologies: Corvio, Arcera and Pinacas sandstones and Blanco Mera granite. The experiments were performed under ambient conditions and the same loading rate. The effects of specimen size, notch length, and material properties were investigated. From this study, the following conclusions are drawn:

1. The combination of small displacement (allowing extremely small strain rates), high load capacity and high stiffness of the testing system makes it convenient for the analysis of the toughness of rocks (either fragile or ductile rocks). Moreover, the simpler sample preparation methodology of the *p*CT test compared to other tests makes it an interesting candidate for routine fracture toughness testing.
2. According to our experimental results, it is advisable to use medium-sized (D = 50 mm) *p*CT specimens with a relatively large notch length ratio (a/b > 0.25) to obtain more consistent results.
3. In this test, crack propagation is slow and can be controlled even after the peak strength is reached. Load-displacement curves are well defined beyond P_{max}, providing insight into the post-peak behaviour.
4. In general, mode I fracture toughness was found to be positively related to the specimen size and negatively related to the notch length. However, the effect is less influential for weakly cemented rocks.
5. Rock properties such as grain size and particle arrangement, together with the shape of the notch tip, determine the point of generation of the crack and its propagation path during testing.
6. Fracture toughness and tensile strength were found to be strongly correlated.

The *p*CT test seems to be a promising approach for assessing mode I fracture toughness in rock. However, it should be noted that the expression of the

dimensionless stress intensity factor derived here for this testing configuration was computed assuming an isotropic rock material. In addition, and as previously reported by different authors, a number of factors, such as moisture content, temperature, confining pressure, or pore pressure, are expected to affect K_{IC} (Matsuki and Aoki 1990; Balme et al. 2004; Nara et al. 2012; Kataoka et al. 2017). Further work is needed to address the effect of rock anisotropy and testing conditions on fracture toughness.

3.7. References

ABAQUS (2014) ABAQUS Version 6.14 / Analysis user's guide. Dassault Systemes Simulia Corporation, Providence, Rhode Island, USA

Al-Rkaby AHJ, Alafandi ZMS (2015) Size effect on the unconfined compressive strength and modulus of elasticity of limestone rock. *Electronic Journal of Geotechnical Engineering* 20:5143–5149

Alber M, Brardt A (2003) Factors influencing fracture toughness KIC from simple screening tests. *International Journal of Rock Mechanics and Mining Sciences* 40:779–784

Aliha MRM, Mahdavi E, Ayatollahi MR (2017) The Influence of Specimen Type on Tensile Fracture Toughness of Rock Materials. *Pure and Applied Geophysics* 174:1237–1253

Aliha MRM, Sistaninia M, Smith DJ, Pavier MJ, Ayatollahi MR (2012) Geometry effects and statistical analysis of mode I fracture in guiting limestone. *International Journal of Rock Mechanics and Mining Sciences* 51:128–135

Alkiliçgil C (2010) Development of specimen geometries for mode I fracture toughness testing with disc type rock specimens. PhD thesis, Middle East Technical University, Ankara, Turkey

Almeida LCR, Vargas E d. A, de Figueiredo RP (2006) Mechanical characterization of rock splitting planes in granitic rocks. *International Journal of Rock Mechanics and Mining Sciences* 43:1139–1145

Anderson TL (2005) Fracture mechanics: Fundamentals and applications, Third Edition. CRC Press

ANSYS (2012) ANSYS User's Manual Revision 12.1. ANSYS, Inc., Canonsburg, Pennsylvania, USA

Arzúa J, Alejano LR (2013) Dilation in granite during servo-controlled triaxial strength tests. *International Journal of Rock Mechanics and Mining Sciences* 61:43–56

ASTM D3967-05 (2008) Standard test method for splitting tensile strength of intact rock core specimens. In: Annual Book of ASTM Standards. ASTM International, West Conshohocken, PA, USA

ASTM E999-90 (1997) Standard test method for plane-strain fracture toughness of metallic materials. In: Annual Book of ASTM Standards. ASTM International, West Conshohocken, PA, USA

Ayatollahi MR, Mahdavi E, Alborzi MJ, Obara Y (2016) Stress intensity factors of semi-circular bend specimens with straight-through and chevron notches. *Rock Mechanics and Rock Engineering* 49:1161–1172

Backers T (2004) Fracture toughness determination and micromechanics of rock under mode I and mode II loading. PhD thesis, University of Potsdam, Potsdam, Germany

Backers T, Fardin N, Dresen G, Stephansson O (2003) Effect of loading rate on Mode I fracture toughness, roughness and micromechanics of sandstone. *International Journal of Rock Mechanics and Mining Sciences* 40:425–433

Backers T, Stephansson O (2012) ISRM suggested method for the determination of mode II fracture toughness. *Rock Mechanics and Rock Engineering* 45:1011–1022

Balme MR, Rocchi V, Jones C, Sammonds PR, Meredith PG, Boon S (2004) Fracture toughness measurements on igneous rocks using a high-pressure, high-temperature rock fracture mechanics cell. *Journal of Volcanology and Geothermal Research* 132:159–172

Bearman RA (1999) The use of the point load test for the rapid estimation of Mode I fracture toughness. *International Journal of Rock Mechanics and Mining Sciences* 36:257–263

Brevik NØ (2016) Experimental study of fracture toughness in sedimentary rocks. PhD thesis, Norwegian University of Science and Technology, Trondheim, Norway

Brown GJ, Reddish DJ (1997) Experimental relations between rock fracture toughness and density. *International Journal of Rock Mechanics and Mining Sciences* 34:153–155

Canal-Vila J (2016) Experimental study of effect of CO_2 injection on rocks: coupling hydrodynamic, mechanical and geochemical processesrim. PhD thesis, University of A Coruña, A Coruña, Spain

Chandler MR, Mecklenburgh J, Rutter E, Lee P (2019) Fluid injection experiments in shale at elevated confining pressures: determination of flaw sizes from mechanical experiments. *Journal of Geophysical Research: Solid Earth* 1–21

Chang SH, Lee CI, Jeon S (2002) Measurement of rock fracture toughness under modes I and II and mixed-mode conditions by using disc-type specimens. *Engineering Geology* 66:79–97

Cifuentes H, Lozano M, Holušová T, Medina F, Seitl S, Fernández-Canteli A (2017) Modified Disk-Shaped Compact Tension Test for Measuring Concrete Fracture Properties. *International Journal of Concrete Structures and Materials* 11:215–228

Dwivedi R., Soni A., Goel R., Dube A. (2000) Fracture toughness of rocks under sub-zero temperature conditions. *International Journal of Rock Mechanics and Mining Sciences* 37:1267–1275

Erarslan N (2016) Microstructural investigation of subcritical crack propagation and Fracture Process Zone (FPZ) by the reduction of rock fracture toughness under cyclic loading. *Engineering Geology* 208:181–190

Falcon-Suarez I, Canal-Vila J, Delgado-Martin J, North L, Best A (2017) Characterisation and multifaceted anisotropy assessment of Corvio sandstone for geological CO_2 storage studies. *Geophysical Prospecting* 65:1293–1311

Fett T, Munz D (1997) Stress intensity factors and weight functions. Computational Mechanics Publications, Southampton, UK

FITNET (2006) Fitness-for-Service (FFS) - Final Draft MK7 (Vol. III). Annex A: Stress intensity factor (SIF) solutions. pp A1–A149

Fowell RJ, Hudson JA, Xu C, Chen JF (1995) Suggested Method for Determining Mode-I Fracture-Toughness Using Cracked Chevron-Notched Brazilian Disc (CCNBD) Specimens. *International Journal of Rock Mechanics and Mining Sciences & Geomechanics Abstracts* 32:57–64

Funatsu T, Seto M, Shimada H, Matsui K, Kuruppu M (2004) Combined effects of increasing temperature and confining pressure on the fracture toughness of clay bearing rocks. *International Journal of Rock Mechanics and Mining Sciences* 41:927–938

Funatsu T, Shimizu N, Kuruppu M, Matsui K (2015) Evaluation of Mode I Fracture Toughness Assisted by the Numerical Determination of K-Resistance. *Rock Mechanics and Rock Engineering* 48:143–157

Gao F, Cai C, Yang Y (2018) Experimental research on rock fracture failure characteristics under liquid nitrogen cooling conditions. *Results in Physics* 9:252–262

Guan JF, Hu XZ, Xie CP, Li QB, Wu ZM (2018) Wedge-splitting tests for tensile strength and fracture toughness of concrete. *Theoretical and Applied Fracture Mechanics* 93:263–275

Han Q, Wang Y, Yin Y, Wang D (2015) Determination of stress intensity factor for mode I fatigue crack based on finite element analysis. *Engineering Fracture Mechanics* 138:118–126

Hoek E, Brown ET (1997) Practical estimates of rock mass strength. *International Journal of Rock Mechanics and Mining Sciences* 34:1165–1186

Iesulauro E (2009) FRANC2D/L: A crack propagation simulator for plane layered structures. Version 1.5 User's Guide. Ithaca, NY, USA

Ingraffea AR (2007) Computational fracture mechanics. In: Encyclopedia of Computational Mechanics. John Wiley & Sons, Ltd, Ithaca, NY, USA

Iqbal MJ, Mohanty B (2007) Experimental calibration of ISRM suggested fracture toughness measurement techniques in selected brittle rocks. *Rock Mechanics and Rock Engineering* 40:453–475

Iqbal MJ, Mohanty B (2006) Experimental calibration of stress intensity factors of the ISRM suggested cracked chevron-notched Brazilian disc specimen used for determination of mode-I fracture toughness. *International Journal of Rock Mechanics and Mining Sciences* 43:1270–1276

Irwin GR (1958) Fracture. In: Handbook on physics. Springer Verlag, Berlin, pp 551–590

ISRM (1978) Suggested methods for determining tensile strength of rock materials. *International Journal of Rock Mechanics and Mining Sciences & Geomechanics Abstracts* 15:99–103

ISRM (1988) Suggested methods for determining the fracture toughness of rock. *International Journal of Rock Mechanics and Mining Science & Geomechanics Abstracts* 25:71–96

ISRM Testing Commission (1988) Suggested methods for determining the fracture toughness of rock. *International Journal of Rock Mechanics and Mining Science & Geomechanics Abstracts* 25:71–96

Jameel A, Harmain GA (2015) Fatigue crack growth in presence of material discontinuities by EFGM. *International Journal of Fatigue* 81:105–116

Jeong SS, Nakamura K, Yoshioka S, Obara Y, Kataoka M (2017) Fracture Toughness of Granite Measured Using Micro to Macro Scale Specimens. *Procedia Engineering* 191:761–767

Jian-An H, Sijing W (1985) An experimental investigation concerning the comprehensive fracture toughness of some brittle rocks. *International Journal of Rock Mechanics and Mining Sciences & Geomechanics Abstracts* 22:99–104

Kataoka M, Mahdavi E, Funatsu T, Takehara T, Obara Y, Fukui K, Hashiba K (2017) Estimation of Mode I Fracture Toughness of Rock by Semi-Circular Bend Test under Confining Pressure Condition. *Procedia Engineering*

191:886–893

Kataoka M, Obara Y (2015a) Size Effect in Fracture Toughness of Sandstone. In: 13th ISRM International Congress on Rock Mechanics. 10-14 May, Montréal, Canada

Kataoka M, Obara Y (2015b) Anisotropy in fracture toughness of sedimentary and crystalline rocks estimated by semi-circular bend test. In: ISRM Regional Symposium, EUROCK 2015. 7-10 October, Salzburg, Austria. pp 695–700

Kataoka M, Yoshioka S, Cho S-H, Soucek K, Vavro L, Obara Y (2015) Estimation of Fracture Toughness of Sandstone by Three Testing Methods. In: Vietrock2015: an ISRM specialized conference, Hanoi, Vietnam, 12-13 March

Khan K, Al-Shayea NA (2000) Effect of specimen geometry and testing method on mixed Mode I-II fracture toughness of a limestone rock from Saudi Arabia. *Rock Mechanics and Rock Engineering* 33:179–206

Khayal OMES (2017) Literature review on imperfection of composite laminated plates. *Journal of Microscopy and Ultrastructure* 5:119–122

Ko TY, Kemeny J (2013) Determination of the subcritical crack growth parameters in rocks using the constant stress-rate test. *International Journal of Rock Mechanics and Mining Sciences* 59:166–178

Kozak D, Blaj L, Matejiček F (2003) State of stress modelling by 2-D finite element analysis of fracture toughness specimens. In: Dobre I, Faur N (eds) Proceedings of the 6th International Conference on Boundary and Finite Element. Timisoara: Editura Politehnica, pp 303–312

Kuruppu MD, Obara Y, Ayatollahi MR, Chong KP, Funatsu T (2014) ISRM-suggested method for determining the mode I static fracture toughness using semi-circular bend specimen. *Rock Mechanics and Rock Engineering* 47:267–274

Levén M, Rickert D (2012) Stationary 3D crack analysis with Abaqus XFEM for integrity assessment of subsea equipment. Chalmers University of Technology, Göteborg, Sweden

Lim IL, Johnston IW, Choi SK, Boland JN (1994) Fracture testing of a soft rock with semi-circular specimens under three-point bending. Part 1—mode I. *International Journal of Rock Mechanics and Mining Sciences & Geomechanics Abstracts* 31:185–197

Linsbauer HN, Tschegg EK (1986) Fracture energy determination of concrete with cube shaped specimens. *Zement und Beton* 31:38–40

Liu A (1996) Summary of stress-intensity factors. In: ASM Handbook. Fatigue and Fracture. Volume 19. ASM International, pp 980–1000

Major JR, Eichhubl P, Dewers TA, Urquhart AS, Olson JE, Holder J (2014) The effect of CO_2-related diagenesis on geomechanical failure parameters; fracture testing of CO_2-altered reservoir and seal rocks from a natural analog at Crystal Geyser, Utah. *48th US Rocks Mechanics/Geomechanics Symposium* 14–7463:1–5

Matsuki K, Aoki T (1990) The effect of confining and pore pressures on fracture toughness of rocks. *Shigen-to-Sozai* 106:713–718

Müller W, Rummel F (1984) Bruchzähigkeitsmessungen an Gesteinen. Bericht zu den BMFT-FE-Vorhaben 03E-3068-B

Nara Y, Morimoto K, Hiroyoshi N, Yoneda T, Kaneko K, Benson PM (2012) Influence of relative humidity on fracture toughness of rock: Implications for subcritical crack growth. *International Journal of Solids and Structures* 49:2471–2481

Nasseri MHB, Mohanty B (2008) Fracture toughness anisotropy in granitic rocks. *International Journal of Rock Mechanics and Mining Sciences* 45:167–193

Nasseri MHB, Schubnel A, Young RP (2007) Coupled evolutions of fracture toughness and elastic wave velocities at high crack density in thermally treated Westerly granite. *International Journal of Rock Mechanics and Mining Sciences* 44:601–616

Oliveira FXGZ de O (2013) Crack modelling with the eXtended finite element method. Master thesis, Instituto Superior Técnico, Lisboa, Portugal

Ouchterlony F (1987) A presentation of the ISRM suggested methods for

determining fracture toughness of rock material. *Proc 6th Int Congr Rock Mechanics* 2:1181–1186

Perez N (2004) Fracture mechanics. Kluwer Academic Publishers, Boston, MA, USA

Qian G, González-Albuixech VF, Niffenegger M, Giner E (2016) Comparison of K_I calculation methods. *Engineering Fracture Mechanics* 156:52–67

Sato N, Takahashi K (2018) Evaluation of Fracture Strength of Ceramics Containing Small Surface Defects Introduced by Focused Ion Beam. *Materials* 11:457

Schreurs PJG (2012) Fracture Mechanics. Lecture notes - course 4A780. Concept version. Eindhoven University of Technology. Department of Mechanical Engineering

Simulia (2007) Abaqus Technology Brief. Fracture Mechanics Study of a Compact Tension Specimen Using Abaqus/CAE. Dassault Systemes

Simulia (2009) Modeling Fracture and Failure with Abaqus. Dassault Systemes

Singh RN, Sun GX (1990) An investigation into factors affecting fracture toughness of coal measures sandstones. *Journal of Mines, Metals and Fuels* 38:111–118

Sun Z, Ouchterlony F (1986) Fracture toughness of stripa granite cores. *International Journal of Rock Mechanics and Mining Sciences & Geomechanics Abstracts* 23:399–409

Takahashi K, Osedo H, Suzuki T, Fukuda S (2018) Fatigue strength improvement of an aluminum alloy with a crack-like surface defect using shot peening and cavitation peening. *Engineering Fracture Mechanics* 193:151–161

Talukdar M, Guha Roy D, Singh TN (2018) Correlating mode-I fracture toughness and mechanical properties of heat-treated crystalline rocks. *Journal of Rock Mechanics and Geotechnical Engineering* 10:91–101

Thuro K, Plinninger R, Zah S, Schutz S (2001) Scale effects in rock strength properties. Part 1: Unconfined compressive test and Brazilian test. In:

Elorante P, Sarkka P (eds) Rock mechanics : a challenge for society : proceedings of the ISRM Regional Symposium Eurock 2001, 3-7 June. Swets & Zeitlinger Lisse, Espoo, Finland, pp 169–174

Tutluoglu L, Keles C (2011) Mode I fracture toughness determination with straight notched disk bending method. *International Journal of Rock Mechanics and Mining Sciences* 48:1248–1261

Ueno K, Funatsu T, Shimada H, Sasaoka T, Matsui K (2013) Effect of Specimen Size on Mode I Fracture Toughness by SCB Test. In: The 11th International conference on Mining, Materials and Petroleum Engineering; the 7th International Conference on Mining, Materials and Petroleum Engineering. Chiang Mai, Thailand, 11-13 November

Veselý V, Holusová T, Seitl S (2012) Numerical prediction of parasitic energy dissipation in wedge splitting tests on concrete specimens. In: 18th International Conference Engineering Mechanics. 14-17 May, Svratka, Czech Republic. pp 1497–1504

Wang QZ (1998) Stress intensity factors of the ISRM suggested CCNBD specimen used for mode-I fracture toughness determination. *International Journal of Rock Mechanics and Mining Sciences* 35:977–982

Wang QZ, Fan H, Gou XP, Zhang S (2013) Recalibration and clarification of the formula applied to the ISRM-suggested CCNBD specimens for testing rock fracture toughness. *Rock Mechanics and Rock Engineering* 46:303–313

Wang QZ, Jia XM, Kou SQ, Zhang ZX, Lindqvist PA (2003) More accurate stress intensity factor derived by finite element analysis for the ISRM suggested rock fracture toughness specimen - CCNBD. *International Journal of Rock Mechanics and Mining Sciences* 40:233–241

Wei MD, Dai F, Xu NW, Liu JF, Xu Y (2016a) Experimental and numerical study on the cracked chevron notched semi-circular bend method for characterizing the mode I fracture toughness of rocks. *Rock Mechanics and Rock Engineering* 49:1595–1609

Wei MD, Dai F, Xu NW, Zhao T, Xia KW (2016b) Experimental and numerical

study on the fracture process zone and fracture toughness determination for ISRM-suggested semi-circular bend rock specimen. *Engineering Fracture Mechanics* 154:43–56

Whittaker BN, Singh RN, Sun G (1992) Rock fracture mechanics: Principles, design, and applications. Elsevier, Amsterdam

Yu Y, Yin J, Zhong Z (2006) Shape effects in the Brazilian tensile strength test and a 3D FEM correction. *International Journal of Rock Mechanics and Mining Sciences* 43:623–627

Zalnezhad E, D Sarhan AA, Hamdi Abd Shukor M, Sarhan AA, Hamdi M, Asri B (2012) A Fuzzy Logic Based Model to Predict the Fretting Fatigue Life of Aerospace Al7075-T6 Alloy. *Caspian Journal of Applied Sciences Research* 39–48

Zhang J, Little DN, Grajales J, You T, Kim Y-R (2017) Use of Semicircular Bending Test and Cohesive Zone Modeling to Evaluate Fracture Resistance of Stabilized Soils. *Transportation Research Record: Journal of the Transportation Research Board* 2657:67–77

Zhang K, Fan F, Li C, Pan R, Xie R, Xue D (2016) Experimental investigations on the relationships between rock toughness and physical properties of shale. *International Journal of Simulation: Systems, Science and Technology* 1–5

Zhang ZX (2002) An empirical relation between mode I fracture toughness and the tensile strength of rock. *International Journal of Rock Mechanics and Mining Sciences* 39:401–406

4. Experimental investigation on the size and other effects on mode I fracture toughness in selected rock types using the *p*CT and SCB testing methods

This chapter has been submitted to '*International Journal of Rock Mechanics and Mining Sciences*'

Andrea Muñoz-Ibáñez[1], Jordi Delgado-Martín[1], and Ricardo Juncosa-Rivera[1]

4.1. Abstract

Mode I fracture toughness (K_{IC}) is an intrinsic material property that quantifies its resistance to initiation and propagation of tensile cracks. Among the different methods developed to determine K_{IC} in rock, the International Society for Rock Mechanics (ISRM) has endorsed four suggested methods, namely Short Rod (SR), Chevron Bend (CB), Cracked Chevron Notched Brazilian Disc (CCNBD), and the Semi-Circular Bend (SCB) method. In this study, we use the SCB technique to compare the results obtained with the new pseudo-compact tension (*p*CT) test, which has proved to be convenient for the assessment of K_{IC} on both fragile and ductile rocks. We have selected the SCB as a benchmark method due to its popularity, simplicity (in terms of sample preparation) and straightforward testing configuration. We discuss the results of 146 tests performed with four different lithologies (Arcera, Pinacas and Corvio sandstones, and Blanco Mera granite), sample size (100, 50 and 38 mm-diameter), and a range of notch lengths. Based on that we assess size-, notch length- and rock type-effects all of them potentially affecting K_{IC}. Our results suggest that both

[1] School of Civil Engineering, University of A Coruña, Campus de Elviña s/n, 15071 A Coruña, Spain

specimen size and notch length have an impact on K_{IC}, although the magnitude of their influence is closely related to lithology. In general, *p*CT specimens yield more consistent values than those samples tested with the SCB method. It also allows for a greater wealth of fracture mechanics information (e.g., fracture energy evolution) and improved control before and after peak load. We discuss additional methodological considerations in the text.

4.2. Introduction

Fracture toughness (K_C) represents the ability of a material to resist crack initiation and propagation. Although it is a strength-related property, testing requires specially conditioned samples in which cracks are geometrically constrained to develop in a prescribed direction (i.e. with a starter notch) in order to apply the fundamental approaches of fracture mechanics. Several testing methods with well-defined sample geometries are currently in use in rock mechanics to determine mode I fracture toughness (K_{IC}) in rocks. The International Society for Rock Mechanics (ISRM) endorses four of them considering cores as the preform for the tested samples: Short Rod (SR), Chevron Bend (CB), Cracked Chevron Notched Brazilian Disc (CCNBD) and the Semi-Circular Bend (SCB) methods (ISRM Testing Commission 1988; Ouchterlony 1989; Fowell et al. 1995; Kuruppu et al. 2014). Recently Muñoz-Ibáñez et al. (2020) have introduced the pseudo-compact tension (*p*CT) test as potential alternative to overcome some of the drawbacks associated with the mentioned suggested methods (e.g. large sample size and cumbersome preparation). The claimed advantages of *p*CT would include: a) reduced rock requirement (disc-shaped specimen with a diameter-to-thickness ratio of 2); b) simpler sample preparation (straight groove and thin starter notch); c) enhanced control of crack propagation (especially beyond peak strength); and d) pure tensile loading.

Based on fracture mechanics premises, fracture toughness is an intrinsic material property. Accordingly, its experimental determination should render consistent results irrespective of the geometry of the specimen and configuration of loading. However, when applied to rocks, the experimentally determined K_{IC}

values reported by many authors contend with such generally assumed behaviour. Indeed, significant discrepancies on the K_{IC} values can be identified from publications using the same rock type but different testing methods (Alkiliçgil 2010; Aliha et al. 2012; Kataoka et al. 2015; Erarslan 2018). The ISRM suggested methods are not exempt of this problematic (Iqbal and Mohanty 2007; Aliha et al. 2017; Erarslan 2018) and further efforts are still needed to fill the gaps linking the intercomparability of fracture toughness testing methods in rocks. In this line and based on 146 tests, in this contribution we compare K_{IC} values derived using the *p*CT approach with determinations performed according to the SCB method. We have selected SCB as benchmark due to its popularity, simplicity (in terms of sample preparation), and straightforward testing configuration. In the assessment we have considered lithology (four rock types: Corvio Sst, Arcera Sst, Pinacas Sst, and Blanco Mera Grt), and size effects, as well as other geometrical constrains like notch length. The objective of this study is to check the mutual consistency of the K_{IC} values obtained using both testing methodologies while considering a number of relevant properties (sample size, notch length, and lithology). For each test, we use the corresponding load-displacement curves to characterize the energy content of the fracturing process. In selected tests we also monitored the acoustic emission (AE) activity. Based on that information, we explore the relationship between the energy release associated to the fracture process and that captured by AE. Finally, we also present some methodological considerations about the SCB testing method.

4.3. Materials and methods

4.3.1. Materials

In order to provide a common ground for the comparison of K_{IC} values derived from the SCB and *p*CT testing methods, we have employed four different rock types: Corvio (C), Arcera (AR), and Pinacas (PN) sandstones, and Blanco Mera granite (GR). All these rocks are nearly isotropic but differ in strength and mechanical performance. Corvio and Arcera sandstones have a relatively low strength, reduced grain size (< 1mm), high porosity and low elastic moduli. However, the Pinacas sandstone, while having a similar grain size, is significantly

tougher and has lower porosity and higher elastic modulus. The Blanco Mera granite is a homogeneous rock of medium grain size (1-6 mm), low porosity and moderate strength. Relevant properties of these rocks (mineralogy, porosity, uniaxial compressive strength, indirect tensile strength, V_P & V_S, etc.) have been reported in previous studies (Arzúa and Alejano 2013; Canal-Vila 2016; Falcon-Suarez et al. 2017; Muñoz-Ibáñez et al. 2020) and only a short summary is compiled in Table 4.1.

Table 4.1: Rock properties obtained from non-destructive tests: effective porosity (n_e), bulk density (ρ_{bulk}), and ultrasonic velocities (V_p and V_s) Selected properties of the rocks used in the study. σ_c = Compressive strength; σ_t = Tensile strength; E = Young's modulus; ν = Poisson's ratio; n_e = Effective porosity. Data for the Corvio Sst (C) is reported in Falcon-Suarez et al. (2017), while data for Arcera Sst (AR), Pinacas Sst (PN), and Blanco Mera Grt (GR) can be found in Muñoz-Ibáñez et al. (2020).

Rock	σ_c (MPa)	σ_t (MPa)	E (GPa)	v	n_e (%)
C	35.4 – 44.4	1.9 – 3.1	9.7 – 19.7	0.3 – 0.4	18.4 – 23.5
AR	40.2	4.1 – 4.9	12.2	0.4	17.3 – 18.2
PN	129.5	11.2 – 11.9	35.0	0.2	5.5. – 6.5
GR	60.4 – 83.5	9.6 – 9.7	33.0	0.3	1.2 – 1.3

4.3.2. Sample preparation

Figure 4.1 shows a schematic diagram of the specimens employed in the SCB and *p*CT testing as well as some relevant reference properties. We see that, while the geometry of the SCB specimen is that of a short semi-cylinder with a single thin notch located at the middle of its flat face, the *p*CT sample is a short full-cylinder with a U-shaped groove and a thin notch along its generatrix. In the present study, we cored the tested samples from homogeneous rock blocks using diamond drill bits to produce plugs of 38, 50, and 100 mm in diameter. The plugs were then sliced into discs with a diameter-to-thickness (*D/B*) ratio of 2. For the SCB specimens, we diametrically halved the discs with a modified tile saw. The thin straight notch in the centre of the flat face was cut with a 1 mm-thick diamond

disc whose vertical position (that determines the depth of the notch) can be set with the aid of a vertical spindle. Good alignment of the sample with respect to the saw is ensured with the aid of reference marks (laser level, set square) and the use of a grip fixed to a horizontal movable stand connected to a horizontal spindle. In order to systematize the fabrication process, we used 3D-printed special fixtures (Figure 4.2). In the case of the *p*CT specimens, we used the same approach but for the U-shaped groove, we carved it using a thicker diamond disc (2 mm) and making several saw-passes while displacing horizontally the sample after each pass (Figure 4.2). Then, we cut the thin notch using the same 1 mm-thick disc described for the SCB specimens. The samples elaborated according with the previous description were oven-dried at 60ºC for a minimum of 24 hours. The reference dimensions of SCB and *p*CT specimens are reported in Table 4.2.

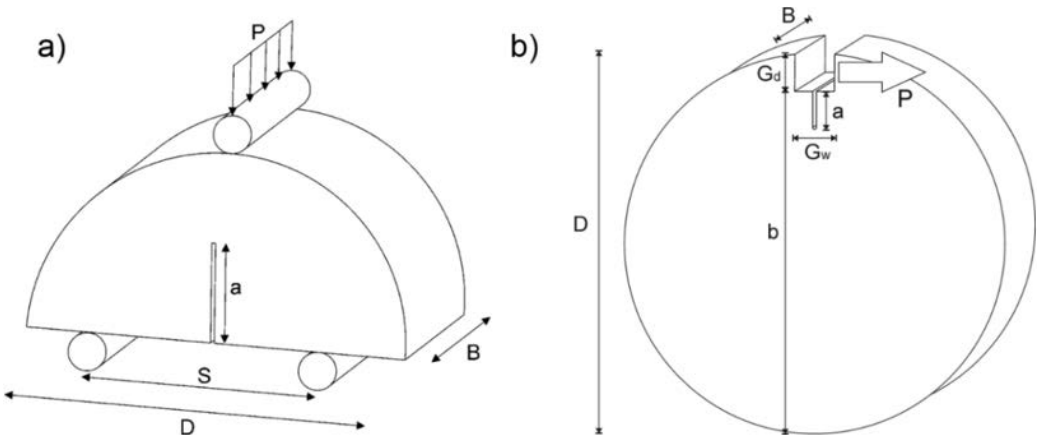

Figure 4.1: Schematic illustration of specimen geometries and loading configurations for the SCB (1) and *p*CT (2) specimens. *P* = applied load; *D* = diameter; *B* = thickness; *a* = notch length; *s* = span length; G_d = groove depth; G_w = groove width; *b* = distance from the base of the groove to bottom of the specimen.

In order to assess the crack mouth opening displacements (CMOD) we have used different displacement sensors (Figure 4.3) in some of the tests: a) For the SCB tests, a pair of horizontally-laid linear variable differential transducers (LVDTs); b) For the *p*CT tests, a crack opening displacement (COD) gauge clipped to a pair of glued steel knife-edge plates. In the case of the SCB test, LVDTs were selected to circumvent the problems inherent to the use of clip-on gauges with small size samples. We installed the LVDTs coplanar to the flat face

of the sample. However, due to the curved nature of the top surface and the magnification of contact errors associated with the rotation of this surface as the test progresses, we glued 3D printed T-plates to the corresponding edges. Additionally, 6 mm-diameter, 3 mm-thickness magnets were also glued on the surface of the specimens to hold acoustic emission (AE) sensors.

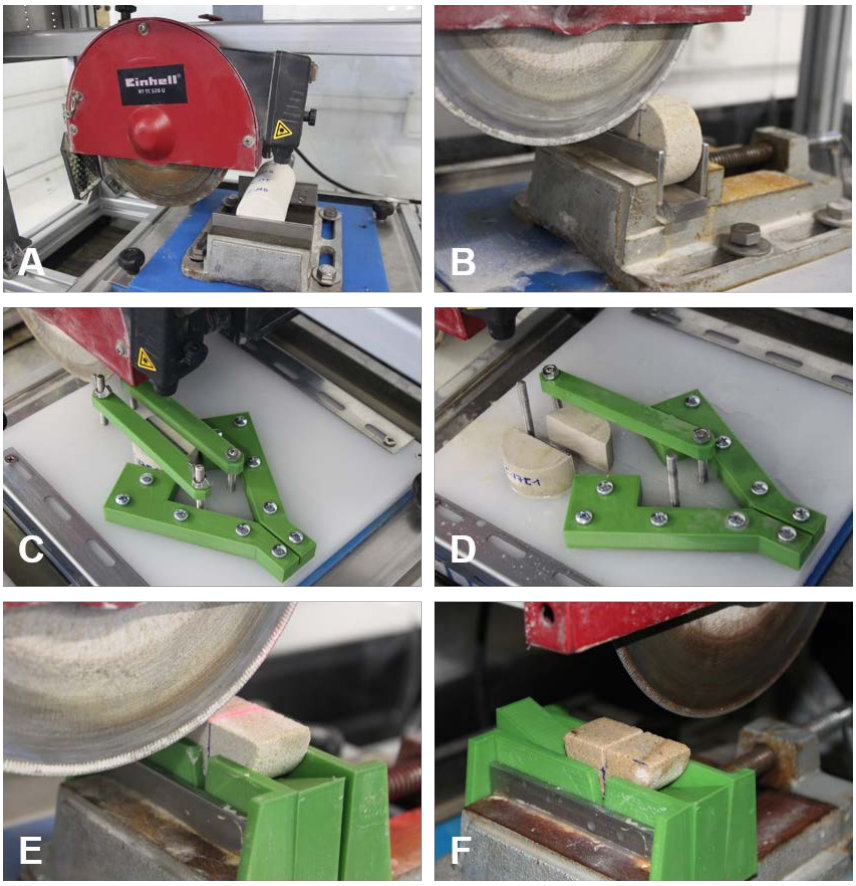

Figure 4.2: Preparation of samples for SCB and *p*CT testing. A) Plug slicing; B) U-shaped groove carving; C and D) Halving SCB specimens; E) Laser alignment for straight thin-notch cutting; F) SCB sample finished after a single pass of the diamond saw.

Although the suggestions of the ISRM consider the use of a minimum sample diameter of 76 mm for SCB testing (Kuruppu et al. 2014), in order to assess eventual size effects on K_{IC}, in this study we also consider bigger (100 mm) and smaller sizes (50 and 38 mm). The same was done for *p*CT. In addition,

we have analysed the effect of notch length by testing specimens with *a/R* (*a* = notch length; *R* = radius of the specimen) and *a/b* (*b* = distance from the base of the groove to the bottom of the specimen) ratios of 0.4-0.6 and 0.1-0.4 for the SCB and *p*CT specimens, respectively. However, following different lines of evidences reported by several authors (Kobayashi et al. 1986; Singh and Sun 1990; Khan and Al-Shayea 2000) we have not considered the effect of variable specimen thickness over K_{IC} and we have prescribed a constant *D/B* ratio of 2 for all the experiments.

Table 4.2: Geometrical dimensions of the SCB and *p*CT specimens. *D* = Diameter; *B* = Thickness; *s/D* = span length ratio; *a/R* = notch length ratio; G_d = U-shaped groove depth; G_w = U-shaped groove width; *a/b* = notch length ratio.

		SCB specimens		*p*CT specimens		
D (mm)	*B* (mm)	*s/D*	*a/R*	G_d (mm)	G_w (mm)	*a/b*
100	50	0.55 – 0.65	0.4 – 0.6	10	10	0.1 – 0.4
50	25	0.55 – 0.65	0.4 – 0.6	5	10	0.1 – 0.4
38	19	0.55 – 0.65	0.4 – 0.6	5	10	0.1 – 0.4

4.3.3. Experimental setup

The SCB test was selected due to its simplicity in terms of specimen geometry, sample preparation, loading configuration, and testing procedure (Wei et al. 2016). We tested these specimens under three-point bending on a stiff servo-electric frame equipped with a 4.448,22 N load cell (Figure 4.3A, C). In this configuration, we use an upper steel roller to transfer a linear load on the top of the sample, while two additional lower rollers, separated by a fixed distance (*s*), support the sample. When testing weak materials, Kuruppu et al. (2014) suggest a value for the span-to-diameter ratio (*s/D*) close to 0.5 while this value increases to 0.8 for the stronger ones. Based on that and considering the varied nature of the tested rocks, we selected a value of *s/D* of ~0.55 when testing the softer Arcera and Corvio sandstones, and ~0.65 for the tougher Pinacas sandstone and Blanco Mera granite.

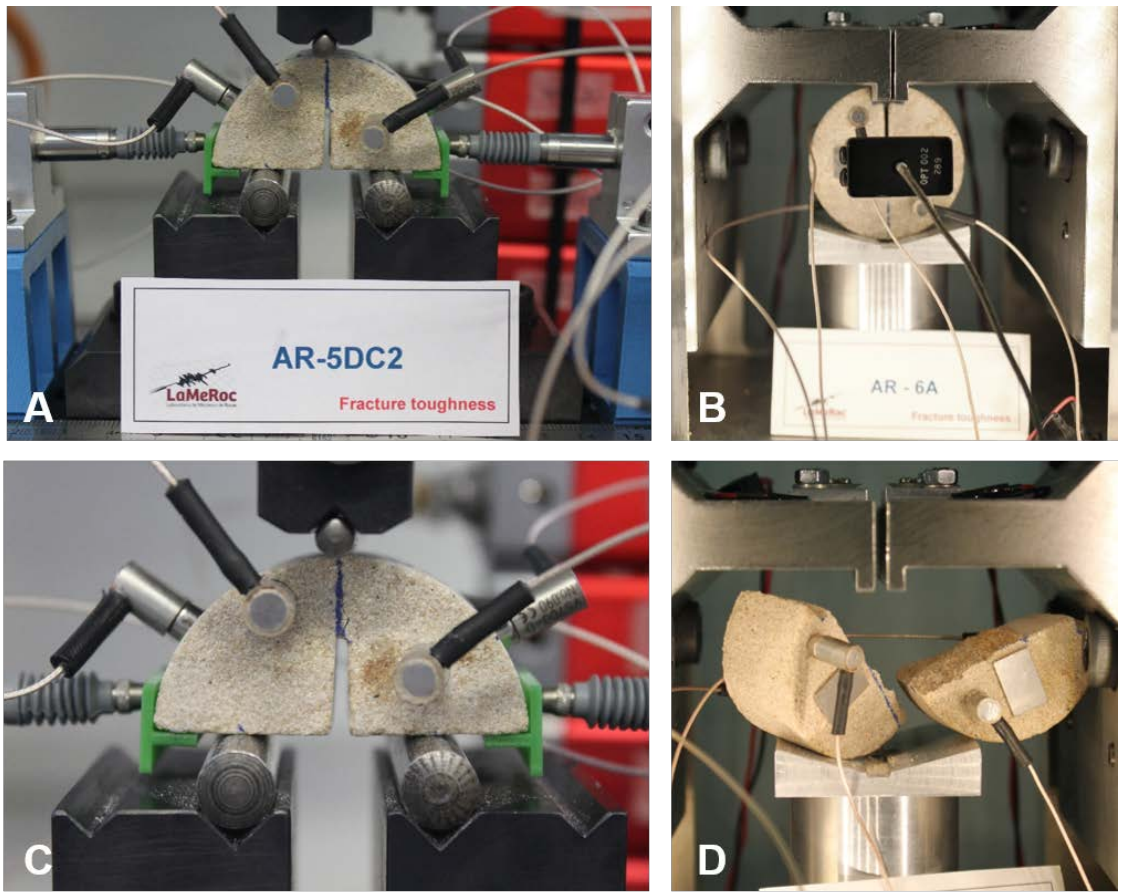

Figure 4.3: SCB (left) and *p*CT (right) loading fixtures. The pictures illustrate two samples of 50 mm-diameter corresponding to the Arcera sandstone before (A, B) and after (C, D) the corresponding tests. The SCB samples (A, C) show the disposition of two horizontal displacement transducers (LVDT-type) and the *p*CT (B, D) a COD gauge. SCB and *p*CT samples illustrated are also equipped with six and four acoustic emission sensors, respectively.

In the SCB tests, the load point displacement (LPD) corresponds to the vertical displacement of the loading roller. In that case, we assessed CMOD using the two LVDTs placed perpendicularly to the notch plane and facing each other along the diametric plane of the specimen. The 3D-printed T-plates glued to both sides of the specimen provide a flat contact surface for them and, considering the magnitude of LPD it is possible to correct the horizontal displacement for the effect of rotation of the T-plates and obtain an accurate estimate of CMOD. For

this testing method, we have recorded for all the specimens the load-CMOD (*P*-CMOD) and load-displacement (*P*-LPD) curves.

*p*CT specimens are loaded in pure tension using the specially-designed testing device described in detail by Muñoz-Ibáñez et al. (2020), which is equipped with a 50 kN load cell. The specimen is placed on a platform and attached to two steel jaws that penetrate into the U-shaped groove cut in the top of the sample (Figure 4.3B, D). With this setup, while one of the jaws remains static, the other one is pulled away at a constant displacement rate. We assess CMOD by means of a clip-on gauge mounted on the knife-edges glued to the surface of the specimen. Two LVDTs placed symmetrically on both sides of the specimen record LPD, that is, the displacement of the mobile steel jaw. While we have recorded *P*-LPD curves for all the specimens tested with the *p*CT methodology, CMOD has been measured only in 11 of them. For both *p*CT and SCB, the experiments were conducted at room temperature and displacement control at an identical rate of 0.1 mm/min.

The data reported in the present study has been determined according to the Level I described in the ISRM suggested methods (ISRM Testing Commission 1988), that is, including in the computations only the value of peak load (P_{max}). Kuruppu and Chong (2012) consider that this is acceptable in many situations. However, due to the inherent complexity of certain matrices like rocks and other brittle engineering materials (e.g. concrete), we believe that it is advisable to take into consideration the properties considered in Level II testing, especially when more sophisticated non-linear fracture mechanics models are to be applied. Accordingly, we have tried to obtain data concerning the post-peak behaviour of the studied rocks by continuing the experiments beyond P_{max}.

Acoustic emission (AE) is a non-destructive testing technique than can provide interesting insights about the processes of crack initiation, propagation and coalescence. To this respect, in some selected specimens we have emplaced up to eight miniature Vallen VS700-D AE sensors (6.3 mm-diameter; 10 mm-length) at different distances of the starter notch. Data acquisition has been performed with a multichannel AMSY-6 AE system (Vallen Systeme GmbH)

equipped with 8 ASIP-2 boards (2 channels per board) with capability of managing up to 16 independent signals. We recorded continuous waveforms at a sampling rate of 10 MHz and, in order to eliminate unwanted frequency components related to environmental or system noises, we set up a band-pass filter (95-850 kHz) and signal threshold level of 40 dB. We attached the AE sensors to the samples via 6 mm-diameter, 3 mm-height magnets that were glued with a thin layer of cyanoacrylate glue (Figure 4.3). A thin layer of multi-silicone grease (1110, OKS) was used as the coupling agent in the interface magnet-sensor, providing good acoustic transmission between both surfaces (ASTM 1997). The number of AE sensors employed was 4 for *p*CT samples (2 on each side of the specimen) and 6 or 8 in the case of 50- and 100-mm diameter SCB samples. Since it is expected that cracks start their propagation from the notch tip, some of the AE sensors were placed close to the ligament plane.

The raw AE signals were enhanced with Vallen AEP5 preamplifiers set with 34 dB gain. With this AE setup, we recorded in real-time a wide number of AE parameters (e.g., counts, amplitude, duration, energy, and frequencies). However, in this study we focus on the assessment of AE energy, which is defined as the integral of the squared voltage signal divided by the 10 kΩ reference resistance over the duration of the AE waveform. We recorded mechanical and AE data separately, so it was necessary to synchronize both records using a common time-stamp for the two computers involved in data acquisition.

4.3.4. Calculations

According to Kuruppu et al. (2014), the computation of mode I fracture toughness (K_{IC}) for the SCB test can be performed based on Equation (4.1):

$$K_{IC}^{SCB} = Y'_{SCB} \frac{P_{max}\sqrt{\pi a}}{2RB} \tag{4.1}$$

where P_{max} is the peak load (in N), a is the notch length (in m), R and B are the specimen radius and thickness (in m), respectively, and Y'_{SCB} is the

specific non-dimensional stress intensity factor associated with the SCB method. This is given by Equation (4.2):

$$Y'_{SCB} = -1.297 + 9.516\left(\frac{s}{2R}\right) - \left(0.47 + 16.457\left(\frac{s}{2R}\right)\right)\beta + \left(1.071 + 34.401\left(\frac{s}{2R}\right)\right)\beta^2 \quad (4.2)$$

in which *s* is the span length (in m) and *β* the notch length ratio (*β* = *a*/*R)*.

In the case of the *p*CT method and following Muñoz-Ibáñez et al. (2020), K_{IC} is derived using Equation (4.3):

$$K_{IC}^{pCT} = Y'_{pCT}\sigma_{max}\sqrt{\pi a} \quad (4.3)$$

where σ_{max} is the applied stress at the critical load ($\sigma_{max} = P_{max} / bB$; in Pa*)* and *B* the specimen thickness (in m). For the computation of the specific non-dimensional stress intensity factor Y'_{pCT}, these authors provide Equation (4.4), whose coefficients C_i (*i* = 0 to 4) are given in Table 4.3.

$$Y'_{pCT} = C_0 + C_1\left(\frac{a}{b}\right) + C_2\left(\frac{a}{b}\right)^2 + C_3\left(\frac{a}{b}\right)^3 + +C_4\left(\frac{a}{b}\right)^4 \quad (4.4)$$

Table 4.3 Specimen size-dependent coefficients (C_i) for the computation of the dimensionless stress intensity factor expression corresponding to the *p*CT specimen (Y'_{pCT}).

D (mm)	C_0	C_1	C_2	C_3	C_4
38	10.278	-24.069	82.329	-136.67	127.89
50	12.651	-47.054	158.72	-247.17	185.22
100	15.341	-74.551	260.03	-404.52	273.19

The total energy (E_{tot}) has been computed taking the integral over the complete load-displacement (*P*-LPD) curve as follows:

$$E_{tot} = \int_0^{\infty} P \, d(LPD) \tag{4.5}$$

To get a deeper insight into the fracturing process, E_{tot} has been split in two contributions: E_{pre} and E_{post} ($E_{tot} = E_{pre} + E_{post}$). E_{pre} represents the pre-peak energy and corresponds to the work done on the specimen to induce the initiation of the crack. It is calculated from the integral over the *P*-LPD curve up to the turning point (P_{max} - d_{peak}; d_{peak} = displacement at the peak load). On the other hand, E_{post} corresponds to the post-peak energy and represents the work done on the specimen to propagate the crack up to the minimum load threshold value associated with the tail of the *P*-LPD curve. Likewise, we have also computed the energy given by the load-CMOD curve ($E_{tot\text{-}CMOD}$). Although we have performed CMOD measurement in most of the SCB specimens, as previously mentioned, in the case of the *p*CT ones this information is only available for 11 specimens. Anyhow, with the data available we have studied the relationship existing between $E_{tot\text{-}CMOD}$ and E_{tot} for both testing methods.

4.4. Results

In the present study, we report the results of 65 and 81 SCB and *p*CT tests, respectively. Figure 4.3 shows representative SCB and *p*CT specimens before and after the corresponding testing. We observe that, in general, the propagation of the fracture occurs along the ligament plane although sometimes it deviates. Following the criterion exposed in Kuruppu et al. (2014), some SCB experiments were given a lower confidence when fracture deviation exceeded a threshold value of >0.05*D* (~9.5º to 14.0º). Likewise, according to Muñoz-Ibáñez et al. (2020), the threshold value was set to >10º in the case of *p*CT specimens. While this limitation may be relevant for the Level II testing (ISRM Testing Commission 1988) this is arguable for Level I, where peak load is the only experimental property considered.

Figure 4.4 illustrates some examples of load-displacement (*P*-LPD) curves for 50 mm-diameter SCB (A to D) and *p*CT (E to H) specimens as a function of notch length ratio (*a/R* and *a/b*, respectively) and rock type. It is interesting to

observe that, in all the SCB tests performed, the loading curves always show a nearly linear increase path until the specimen abruptly fails at the peak load (P_{max}). In the SCB tests performed with sandstones we also see that some of the specimens may develop small loading plateaus that are compatible with local failures likely occurring at the contact points of the steel rods. With the exception of some specimens of Corvio Sst (that is a soft rock), it is apparent that the SCB test does not allow a good control beyond P_{max} and the fracture, once initiated, propagates quickly (dynamically) up to the outer face of the specimen. This behaviour contrasts with what happens with the *p*CT specimens, where the *P*-LPD curves show evidences of good test control in an scenario of slow (static) propagation of the fracture after P_{max} (Muñoz-Ibáñez et al. 2020). Furthermore, when looking to the evolution of P_{max} for different conditions of notch length we see at first glance an ordered trend in the *p*CT results (*i.e.* P_{max} decreases when the notch becomes longer) but this is not obvious in the SCB tests.

Figure 4.5 compares some of the *P*-LPD and *P*-CMOD curves obtained for 50 mm-diameter specimens using the two testing methodologies. It is worth to note that the measurement of CMOD during the SCB tests as performed in this work is not as straightforward as it may appear. Some of the results obtained illustrate the sliding of the sample along its contact points with the rollers. In fact, the geometric configuration of the test requires a perfect vertical alignment between the edge of the notch and the loading line. That means that, unless the load is applied along the vertical radii of the specimen, a lateral displacement (and concomitant horizontal slide) will occur due to the circular nature of the sample. This problem may be circumvented by using clip gauges but this may be difficult when working with small-size specimens. Leaving apart its implications for the interpretation of Level II testing, the previous observation provides with two significant outcomes. First, an inadequate sample dressing (coring, cutting, notching) and/or its careless alignment in the testing jig may induce a mixed mode I/II (tensile/shear) fracture toughness behaviour instead of the expected mode I (tensile). Second, in whatever the case, sample misalignment problems may enhance data scattering. In this regard, Nsengiyumva and Kim (2019) also

reported the great influence that the loading fixtures used to test SCB specimens of asphalt can have on energy or peak load results. However, none of these problems should affect the *p*CT configuration what makes the access to CMOD data easier and more reliable.

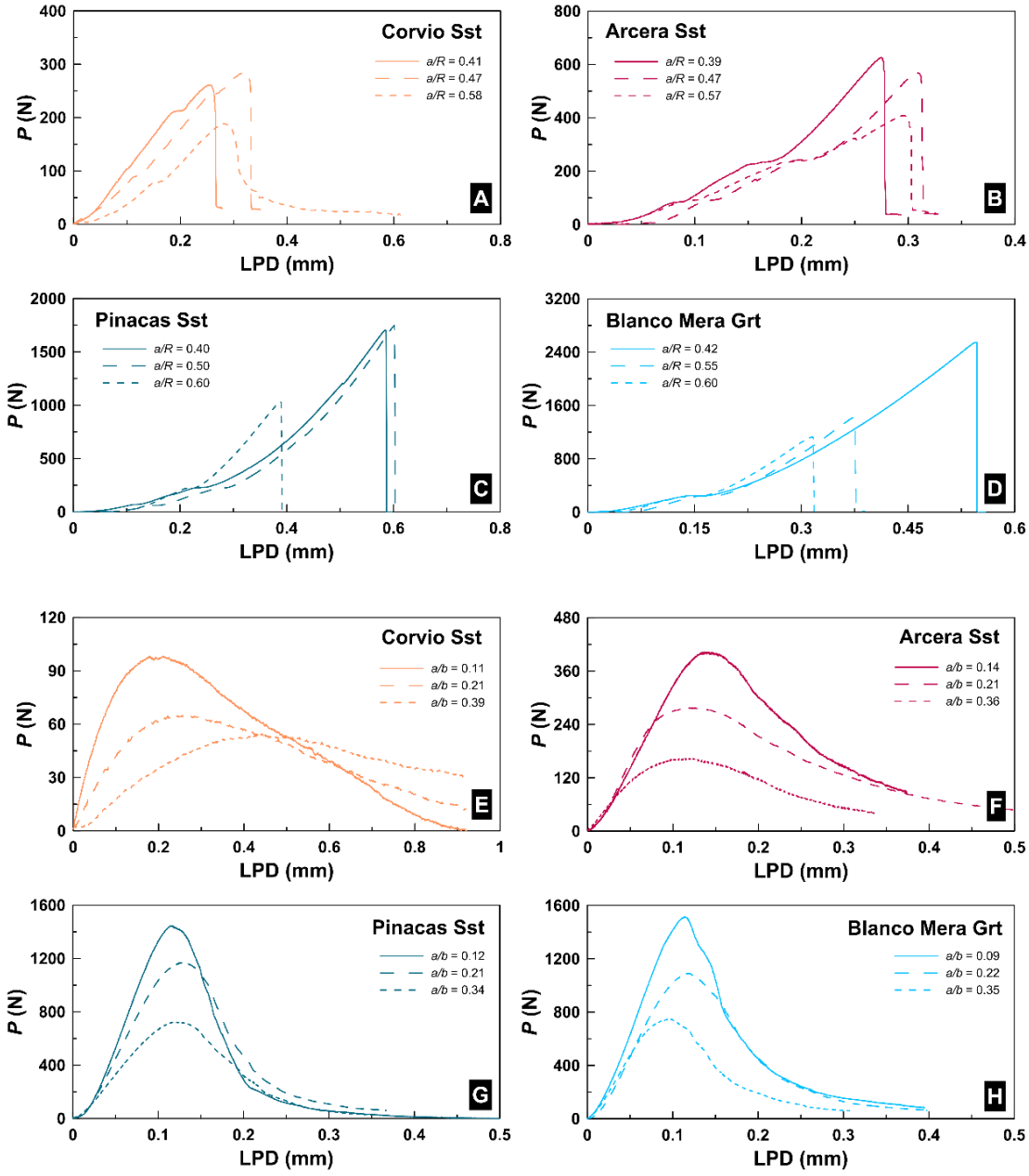

Figure 4.4: Load (*P*) versus load point displacement (LPD) curves obtained for 50 mm-diameter samples tested according with the SCB (A, B, C, D) and *p*CT (E, F, G, H) methods with different rock samples and notch lengths. See Figure 4.1 for notation.

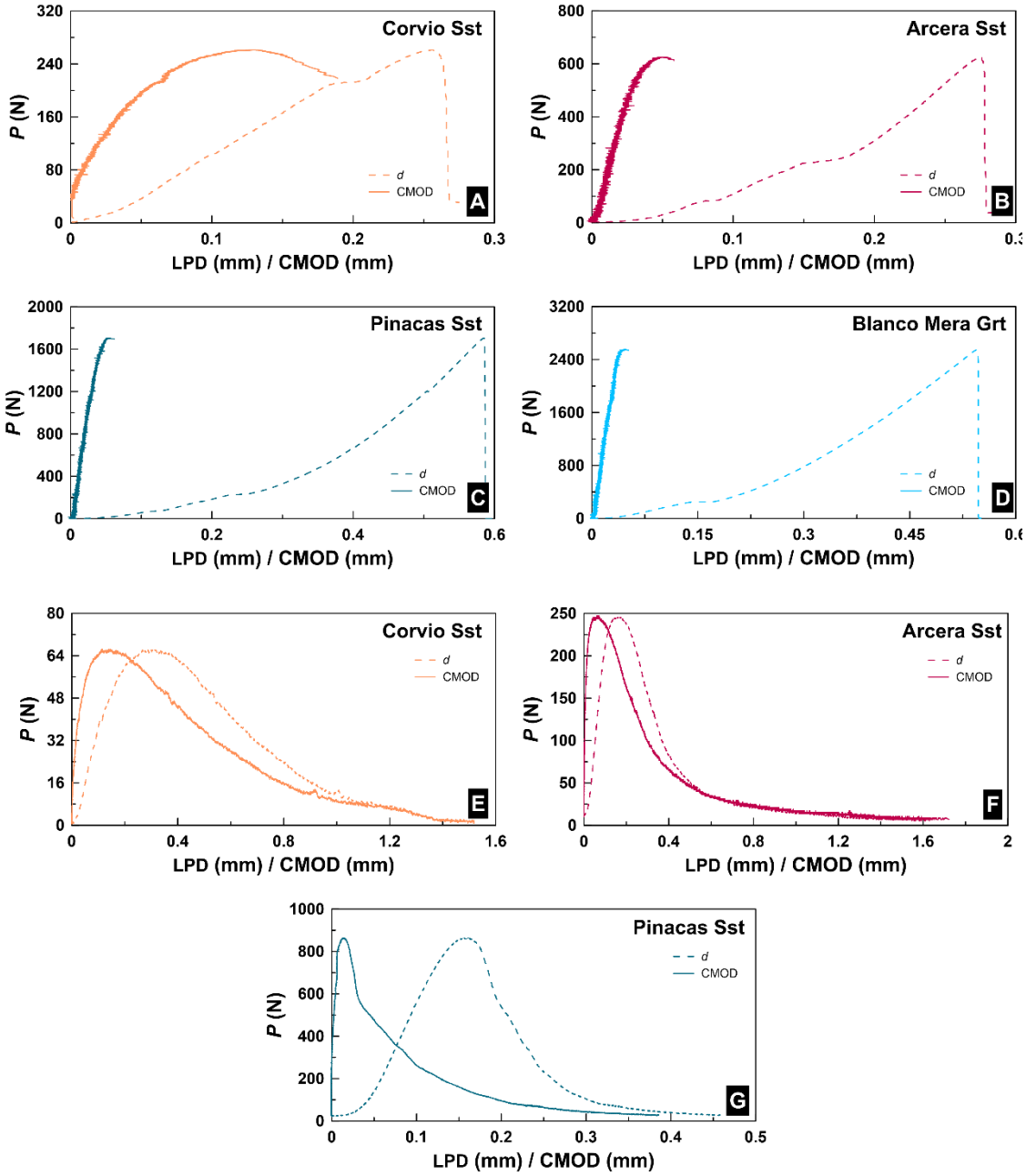

Figure 4.5: Load (*P*) versus load point displacement (LPD) and crack mouth opening displacement (CMOD) curves obtained from 50 mm-diameter samples of different rock types tested according with the SCB (A, B, C, D) and *p*CT (E, F, G) methods. The notch length ratio for all the illustrated experiments is ~ 0.4.

The *P*-CMOD curves associated with the SCB tests performed with hard samples (Figure 4.5C and D) depict a characteristic constant steep-slope ascent followed by a gradual flattening as the load approaches P_{max}. In fact, the slope of the *P*-LPD curve is noticeably shallower what results from the fact that CMOD is

much smaller than LPD. In the case of the weak Corvio Sst, the *P*-CMOD curve is highly non-linear since the beginning of the test. On the other hand, in the *p*CT tests (Figure 4.5E, F, G) we observe a better agreement between the two displacement measurements.

Figure 4.6 shows a series of box&whisker plots with the aggregated results of K_{IC} obtained for the four reference rock types and samples of 38-, 50- and 100-mm diameter tested with the SCB and *p*CT methods. With a wide perspective, we observe that in both cases results are broadly compatible in magnitude for each tested rock. However, in the detail, the 38 mm-diameter samples have lower K_{IC} value, especially in the case of SCB (see also Table 4.4). This clear size effect affects less the *p*CT testing methodology and it is likely related with the presence of heterogeneities in the tested rocks: For equal diameter, the smaller volume of the samples used in the SCB method make them more sensitive to this effect.

The data of the previous figure has been disaggregated in Figure 4.7 and it is presented as a function of the corresponding notch length ratios (*a/R* and *a/b*). In the case of SCB, K_{IC} depends on notch length in hard rocks (Pinacas sandstone and Blanco Mera granite) while this dependence becomes nearly negligible for the weaker ones (Acera and Corvio sandstones). However, it looks like the *p*CT method provides more consistent and sensitive information with respect to this dependence than the SCB. Regarding specimen size, K_{IC} values tend to increase with diameter although results are more scattered for hard-rock small-size samples (D = 38 mm).

We have computed E_{tot} and $E_{tot\text{-}CMOD}$ from the complete *P*-LPD and *P*-*CMOD* curves, respectively, and their relationship is illustrated in Figure 4.8 for the two testing methods. A through-origin linear best fit provides with satisfactory correlation coefficients in both cases (R^2 = 0.85 for SCB and 0.92 for *p*CT). However, the slope of the correlation line is about $1/4^{th}$ smaller than that associated with *p*CT (0.26 *vs.* 1.07). In fact, the nearly 1-slope in the *p*CT relationship suggest that, with this testing configuration, it is not necessary to use clip gauges or other transducers (a problem when space is restricted) since the

measured displacement is virtually equivalent to CMOD. In turn this is not possible with SCB.

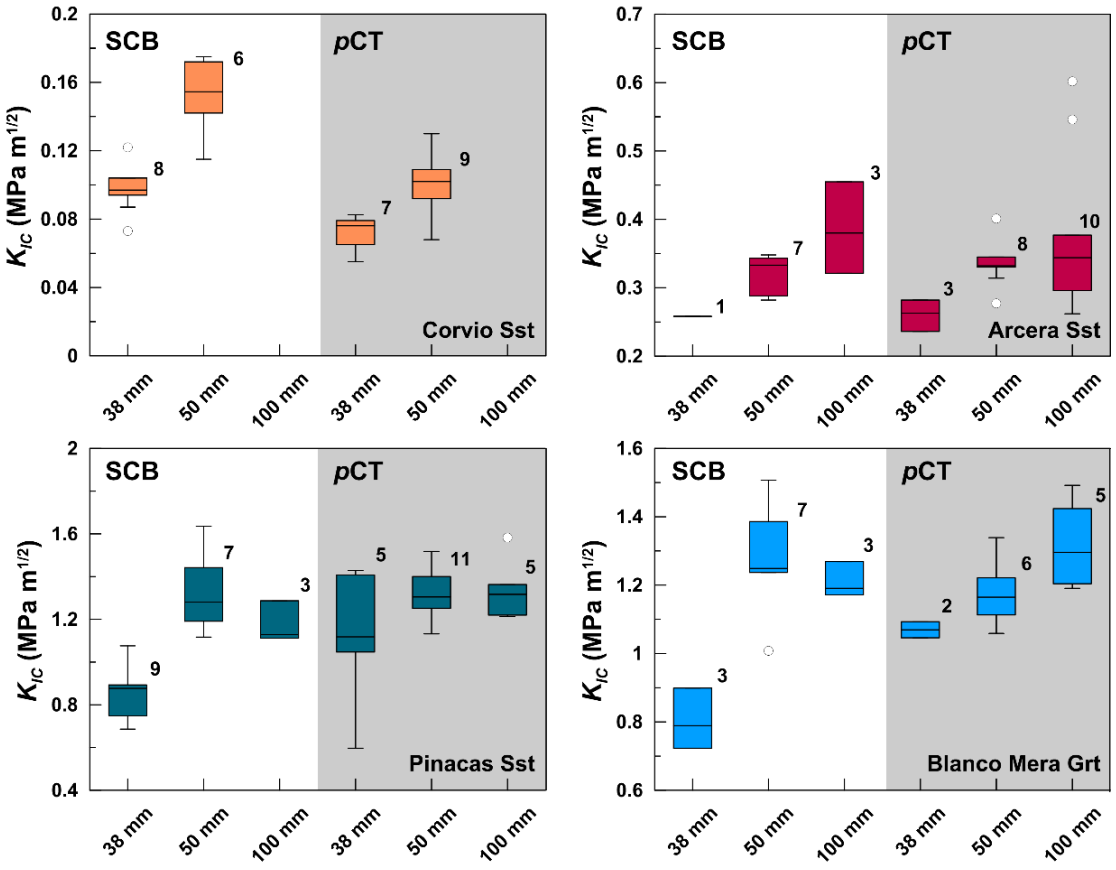

Figure 4.6: Box&whisker plots with the aggregated results of the mode I fracture toughness (K_{IC}) tests of rock specimens of different diameter performed with the SCB and *p*CT methods. The number accompanying each group represents the number of samples and single dots correspond to outliers.

In Figure 4.9 values of E_{tot} are plotted as a function of the notch length ratios and diameter for SCB and *p*CT testing. In both cases, E_{tot} is larger when the diameter of the specimen increases. However, this is more apparent for the *p*CT than for the SCB testing method, especially for large samples (D = 100 mm). Likewise, E_{tot} is also larger for the shorter notch lengths but this effect is more prominent in the harder rock types (PN and GR).

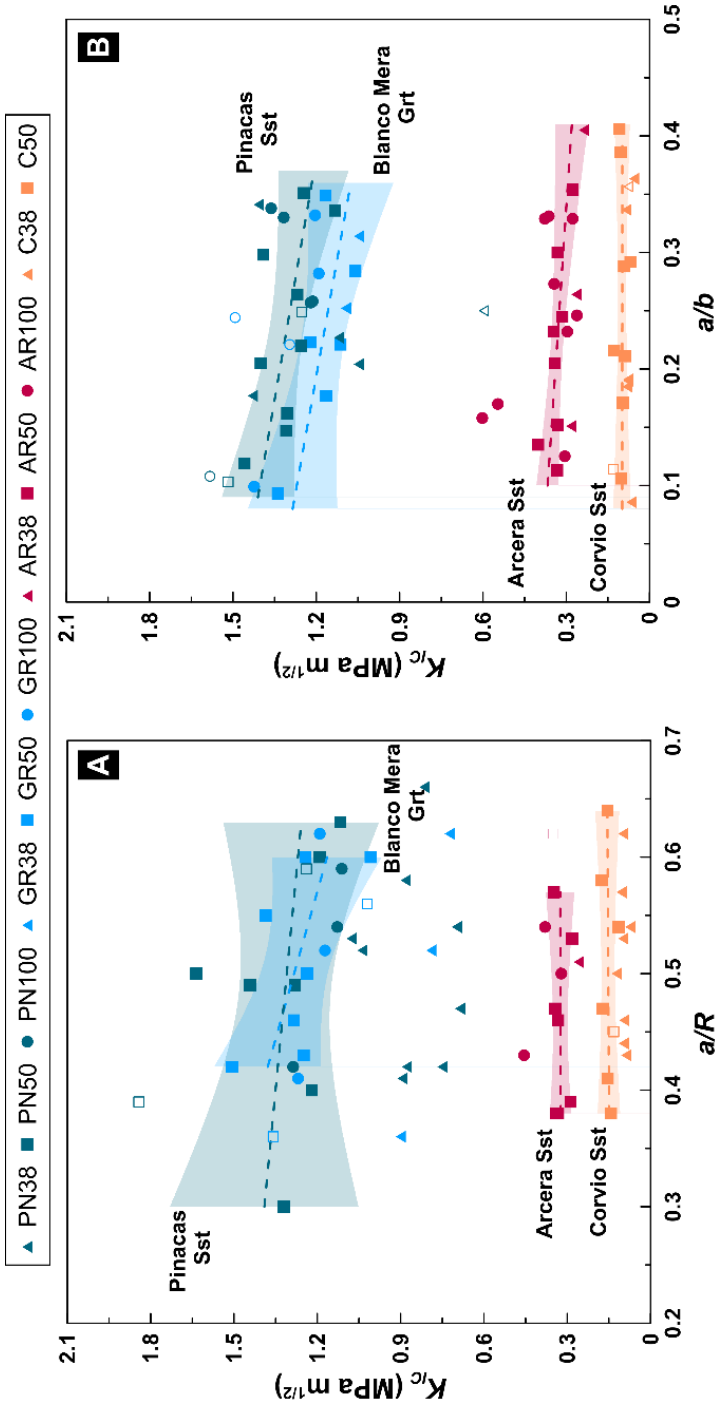

Figure 4.7: Mode I fracture toughness (K_{IC}) results from SCB (A) and *p*CT (B) tests as a function of the notch length ratio (*a*/*R* or *a*/*b*) and diameter of the specimen (triangle = 38 mm; square = 50 mm; circle = 100 mm). High confidence results (fracture deviation <0.05*D* for SCB and <10º for *p*CT; See text) are given with solid symbols while those of lower confidence are illustrated with empty symbols. Dashed lines represent the linear fits computed only with the solid symbols (n=6 for C; n = 7 for AR, PN, and GR). The shaded areas bound the 95% confidence interval of the corresponding linear fit.

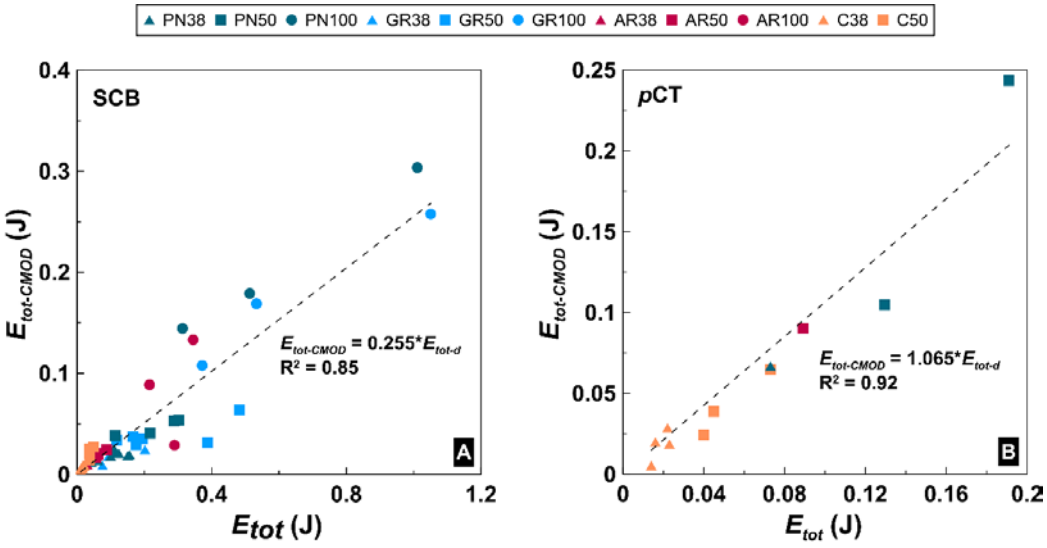

Figure 4.8: Total energy obtained from the integration of the *P*-CMOD curves ($E_{tot\text{-}CMOD}$) versus those computed from the *P*-LPD ones (E_{tot}) associated with SCB (A) and *p*CT testing (B).

Table 4.4: Mode I fracture toughness (K_{IC}) results obtained for the SCB and *p*CT tests performed. Valid tests (see text) are reported for each group of samples within brackets.

Method	Rock	K_{IC} (MPa m$^{1/2}$)		
		D = 38 mm	D = 50 mm	D = 100 mm
SCB	C	0.07 – 0.12 *(8)*	0.12 – 0.18 *(6)*	-
	AR	0.26 *(1)*	0.28 – 0.35 *(7)*	0.32 – 0.46 *(3)*
	PN	0.69 – 1.08 *(9)*	1.12 – 1.64 *(7)*	1.11 – 1.29 *(3)*
	GR	0.72 – 0.90 *(3)*	1.01 – 1.51 *(7)*	1.17 – 1.27 *(3)*
*p*CT	C	0.06 – 0.08 *(5)*	0.07 – 0.12 *(8)*	-
	AR	0.24 – 0.28 *(3)*	0.28 – 0.40 *(8)*	0.26 – 0.60 *(9)*
	PN	1.05 – 1.43 *(4)*	1.13 – 1.46 *(9)*	1.21 – 1.36 *(4)*
	GR	1.05 – 1.09 *(2)*	1.06 – 1.34 *(6)*	1.19 – 1.42 *(3)*

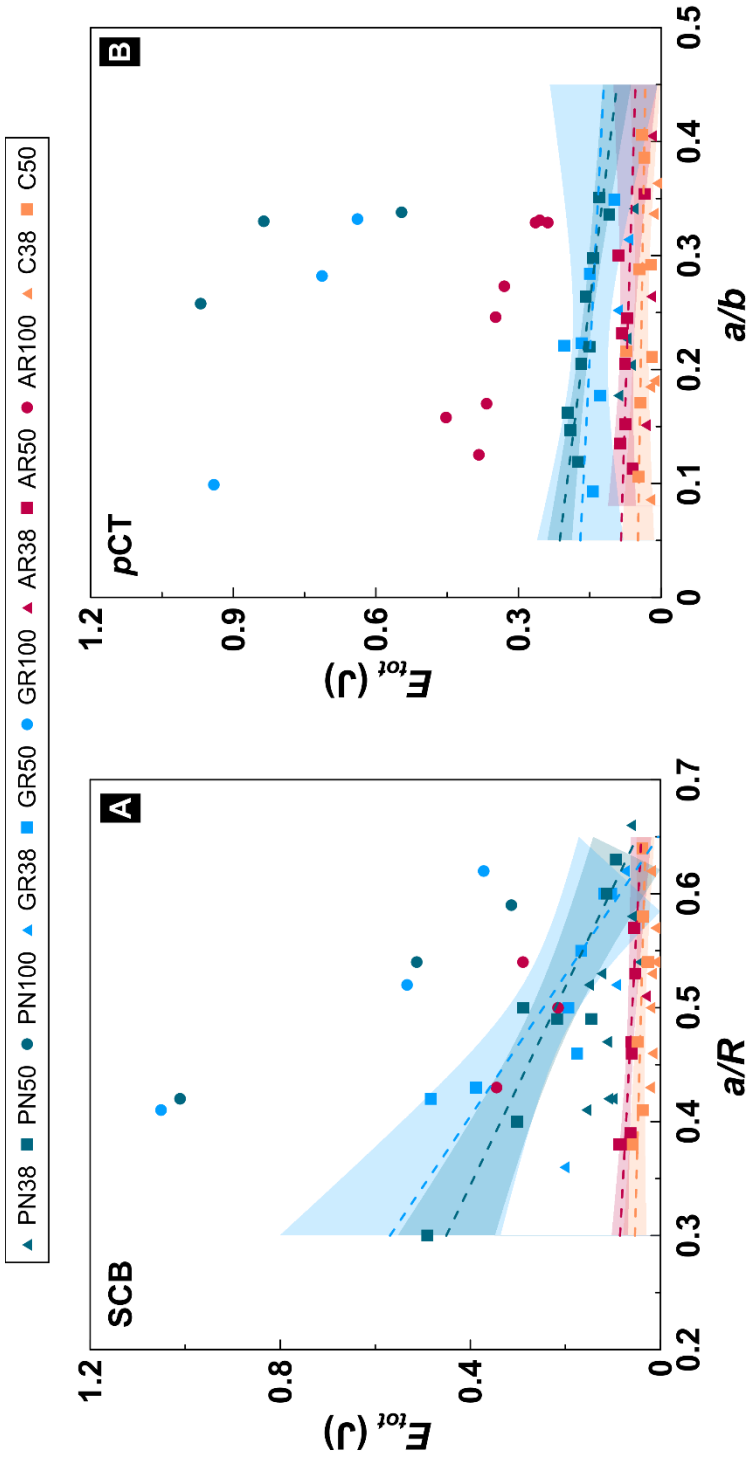

Figure 4.9: Total energy (E_{tot}) values associated with SCB (left) and *p*CT methods (right) represented as a function of notch length ratios (a/R and a/b, respectively) and specimen diameter (D). Dashed lines represent correlation lines computed for high-confidence results performed with 50 mm-diameter specimens of Corvio (C), Arcera (AR) and Pinacas sandstones (PN), as well as the Blanco Mera granite (GR). The shaded areas shown the confidence intervals (95%) in each case.

The good control during the execution of the *p*CT test allows splitting the total energy into two portions: That associated to the *P*-CMOD (or *P*-LPD) curve up to P_{max} (E_{pre}), and that from that point and beyond (E_{post}). These two portions separate the energy needed to initiate the crack and that required for its stable propagation and results are displayed in Figure 4.10.

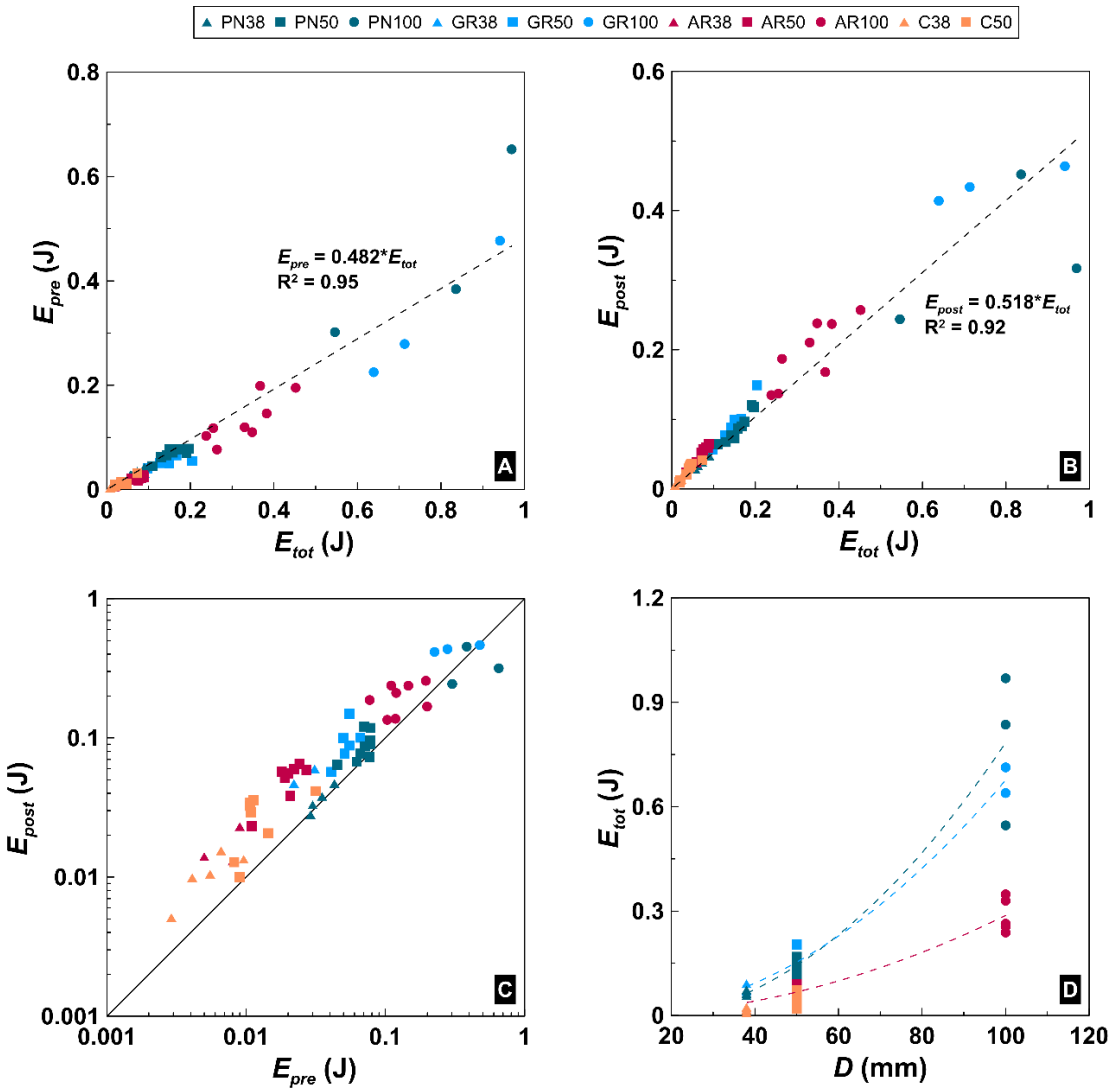

Figure 4.10: Distribution of the energies before (E_{pre}) and after (E_{post}) peak load compared with total energy (E_{tot}) (A and B), cross correlation of E_{pre} and E_{post} (C) and E_{tot} with respect sample diameter for a range of notch ratios of 0.2-0.35 and the different rock types tested (D).

Finally, we have taken advantage of the acoustic emission technique to acquire further insights about the fracturing process. A complete analysis of the results obtained in the AE survey is beyond the scope of this paper and we focus here in the analysis of the recorded acoustic emission energy (E_{AE}) in order to check whether it is possible or not to observe a relationship between this property and E_{tot}. We have summarized the data available in Figure 4.11.

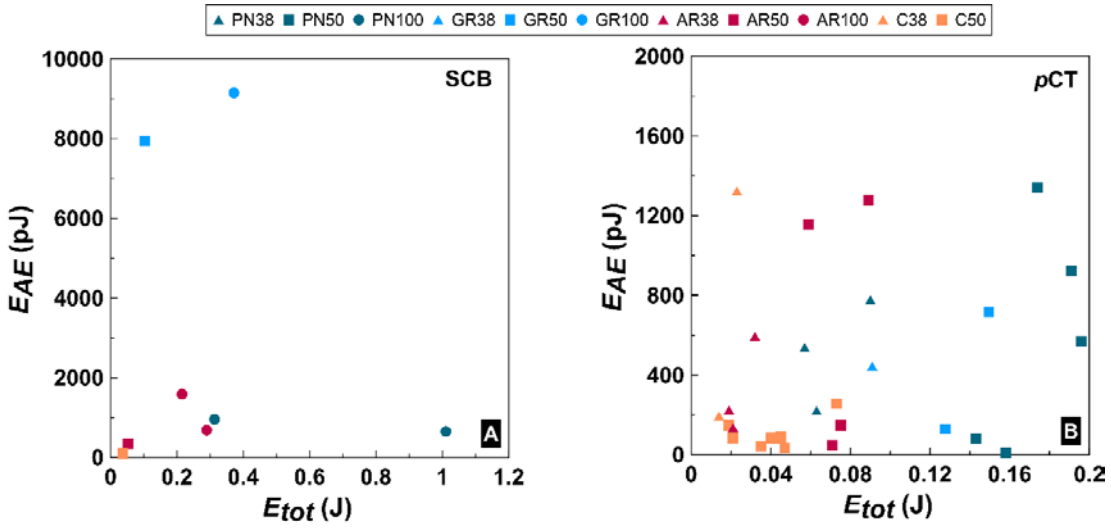

Figure 4.11: Total energy (E_{tot}) versus acoustic emission energy (E_{AE}) associated with tests performed with the SCB (A) and *p*CT (B) testing methods.

4.5. Discussion

4.5.1. Variability of results associated with the method of testing

Mode I fracture toughness derived from *p*CT testing for Corvio (~0.06-0.12 MPa $m^{1/2}$) and Arcera sandstones (~0.24-0.60 MPa $m^{1/2}$) is low, what is consistent with their condition of weak rocks. However, the K_{IC} values for both Pinacas sandstone and Blanco Mera granite are appreciably higher (~1.05-1.4 MPa $m^{1/2}$). For the same rocks, the SCB testing method results in values slightly larger for the Corvio Sst (~0.07-0.18 MPa $m^{1/2}$), but lower for the Arcera Sst (~0.26-0.46 MPa $m^{1/2}$). In the case of the Pinacas Sst and the Blanco Mera Grt, K_{IC} results are also more scattered than for *p*CT testing (~0.69-1.64 and ~0.72-

1.51 MPa $m^{1/2}$, respectively). The K_{IC} values obtained using SCB tests for the Arcera sandstone are of the same magnitude of similar rocks tested with the same method (Singh and Sun 1990). Likewise, the magnitude of SCB results for the Blanco Mera granite compares well with available data reported for the Keochang granite (Chang et al. 2002) and an unidentified fine-grained granite (Donovan and Karfakis 2004).

Different authors have already reported the variability effect induced by employing different testing methods for K_{IC}. For instance, Chang et al. (2002) assessed the fracture toughness of the Keochang granite and the Yeosan marble using four different specimen geometries: uncracked Brazilian disc test (BDT), CCNBD, SCB, and cracked chevron-notched semi-circular bend (CCNSCB). The K_{IC} values obtained in the case of SCB tests were more scattered and lower than those obtained from the CCNBD, CCNSCB, and BDT configurations, especially in the case of the granite. These findings have been supported by the observations of Wei et al. (2016) and Xu et al. (2016) with Dazhou sandstone specimens using SCB and CCNBD methods, respectively. Interestingly, in their work Wei et al. (2016) observed consistent K_{IC} results for the SCB and CCNSCB methods (Dazhou sandstone: ~2% difference; Quingdao granite: ~6% difference). Among the reasons that could have favoured such consistency these authors quote the relative homogeneity of the samples (fine-grain sized), the lack of anisotropy, and the similarities existing between both testing methods (that reduce size or boundary effects). Aliha et al. (2012) have conducted SCB and centre-cracked Brazilian disc (BD) experiments using the Guiting limestone. They report higher K_{IC} values when testing with SCB than with the BD method, and they argue that this difference may be related with the contribution of the high-order, non-linear stress terms into the stress field at the crack tip level. In a more recent contribution, Aliha et al. (2017) have investigated the K_{IC} of the Harsin marble using the four suggested methods of the ISRM (CB, SR, CCNBD, and SCB). Their results show a clear sensitivity of the K_{IC} value obtained when considering the different methods, with SR and CCNBD resulting in the highest and lowest values, respectively. The authors attributed the variability to effects

associated with a non-singular T-stress, which is a property that depends on geometry and loading configuration of the specimen. Conversely, Iqbal and Mohanty (2007) report a negligible discrepancy between K_{IC} values obtained with CB and CCNBD test, as long as the effects of specimen size and anisotropy are minimized. Tutluoglu and Keles (2011) point out significantly lower K_{IC} values for SCB testing compared to CCBND when testing the Ankara andesite (~35%) and the Afyon marble (~47%). These authors interpret the difference as arising from the size of the fracture process zone (FPZ) around the crack tip. They conjecture that a larger FPZ compared with sample size (like in the case of the geometry of the SCB specimen) determines a greater impact over K_{IC}. Funatsu et al. (2015) have also reported lower K_{IC} for SCB specimens when comparing the same rock with the CB and CCNBD methods. In that case, the authors attribute the variability in the results to differences in the characteristics of the notch type (i.e. chevron or straight-type), but also to the influence of the FPZ.

In order to satisfy the conditions for the application of the relationships of linear elastic fracture mechanics (LEFM) and to guarantee a linear-elastic behaviour of the material, the size of the FPZ ahead of the crack tip should be small-enough compared with the dimensions of the sample. According to Schmidt (1980), the radius of the FPZ (r_{FPZ}) can be assessed as follows:

$$r_{FPZ} = \frac{1}{2\pi}\left(\frac{K_{IC}}{\sigma_t}\right)^2 \tag{4.6}$$

where σ_t is the tensile strength of the rock. Due to the large number of samples tested in the present study, rather than single-value properties (namely K_{IC} and σ_t), we have ranges of values describing them. Accordingly, we have computed a theoretical minimum (r_{min}) and maximum (r_{max}) radii for the FPZ for each specimen size, lithology and testing method. While we computed r_{min} using the minimum K_{IC} and the maximum value of σ_t, we assessed r_{max} based on the maximum K_{IC} and minimum σ_t. This maximizes the corresponding lengths of the FPZ. The values resulting from the computations are reported in Table 4.5. We see that, in general, the size of the FPZ increases with the size of the specimen. This has been also reported by Tarokh et al. (2017). With the exception of the

Arcera sandstone, for the 50-mm diameter samples the FPZ is larger in SCB than in the *p*CT. For smaller (D = 38 mm) and larger diameters (D = 100 mm) the trends are the opposite. The larger theoretical FPZ associated with the *p*CT specimens should led to a potentially greater scatter in the K_{IC} results. However, what we observe is the contrary, what suggests that FPZ would not be playing a significant role in the *p*CT testing mode. We conjecture that this is associated with the larger ligament length of *p*CT compared with the SCB specimens (~3 times). In the case of SCB results, the greater experimental scattering may connect with the fact that the 38- and 50-mm diameter specimens fall below the minimum size suggested by Kuruppu et al. (2014) to satisfy the requirements of LEFM. However, Chang et al. (2002) have also found a significant dispersion in the experimental results of the SCB method (D = 75 and 100 mm), what was interpreted by the same authors as the result of the absence of a starter crack (i.e. pre-cracking) ahead the notch cut in the sample. Since our *p*CT specimens were not pre-cracked (in the previous sense) and still yield consistent results for the three sample sizes considered, we believe that this is not a critical issue to justify data variability.

4.5.2. Specimen size and notch length effects

We can accept as general that, within the bounds of the representative elementary volume, the mechanical properties of rocks derived from experiments should be independent of the specimen size. However, different authors have reported a lessening in certain properties (e.g. unconfined compressive and tensile strengths) when the size of the specimen increases (Hoek and Brown 1980; Klanphumeesri 2010; Quiñones et al. 2017). However, in the case of fracture toughness, this property has been described to increase with increasing the size of the specimens for quasi-brittle materials, such as rock or concrete (Iqbal and Mohanty 2007; Ueno et al. 2013; Brevik 2016; Jeong et al. 2017).

Our experimental database allows us to make some observations on eventual size effects on K_{IC} derived from SCB and *p*CT testing methods. This is illustrated in Figure 4.6, where a first glance inspection reveals a more notorious size-effect associated with SCB than the *p*CT method. As we pointed out earlier,

K_{IC} increases in general when the size of the specimen also increases. Although *p*CT testing results are consistent when considering the range of variability of each size, it is a fact that the largest K_{IC} values correspond to the largest samples (D = 100 mm). This also happens with the SCB specimens of the weak Arcera and Corvio sandstones. But for the tougher Pinacas sandstone and Blanco Mera granite, the K_{IC} maxima correspond to the intermediate-size samples (D = 50 mm) while minima belong to the smaller ones (D = 38 mm).

Table 4.5: Estimated size of the FPZ expressed as minimum (r_{min}) and maximum radii (r_{max}), in mm, computed for SCB and *p*CT specimens of different diameter (D).

Method	Rock	D = 38 mm		D = 50 mm		D = 100 mm	
		r_{min} (mm)	r_{max} (mm)	r_{min} (mm)	r_{max} (mm)	r_{min} (mm)	r_{max} (mm)
SCB	C	0.09	0.66	0.22	1.35	-	-
	AR	0.44	0.64	0.53	1.17	0.68	1.96
	PN	0.53	1.47	1.40	3.41	1.39	2.10
	GR	0.88	1.40	1.72	3.92	2.32	2.79
*p*CT	C	0.05	0.30	0.08	0.71	-	-
	AR	0.37	0.75	0.51	1.52	0.46	3.43
	PN	1.23	2.59	1.44	2.70	1.65	2.36
	GR	1.85	2.20	1.90	3.10	2.40	3.50

In order to minimize size effects, the ISRM suggests the use of samples with a minimum diameter above 50 mm in the case of CB and SR testing methods (ISRM Testing Commission 1988), and that value rises to 76 mm in the case of SCB (Kuruppu et al. 2014). However, Kataoka and Obara (2015) have reported that a minimum diameter of 140 mm is needed to obtain consistent K_{IC} values for SCB testing. Our findings are in the line of the previous contributions, cautioning against the use of small-size specimens with the SCB test method. In the case of Ueno et al. (2013), they have observed an increase in K_{IC} with increasing the

diameter of the SCB specimens (D = 50-100 mm) of the Kimachi and Isahaya sandstones. These authors also report a greater impact of the fracture process zone when the size of the specimen was decreased, as seen from the enhancement of non-linearity in the P-LPD curves close to P_{max}. In our case, experimental results suggest that the evolution of the slope of the P-LPD curves would depend more on the rock type than the size of the specimen. Thus, the weaker materials (e.g. Corvio Sst) show a greater degree of non-linearity even for large specimens. Lithology seems also to magnify the influence of specimen size on K_{IC}, and this circumstance can be determinant for the harder materials (Pinacas Sst and Blanco Mera Grt). In our opinion, in addition to geometric constrains, the characteristics of the rock tested must be taken into account in order to set up minimum requirements for specimen size in fracture toughness testing.

The influence of notch length on mode I fracture toughness has been assessed by different researchers. Although some authors point out a negligible impact (e.g., Lim et al. (1994); Funatsu et al. (2015)), others suggest that K_{IC} tends to be smaller as the notch length increases (Rivera-Perez 2017; Zhang et al. 2017). Data elaborated by Muñoz-Ibáñez et al. (2020) for the *p*CT method support this conclusion. In the case of the SCB tests reported here, despite having used the range of a/R ratios ($0.4 \leq a/R \leq 0.6$) recommended by the ISRM (Kuruppu et al. 2014), we also observe dependency of K_{IC} on the a/R ratio (see Figure 4.7). However, the effect is more pronounced in the case of the harder rocks (high relative K_{IC} values) and almost imperceptible for the weaker ones (lower relative K_{IC}). Once more, it is apparent that lithology may determine the degree of influence of a geometrical factor on mode I fracture toughness.

4.5.3. Energy assessment

In fracture mechanics, a crack grows when the stress intensity factor (K_I) reaches a critical value that is referred as the fracture toughness (K_{IC}) of the corresponding material (Anderson 2005). From the energy balances viewpoint, a crack will propagate when the energy available for crack growth exceeds the resistance of the material (Şener and Tutluoglu 2003). Accordingly, fracture

toughness can also be regarded as the energy release rate needed to create new crack surfaces, that is two surfaces per crack tip (ISRM Testing Commission 1988). This energy can be accounted by computing the surface under the experimental *P*-CMOD curves that formally corresponds to the $E_{tot\text{-}CMOD}$ described with Equation 4.5. From the beginning of a test up to the point of failure (where the crack starts to propagate), the energy delivered by the testing device is mainly invested in subcritical crack growth (Atkinson 1984) while approaching K_{IC}. Depending on the methodology, a fraction of this energy can be elastically stored in the sample and, under ideal testing conditions, the elastic storage should occur in a small volume around the starter notch of the sample. Once K_{IC} is reached, the energy delivered is then consumed to unstably propagate the crack. In a test with a satisfactory control it is possible to obtain a continuous *P*-CMOD curve allowing to split the total energy ($E_{tot\text{-}CMOD}$) into the two described stages and we may refer them as E_{pre} and E_{post}, respectively. However, the geometry of the tested specimen as well as the way in which the load is applied determine the success in obtaining a complete *P*-CMOD curve. To this respect, it is apparent that the *p*CT method provides with a good control of the process while the SCB not. It can be argued that improving control electronics and system stiffness (to avoid elastic energy storage in the testing device) may improve the quality of the SCB results. However, in our opinion the key point determining its poorer performance in the post-peak region is that the energy storage in the sample takes place in a volume significantly larger than that surrounding the crack tip (e.g., at the contact point of the rollers and along the ligament up to the starter notch). When load attains P_{max}, all this energy stored in the sample is released suddenly and the crack propagates dynamically. However, in the case of the *p*CT test, the load is transferred to the sample along the contact lines of the pulling jaws (Muñoz-Ibáñez et al. 2020) and from there directly to the starter notch.

The relationships among E_{pre} and E_{post} with E_{tot} are highly linear (Figure 4.10A, B), with correlation coefficients (R^2) of 0.95 and 0.92, respectively. The slopes of both lines are 0.482 (E_{pre}) and 0.518 (E_{post}). These numbers suggest

that, irrespective of lithology, sample size and notch length, the same energy level is required to initiate the fracture or to propagate it once initiated. Figure 4.10C shows the relationship between E_{pre} and E_{post} and, not surprisingly, they conform a nearly one-to-one correlation although in the detail E_{post} is ~4% larger than E_{pre}.

Zhang et al. (2017) have performed SCB tests to characterize the fracture properties of some stabilized soils. They found that ligament area-normalized fracture energy ($E_{tot}/[(R\text{-}a)\cdot B]$) tends to reduce as the notch length increases, and a similar tendency has been reported by Rivera-Perez (2017) when computing E_{tot} based on the Illinois Flexibility Index Test (I-FIT), which is an adaptation for asphalt materials of the SCB test. In Figure 4.9 we illustrate our results and we conclude that they are consistent with observations of the previous authors: Less clearly in the SCB tests but with significant trends in the *p*CT. Rivera-Perez (2017) attributes this effect to the reduction of the ligament area available for fracture propagation. That would mean that, for a constant notch length, the change in size of the specimen should result in a quadratic distribution of E_{tot}. We have check this assumption by plotting in Figure 4.10D E_{tot} versus D for notch ratios (a/b) comprised between 0.2 and 0.35, and we confirm it because the best fit that can be obtained is quadratic what implies a non-constant rate of change. It is interesting also to observe that this relationship appears to be a function of lithology, what it is also observed from the slopes of E_{tot} *vs.* a/b in Figure 4.9.

4.5.4. Acoustic emission energy

According to Landis and Baillon (2002), a certain fraction of the energy evolved during crack generation and propagation is amenable of monitoring taking advantage of AE techniques. Although the energy magnitudes associated with fracturing and local emission of AE are broadly different (AE can be unevenly scattered and/or attenuated in the sample and interfaces), it may be possible to identify a formal relationship between both properties so that AE energy can be regarded as a proxy for the energy dissipated during the fracture process. In fact, considering that the AE activity is proportional to the number and magnitude of growing cracks, it is reasonable to assume that there might be a relation between

AE energy (E_{AE}) and fracture energy. Published results are, however, contradictory. For instance, Landis and Baillon (2002) have reported a good correlation for mortar specimens, although they could not provide with a functional relationship between E_{AE} and fracture energy. Contrary, their results show no clear correlation in the case of concrete specimens. On the other hand, Han et al. (2018) have observed a linear correlation between both parameters in 3-point bending tests made on samples of crumb rubber concrete.

The values of the total emitted E_{AE} obtained at the end of the SCB and *p*CT tests where such measurements are available have been plotted as a function of E_{tot} in Figure 4.11. For that purpose, E_{AE} was taken as the average value from all the AE transducers installed in the sample after summing up the AE energy released for each AE event. No clear relationship arises from the plots, in neither the SCB nor the *p*CT tests. In addition, it is worth to note that there is no direct correlation between E_{AE} and specimen size. However, we believe that more work needs to be done in this line and we cannot discard non-apparent correlations that are not manifested from the available database.

4.6. Conclusions

We have experimentally investigated the mode I fracture toughness (K_{IC}) of three sedimentary (Arcera, Pinacas and Corvio sandstones) and one igneous rock (Blanco Mera granite) by means of two different testing methods: the ISRM-suggested SCB method, and the *p*CT technique.

From a methodological point of view, a good sample alignment is essential in the SCB method to avoid mixed modes (I / II) in fracture toughness determinations. Furthermore, we also caution about the propensity of this configuration to lateral sliding when applying a linearly distributed force due to the circular nature of the loading surface. None of the two problems is significant with the *p*CT technique.

The *p*CT method also provides a good post-peak control in all the experiments but this does not happen in the SCB experiments except for some specimens of Corvio Sst. The reason is not associated with a better/worse

electronic control or a high/low stiffness of the testing devices. It is likely connected to the way fracture energy is delivered to the tested specimen: Direct to the starter notch tip (*p*CT), or distributed along the ligament volume and around the contact points of the rollers (SCB). The second case is more prone to a significant elastic energy storage and its sudden release when approaching the critical stress value. This would induce the unstable propagation of the fracture.

The difficulties encountered to control the propagation of the crack in the SCB tests makes impossible the access to Level II testing when using this technique, but this is feasible with the *p*CT method. In fact, the good correlation found between LPD and CMOD makes possible the direct assessment of CMOD without employing direct contact transducers (clip gauges or similar), what is advantageous with small size samples.

Considering selected geometrical properties like sample size and notch length, we conclude that both variables have an influence in the derived fracture toughness values. Despite data scattering, K_{IC} generally increases for larger samples and for smaller notch lengths. However, the size effect has a lesser impact in the *p*CT compared with the SCB method. In the case of the SCB testing, the variability induced over K_{IC} by changing notch length ratios (a/R) is of less importance than the effect of sample size. However, both effects are subsidiary of rock type, with the harder materials showing higher dependency.

Regarding the testing method, when the size of the specimen is large (D = 50 and 100 mm) we observe a significant similarity in the average K_{IC} results obtained with the SCB and *p*CT configurations. For the smallest samples (D = 38 mm) the values obtained with both methods differ more. In that case, *p*CT specimens yield more consistent fracture toughness values (which are comparable to those of the larger samples) compared with the SCB ones, especially for the harder materials for which the K_{IC} difference may reach a 40% lower values than for the larger-size samples.

The detailed analysis of the fracture energy derived from the *p*CT tests reveals a good linear correlation between the pre- (E_{pre}) and post-peak (E_{post})

fracture energies with respect total energy (E_{tot}). The magnitude of both properties is very similar, what means that irrespective of lithology, sample size and notch length, the same level of energy is required to initiate the fracture and to stably propagate it. The energy balances obtained have made also possible to support the conjecture of the size-dependent fracture energy value given a constant notch length. However, our results indicate a more complex dependencies, with lithology playing a significant role.

The assessment of E_{AE} to try to identify functional relationships with fracture energy has been unsuccessful in the present survey. We cannot discard eventual relationships but a more comprehensive AE database is still needed.

4.7. References

Aliha MRM, Mahdavi E, Ayatollahi MR (2017) The Influence of Specimen Type on Tensile Fracture Toughness of Rock Materials. *Pure and Applied Geophysics* 174:1237–1253

Aliha MRM, Sistaninia M, Smith DJ, Pavier MJ, Ayatollahi MR (2012) Geometry effects and statistical analysis of mode I fracture in guiting limestone. *International Journal of Rock Mechanics and Mining Sciences* 51:128–135

Alkiliçgil C (2010) Development of specimen geometries for mode I fracture toughness testing with disc type rock specimens. PhD thesis, Middle East Technical University, Ankara, Turkey

Anderson TL (2005) Fracture mechanics: Fundamentals and applications, Third Edition. CRC Press

Arzúa J, Alejano LR (2013) Dilation in granite during servo-controlled triaxial strength tests. *International Journal of Rock Mechanics and Mining Sciences* 61:43–56

ASTM (1997) Standard guide for mounting piezoelectric acoustic emission sensors, E650-97. In: Annual Book of ASTM Standards. ASTM International, West Conshohocken, PA

Atkinson BK (1984) Subcritical crack growth in geological materials. *Journal of*

Geophysical Research: Solid Earth 89:4077–4114

Brevik NØ (2016) Experimental study of fracture toughness in sedimentary rocks. PhD thesis, Norwegian University of Science and Technology, Trondheim, Norway

Canal-Vila J (2016) Experimental study of effect of CO_2 injection on rocks: coupling hydrodynamic, mechanical and geochemical processesrim. PhD thesis, University of A Coruña, A Coruña, Spain

Chang SH, Lee CI, Jeon S (2002) Measurement of rock fracture toughness under modes I and II and mixed-mode conditions by using disc-type specimens. *Engineering Geology* 66:79–97

Donovan JG, Karfakis MG (2004) Adaptation of a simple wedge test for the rapid determination of mode I fracture toughness and the assessment of relative fracture resistance. *International Journal of Rock Mechanics and Mining Sciences* 41:695–701

Erarslan N (2018) The importance of testing method to evaluate the most representative mode I fracture toughness value of brittle rocks. *MOJ Civil Engineering* 4:437–441

Falcon-Suarez I, Canal-Vila J, Delgado-Martin J, North L, Best A (2017) Characterisation and multifaceted anisotropy assessment of Corvio sandstone for geological CO_2 storage studies. *Geophysical Prospecting* 65:1293–1311

Fowell RJ, Hudson JA, Xu C, Chen JF (1995) Suggested Method for Determining Mode-I Fracture-Toughness Using Cracked Chevron-Notched Brazilian Disc (CCNBD) Specimens. *International Journal of Rock Mechanics and Mining Sciences & Geomechanics Abstracts* 32:57–64

Funatsu T, Shimizu N, Kuruppu M, Matsui K (2015) Evaluation of Mode I Fracture Toughness Assisted by the Numerical Determination of K-Resistance. *Rock Mechanics and Rock Engineering* 48:143–157

Han QH, Yang G, Xu J (2018) Experimental study on the relationship between acoustic emission energy and fracture energy of crumb rubber concrete.

Structural Control and Health Monitoring 25:1–13

Hoek E, Brown ET (1980) Underground excavations in rock. London: Transactions of the Institution of Mining and Metallurgy

Iqbal MJ, Mohanty B (2007) Experimental calibration of ISRM suggested fracture toughness measurement techniques in selected brittle rocks. *Rock Mechanics and Rock Engineering* 40:453–475

ISRM Testing Commission (1988) Suggested methods for determining the fracture toughness of rock. *International Journal of Rock Mechanics and Mining Science & Geomechanics Abstracts* 25:71–96

Jeong SS, Nakamura K, Yoshioka S, Obara Y, Kataoka M (2017) Fracture Toughness of Granite Measured Using Micro to Macro Scale Specimens. *Procedia Engineering* 191:761–767

Kataoka M, Obara Y (2015) Size Effect in Fracture Toughness of Sandstone. In: 13th ISRM International Congress on Rock Mechanics. 10-14 May, Montréal, Canada

Kataoka M, Yoshioka S, Cho S-H, Soucek K, Vavro L, Obara Y (2015) Estimation of Fracture Toughness of Sandstone by Three Testing Methods. In: Vietrock2015: an ISRM specialized conference, Hanoi, Vietnam, 12-13 March

Khan K, Al-Shayea NA (2000) Effect of specimen geometry and testing method on mixed Mode I-II fracture toughness of a limestone rock from Saudi Arabia. *Rock Mechanics and Rock Engineering* 33:179–206

Klanphumeesri S (2010) Direct Tension Testing of Rock Specimens. Suranee University of Technology

Kobayashi R, Matsuki K, Otsuka N (1986) 2. Size effect in the fracture toughness of Ogino tuff. *International Journal of Rock Mechanics and Mining Sciences and* 23:13–18

Kuruppu MD, Chong KP (2012) Fracture toughness testing of brittle materials using semi-circular bend (SCB) specimen. *Engineering Fracture Mechanics*

91:133–150

Kuruppu MD, Obara Y, Ayatollahi MR, Chong KP, Funatsu T (2014) ISRM-suggested method for determining the mode I static fracture toughness using semi-circular bend specimen. *Rock Mechanics and Rock Engineering* 47:267–274

Landis EN, Baillon L (2002) Experiments to Relate Acoustic Emission Energy to Fracture Energy of Concrete. *Journal of Engineering Mechanics* 128:698–702

Lim IL, Johnston IW, Choi SK, Boland JN (1994) Fracture testing of a soft rock with semi-circular specimens under three-point bending. Part 1—mode I. *International Journal of Rock Mechanics and Mining Sciences & Geomechanics Abstracts* 31:185–197

Muñoz-Ibáñez A, Delgado-Martín J, Costas M, Rabuñal-Dopico J, Alvarellos-Iglesias J, Canal-Vila J (2020) Pure mode I fracture toughness determination in rocks using a pseudo-compact tension (*p*CT) test approach. *Rock Mechanics and Rock Engineering* 53: 3267-3285

Nsengiyumva G, Kim YR (2019) Effect of Testing Configuration in Semi-Circular Bending Fracture of Asphalt Mixtures: Experiments and Statistical Analyses. *Transportation Research Record* 2673:320–328

Ouchterlony F (1989) Fracture toughness testing of rock with core based specimens, the development of an ISRM standard. *Fracture Toughness and Fracture Energy* 231–251

Quiñones J, Arzúa J, Alejano LR, García-Bastante F, Mas Ivars D, Walton G (2017) Analysis of size effects on the geomechanical parameters of intact granite samples under unconfined conditions. *Acta Geotechnica* 12:1229–1242

Rivera-Perez JJ (2017) Effect of specimen geometry and test configuration on the fracture process zone for asphalt materials

Schmidt RA (1980) A Microcrack Model And Its Significance to Hydraulic Fracturing And Fracture Toughness Testing. In: The 21st U.S. Symposium

on Rock Mechanics (USRMS), 27-30 May, Rolla, Missouri

Şener S, Tutluoglu L (2003) Fracture Toughness Analysis of Ankara Andésite. In: Proceedings of 18th International Mining Congress and Exhibition of Turkey, IMCET. pp 89–92

Singh RN, Sun GX (1990) An investigation into factors affecting fracture toughness of coal measures sandstones. *Journal of Mines, Metals and Fuels* 38:111–118

Tarokh A, Makhnenko RY, Fakhimi A, Labuz JF (2017) Scaling of the fracture process zone in rock. *International Journal of Fracture* 204:191–204

Tutluoglu L, Keles C (2011) Mode I fracture toughness determination with straight notched disk bending method. *International Journal of Rock Mechanics and Mining Sciences* 48:1248–1261

Ueno K, Funatsu T, Shimada H, Sasaoka T, Matsui K (2013) Effect of Specimen Size on Mode I Fracture Toughness by SCB Test. In: The 11th International conference on Mining, Materials and Petroleum Engineering; the 7th International Conference on Mining, Materials and Petroleum Engineering. Chiang Mai, Thailand, 11-13 November

Wei MD, Dai F, Xu NW, Zhao T, Xia KW (2016) Experimental and numerical study on the fracture process zone and fracture toughness determination for ISRM-suggested semi-circular bend rock specimen. *Engineering Fracture Mechanics* 154:43–56

Xu Y, Dai F, Zhao T, Xu N wen, Liu Y (2016) Fracture Toughness Determination of Cracked Chevron Notched Brazilian Disc Rock Specimen via Griffith Energy Criterion Incorporating Realistic Fracture Profiles. *Rock Mechanics and Rock Engineering* 49:3083–3093

Zhang J, Little DN, Grajales J, You T, Kim Y-R (2017) Use of Semicircular Bending Test and Cohesive Zone Modeling to Evaluate Fracture Resistance of Stabilized Soils. *Transportation Research Record: Journal of the Transportation Research Board* 2657:67–77

5. Acoustic emission monitoring of mode I fracture toughness tests on sandstone rocks

This chapter will be submitted to '*Journal of Petroleum Science and Engineering*'

Andrea Muñoz-Ibáñez[1], Jordi Delgado-Martín[1], Miguel Herbón-Penabad[1], and José Alvarellos-Iglesias[2]

5.1. Abstract

A series of mode I fracture toughness test employing the semi-circular bend (SCB) and the pseudo-compact tension (*p*CT) methodologies have been performed with two sandstone types and specimens of 50- and 100-mm diameter. The tests were complemented with the monitoring of acoustic emission (AE) activity using a multi-sensor array. With the obtained data we compare and analyse the different testing methods, the mechanical evolution along the experiments and the significance of different acoustic emission parameters. The hypocenter location of AE events allows a better understanding of the processes occurring in the tests and the analysis of properties like amplitude or peak frequencies are valuable complements. Crack modes have been assessed using a parameter-based strategy (comparison of the average frequency, AF and rise angle, RA, as per RILEM), and the I*b-value* has been explored to check its potential for cracking process discrimination in fracture toughness tests. Results show that the *p*CT test provides more comprehensive and detailed results, both in terms of mechanical information and acoustic emission data. We discuss the applicability of the generally accepted models of small-strain brittle material

[1] School of Civil Engineering, University of A Coruña, Campus de Elviña s/n, 15071 A Coruña, Spain
[2] Centro de Tecnología de Repsol, Ctra. Extremadura, N-V Km 18, 28935 Móstoles, Spain

failure typically applied to compressive tests (including or not AE data) and further methodological questions of interest when considering AE monitoring in fracture toughness tests.

5.2. Introduction

Fracture toughness (K_C) represents the resistance of a material against the propagation of pre-existing cracks. According to fracture mechanics, a crack can experience three basic modes of loading: a) pure tension or mode I; b) sliding or shearing-in-plane or mode II; and c) tearing or shearing-out-of-plane or mode III (Irwin 1958). Among them, mode I (i.e. when the crack develops in a direction normal to the largest tensile load) is especially relevant in rocks due to their small tensile strength compared with the corresponding compressive or shear resistance.

In the oil and gas industry fracture toughness has a crucial importance and the limited availability of in situ samples amenable of multiple laboratory testing is challenging. In the past years, a number of experimental procedures have been proposed for the successful determination of mode I fracture toughness (K_{IC}) in rocks. Worth mentioning among them are the four suggested methods endorsed by the International Society for Rock Mechanics (ISRM). These are the short rod (SR), chevron bend (CB), cracked chevron notched Brazilian disc (CCNBD), and the semi-circular bend (SCB) (Ouchterlony 1989; Fowell et al. 1995; Kuruppu et al. 2014) test methods.

Recently, Muñoz-Ibáñez et al. (2020) have proposed a new method (pseudo-compact tension or *p*CT test) useful to assess the K_{IC} of rocks and other materials using disc-shaped specimens loaded under pure tension conditions. In contrast to the methods proposed by the ISRM, the *p*CT method has several advantages like simple sample preparation, small sample requirement, limited size effects, and steady propagation of crack beyond peak load. All of these attributes are valuable to fulfil the necessities of the industry.

Acoustic emission (AE) is a non-destructive testing technique widely used to monitor the evolution of damage in rocks. When a fracture growths, crack

energy is released in the form of elastic waves that travel through the material and can be recorded in real time by AE sensors placed on the specimen surface (Mix 2005). However, the processes involved are far from simple and, as the fracturing process occurs, the AE activity exhibits significant variations (Moradian et al. 2016) mostly linked to the different processes occurring since crack initiation and propagation up to final coalescence and fracturing. For instance: The higher the number of growing cracks, the higher the number of AE hits. In fact, an impending failure is usually evidenced by the increase in the rate (i.e. speed-up) of the AE activity (Zang et al. 1998).

In the past years several researchers have described on a qualitative basis the level of damage in rocks using AE parameters such as energy, amplitude or counts (Rodríguez 2016; Moradian et al. 2016; Zhang et al. 2019). Some others have found that the analysis of features in the frequency domain (e.g., peak and centroid frequencies) may be useful to discriminate among the signals induced by different damage mechanisms in concrete (Farnam et al. 2015).

For the assessment of fracture kinematics and cracking modes (i.e. dilatational or tensile, shear, compression, or mixed-modes) different authors have applied a variety of analytical strategies. A first and simple approach is the analysis of the polarity of the first motion of the P-wave arrival. That allows to distinguish among tensile, compressional, or shear events (Zang et al 1998; Lei 2000; Backers 2004; Stanchits et al. 2011; Molenda 2015). More elaborated approaches include moment tensor inversion, which provide a more general elastodynamic framework to describe seismic (or acoustic) forces acting at the source of movement (e.g., Feignier and Young 1992; Graham et al. 2010; Kwiatek et al. 2014; McLaskey and Lockner 2018). An alternative method is to use two indices founded on time-based AE parameters: The average frequency (AF) and the rise angle (RA) value, which allow to discriminate between tensile and shear cracks in materials such as rock (Tsangouri et al. 2015; Wang et al. 2017) or concrete (Ohno and Ohtsu 2010; Aldahdooh and Muhamad-Bunnori 2013). Low RA - high AF values are typically associated with tensile cracks, while high RA - low AF values would be related with shearing. An additional property

grounded on seismological studies in the so-called *b-value*, which has been used to qualitative assess the level of damage in rock-like materials (Carpinteri et al. 2013 and references therein). The variations in the *b-value* during a test are deemed to be indicative of different cracking mechanisms. For instance: A decrease in the *b-value* is generally interpreted as resulting from an increase in the stress level and accordingly, associated with an impending failure. Likewise, high *b-values* could be indicative of the growth and slow propagation of cracks while low *b-values* would suggest the opposite, that is unstable crack growth (Proverbio 2011).

In this study we present and discuss the acoustic emission results associated with a series of mode I fracture toughness tests in rocks. In the experiments, we have applied two different testing approaches (SCB and *p*CT methods) over two different rock types. In the reported tests, which have been conducted at room conditions, we have applied a slow loading rate with the concurrent monitoring of AE signals. For each test we recorded a number of AE parameters (e.g., counts, amplitude, duration, or peak frequency) useful to compute properties of interest to assess stages and processes, failure advent and cracking modes (e.g., AF:RA ratio and the improved *b*-value). In addition, using a multi-sensor array, we have computed the location of the AE hypocentres as a function of testing time, what it is useful to analyse the evolution and propagation of cracks along the ligament length.

5.3. Materials and methods

5.3.1. Materials and specimen preparation

In this study we have used two different rock types to perform the K_{IC} tests: Arcera (AR) and Pinacas (PN) sandstones, of Cretaceous and Jurasic age, respectively. Properties such as porosity, uniaxial compressive strength, and indirect tensile strength have been reported previously in other works (Muñoz-Ibáñez et al. 2020.; Muñoz-Ibáñez et al. *subm.*), and a summary is provided in Table 5.1. The *p*CT specimen is a cylindrical disc-shaped sample with a thickness-to-diameter ratio (*B/D*) of ~0.5 and a U-shaped groove to allow loading.

In the middle of the groove, a thin starter notch is also cut to provide the location for crack initiation (Muñoz-Ibáñez et al. 2020) .The SCB test employs a semi-circular disc (*B/D* ~0.5) with a straight notch that acts as stress concentrator (Kuruppu et al. 2014). A schematic illustration of both *p*CT and SCB specimens as well as the corresponding reference dimensions (Table 5.2; *D* = diameter; *B* = thickness; *R* = radius; *a* = initial length of the starter notch; G_d = groove depth; G_w = groove width; *b* = distance from the base of the groove to the bottom of the specimen; *s* = span length) are shown in Figure 5.1. The specimens were carefully prepared using a customized tile saw in which long rock cores were sliced into thinner discs according to the prescribed *B/D* ratio of 0.5. Some of the discs were also halved for the SCB tests. In the case of the *p*CT test, the loading groove was carved using a 2 mm- thick diamond saw-blade and several passes. A thinner diamond blade (1 mm- thick) was used to cut the starter notch to the prescribed depth in both the SCB and *p*CT tests. The conditioned specimens were then dried at 60 ºC for a minimum of 24 hours in an electric oven and then stored at ambient conditions. Before testing, magnets with 6 mm-diameter, 3 mm-thickness were glued on the surface of the specimens to hold the acoustic emission sensors (Figure 5.1).

Table 5.1: Selected properties of the Arcera (AR) and Pinacas (PN) sandstones: σ_c = Compressive strength; σ_t = Tensile strength; *E* = Young's modulus; ν = Poisson's ratio; n_e = Effective porosity.

Material	σ_c (MPa)	σ_t, (MPa)	*E* (GPa)	ν	n_e (%)
AR	40.2	4.1 - 4.9	12.2	0.4	17.3 - 18.2
PN	129.5	11.2 - 11.9	35.0	0.2	5.5 - 6.5

Table 5.2: Geometrical dimensions corresponding to the SCB and *p*CT test specimens: *D* = diameter; *B* = thickness; *s/D* = span length ratio; *a/R* = notch length ratio (for SCB specimens); *a/b* = notch length ratio (for *p*CT specimens); G_d = groove depth; G_w = groove width.

Method	*D* (mm)	*B* (mm)	*s/D*	*a/R*	G_d (mm)	G_w (mm)	*a/b*
SCB	100	50	0.55 - 0.65	0.4 - 0.6	-	-	-
SCB	50	25	0.55 - 0.65	0.4 - 0.6	-	-	-
pCT	50	25	-	-	5	10	0.1 - 0.4

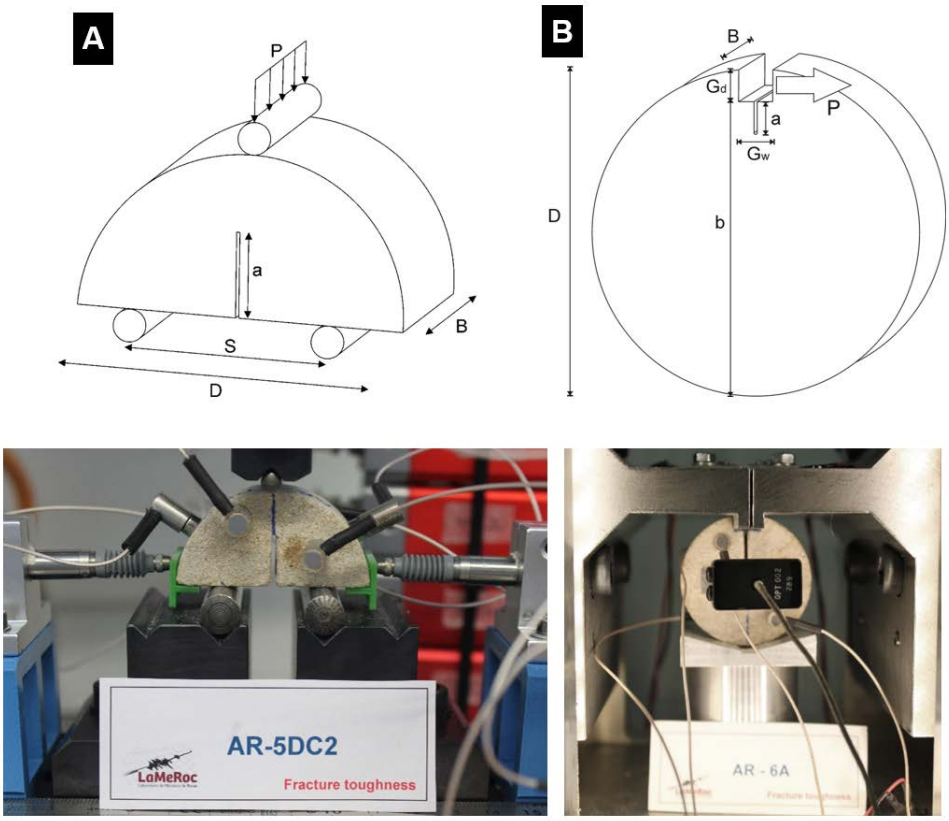

Figure 5.1: Schematic illustration of specimen geometries and loading configurations of the SCB (A) and *p*CT (B) tests and examples with 50 mm-diameter samples. Notes: *P* = applied load; *D* = sample diameter; *B* = sample thickness; *a* = notch length; *s* = span length; G_d = groove depth; G_w = groove width; *b* = distance from the base of the groove to the specimen bottom.

5.3.2. Experimental setup

Three-point bending SCB tests were performed in a stiff servo-electric frame equipped with a 4.448,22 N load cell. In this configuration, an upper steel roller transfers a linear load on the top of the specimen while two additional lower rollers, separated by a fixed distance (*s*), support the sample. On the other hand, the *p*CT specimens are loaded in pure tension using the specially-designed testing device described in detail in Muñoz-Ibáñez et al. (2020), which is equipped with a 50 kN load cell. The specimen is placed on a platform and attached to two steel jaws that penetrate into the U-shaped groove cut in the top of the sample. With this setup, while one of the jaws remains static, the other one is pulled away at a constant displacement rate. Further details of both systems can be found in Muñoz-Ibáñez et al. (2020) and Muñoz-Ibáñez et al. (*subm.*)

Tests were performed at a slow rate of 100 µm/min to avoid dynamic effects. Load (*P*), load point displacement (LPD), and crack mouth opening displacement (CMOD) were continuously monitored in the tests. In the case of the SCB tests, LPD corresponds to the vertical displacement of the top roller, and CMOD is computed as the sum of the normalised displacements measured by two horizontal linear variable differential transducers (LVDTs) located at the level of the base plane of the SCB sample. In the case of the *p*CT, LPD corresponds to the displacement of the mobile jaw, and CMOD is measured using a clip-on gauge attached to the specimen surface at the level of the notch tip. Steel knife-edge blades were glued to the samples to make possible this arrangement (Figure 5.1).

5.3.3. AE equipment and methods

Mode I fracture toughness tests performed with either the *p*CT or the SCB methods were instrumented for the concurrent monitoring of AE activity. The corresponding records were collected using a 16-channel monitoring system (AMSY-6; Vallen Systeme GmbH, Germany). We equipped the 50 mm-diameter *p*CT specimens with four wide band AE sensors (Vallen VS700-D; frequency range: 150-800 kHz; peak frequency: 600-800 kHz), while we used six and eight sensors for the SCB samples of 50 and 100 mm-diameter, respectively. The AE

sensors were mounted on magnets which were glued with cyanoacrylate to the surface of the specimen. The arrangement of AE sensors is illustrated in Figure 5.2. Since it is expected that cracks initiate their propagation from the tip of the starter notch, some sensors of the AE array were placed in the neighbourhood of the ligament volume.

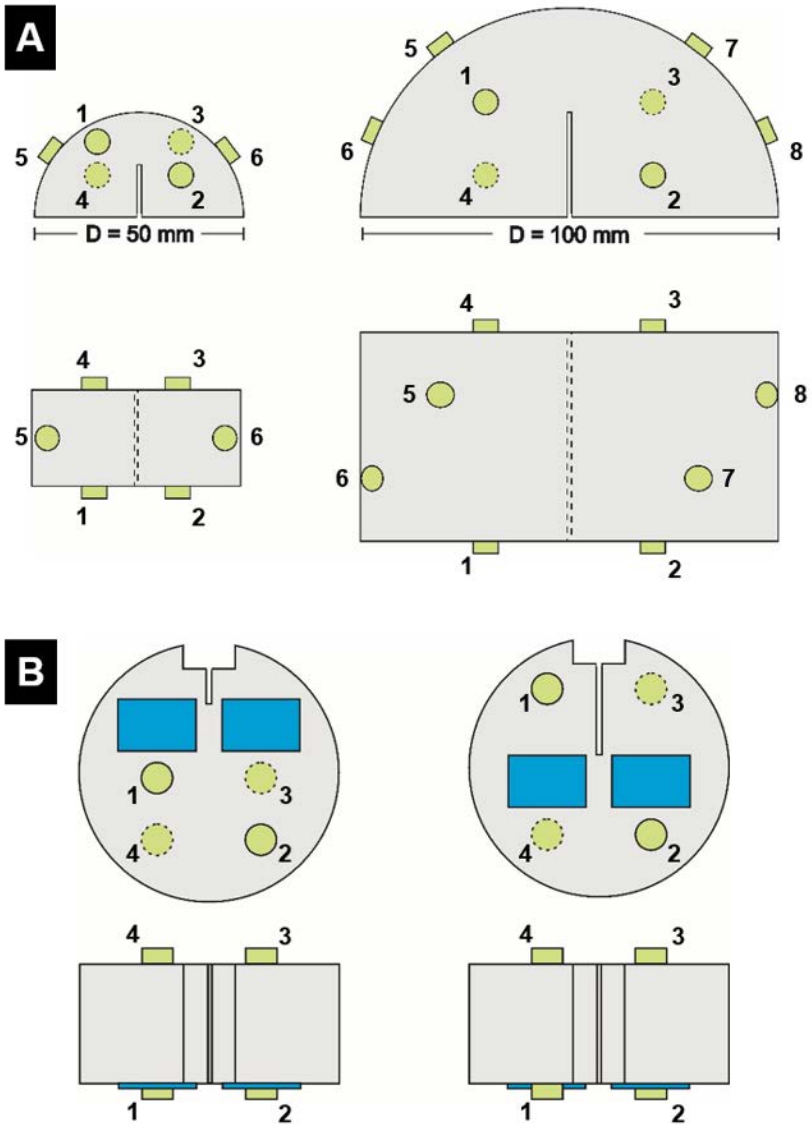

Figure 5.2: In A: Location of the AE sensors in 50 and 100 mm-diameter SCB specimens (left and right, respectively). In B: Emplacement of the AE sensors in 50 mm-diameter *p*CT specimens with two different starter notch lengths (left: $a/b \leq 0.2$; right: $a/b > 0.2$).

To improve the coupling of the transducer with the magnet and to obtain adequate acoustic transmission, we used a thin layer of OKS 1110 silicone grease (ASTM 1997). The detected AE signals were amplified using AEP5 preamplifiers set to a 34 dB-gain for each channel. We also prescribed a continuous waveform sampling frequency of 10 MHz, a threshold value of 40 dB, and a band-pass filter configuration of 95-850 kHz, what provides the full bandwidth of the sensors while still eliminating unwanted low and high frequency noise components.

Time-resolved AE parameters including signal peak amplitude (A), counts, event duration, rise time, and energy (E_{AE}) were recorded in real-time. E_{AE} is computed in aJ (10^{-18} J) from the root-mean square of the integral of the squared voltage signal divided by a reference resistance (10 kΩ in the AE system used) over the duration of the recorded AE transient (Vallen Systeme GmbH 2017). Due to the way it is estimated, E_{AE} must be regarded as a practical energy indicator to analyse the cracking process rather than a true energy measurement amenable of accurate balances (Lin et al. 2020).

Other properties like the average frequency (AF = counts/duration) and the rise angle values (RA = rise time/peak amplitude) were computed afterwards. Likewise, stored waveforms of the recorded events were post-processed in order to determine time-frequency descriptors (e.g., centroid and peak frequencies) based on an automatic Fast Fourier Transform (FFT) algorithm. We also used the data gathered with the multi-sensor array to compute the hypocenter location of the AE events. To do that it was first necessary to verify the cross-coupling quality of the sensors (i.e. the strength in the propagation of a synthetic pulse) as well as the average velocity (v) field in each tested specimens (v ~2000 and ~1200 m/s for the Pinacas and Arcera sandstones, respectively). We performed both checks with the aid of the Vallen AE-Suite software package in pulsing-mode (Vallen Systeme GmbH 2017) with which it is possible to identify a 3D velocity field making more accurate event location (Molenda 2015).

The *b-value* is a seismology-derived parameter based on the Gutenberg-Richter relationship that has been proposed by the ISRM as an index value for

recognizing the onset of rock cracking (Ishida et al. 2017). The early expression of the *b-value* was used to estimate the likelihood of occurrence of an earthquake above a given magnitude but it has been adapted to the study of AE in rocks by applying the correction introduced in Equation (5.1):

$$\log_{10} N = a - b\frac{A}{20} \tag{5.1}$$

where *N* is the number of AE hits whose amplitude is greater than a given threshold value, *a* an empirical constant, *b* is the *b*-value, and *A* is the peak amplitude of the corresponding AE hit, in dB. To compute the *b-value*, we have grouped the experimental dataset into subsets including one hundred AE hits. Due to the variability in amplitude of the acoustic signals, Rao and Lakshmi (2005) suggest a weighting scheme based on the grouping of the experimental dataset into subsets of N hits (N = 100 in our case) and to take into account the mean amplitude (μ), standard deviation (σ) and a lower and upper amplitude bounds (α_1 and α_2, respectively) to obtain the so-called improved *b-value, or* I*b-value*:

$$\mathrm{I}b = {[logN(\mu - \alpha_1\sigma)] - logN(\mu + \alpha_2\sigma)}\Big/{[(\alpha_1 + \alpha_2)]\sigma} \tag{5.2}$$

5.4. Results

5.4.1. P-LPD curves and AE activity

Some representative load-displacement curves (*P*-LPD, where LPD corresponds to the load point displacement) obtained with the two selected testing methods and rocks are illustrated in Figure 5.3. There we observe that the shape of the curves associated to each testing method are clearly different both before and after peak load (P_{max}). Thus, while the *p*CT curve is smooth up to P_{max}, the SCB curve in the same region is notoriously less homogeneous. Likewise, while in the SCB tests we observe a sharp strength drop right after P_{max}, in *p*CT the strength reduction is more progressive, evidencing a significantly better test control in the post-peak region. These circumstances, which are not unusual, have been discussed in more detail in Muñoz-Ibáñez et al. (*subm.*). The

connection of the stress-strain evolution with that of the AE activity will be discussed in another section of this study.

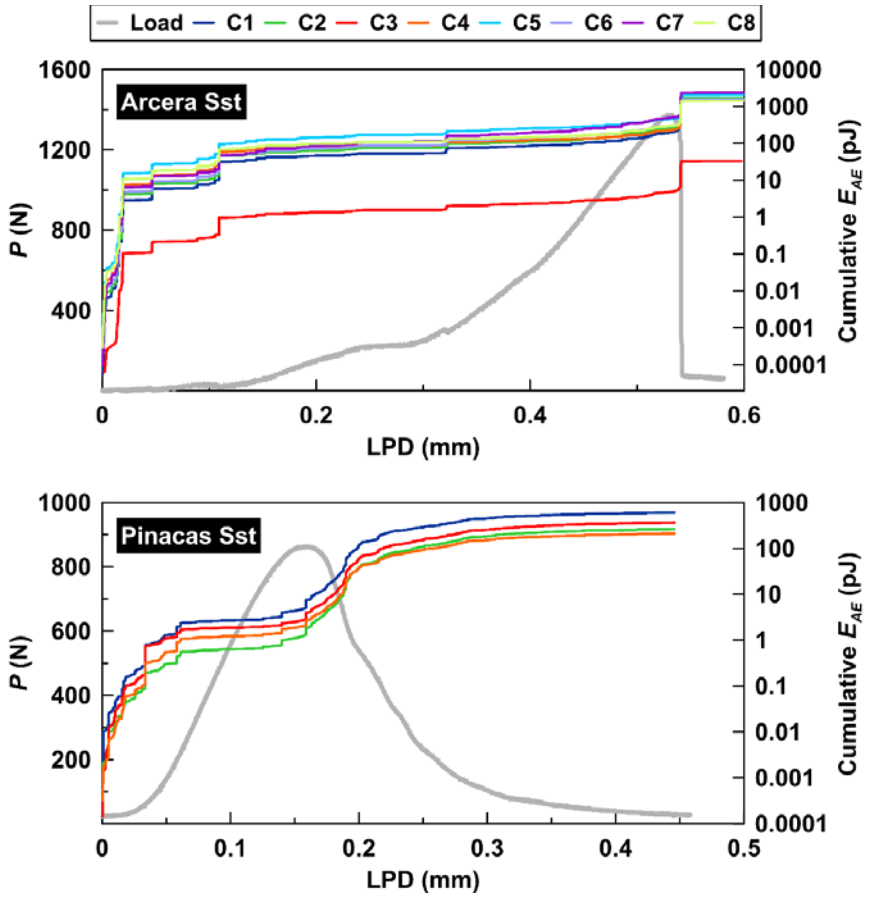

Figure 5.3: Cumulative AE energies (E_{AE}) recorded during a SCB test with the Arcera sandstone (top) and a *p*CT test performed with the Pinacas sandstone (bottom). Curves illustrate the results of each available AE sensor. The load *vs.* displacement (*P*-LPD) curves are is also given for reference.

Figure 5.3 also presents some typical cumulative AE energy (E_{AE}) results associated with the two tested lithologies (Arcera and Pinacas Sst) and methods (*p*CT and SCB). We have represented in separated curves the results of each independent measuring channel. It is interesting to observe that, for all the sensors in the same experiment, the curves are parallel but the individual sensitivity is different so that, at the end of the test, the final cumulative E_{AE} value differs. For the SCB test shown and, with the exception of the observation

channel C3 (whose lower values may obey to a poorer coupling), we verify the same effect. The reason for that is linked to the attenuation of the acoustic signal, which is inherent to the location of the corresponding sensor (spreading increases exponentially with the distance; Spasova et al. 2007) and the dispersive properties of the studied medium along wave path connecting them with the acoustic source (i.e. dispersion, inelastic interactions, scattering and diffraction).

5.4.2. Frequency analysis of the AE signals

Figure 5.4A illustrates the time evolution of peak frequency (f_{peak}) values recorded during typical SCB and *p*CT tests performed with the Pinacas sandstone. In the plot we have marked with a different color each monitoring channel. In general, three distinct peak frequency bands manifest: Band-I (f_{peak} ~100-300 kHz, observed all along the test); Band-II (f_{peak} ~300-600 kHz, starting at ~0.5P_{max}); and Band-III (f_{peak} ~600-800 kHz, starting at ~0.8P_{max} for the SCB test, and above P_{max} for the *p*CT test). Although these frequency bands are comparable for both testing methods, the *p*CT test provides a larger amount of information than the SCB test, which is especially noticeable at high peak frequency values. In fact, for the *p*CT test it seems that the high frequency band can even be split into two separate subgroups, taking the value of f_{peak} = 700 kHz as boundary. This is better illustrated in Figure 5.4B, in which the normalized amplitude ($A_{norm}=A/A_{max}$; where A_{max} is the maximum amplitude) is plotted as a function of the peak frequency (f_{peak}) for two AE channels involved in data acquisition: one corresponding to a sensor placed closer to the notch tip (C4 and C1 in SCB and *p*CT tests, respectively), and other placed farther from this location (C6 and C4 in SCB and *p*CT tests, respectively; see Figure 5.2). In general, we observe a progressive decrease in the number of AE events (and the associated A_{norm}) as f_{peak} increases. In addition, the location of the sensors in relation to the notch tip (where the major part of the AE signals is expected to occur) influences the frequency content recorded: as distance from the notch tip increases, lower f_{peak} values are detected for the same frequency band. The scarcity of data at f_{peak} ~500 kHz in all cases would be related with the limited acoustic response of the sensors at this frequency value.

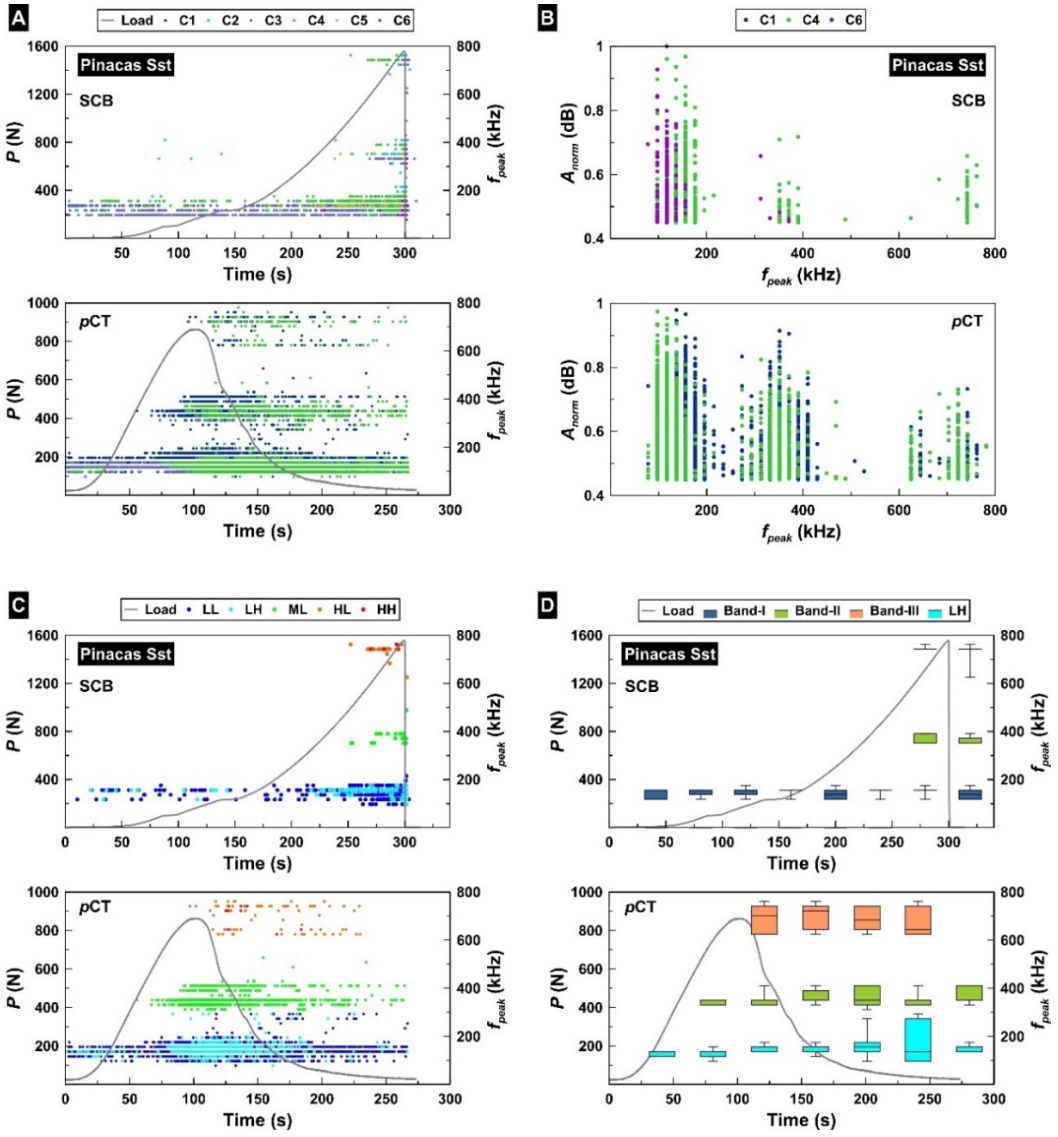

Figure 5.4: A: Time-distribution of peak frequencies (f_{peak}) obtained with Pinacas sandstone specimens. Results for each monitoring channel are illustrated with a different colour. B: Normalised amplitude (A_{norm}) *vs.* peak frequency (f_{peak}) for two AE channels. C: Time-distribution of peak frequencies (f_{peak}) as a function of data grouping into LL, LH, ML, HL, and HH (see text for explanation). D: Box & whisker plots illustrating the peak frequencies (f_{peak}) associated with three frequency bands. The box extends from Q_1 to Q_3, while the whiskers go from P_5 to P_{95}. The horizontal line in the middle of each box represents the corresponding median. Note: In all figures, results for the SCB and the *p*CT tests are given on the top and the bottom, respectively. In figures A, C, and D the load *vs.* time curves are also given for reference.

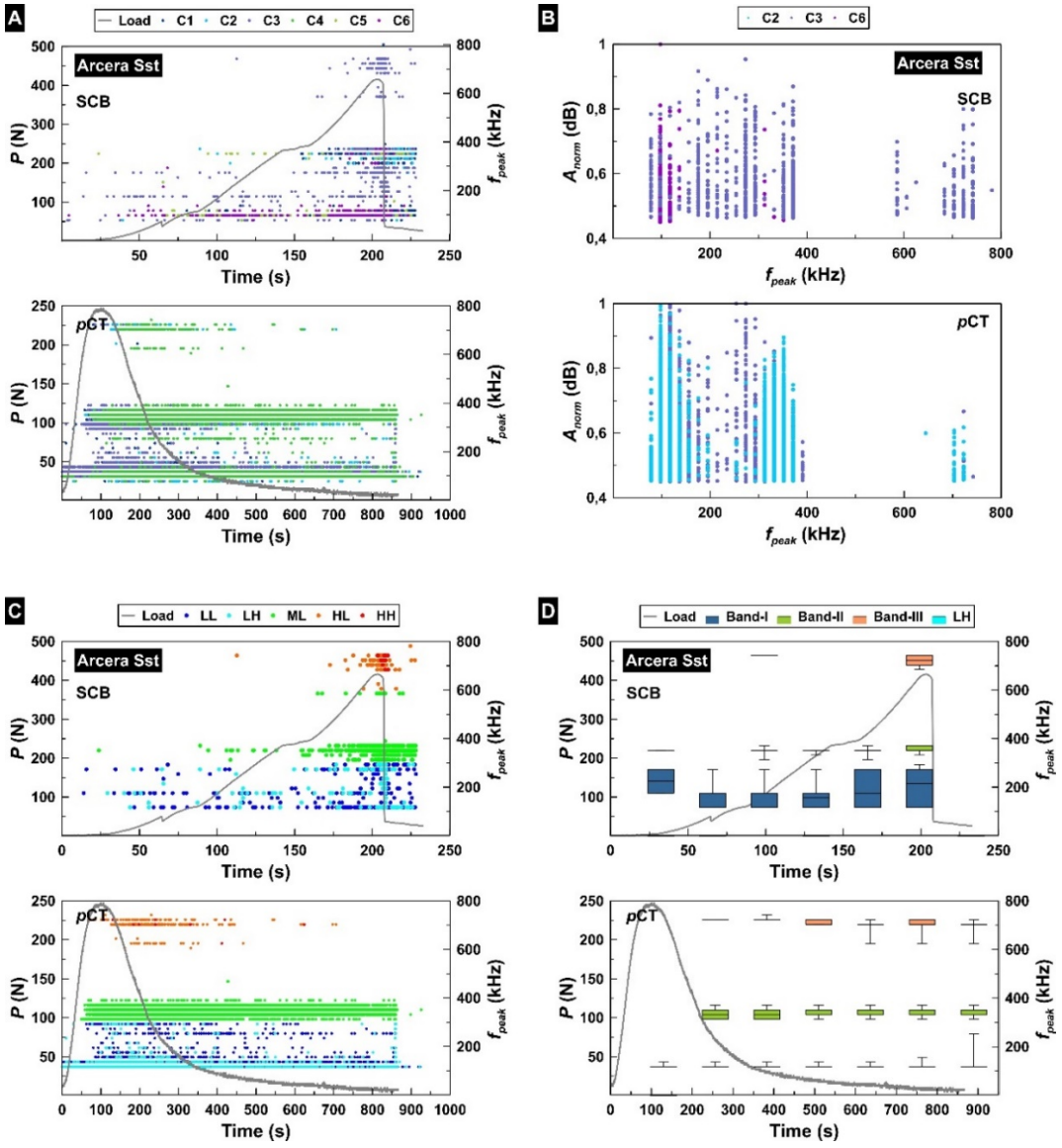

Figure 5.5: A: Time-distribution of peak frequencies (f_{peak}) obtained with Arcera sandstone specimens. Results for each monitoring channel are illustrated with a different colour B: Normalised amplitude (A_{norm}) vs peak frequency (f_{peak}) for two AE channels. C: Time-distribution of peak frequencies (f_{peak}) as a function of data grouping into LL, LH, ML, HL, and HH (see text for explanation). D: Box & whisker plots illustrating the peak frequencies (f_{peak}) associated with three frequency bands. The box extends from Q_1 to Q_3, while the whiskers go from P_5 to P_{95}. The horizontal line in the middle of each box represents the corresponding median. Note: In all figures, results for the SCB and the *p*CT tests are given on the top and the bottom, respectively. In figures A, C, and D the load vs. time curves are also given for reference.

Following a similar analysis to that performed by Chen et al. (2020), we have divided the AE signals recorded by one of the AE channels into five different groups according to their peak frequency and normalized amplitude (Figure 5.4C; Table 5.3): LL, LH, ML, HL, and HH. The first letter designates the low (L: 100-300 kHz), medium (M: 300-600 kHz), or high (H: 600-800 kHz) f_{peak} range while the second one indicates the low (L: 0.4-0.6) or high (H: 0.6-1) A_{norm} range. Although LL signals are observed all along the experiments, LH signals noticeably occur as the load approaches P_{max}. The trend is similar to that observed for ML signals, which suggests a relationship between both types of events. However, during the post-peak region in the *p*CT test, LH signals tend to vanish before ML signals do. High frequency signals (HL and HH) clearly appear after P_{max}, which would be indicating the emergence of a different process that cannot be captured at low- and medium- frequency ranges. To gain a deeper insight into the evolution of the three frequency bands defined above, in Figure 5.4D we show the average values and spread in f_{peak} at different stages of the tests. It must be noted that for the *p*CT test, at low frequencies (Band-I) we have only plotted the data for group LH. For this testing method, the average value of Band-III first increases and then decreases. With the exception of the last group, this trend is also observed for the Band-II and for the group LH, although in these cases the scattering enlarges as the test approaches its final stage. The poorer quality of data for the SCB hampers to perform a similar analysis. Although the mean value at low frequencies (Band-I) shows small fluctuations, the sensitivity is lower than in the *p*CT test.

Table 5.3: AE signal grouping: f_{peak} = peak frequency; A = amplitude.

	LL	LH	ML	HL	HH
f_{peak} (kHz)	100-300	100-300	300-600	600-800	600-800
A (dB)	40-60	60-100	40-60	40-60	60-100

A similar analysis was also carried out for two specimens of Arcera sandstone, and results are plotted in Figure 5.5. Although the type of rock does not appear to have a significant impact in the f_{peak} (the frequency bands observed are comparable despite of being noisier), for the weaker Arcera Sst there is a major abundance of events in the range of 200-300 kHz, especially when approaching P_{max}. For the *p*CT specimen, we also observe a lower amount of high frequency (Band-III) signals (Figure 5.5A). In addition, the values of A_{norm} remain high even for events in Band-II, and the effect of attenuation is only evident at high frequency ranges (Figure 5.5B). Here we also observe that, for each frequency band, the AE sensors placed closer to the notch tip (C3 for both testing methods) provide higher frequency values than those located farther (C6 and C2 for SCB and *p*CT tests, respectively), although the effect is less clear than for the Pinacas Sst. In the *p*CT test of the Arcera Sst, the division of the low frequency signals into two separate groups (LL and LH) does not reveal any distinct pattern between them (Figure 5.5C). In fact, the mean values of f_{peak} in Band-I and Band-II, as well as the spread, are almost uniform all along the test, with the exception of the last group. For Band-III, we observe a slight decrease in the mean value during the post-peak region, and higher scattering as the specimen loses cohesion (Figure 5.5D). Results for the SCB specimen show large scattering at low frequencies, and a decrease and a subsequent recovery in the average f_{peak} during the linear and non-linear elastic stages of the test for Band-I.

5.4.3. AE hypocenter location

The location of the AE events is based on those signals whose amplitude is greater than 70 (*p*CT) or 60 (SCB) dB. These values are seldom found before P_{max} and, therefore, they have not been included in the presentation. The given cut off values were set to filter weak signals and to improve the rate of successful event location.

Figure 5.6 shows an aggregate panel with the *P*-time curves of the *p*CT tests performed with the Pinacas and Arcera sandstones together with a series of images illustrating the projection of acoustic events over the tested samples.

The coloured arrows highlighted in the *P*-time curve select six specific time-windows (from P_{max} onwards) for which the hypocentre location has been also windowed. The colour code of the arrows corresponds with that of the dots used to overlap the sample pictures. It is important to mention that, while the hypocentre location is performed in a 3D volume, the dots are projected in a flat surface. Thus, the depth-dimension is lost in this representation and, in the case that the developed fracture plane was not orthogonal to that of projection, an increased horizontal spread would appear. In fact, the lateral spread could be used as indicator of fracture waviness. We have not selected any time-window before P_{max}. The reason for that is the scarcity of signals whose amplitude were above the minimum threshold value set.

The careful observation of the event distribution in the tested rocks evidences that most of the events identified during P_{max} and early post-P_{max} are located in the theoretically expected region: the notch tip. The distribution of events up to a load value of ~0.3P_{max} (~70% drop) conforms to a vertical crack with limited lateral spread. This is true for the hard, short-notched Pinacas Sst sample and the weak, long-notched Arcera specimen. For lower strengths (P < 0.3P_{max}) the located events deviate from the vertical (Pinacas Sst) or increase the lateral spread (Arcera Sst), both observations consistent with the observed macrocracks. This period corresponds with the later stage of experiments, when the failure process is dominated by the coalescence of the cracks already formed. One significant contrast observed when comparing the two sandstones tested with the *p*CT method is that, in the Arcera specimen and for the same time-window, the AE events extend over a larger area of the ligament. For instance, at P_{max} they reach approximately half of the length of the ligament. This is consistent with the lower energy requirement to propagate a fracture trough this weaker rock.

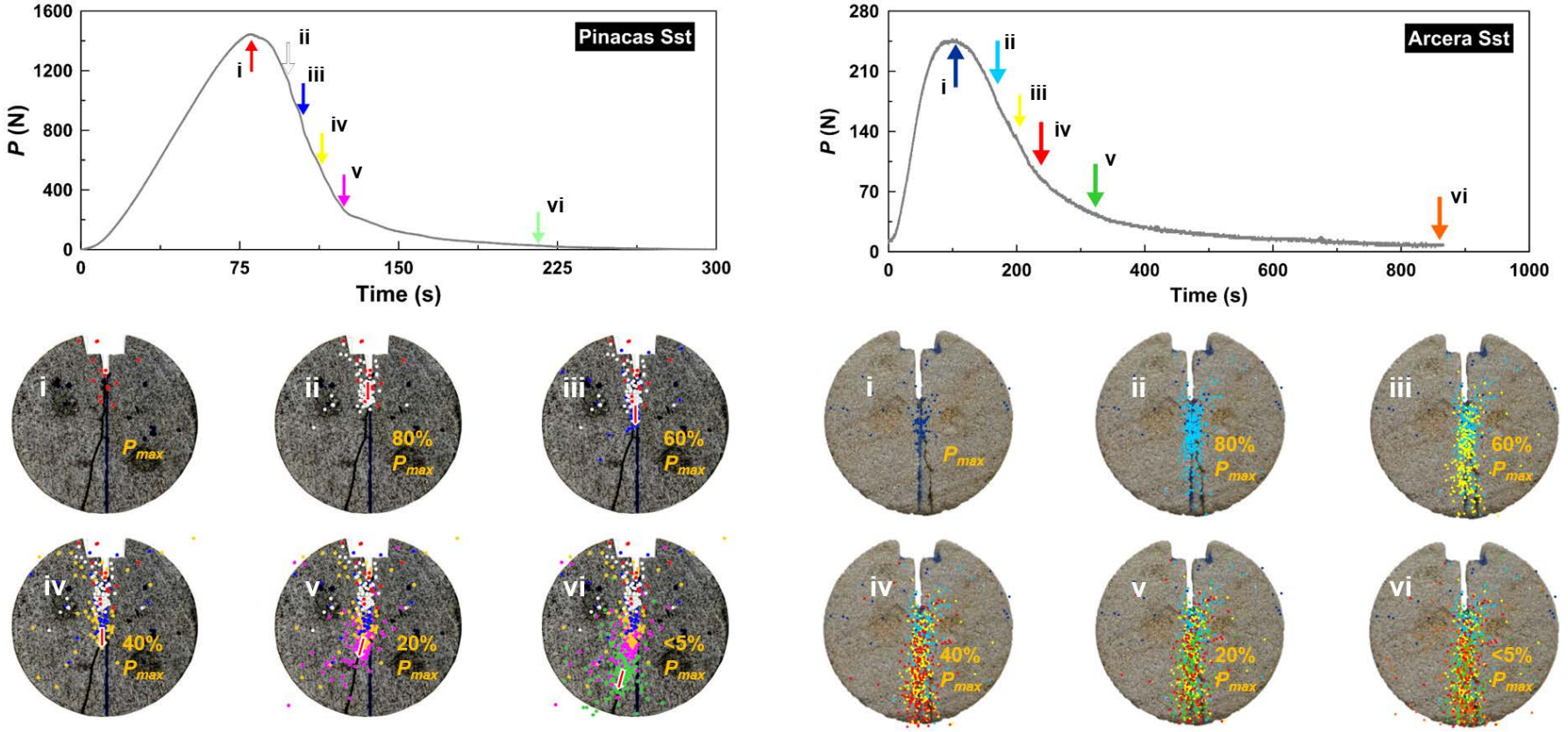

Figure 5.6: Spatial distribution of AE events with amplitude >70 dB during the different stages of *p*CT tests performed with Pinacas (left) and Arcera (right) sandtone specimens. The labels in the pictures reffer to the %drop in P_{max}. The diammetral (vertical) lines draw on the recovered rock specimens represent the theoretical crack paths and they are compared with the actual trace of the developed crack. See text for explanation.

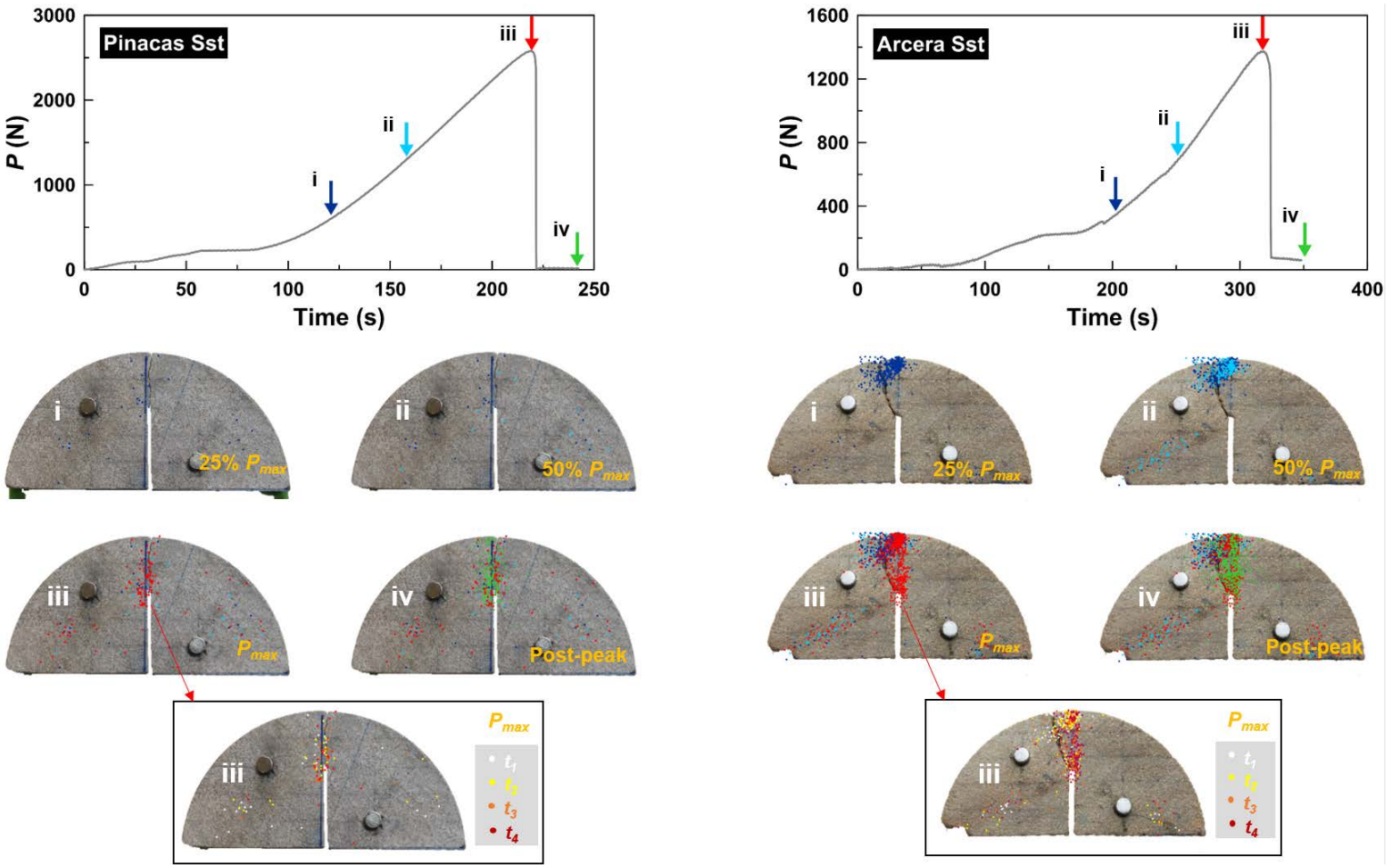

Figure 5.7: Spatial distribution of AE events with amplitude >60 dB during the different stages of SCB tests performed with Pinacas (left) and Arcera (right) sandstone specimens. Time-window III (P_{max}) has been split into four subtimes (t_1, t_2, t_3 and t_4) which are presented in the inset. The labels in the pictures refer to the %drop in P_{max}. The radial (vertical)

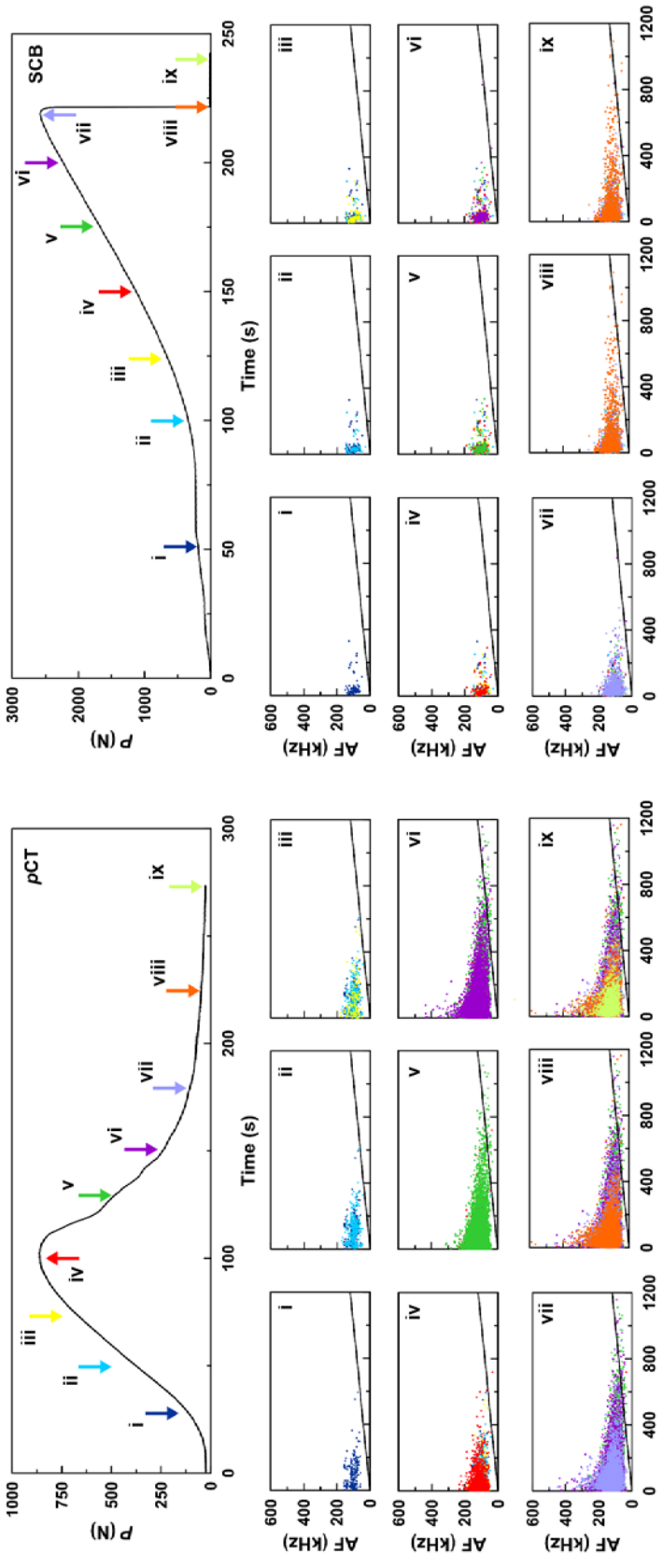

Figure 5.8: Evolution of the ratio AF:RA according to selected time-windows associated with *p*CT (left) and SCB (right) tests performed with specimens of the Pinacas Sst. The colour code and roman numerals of the arrows are the same than in the panel below.

Figure 5.7 presents the same analysis approach for two tests performed with the same sandstones using the SCB method. As for the *p*CT specimens, the Pinacas Sst (Figure 5.7, left) reveals few AE signals before P_{max} along the theoretical fracture plane. Then, when P_{max} is attained and thereafter (in the short time period preceding full failure), a more significant number of events concentrate near the notch tip. The final stages of the test of the illustrated Pinacas sandstone evidence the upwards migration of the AE events, as expected from the theoretical considerations of the SCB method (Kuruppu et al. 2014). Conversely the results for the Arcera Sst (Figure 5.7, right) differ significantly from those of the Pinacas. The most relevant difference is the high density of events located in the external upper section of the sample at early stages of the test. This location is next to the contact point of the top roller. In this case, we observe a progressive damage originated at the left side of the contact point of the roller (time-window *i*) that migrates rightwards (time-window *ii*) and originates the failure of the sample once P_{max} is approached (time-window *iii*). In this situation, the orientation of the stress tensor determines that failure does not initiate at the expected point (the notch tip). It develops from the top surface of the sample to the notch tip originating an oblique macrocrack. While the results of this particular test are useless for mode I fracture toughness assessment, they are highly illustrative of: a) One of the troubles associated with the SCB testing method (see Muñoz-Ibáñez et al. (*subm.*) for a wider discussion), and b) The significant potential of AE monitoring to better understand fundamental processes associated to fracture toughness testing.

5.4.4. AF vs. RA plots

So far, a number of criteria based on the investigation of cracking modes have been published to characterize damage in engineering materials. In this study we focus on the parameter-based methodology proposed by the *Federation of Construction Materials Industries of Japan* (JCMS-III B5706 2003; Ohno and Ohtsu 2010), later incorporated as recommendation for concrete materials by the RILEM (Ohtsu 2010). This is grounded on an experimental database of four-point bending and direct shear tests performed with concrete-type materials, and

indicates that it is possible to discriminate among tensile, shear or mixed-mode (tensile-shear) cracks according to the ratio existing between the average frequency (AF) and rise angle (RA) obtained from AE testing (see section 5.3.3): If the AF *vs.* RA ratio is >0.1 Hz·s/V, the AE events are considered to be originated by tensile stresses, while ratios <0.1 Hz·s/V would correspond to crack shearing. Those events with a ratio of ~0.1 Hz·s/V are likely to be occasioned by a mix-mode of cracking.

Figure 5.8 illustrates the distribution of the AF:RA ratio in nine different time-windows of *p*CT and SCB tests performed with the same rock type (Pinacas Sst). In both cases we observe that, for loads <P_{max}, the events locate in the assumed tensile field. As we approach P_{max}, the AE activity extends towards (but does not reach) the border line of mixed-mode, while for post-peak conditions (time window *v* in *p*CT, and *viii* – *ix* in SCB) this boundary is clearly reached and significant AE activity develops in the shear field. Although both tests illustrate the same features, the *p*CT allows the identification of further details. In Figure 5.9 we have tried to summarize as box & whisker plots the spread in RA for the selected time-windows presented before. For the SCB test we observe a nearly constant spread before P_{max} and a significant increase onwards. However, in the *p*CT test we see a more complex pattern, including a progressive reduction in the absolute value of RA (and spread) at peak load, (what reinforces the perception of tensile mode of this stage), a notorious spread increase in the early post-peak (suggesting a greater contribution of mixed-mode and shear cracking) and a spread reduction in the late post-peak stages (*i.e.* a renewed tendency to tensile cracking). It is interesting to note that, while the average RA value at P_{max} is higher than in pre-peak conditions for the SCB method, the situation is the opposite to the *p*CT (lower RA in P_{max} than in pre-peak conditions). Leaving apart the wealth of information provided by the *p*CT methodology, the observed contrast suggests certain fundamental differences in the cracking processes operating when testing with the two methods. However, this parameter-based analysis has a limited scope (for instance, it does not include the assessment of compression modes) and lacks the analysis potential of other techniques (e.g., moment tensor

inversion of amplitudes of first motions; Graham et al. 2010) amenable of better characterization of source mechanisms.

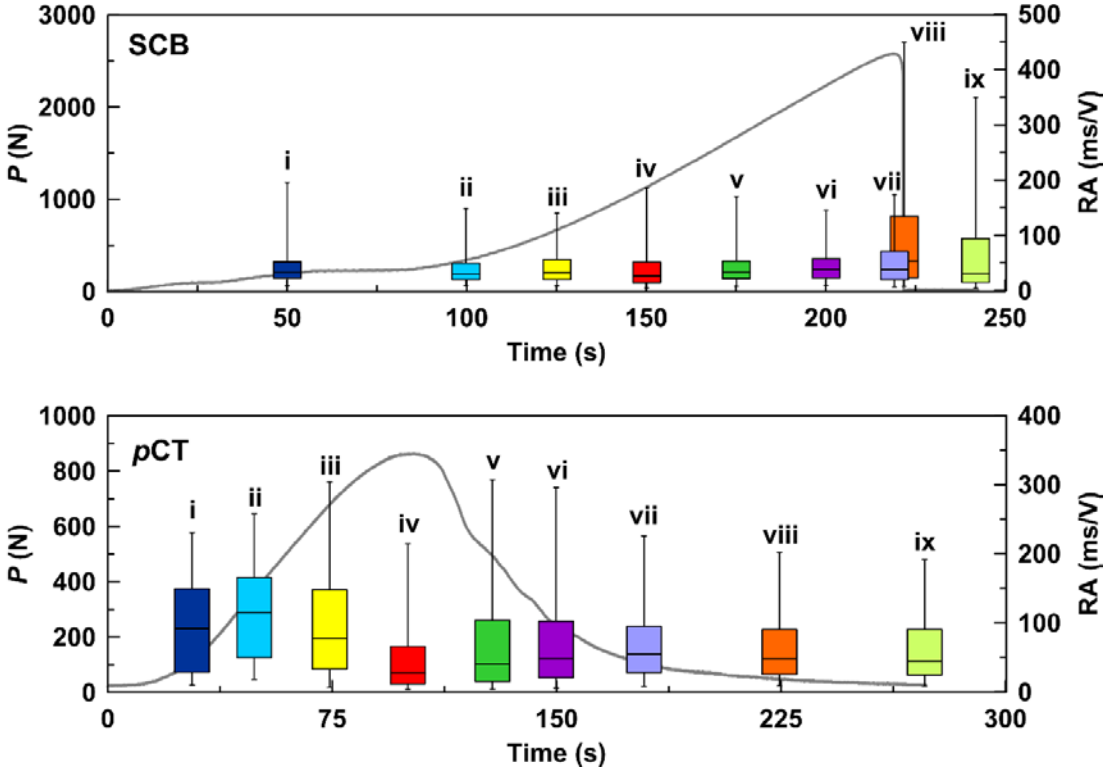

Figure 5.9: Box & whisker plots illustrating the RA-value associated with the different stages of a SCB (top) and *p*CT (bottom) tests. The box extends from Q_1 to Q_3, while the whiskers go from P_5 to P_{95}. The horizontal line in the middle of each box represents the corresponding median. Roman numerals are the same identified in Figure 5.8. The load *vs.* time curves are given for reference.

5.4.5. Ib-value

The evolution of the I*b-value* during SCB and *p*CT tests performed with specimens of Pinacas sandstone is illustrated in Figure 5.10. In a first approach, we computed the I*b-value* following the procedure of Rao and Lakshmi (2005), and using the same criterion for data grouping (N = 100) for both testing methods. The number of AE hits recorded in the SCB tests is significantly lower than in the *p*CT ones. This is mainly associated with the nearly complete absence of AE data associated with the post-peak region. For this reason, the SCB-derived I*b-value* displays a smoother curve than the one of the *p*CT test, which is highly scattered

specially after P_{max}. For better visualization of the main trend, the I*b-value* computed at intervals of 20 seconds (I*b-value* (t)) is also displayed in the same figure. The time window was reduced to 10 or even 5 seconds to improve accuracy of results at certain stages of the tests. Leaving apart these questions, it appears that the magnitude of the I*b-value* rises along the elastic stage and attains its maximum in advance to P_{max} in both cases. By when the load peaks in the *p*CT test, the I*b-value* descends to a value ~1 and remains low and fluctuating as the fracture unstably propagates. The oscillation observed contrasts with the sharp drop to even lower values (~0.5-0.6) at and after failure in the case of the SCB test.

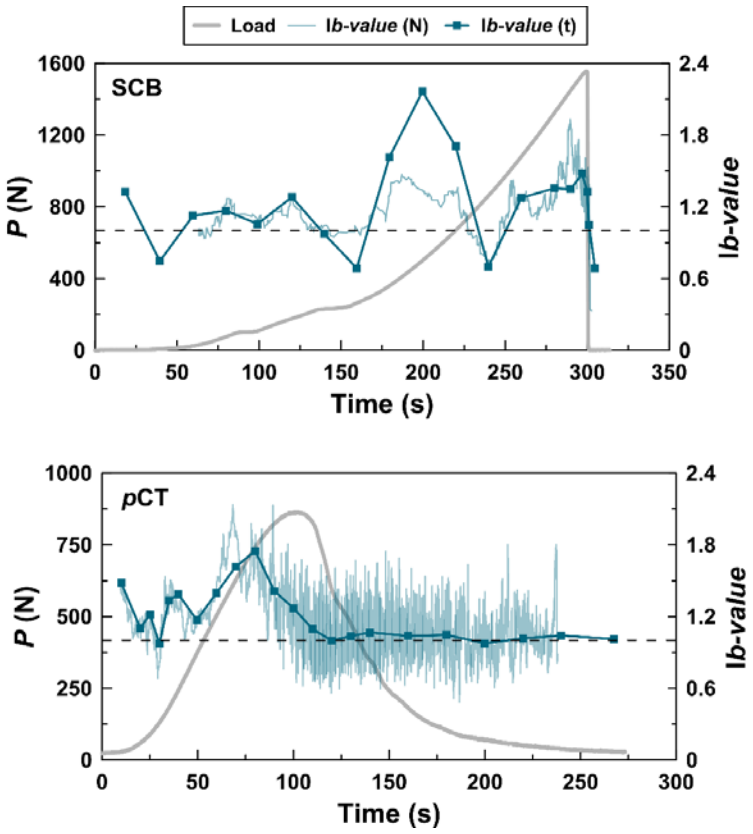

Figure 5.10: Time evolution of the I*b-value* computed for Pinacas Sandstone specimens during SCB (top) and *p*CT (bottom) tests: in light colour, I*b-value* taking N = 100; and in dark colour, I*b-value* for defined time windows (see text for explanation). The load *vs.* time curves are also given for reference. Dashed line refers to I*b-value* = 1.

5.5. Discussion

According to Carpinteri et al. (2013), specimen size and transducer spacing are critical features in quantitative AE analysis: The larger the distance between the source of the events and the sensors, the stronger the attenuation of the AE signals. In line with the data reported by the previous authors, our results reveal that higher E_{AE} is recorded for those sensors placed close to the notch tip in *p*CT (sensors C1 and C3), where the major concentration of generated events is to be expected. However, for the SCB specimen of Arcera Sst the final cumulative E_{AE} is larger for the sensors located near the contact point of the top roller (sensors C5 and C7). Signal attenuation may be frequency selective (Aggelis and Philippidis 2004), what makes difficult the proper scaling of E_{AE} to compare with the values derived from mechanical tests (e.g., fracture energy). In our case, in spite of these differences, the main trends are similar for all sensors involved in data acquisition. That suggests that the acoustic characteristics of the rock located between each AE sensor and the generated foci are similar (i.e. isotropic and homogeneous media). This is consistent with the known properties of the tested rocks as well as the macroscopic observation of the specimens.

5.5.1. Stress-strain and damage evolution

The shape of *P*-LPD curves includes information about fundamental processes occurring in the specimens as they are tested. To this respect, the general model of Martin and Chandler (1994) about the progressive failure of brittle rocks for small strains provides a workable framework with which to describe the fracturing process. This has been also used by Zhang et al. (2018) to describe damage in rocks during tensile tests. In the present study, we use two selected specimens of the Arcera Sst tested with the *p*CT and SCB methods to illustrate the failure process (Figure 5.11). Stage I represents the closure of pre-existing flaws and microcracks and, to some extent, this preliminary stage may be overlapped by instrumental artefacts associated with the testing device, sample preparation, etc. Stage II develops the elastic component of the material tested and it is characterized by a linear path in the stress-strain space. In stage

III, existing or newly-formed microcracks (which are mainly constrained within single grains) develop into mesocracks (that extend beyond grain boundaries). This transition conducts to a loss of linearity that, depending on the rock type, may be more or less notorious. During this subcritical stage (i.e. load level is below that required to attain K_{IC}) cracks propagate stably (i.e. they grow with the application of a greater load), mainly because of their isolation and spread. However, the progressive coalescence of mesocracks progressively speeds up the damaging process and, once the load attains its maximum corresponding to the critical K_{IC} value, macrocracks form under accelerated growth conditions. Thus, the peak load (P_{max}) marks the initiation of stage IV, where the material still has some cohesion but progressively lower strength. In an advanced level of stage IV, depending on the geometry and orientation of macrocracks, they may mutually interact providing a complementary shear component.

The previous stages are clearly identified in the *P*-LPD curves of the *p*CT tests but this is not the case for the SCB, specially after overcoming the stress needed to attain K_{IC} (i.e. P_{max}): The lack of experimental control during the unstable crack propagation stage prevents it. This has been described and interpreted in greater detail by Muñoz-Ibáñez et al. (*subm.*). Besides, the shape of the *P*-LPD curve in the SCB tests also manifests jumps and plateaus whose explanation is difficult on a general basis. Taking into account the recent observations made by Zhao et al. (2019) in a series of Brazilian tests performed with sandstones, it is likely that these irregularities develop as a result of stress-relief processes product of the oriented emergence of cracks/flaws induced during the compression inherent to the SCB testing method (see Figure 5.7, right). To this respect, the *p*CT method provides with sounder information.

It is generally accepted that AE events developed in rock mechanics tests mainly respond to the manifestation of microcrack growth and propagation (Lockner 1993). The five-stage rock mechanics-based description of progressive failure given before is compatible with the AE data compartmentation proposed by Mogi (2007). This author identifies three progressive stages for AE generation in a rock fracture test. In the first one (stage A), there is no significant AE activity

and it can be related with the crack closing and elastic stages (I and II, respectively). In the second one (stage B), AE events occur often and there is no predominant location within the specimen. Finally, in the third stage (stage C), AE events tend to cluster around the crack plane region as failure advances. The last two Mogi's stages do not differentiate stable (subcritical; stage III) from unstable crack growth (stage IV) or the late coalescence period leading to macroscopic fracturing (stage V). When analysing the hit rates illustrated in Figure 5.11 we observe a good general concordance with Mogi's model. However, further details are also apparent. For instance, the sharp stage-limits, mainly identified from the start/end points of the linear portions of the *P*-LPD curves, are more diffuse (although consistent) when observing AE data. Looking to the *p*CT test (less clear in the SCB) we confirm that, even in the linear stage II, there is AE activity (i.e. non-localized subcritical crack growth takes place in that domain). Hit rate increases in stage III and peaks around peak load. Then, during the post-peak region we first observe a drop (beginning of the unstable mesocrack propagation), then a recovery (growing and interaction of mesocracks), and later a progressive diminution (due to the reduction of the ligament volume).

5.5.2. AE energy

The energy associated to the cracking process can be potentially determined through AE monitoring (E_{AE}). However, this acceptably simplified concept is difficult to reconcile with other independent energy assessments like bulk (macroscopic) fracture energy (Muñoz-Ibáñez et al. *subm.*) or damage indices (Lin et al. 2020 and references therein). The reasons for that are complex and they encompass, at least, geometrical, mechanical and physical issues (see Carpinteri et al. 2016). Its analysis is beyond the scope of this contribution. However, if we accept that there exists a proportionality between rock damage and recorded E_{AE}, it is still possible to gain some qualitative insights through the inspection of the recorded data. To this respect, the cumulative AE energy ($E_{AE,}$) plots presented in Figure 5.11 also illustrate some interesting features that are discussed in more detail in the following sections.

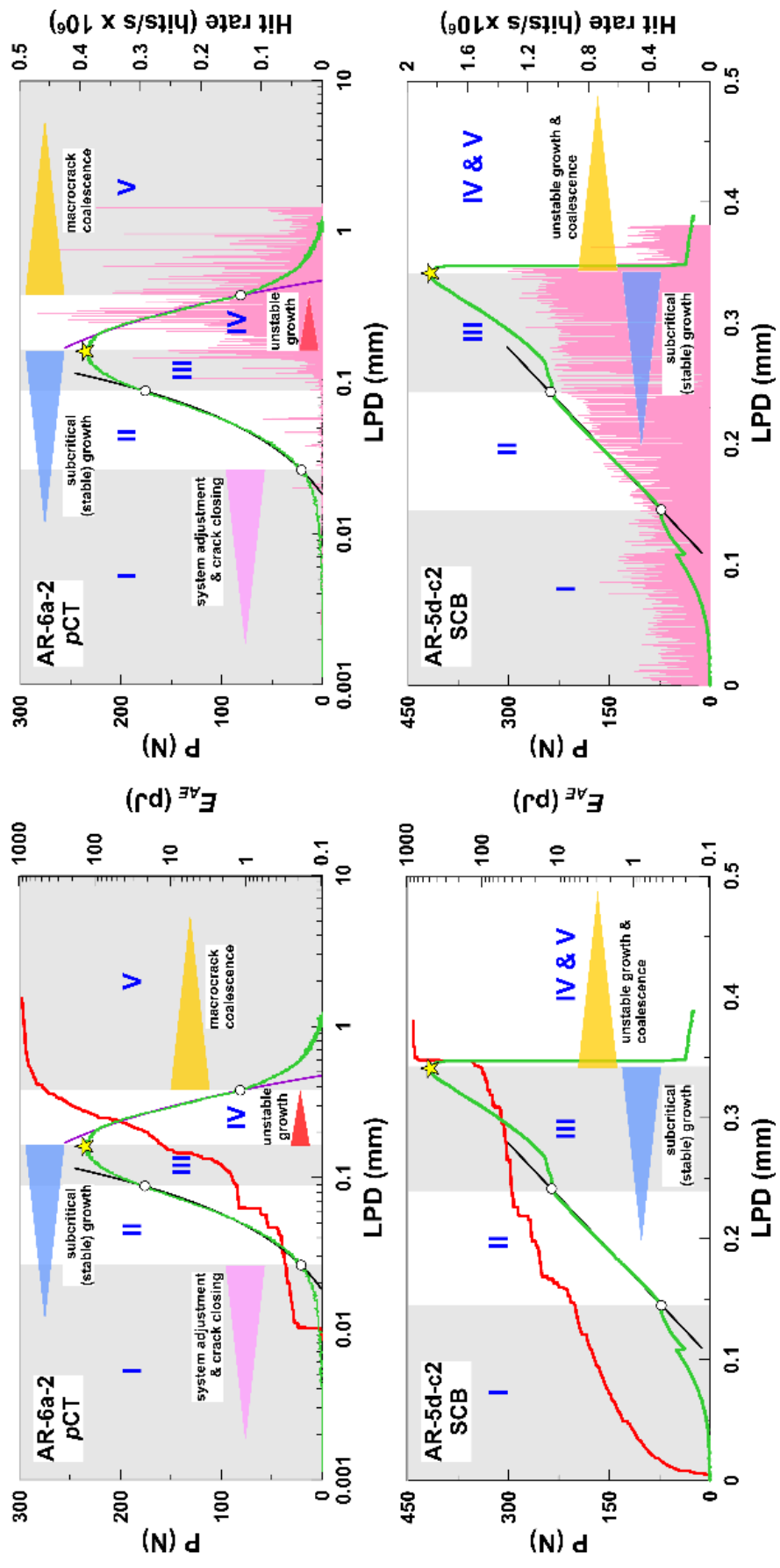

Figure 5.11: Identification of the different stages of crack development in *p*CT and SCB (top and bottom, respectively) fracture toughness test and comparison with the cumulative acoustic emission energy (E_{AE}; left) and hit rate (right). The star symbols identify peak load and empty dots the beginning and end of the proportional (linear) stage. The test illustrated were made with the same rock type (Arcera Sst).

Stage I

As per the Mogi's (2007) model, the E_{AE} at the beginning of the test is very small in the *p*CT test but more significant with the SCB method. Wei et al. (2016) have also reported similar observations using the same testing method and they suggest that this can be associated with the closure of preexisting microcracks, pores, and voids. We consider however that the compressional nature of the SCB test (for which high loads concentrate in small contact surfaces) is a more determining factor to explain the enhanced AE activity in this stage of the SCB test.

Stage II

E_{AE} rises slowly during the linear elastic phase. Farnam et al. (2015) have related this feature to the formation of microcracks with relatively small new surface area. Their results are consistent with those of Nasseri et al. (2006), whom observed in associated thin sections the presence of microcracks around the notch tip. Due to the heterogeneous nature of most rocks, it is expected that microcracks may form at any point of their matrix (Wei et al. 2016). In fact, during the SBC tests we have detected AE activity not only along the ligament but also at a certain distance of this highly stressed volume. In the case of the Arcera sandstone specimen (Figure 5.7, right) we have already mentioned that a significant number of the early events cluster near the top roller, what suggest a high level of stress concentration close to the loading end. Comparable observations have been reported by Wei et al. (2018) for cracked chevron-notched Brazilian disc specimens.

Some discrete AE events occurring in stage II induce sudden jumps in the cumulative E_{AE}. However, it is interesting to note that these jumps occur more at the beginning of this stage. That could be interpreted as the result of the readjustment of the sample due to the varying stress. Zhang et al. (2019) suggest that the presence of grain boundaries and microcracks in a rock may also trigger this phenomenon at the early stages of loading.

Stage III

Going back to Figure 5.11, we observe that, with the onset of the stable crack growth stage, there is a progressive acceleration in the release of E_{AE} and a turn point at P_{max}. This highlights that the subcritical cracking speed is not constant. Lei et al. (2000) have made similar observations for rock specimens tested under triaxial conditions. On the other hand, based on a series of wedge-splitting tests performed with concrete samples, Farnam *et al.* (2015) have interpreted the progressive increase of E_{AE} before P_{max} to result from the convergence of microcracks. The same explanation has been given by Nasseri et al. (2006), in this case for granite samples.

Labuz and Biolzi (1998) describe the clustering of AE events near the notch at ~0.85P_{max} for rock beams loaded in four-point bending. These authors have related this with the appearance of the fracture process zone (FPZ), that is, the microcracked volume located in the neighbourhood of the crack tip. The *p*CT hypocentre location illustrated in Figure 5.6 also supports this in our case.

Stage IV

After peak load (~0.8P_{max} in the post-failure branch of the *p*CT test), the rate of change of the cumulative E_{AE} becomes slower and virtually constant until the end of stage IV (unstable growth). However, the E_{AE} contribution of these events is notoriously higher than the ones conducting to peak load. This is in agreement with the experimental data reported by Wei et al. (2016) for the Dazhou sandstone. In contrast, our data shows that the maximum E_{AE} release is reached before P_{max}. A similar observation is due to Nasseri et al. (2006), who attributed this behaviour to the overlapping of AE events before failure.

Stage V

Once approaching the crack coalescence stage V, there is progressive change in the slope of the cumulative E_{AE} curve and it eventually reaches a maximum value. There are about two orders of magnitude difference between the sum E_{AE} before and after peak load. Based on the works of Carpinteri et al. (2016) we interpret such difference as resulting from the variable amount of energy dissipated (i.e. absorbed to generate new crack surfaces, that is dominant

before peak load) or emitted (more efficiently recorded by AE, and linked to the elastic recoil instabilities ruling the post-peak phase) along the test.

Li et al. (2007) have used the AE technique to investigate the crack path on asphalt mixtures using SCB specimens. They report the formation of the FPZ beyond $0.7P_{max}$ and could identify its migration along the crack line in the post-peak region of the test. In our case, based on the hypocentres location of *p*CT testing, we see that it is also possible to track the development of the fracture, which starts from the notch tip. The distribution of AE events suggests that the FPZ of Arcera sandstone is wider than the one of Pinacas (~5-7 mm wide for Pinacas Sst and ~6-10 mm for Arcera Sst) sandstone. Wide FPZ bands like the one reported for Arcera have been observed by different authors like Wei et al. (2016), who inform about a ~8-10 mm FPZ width for a SCB test of the Dazhou sandstone. To this respect, it is interesting to quote that the Arcera and Dazhou sandstones have similar fracture toughness values: K_{IC} ~ 0.3-0.5 MPa $m^{1/2}$ for Arcera, and K_{IC} = 0.56 MPa $m^{1/2}$ for Dazhou.

5.5.3. Frequency assessment

Peak frequencies of the AE events in stage I are mainly in the range ~100-200 kHz, although some signals up to 300 kHz are also detected for the *p*CT tests. This low-frequency band (Band-I) is present along the whole duration of the tests and, as bulk, it has low process discrimination capability. However, futher insight can be gained by grouping the events in this first band according to their A_{norm}, as we will discuss below. In stage II we observe that, since ~$0.5P_{max}$, a new range of intermediate frequency values (f_{peak} ~300-600 kHz) manifests. Because of the selectivity in its appearance, in a first approach we could attribute this frequency range to a true damage taking place in the rock. In stage III the analysis of f_{peak} in both *p*CT and SCB tests allows to identify the rise of a new bulk f_{peak} fringe (~600-800 kHz) that, like in the previous stage, is deemed to represent true rock damage. This fringe is located in the peak frequency flat-response band of the sensor, where sensitivity attains its maximum. In stages IV and V no new frequency bands manifest while the medium- and higher-end components tend to be attenuated as the test advances. In ultrasonic monitoring of uniaxial

compression tests, Shirole et al. (2020) reported the limited capability of the ultrasonic transducers with low dominant frequency (and large associated wavelength) to characterize the damage evolution in the rock. This would explain the low discrimination sensibility of Band-I in our experiments, and the enhanced sensibility with increasing f_{peak}.

It is attractive to link frequency band ranges to specific values taking the *P*-LPD model as reference (crack closing, microcrack stable growth, etc.). However, a careful observation reveals first order inconsistencies that prevent a trustworthy connection between these “bulk” ranges and the characteristic process operating. For instance: Although we conjecture that microcrack growth and propagation is the leading mechanism in stage III, the absence of high frequencies before P_{max} in the *p*CT test challenges the well-known relationship that connects high frequency with microcracking (Ohnaka and Mogi 1982; Landis and Shah 1995; Carpinteri et al. 2016; Zhang 2018). What is more, the low frequency band, usually associated with macroscopic fracturing, develops not only during the post peak region (when it would be expected to appear) but along the whole duration of the test. In order to reconcile the expectations with the experimental observations, it is necessary to observe in detail the information provided by each specific sensor, since some slight differences in results were detected considering their location with respect to the notch tip (Figure 5.4A and Figure 5.5A). For each frequency band, we see that, while the monitoring channels far from the notch tip display an average constant frequency all along the test, the ones closer to the AE sources do not. In fact, we notice that for the latter sensors signals loose higher frequency components inside Bands-II and III as the test advances and a higher damage level is attained (i.e. when unstable cracking and fracturing is taking place). Because the sensors used in all the tests have been always of the same brand and model, we can discard the heterogeneity in their response as a likely explanation for this inequality.

The effect of acoustic attenuation, which intensifies at high frequency levels (Winkler and Murphy 1995), is clearly evidenced in the f_{peak} *vs.* A_{norm} plots (Figure 5.4B and Figure 5.5B). Similarly, Shirole et al. (2020) also detected a progressive attenuation of the amplitude and mean frequency of the waves at high stress

levels, showing the sensibility of both parameters to detect the presence of damage in the rock, i.e. to track the initiation and propagation of cracks. In our experiments, attenuation is not only observed for sensors placed at different distances from the source of events, but also for the values recorded for each particular sensor: the higher the peak frequency, the lower the amplitude. From this perspective, we could expect that at low frequency levels it would be possible to detect the acoustic signals produced by any kind of process taking part in rock fracture. Contrary, at high (and even intermediate) f_{peak} values part of the events would remain hidden, and only the most energetic signals would be captured. This could explain the gradual appearance of the three frequency bands in our experiments: while Band-I, which would include both low and high energetic events, develops all along the tests, Band-II and Band-III, probably associated with events of higher energy (i.e. microcrack growth, coalescence, or macrocrack propagation), emerge at specific stages of the *P*-LPD curve. In the case of the *p*CT specimen of Pinacas sandstone, we see that the high amplitude events in Band-I (group LH) appear concurrently to those in Band-II (Figure 5.4C). This would suggest a close relationship between both types of events, and even with those in Band-III, considering that a similar trend is observed for the mean values and scattering of Band-II and Band-III, and even LH signals (Figure 5.4D). Another interesting feature observed in the previous test is the increase in scattering with time for events in group LH and Band-II, especially evident during the post-peak region. Scattering occurs when the size of the heterogeneities is within the range of the acoustic wavelength ($\lambda = v / f_{peak}$; v is the wave propagation velocity in the material) (Winkler and Murphy 1995). Considering that the rock matrices used in this study are homogeneous, and that their properties remain sufficiently constant during the tests (i.e., v ~ 1200 and 2000 m/s for Arcera and Pinacas Sst, respectively), we can compute the λ associated to each peak frequency band: for Arcera Sst, λ ~ 6, 3, and 2 mm for Band-I, Band-II, and Band-III, respectively; for Pinacas Sst, λ ~ 10, 4, and 3 mm for Band-I, Band-II, and Band-III, respectively. We interpret the progressive increased scattering observed during the stages IV and V (i.e. unstable crack growth) for the intermediate- and low- frequency bands as the result of growing defects of

medium (3-4 mm) and large (6-10 mm) size. Interestingly, these values are within the range of the estimated dimensions of the FPZ from the AE location of events (see section 5.5.2). Similarly, the large scattering produced at high frequencies all along the post-peak region would reflect sustained small-size damage starting immediately right after P_{max}. It is worth to remember that f_{peak} is a parameter that is automatically computed via Fast Fourier Transform of the raw transients recorded above a certain minimum amplitude threshold. However, transient waveforms may overlap like may also the processes originating the AE events. To this respect, when using it in complex matrices (like many rocks) we should expect a limited ability for process identification. The rock matrices used in this study are homogeneous and the nature of the processes involved in the tests focus the acoustic cracking phenomena in a narrow volume. That provides an adequate environment for the type of analyses made before.

5.5.4. AF vs. RA ratios

According to the AF:RA ratio, the AE events developed in stages I, II and III would be dominantly tensile. However, the growth of the macroscopic cracks would be characterised by a combination of tensile and shear modes. Backers et al. (2005), in a study using sandstones, classified the AE source types based in the average polarity of the acoustic signals (i.e. tensile, shear, or pore-collapse). Their results show that macrocrack propagation under pure tensile conditions includes the formation of tensile cracks but also shear cracks. This is in line with the work of Wang et al. (2017) that have reported that the generation of shear cracks also in a dominant tensile regime. In the fracture toughness tests performed, where the tensile component should be dominant according to the orientation of the major stress components, shearing appears in the post-peak region, when the fracture nucleates due to the convergence of micro-mesocracks. It is interesting to note that, in sandstone rocks and under dry conditions, the orientation of cracks will depend on features such as mineralogy, grain size, cementation and homogeneity. If the energy needed to crack a single grain is greater than to fissure the cement, the cracking line will follow a tortuous path, mainly around the grain boundaries. Due to that, the orientation of the crack

plane will not be necessarily orthogonal to the tensile load what may conduct to local shearing. This out-off plane development may also conduct to geometric features like those illustrated in Figure 5.6: a) the progressive deviation of the crack plane (e.g., Pinacas Sst), and b) branching in the crack plane (e.g., Arcera Sst).

5.5.5. Ib-value

The evolution of the I*b-value* along the test has significant oscillations when observed in high frequency. For instance: In the elastic stage of the SCB and *p*CT tests, we note a reduction of its value to near one followed by a recovery. Although values below unity are usually interpreted as resulting from the growth of macrocracks (Kaklis et al., 2017), neither the loading curve, the available AE parameters, or the macroscopic examination of the tested specimens support any severe damage during this stage. Although this fluctuation could be considered an artefact at first glance, Shah and Chandra Kishen (2012) reported a similar behaviour for concrete beams loaded under three-point bending, relating this decrease in the *b-value* to the friction between grains produced by crack opening at the notch tip.

According to Rao and Lakshmi (2005), in the post-peak region (unstable crack growth) a decrease and a subsequent increase in the I*b-value* would indicate microcrack formation and growth, respectively. Even before P_{max} our results for the *p*CT test show a fluctuation of the I*b-value* (between ~1.4-1.9) with a general trend to decrease, that may indicate a continuous generation and propagation of microcracks. Afterwards (stages IV and V), the sharp oscillations at even lower values (between ~0.7-1.4, the I*b-value* is ~1 in average) could be reflecting a growing macrocrack scenario (Rao and Lakshmi, 2005). Similarly, in the SCB test we observe an increase (up to ~1.8) of the I*b-value* a few seconds before P_{max}. However, in this case it is followed by a sudden decrease (~0.5-0.6) that would be compatible with the unstable cracking that follows P_{max}. This is supported by the high amount of energy released at this moment (Landis and Baillon 2002).

5.6. Conclusions

Mode I fracture toughness tests performed with the *p*CT method and two different sandstone materials offer more consistent and comprehensive information than those made with SCB tests. That includes both the mechanical and acoustical aspects. From a methodological standpoint and, in line with the contributions made by other authors, we observe a significant dependence of the intensity of signals received and the location of the AE sensor. However, their evolution is consistent for all the sensors what suggest that the rock behaves homogeneously.

Damage evolution in the tested samples is compatible with the five-stage model of Martin and Chandler (1994) for brittle rocks under small-strain conditions as well as that of Mogi (2007) based on AE activity. The qualitative evolution of E_{AE} illustrates well the mechanical process occurring in the tested samples, with net rate changes (acceleration/deceleration) coinciding well with the mechanical transitions observed. However, the sharp stage-limits identified from the linear portions of the *P*-LPD curves are more diffuse when looking to AE data. That suggests that boundaries such as that of crack initiation or crack damage should not envisaged as a constant or intrinsic property values.

Likewise, the analysis of peak frequencies in the tests performed reveals apparent inconsistencies with generally accepted behaviour (i.e. high frequencies are expected in connection with microcrack development while low ones with fracturing). However, considering the effect of acoustic attenuation it is possible to relate the appearance/disappearance of signals with specific characteristics (f_{peak} and A_{norm}) with the facture processes occurring at different stress levels. In addition, the increased scattering at certain frequency ranges could be linked to the size of the growing defects.

The parametric analysis based in the AF *vs*. RA ratios, although simple, provides interesting information regarding the cracking modes associated with the AE events. Based on this analysis we confirm that the dominant cracking mode in the *p*CT tests is tensile and only after P_{max} has been overcome a mixed-mode (tensile-shear) appears in a limited extent. This approach, that is very

useful for screening purposes, has a limited scope in general cases as it does not identify compressive events. The appearance of a non-tensile cracking mode in a quasi-pure tension test (*p*CT) may be explained by the type of the rock and properties. Thus, from an energetic point of view, if cracking requires less energy to advance through the cement than across grains, that will be the preferred cracking path. That determines a greater tortuosity in the development of the crack plane and to the easier development of shear components. Furthermore, this may also explain the observed deviation and branching features observed in some of the tested rocks.

The analysis of the I*b-values* also let us identify a relevant potential to discern the onset separating the stable and unstable crack growth. Anyhow, more specific filtering techniques are required to perform a more detailed analysis.

5.7. References

Aggelis DG, Philippidis TP (2004) Ultrasonic wave dispersion and attenuation in fresh mortar. *NDT & E International* 37:617–631

Aldahdooh MAA, Muhamad Bunnori N (2013) Crack classification in reinforced concrete beams with varying thicknesses by mean of acoustic emission signal features. *Construction and Building Materials* 45:282–288

ASTM (1997) Standard guide for mounting piezoelectric acoustic emission sensors, E650-97. In: Annual Book of ASTM Standards. ASTM International, West Conshohocken, PA

Backers T (2004) Fracture toughness determination and micromechanics of rock under mode I and mode II loading. PhD thesis, University of Potsdam, Potsdam, Germany

Backers T, Stanchits S, Dresen G (2005) Tensile fracture propagation and acoustic emission activity in sandstone: The effect of loading rate. *International Journal of Rock Mechanics and Mining Sciences* 42:1094–1101

Carpinteri A, Lacidogna G, Accornero F, Mpalaskas AC, Matikas TE, Aggelis DG

(2013) Influence of damage in the acoustic emission parameters. *Cement and Concrete Composites* 44:9–16

Carpinteri A, Lacidogna G, Corrado M, Di Battista E (2016) Cracking and crackling in concrete-like materials: A dynamic energy balance. *Engineering Fracture Mechanics* 155:130–144

Chen G, Sun X, Wang J, Wang D, Zhu Z (2020) Detection of cracking behaviors in granite with open precut cracks by acoustic emission frequency spectrum analysis. *Arabian Journal of Geosciences* 13:258

Farnam Y, Geiker MR, Bentz D, Weiss J (2015) Acoustic emission waveform characterization of crack origin and mode in fractured and ASR damaged concrete. *Cement and Concrete Composites* 60:135–145

Feignier B, Young RP (1992) Moment tensor inversion of induced microseisnmic events: Evidence of non-shear failures in the −4 < M < −2 moment magnitude range. *Geophysical Research Letters* 19:1503–1506

Fowell RJ, Hudson JA, Xu C, Chen JF (1995) Suggested Method for Determining Mode-I Fracture-Toughness Using Cracked Chevron-Notched Brazilian Disc (CCNBD) Specimens. *International Journal of Rock Mechanics and Mining Sciences & Geomechanics Abstracts* 32:57–64

Graham CC, Stanchits S, Main IG, Dresen G (2010) Comparison of polarity and moment tensor inversion methods for source analysis of acoustic emission data. *International Journal of Rock Mechanics and Mining Sciences* 47:161–169

Irwin GR (1958) Fracture. In: Handbook on physics. Springer Verlag, Berlin, pp 551–590

Ishida T, Labuz JF, Manthei G, Meredith PG, Nasseri MHB, Shin K, Yokoyama T, Zang A (2017) ISRM Suggested Method for Laboratory Acoustic Emission Monitoring. *Rock Mechanics and Rock Engineering* 50:665–674

JCMS-III B5706 (2003) Monitoring method for active cracks in concrete by

acoustic emission

Kaklis K, Mavrigiannakis S, Saltas V, Vallianatos F, Agioutantis Z (2017) Using acoustic emissions to enhance fracture toughness calculations for CCNBD marble specimens. *Frattura ed Integrità Strutturale* 11:1–17

Kuruppu MD, Obara Y, Ayatollahi MR, Chong KP, Funatsu T (2014) ISRM-suggested method for determining the mode I static fracture toughness using semi-circular bend specimen. *Rock Mechanics and Rock Engineering* 47:267–274

Kwiatek G, Charalampidou EM, Dresen G, Stanchits S (2014) An improved method for seismic moment tensor inversion of acoustic emissions through assessment of sensor coupling and sensitivity to incidence angle. *International Journal of Rock Mechanics and Mining Sciences* 65:153–161

Labuz JF, Biolzi L (1998) Characteristic strength of quasi-brittle materials. *International Journal of Solids and Structures* 35:4191–4203

Landis EN, Baillon L (2002) Experiments to Relate Acoustic Emission Energy to Fracture Energy of Concrete. *Journal of Engineering Mechanics* 128:698–702

Landis EN, Shah SP (1995) Frequency-Dependent Stress Wave Attenuation in Cement-Based Materials. *Journal of Engineering Mechanics* 121:737–743

Lei X, Kusunose K, Rao MVMS, Nishizawa O, Satoh T (2000) Quasi-static fault growth and cracking in homogeneous brittle rock under triaxial compression using acoustic emission monitoring. *Journal of Geophysical Research: Solid Earth* 105:6127–6139

Li X, Marasteanu M, Iverson N, Labuz J (2007) Observation of Crack Propagation in Asphalt Mixtures with Acoustic Emission. *Transportation Research Record: Journal of the Transportation Research Board* 1970:171–177

Lin Q, Wang S, Wan B, Lu Y, Wang Y (2020) Characterization of Fracture Process in Sandstone: A Linear Correspondence Between Acoustic

Emission Energy Density and Opening Displacement Gradient. *Rock Mechanics and Rock Engineering* 53:975–981

Lockner D (1993) The role of acoustic emission in the study of rock fracture. *International Journal of Rock Mechanics and Mining Sciences & Geomechanics Abstracts* 30:883–899

Martin CD, Chandler NA (1994) The progressive fracture of Lac du Bonnet granite. *International Journal of Rock Mechanics and Mining Sciences and* 31:643–659

McLaskey GC, Lockner DA (2018) Shear failure of a granite pin traversing a sawcut fault. *International Journal of Rock Mechanics and Mining Sciences* 110:97–110

Mix PE (2005) Introduction to Nondestructive Testing. A Training Guide. Second Edition. Wiley-Interscience

Mogi K (2007) Experimental Rock Mechanics. Taylor & Francis, London

Molenda M (2015) Acoustic Emission monitoring of laboratory scale hydraulic fracturing experiments. PhD thesis, Ruhr-University Bochum, Bochum, Germany

Moradian Z, Einstein HH, Ballivy G (2016) Detection of cracking levels in brittle rocks by parametric analysis of the acoustic emission signals. *Rock Mechanics and Rock Engineering* 49:785–800

Muñoz-Ibáñez A, Delgado-Martín J, Costas M, Rabuñal-Dopico J, Alvarellos-Iglesias J, Canal-Vila J (2020) Pure mode I fracture toughness determination in rocks using a pseudo-compact tension (pCT) test approach. *Rock Mechanics and Rock Engineering* 53: 3267-3285

Muñoz-Ibáñez A, Delgado-Martín J, Juncosa-Rivera R (*subm.*) Experimental investigation on the size and other effects on mode I fracture toughness in selected rock types using the *p*CT and SCB testing methods. *International Journal of Rock Mechanics and Mining Sciences*

Nasseri MHB, Mohanty B, Young RP (2006) Fracture toughness measurements and acoustic emission activity in brittle rocks. *Pure and Applied Geophysics* 163:917–945

Ohnaka M, Mogi K (1982) Frequency characteristics of acoustic emission in rocks under uniaxial compression and its relation to the fracturing process to failure. *Journal of Geophysical Research: Solid Earth* 87:3873–3884

Ohno K, Ohtsu M (2010) Crack classification in concrete based on acoustic emission. *Construction and Building Materials* 24:2339–2346

Ohtsu M (2010) Recommendation of RILEM TC 212-ACD: Acoustic emission and related NDE techniques for crack detection and damage evaluation in concrete: Test method for classification of active cracks in concrete structures by acoustic emission. *Materials and Structures/Materiaux et Constructions* 43:1187–1189

Ouchterlony F (1989) Fracture toughness testing of rock with core based specimens, the development of an ISRM standard. *Fracture Toughness and Fracture Energy* 231–251

Proverbio E (2011) Evaluation of deterioration in reinforced concrete structures by AE technique. *Materials and Corrosion* 62:161–169

Rao MVMS, Lakshmi KJP (2005) Analysis of b -value and improved b -value of acoustic emissions accompanying rock fracture. *Curreent Science* 89:1577–1582

Rodríguez P (2016) Applications of acoustic emission monitoring to the assessment of structural integrity of rocks. In: 22nd International Congress on Acoustics

Shah SG, Chandra Kishen JM (2012) Use of acoustic emissions in flexural fatigue crack growth studies on concrete. *Engineering Fracture Mechanics* 87:36–47

Shirole D, Hedayat A, Ghazanfari E, Walton G (2020) Evaluation of an Ultrasonic

Method for Damage Characterization of Brittle Rocks

Spasova LM, Ojovan MI, Scales CR, Robert S, Building H, Solutions N (2007) Acoustic Emission Technique Applied for Monitoring and Inspection of Cementitious Structures Encapsulating Aluminium. *Journal of Acoustic Emission* 25:51–68

Stanchits S, Mayr S, Shapiro S, Dresen G (2011) Fracturing of porous rock induced by fluid injection. *Tectonophysics* 503:129–145

Tsangouri E, Aggelis D, Matikas T, Mpalaskas A (2015) Acoustic Emission Activity for Characterizing Fracture of Marble under Bending. *Applied Sciences* 6:6

Vallen (2017) AMSY-6 Operation Manual

Wang M, Tan C, Meng J, Yang B, Li Y (2017) Crack classification and evolution in anisotropic shale during cyclic loading tests by acoustic emission. *Journal of Geophysics and Engineering* 14:930–938

Wei MD, Dai F, Xu NW, Zhao T (2018) Experimental and numerical investigation of cracked chevron notched Brazilian disc specimen for fracture toughness testing of rock. *Fatigue & Fracture of Engineering Materials & Structures* 41:197–211

Wei MD, Dai F, Xu NW, Zhao T, Xia KW (2016) Experimental and numerical study on the fracture process zone and fracture toughness determination for ISRM-suggested semi-circular bend rock specimen. *Engineering Fracture Mechanics* 154:43–56

Winkler KW, Murphy WF (1995) Acoustic Velocity and Attenuation in Porous Rocks. In: Rock Physics and Phase Relations: A Handbook of Physical Constants. pp 20–34

Zang A, Wagner FC, Stanchits S, Dresen G, Andersen R, M.Haidekker (1998) Source analysis of acoustic emission in Aue granite cores under symmetric and asymmetric loads. *Geophysical Journal International* 135:1113

Zhang G, Li H, Wang M, Li X, Wang Z, Deng S (2019) Crack-induced acoustic emission and anisotropy variation of brittle rocks containing natural fractures. *Journal of Geophysics and Engineering* 16:599–610

Zhang J (2018) Investigation of Relation between Fracture Scale and Acoustic Emission Time-Frequency Parameters in Rocks. *Shock and Vibration* 2018:1–14

Zhang Q, Duan K, Xiang W, Yuan S, Jiao Y (2018) Direct Tensile Test on Brittle Rocks with the Newly Developed Centering Apparatus. *Geotechnical Testing Journal* 41:92–102

Zhao S, Zhang Q, Liu L (2019) Crack Initiation, Propagation, and Coalescence Experiments in Sandstone Brazilian Disks Containing Pre-Existing Flaws. *Advances in Civil Engineering* 2019:1–11

6. Conclusions and future work

6.1. Conclusions

The main aim of this doctoral work was to deepen into the knowledge of stable crack propagation in rock materials by developing a new testing method (pseudo-compact tension, *p*CT) for the assessment of mode I fracture toughness. The *p*CT test uses disc-shaped specimens loaded under pure tensile conditions. Tests are performed at ambient conditions and slow loading rate in a specially designed testing device of high stiffness and high strength. Four different rock types (three sandstones and one granite) were used to assess their corresponding K_{IC}. In order to check mutual consistency, results were compared with those obtained using one of the suggested methods proposed by the International Society for Rock Mechanics (ISRM), the semi-circular bend (SCB) test. We chose the SCB as a benchmark method due to its popularity, simple sample preparation, and straightforward testing configuration. Based on the results of 146 tests performed using the *p*CT and SCB methodologies, we assessed size-, notch length- and rock type-effects on K_{IC}. For each test, we used the corresponding load-displacement curves to characterize the energy content of the fracture process. Some selected *p*CT and SCB tests were complemented with the concurrent monitoring of acoustic emission (AE) activity using a multichannel AE system. Based on that information, we explored the relationship between the energy release associated to the fracture process and that captured by AE (E_{AE}), as well as the evolution of different AE parameters (e.g., amplitude or peak frequency) along the experiments. Using the AE data we also assessed the cracking modes (tensile/shear) using a parameter-based strategy (AF:RA ratio), and we explored the potential of the I*b-value* to discriminate cracking

processes. Finally, the multi-sensor array allowed determining the location of the AE hypocentres and the evolution of the fracture process zone (FPZ) as a function of the testing time. From this study the following conclusions are drawn:

- The *p*CT method is convenient for the assessment of K_{IC} of both fragile and ductile rocks due to the combination of small displacement, high load capacity and high stiffness of the testing system.
- In contrast with the four methods suggested by the ISRM for determining K_{IC}, the *p*CT test has favourable features such as simple specimen geometry and minimal machining requirement (straight groove and thin starter notch), small sample volume, direct generation of tensile loads, and enhanced control of crack propagation even beyond the peak strength. All these features convert the *p*CT method in an interesting candidate for routine fracture toughness testing.
- The *p*CT specimens yield more consistent K_{IC} values than the SCB specimens, especially for harder materials, suggesting that the presence of the FPZ would be less influential in *p*CT testing due to the comparatively larger ligament length of the *p*CT specimens.
- The *p*CT method offers good testing control before and even beyond the peak load, enabling to study the post-peak behaviour of the material and providing more comprehensive and detailed results. In this regard, a greater wealth of fracture mechanics information (e.g., energy evolution) and AE data can be obtained from a single test in comparison with the SCB test. For instance, not only the energy needed to initiate the crack (pre-peak energy) can be determined but also the energy required for subsequent crack propagation (post-peak energy).
- The simpler loading configuration of the *p*CT test makes the access to crack mouth opening displacement (CMOD) data easier, even for small-size specimens. What is more, the good correlation found between LPD and CMOD makes possible the direct assessment of CMOD without employing direct contact transducers such as clip gauges. In turn, this is not possible with the SCB.

- Both specimen size and notch length have an impact on K_{IC} although the magnitude of these effects is closely related to lithology, being less influential for weakly cemented rocks. In fact, rock properties such as the grain size and particle arrangement were found to determine the point of generation of the crack at the notch tip and its propagation path during testing. Although K_{IC} was found to be positively related to the specimen size and negatively related to the notch length, the size effect has a lesser impact in the *p*CT compared with the SCB method. The variability induced by the notch length ratio over K_{IC} is less important than the effect of sample size in SCB testing. However, the lithology may magnify both effects, with the harder materials showing higher dependency.
- Tensile strength and mode I fracture toughness obtained from *p*CT experiments were found to be strongly correlated.
- From the energy assessment of the *p*CT tests, a good linear correlation was found between the pre- and post-peak fracture energies with respect to the total energy. The similarity between pre- and post-peak energies suggests that the same level of energy is required to initiate the fracture and to propagate it with independence of the lithology, sample size, and notch length.
- No clear relationship was found between fracture energy and AE energy (E_{AE}) neither in the *p*CT nor in the SCB tests.
- In general, the qualitative evolution of E_{AE} illustrates well the mechanical processes occurring in the tested samples, with net rate changes (acceleration/deceleration) coinciding well with the mechanical transitions.
- The location of the AE hypocentres was useful to analyse the evolution and propagation of the crack along the ligament length. As expected, at peak load the events were mainly located around the notch tip for both testing methods. In the post-peak region of the *p*CT tests, the distribution conforms a vertical crack, which slightly deviates or increases lateral spread (depending on the material) as the rock loses cohesion in the

later stage of the experiments. These observations are consistent with the macrocracks observed in the specimens after testing. In the SCB tests, the results for the harder material (Pinacas sandstone) evidence the upwards migration of the AE events from the notch tip up to the top roller at specimen failure. However, for the softer material (Arcera sandstone) we observe a progressive damage in the area next to the loading end that originates an oblique macrocrack. This evidences the potential of the AE technique to better understand the processes associated with fracture toughness testing. In addition, from the location of the AE events it was possible to determine the approximate dimensions of the FPZ.

- The analysis of peak frequencies (f_{peak}) reveals apparent inconsistencies with generally accepted behaviour (i.e. high values are expected in connection with microcrack development and low values with fracturing). However, considering the effect of acoustic attenuation it is possible to relate the appearance/disappearance of signals with specific f_{peak} and normalized amplitude (A_{norm}) with the facture processes occurring at different stress levels. In addition, the increased scattering at certain frequency ranges could be linked to the size of the growing defects.
- The tensile mode is predominant in the pre-peak and late post-peak stages of the *p*CT tests according to the parametric analysis based in the AF *vs*. RA ratios. Only in the early post-peak region, where the macroscopic cracks grow due to the convergence of micro-mesocracks, a mixed-mode (tensile/shear) appears in a limited extent. The appearance of a non-tensile cracking mode may be explained by the type or rock and properties (e.g., mineralogy, grain size, cementation or homogeneity) which determine the orientation of the crack. According to this, if cracking requires less energy to advance through the cement than across grains, the crack plane might not be orthogonal to the tensile load and may conduct to local shearing due to the increase in tortuosity. This is supported by the geometrical features (deviation and branching in the crack plane) observed in the location of the AE events, as well as in the

X-ray micro tomography. The analysis of the I*b-values* let us identify a relevant potential to discern the onset separating the stable and unstable crack growth. Anyhow, more specific filtering techniques are required to perform a more detailed analysis.

6.2. Methodological considerations

Here we draw attention to some methodological considerations emerged during the experimental work. We present some recommendations for performing *p*CT and SCB methods, as well as two common evidences.

6.2.1. pCT method

i) It is advisable to use medium-sized (D = 50 mm) *p*CT specimens with a relatively large notch length ratio (a/b > 0.25) to obtain more consistent K_{IC} results.

ii) It should be noted that the expression of the dimensionless stress intensity factor derived for the *p*CT specimen geometry and loading configuration was computed assuming an isotropic rock material. Further work is needed to address the effect of rock anisotropy.

iii) A number of tests were considered as invalid due to specimen failure at the contact between the flat side of the steel jaws and the specimen. To reduce the stress concentration in this area, it would be suggested to include a pair of thin high-strength steel rollers along the jaws, so that the applied load would be distributed linearly along the U-shaped groove throughout the test.

iv) The testing configuration of the *p*CT test allows keeping the samples immersed into a fluid bath, and therefore saturated, all along the experiments. This feature makes the *p*CT test suitable for studying the potential impact of saturating fluids on K_{IC}.

v) The good correlation between load point displacement (LPD) and crack mouth opening displacement (CMOD) allows the direct assessment of CMOD in *p*CT tests without employing clip gauges or other direct contact transducers on the specimen. This is especially

advantageous when the space is limited, such as in small-size samples or specimens immersed in fluid during testing.

6.2.2. SCB method

i) Imprecisions in sample preparation (coring, cutting, notching) and/or inaccurate alignment of the specimen in the testing jig may induce a mixed mode I/II (tensile/shear) fracture toughness behaviour instead of the expected mode I (tensile). This was also evidenced by the location of the AE hypocentres.

ii) We report the propensity of the SCB testing configuration to lateral sliding of the specimen over the bottom (support) rollers as a consequence of applying a distributed force on the circular loading surface of the sample. To avoid this situation, it is crucial that the load is applied exactly along the vertical radii of the specimen, that is, it is needed a perfect vertical alignment between the notch tip and the loading line (defined by the contact point of the top roller). Due to sliding, the measurement of CMOD as performed in this work (i.e., with two LVDTs facing each other along the diametral plane of the specimen, perpendicularly to the notch plane) is not straightforward. The use of clip gauges would be an alternative to circumvent this problem, but its use is limited to medium- or large-size samples.

iii) It is apparent that the performance of SCB methodology in the post-peak region is poorer in comparison with the *p*CT test: at the peak load, all the energy stored is released suddenly and fast crack growth occurs. As a consequence, the SCB configuration makes it impossible to access to Level II testing. Although it can be argued that better quality results may be obtained by improving the characteristics of the testing system (in terms of control electronics and stiffness to avoid elastic energy storage in the device), we consider that the key point is the way the fracture energy is delivered to the tested sample. In the SCB specimen, energy is not only stored in the area surrounding de crack tip but also at the contact point of

the rollers and along the ligament length, involving a significantly larger sample volume than the *p*CT configuration, in which the load is transferred from the contact line to the pulling jaws directly to the starter notch.

6.2.3. General considerations

i) Our results show that the influence of specimen size or notch length on K_{IC} is subsidiary of the rock type. Consequently, we consider that not only the geometric constrains but also the characteristics of the rock tested must be considered for setting up the minimum requirements for specimen size in fracture toughness testing.

ii) In line with previous contributions, we observed that the intensity of the acoustic signals recorded highly depends on the location of the AE sensors. The consistent evolution observed in this study for all the sensors involved in data acquisition suggests that the two sandstones (Arcera and Pinacas) could be considered isotropic and homogenous. However, the effect of attenuation may be frequency selective, what must be considered for the proper scaling of the AE energy to compare with the values derived from mechanical tests.

6.3. Future work

During the discussion of the results, some aspects could not be satisfyingly explained or remained unconsidered. In the following, possible future research topics are outlined:

- In this study it was not possible to determine the minimum specimen size that provides consistent K_{IC} results for the *p*CT method. In order to verify the convergence of K_{IC}, it would be suggested to follow this line of work by testing specimens with diameters above 100 mm. Similarly, it is expected that using *p*CT specimens with notch length ratios larger than those tested here would result in a higher rate of success of the experiments. Further testing would be advisable in this sense.

- Although no apparent correlation between the fracture and the acoustic emission energies was identified in the present survey, we cannot discard eventual relationships. It is reasonable to assume that both magnitudes might be related since the AE energy is proportional to the number and magnitude of growing cracks (i.e. rock damage). Therefore, we consider necessary to carry out further research with a more comprehensive AE database.
- In this contribution, only level I tests were reported. However, the features and characteristics of the testing equipment, which allow controlling crack propagation in the post-peak region, makes the *p*CT method also feasible for level II testing. Due to the inherent complexity of certain matrices like rocks and other brittle engineering materials (e.g. concrete), we believe that it is advisable to take into consideration the properties considered in level II testing, especially when more sophisticated non-linear fracture mechanics models are to be applied.
- In this study, we assessed the influence of specimen size, notch length, and lithology on K_{IC}, and a first approach to the effect of saturating fluids was also presented. In addition, it would be necessary to study the influence of other factors potentially affecting K_{IC} such as loading rate, confining pressure, anisotropy or temperature,.
- The use of high resolution digital image (micro CT scanning) during the fracture toughness experiments could be useful to better understand the fracture processes conducting to rock failure.
- The applicability of the *p*CT methodology to other fields of potential interest (i.e. cementitious materials, bituminous mixtures, ceramics, plastics, etc.) could be explored.

APPENDIX A: Extended abstracts in Spanish and Galician

A1. Resumen extendido

Todos los materiales contienen defectos como poros o grietas, que pueden desarrollarse durante su vida útil o incluso ser inherentes a su naturaleza. Los criterios de rotura más simples asumen que todos los materiales son perfectamente homogéneos, isótropos y libres de defectos. Según esto, una muestra se romperá cuando la tensión supere la resistencia última del material. Sin embargo, esto no suele ocurrir en la realidad, ya que la inevitable presencia de discontinuidades o defectos que puede generar concentración de tensiones de manera localizada, reduciendo la resistencia general del material y conduciendo a una rotura prematura e inesperada. La necesidad de conocer estos procesos con mayor profundidad originó el desarrollo de la mecánica de la fractura. Al contrario que los enfoques más tradicionales, la mecánica de la fractura tiene en cuenta el tamaño de los defectos en la evaluación de la resistencia a la rotura. El objetivo principal de esta rama es, por tanto, cuantificar la relación crítica que existe entre la tensión aplicada y el tamaño del defecto que producirá la rotura antes de que se alcance la resistencia última del material. La propiedad que une estos dos parámetros (tensión y tamaño del defecto) y por tanto mide la resistencia de un material a la propagación de una fisura se conoce como tenacidad de fractura (K_C). La mecánica de fractura distingue tres modos básicos de carga: a) modo I, o modo de apertura/tracción; b) modo II, o modo de cortante en el plano/deslizamiento; y c) modo II, o modo de cortante fuera del plano/cizalladura.

En mecánica de rocas, predecir la rotura es una de las mayores preocupaciones. Sin embargo, es básico considerar que las rocas son materiales

discontinuos a todas las escalas. Por ejemplo, a escala microscópica, contienen discontinuidades como poros, granos o microfisuras, que pueden producir altas concentraciones de tensión bajo carga. En rocas, la resistencia a tracción es comparativamente más baja que la resistencia a compresión o cortante. Por tanto, la tenacidad de fractura en modo I (K_{IC}) es uno de los parámetros más importantes y más estudiados en la mecánica de fractura aplicada a rocas: cuanto más alto sea el valor de K_{IC}, más alta será la resistencia a la propagación de fracturas a tracción.

La tenacidad de fractura puede tener una importancia crucial en los proyectos que involucren materiales rocosos, como en ingeniería térmica (por ejemplo, la energía geotérmica o la gestión de residuos radioactivos), mecánica (por ejemplo, la estabilidad de estructuras mineras), hidráulica/química (por ejemplo, la fracturación hidráulica, el almacenamiento geológico de CO_2 o la gasificación subterránea del carbón), o de procesos (por ejemplo, la perforación y corte de rocas, o la trituración de minerales). En los últimos años, la investigación de los procesos de inicio y propagación de fracturas en materiales geológicos ha ganado importancia debido a la necesidad de resolver problemas de fracturación en geofísica. En particular, la creciente demanda de hidrocarburos ha favorecido la investigación de los procesos de fracturación en ciertas litologías (por ejemplo, areniscas compactas o pizarras). Por este motivo, es esencial desarrollar métodos de ensayo apropiados que ayuden a mejorar la precisión en los valores de tenacidad de fractura. La Sociedad Internacional para la Mecánica de Rocas (ISRM) ha propuesto cuatro métodos de ensayo para determinar K_{IC} usando muestras cilíndricas, llamados '*short rod*' (SR), '*chevron bend*' (CB), '*cracked chevron notched Brazilian disc*' (CCNBD) y '*semi-circular bend*' (SCB). Sin embargo, estos métodos pueden ser difíciles de aplicar de manera rutinaria debido a aspectos como: a) las bajas cargas a las que se produce la rotura, que obligan a tener un excelente control de ensayo; b) el tamaño de muestra que requieren es relativamente grande (CB); c) la preparación de las muestras es difícil y problemática (SR, CB y CCNBD); d) el cálculo del factor de intensidad de tensiones es impreciso (CCNBD); e) la generación de cargas de tracción se realiza de manera indirecta a través de la

compresión de la muestra (especialmente en SCB y CCNBD); y f) la propagación de la fractura se produce muy rápidamente una vez se ha alcanzado la resistencia pico.

Para superar estas limitaciones, el objetivo principal de esta tesis es desarrollar un método de ensayo alternativo y simple, denominado '*pseudo-compact tensión*' (*p*CT), que permita medir K_{IC} en rocas usando muestras cilíndricas bajo condiciones de tracción pura. El *p*CT se basa en una modificación de la probeta '*compact tensión*' (CT) descrita en el método estandarizado E399-90 de la ASTM (1997) para metales. La muestra *p*CT es un disco (con un ratio diámetro-espesor de ~2) que se puede obtener a partir de testigos de roca. Los dos agujeros que se usan en la muestra CT para aplicar la carga se han remplazado en el ensayo *p*CT por una muesca en forma de U. Además también se introduce una entalla fina que actúa como concentrador de tensiones, forzando a que ése sea el punto de inicio de la fractura. La geometría de la probeta *p*CT presenta ventajas sobre las que se utilizan en otros métodos debido a su simplicidad, pequeña cantidad de material necesario y mínima preparación. Una vez que la muestra está lista, el procedimiento de ensayo es simple y directo: la probeta se sitúa en una plataforma y se pone en contacto con un par de mordazas de acero de alta resistencia y rigidez que encajan en la muesca en U y transmiten la fuerza de tracción a la muestra. Mientras que una de las mordazas permanece inmóvil, la otra se aleja con un ritmo de desplazamiento constante. La tracción que se genera en la entalla provoca que la probeta se rompa en dos mitades simétricas. La fractura se origina en la punta de la entalla y se propaga a lo largo del diámetro vertical de la muestra, es decir, en el plano del ligamento.

Los valores de K_{IC} medidos con el ensayo *p*CT se validan comparándolos con los obtenidos con uno de los métodos sugeridos por la ISRM, el ensayo SCB. La probeta SCB es un semi-cilindro con una entalla recta cortada en el centro de su cara plana. Entre los métodos disponibles, se optó por el SCB como estándar de comparación debido a su popularidad, simplicidad (desde el punto de vista de preparación de la muestra) y configuración de ensayo directa. En este trabajo se

han usado cuatro tipos de roca distintos (areniscas de Corvio, Arcera y Pinacas, y granito Blanco Mera) para evaluar su correspondiente K_{IC} usando los dos métodos de ensayo. Todas estas rocas son prácticamente isótropas pero difieren unas de otras en su resistencia y comportamiento mecánico. Las areniscas de Corvio y Arcera tienen una resistencia relativamente baja, un tamaño de grano pequeño (< 1 mm), elevada porosidad y bajo módulo elástico. Sin embargo, la arenisca de Pinacas, a pesar de tener un tamaño de grano similar, es significativamente más dura, tiene una porosidad más baja y un módulo elástico mayor. El granito Blanco Mera es una roca homogénea de tamaño de grano medio (1-6 mm), baja porosidad y resistencia moderada.

Los testigos de roca necesarios para preparar las muestras se obtuvieron de bloques homogéneos usando una perforadora con corona de diamante. Después, los testigos se cortaron en discos con un ratio diámetro-espesor de 2 usando un disco de diamante circular. Para las muestras SCB, los discos se cortaron diametralmente en dos mitades usando una sierra para cortar azulejos modificada. En el caso de las muestras *p*CT, la muesca en U se introdujo con esta misma sierra usando un disco de diamante de 2 mm de espesor, haciendo varios cortes mientras se desplazaba la muestra de manera horizontal después de cada pasada. La posición vertical del disco, que determina la profundidad de la entalla, se fija con un husillo vertical. Con la ayuda de unos elementos de referencia (nivel laser, escuadra) y un agarre horizontal móvil se asegura el correcto alineamiento de la muestra con respecto al disco de la sierra. Para cortar la entalla fina en los dos tipos de muestra (*p*CT y SCB) se siguió un procedimiento similar, aunque en este caso la entalla se cortó con un disco de diamante más fino (1 mm de espesor) en una única pasada. Una vez preparadas, las muestras se secaron en una estufa a 60ºC por un mínimo de 24 horas.

Para llevar a cabo los ensayos *p*CT se construyó un dispositivo de ensayo especialmente diseñado para tal fin. Entre los requisitos que se tuvieron en cuenta en su diseño se incluyeron la portabilidad de la máquina (lo que supuso importantes restricciones de tamaño, peso y robustez), posibilidad de colocación de muestras de distintos tamaños garantizando la estabilidad mecánica durante

los ensayos, facilidad de instalación de los dispositivos de medida y reemplazo de los elementos dañados, y la rapidez de las operaciones complementarias (posicionamiento de la probeta, limpieza, etc.). El dispositivo de ensayo está formado por un marco de acero de alta rigidez equipado con una célula de carga de tracción/compresión de 50 kN, dos transductores diferenciales de variación lineal (LVDTs) y dos extensómetros de medición de apertura de fisura (COD). Las señales eléctricas de todos los dispositivos de medida se integran en un sistema destinado a la adquisición de datos. El movimiento de la mordaza de acero se consigue a través de un husillo que convierte en desplazamiento lineal el movimiento de rotación de un motor eléctrico paso a paso con un ángulo de paso de 1.8º (equivalente a 200 pasos por revolución). Para mejorar su rendimiento, el motor se conecta a una reductora planetaria con un ratio de reducción de 1:100. Esta configuración, aunque simple, proporciona un elevado nivel de precisión en el posicionamiento (0.018º/paso), equivalente a 0.25 µm/paso desde el punto de vista del desplazamiento lineal del husillo, que se puede mantener desde 0 a 50 kN. Los dos LVDTs, situados simétricamente a ambos lados de la probeta, miden el desplazamiento del punto de carga (LPD), que en este caso se corresponde con el desplazamiento de la mordaza móvil. Al mismo tiempo, y de manera redundante, un extensómetro de clip montado sobre un par de cuchillas unidas a las propias mordazas mide la misma magnitud. Adicionalmente, es posible montar otro extensómetro directamente en la superficie de la muestra (también a través de unas cuchillas) para medir el desplazamiento de apertura de la punta de la fractura (CMOD). Mientras que las curvas carga-desplazamiento (*P*-LPD) se registraron en todos los ensayos *p*CT, CMOD se midió sólo en 11 de ellos.

Las probetas SCB se ensayaron a flexión con tres puntos de apoyo en una prensa servo-controlada equipada con una célula de carga de 4.448,22 N. Con esta configuración, la carga se transfiere a la parte superior de la muestra a través de un cilindro de acero. Otros dos cilindros adicionales, colocados en la parte inferior, sirven para soportar la probeta. En este caso, el LPD se corresponde con el desplazamiento vertical del cilindro de carga superior. Con el objetivo de evitar los problemas inherentes a usar extensómetros de clip en

muestras de pequeño tamaño, CMOD se midió usando dos LVDTs enfrentados colocados perpendicularmente a la entalla en el plano diametral de la muestra. Hay que tener en cuenta que la geometría curva de la muestra magnifica los errores de contacto asociados con la rotación de la superficie superior durante el ensayo. Por ello, y para garantizar el contacto de los LVDTs con la muestra en todo momento, se adhirieron unas piezas en forma de T creadas con una impresora 3D en los dos extremos de la probeta. Con este método de ensayo se registraron para todos los ensayos tanto las curvas *P*-LPD como las *P*-CMOD.

Los resultados de los dos métodos de ensayo (*p*CT y SCB) se analizaron teniendo en cuenta una serie de parámetros relevantes, todos ellos con alguna influencia potencial sobre K_{IC}. Aunque la tenacidad de fractura se considera una propiedad intrínseca del material y por tanto debería ser razonablemente independiente de la geometría de las muestras y la configuración del ensayo, los valores experimentales de K_{IC} obtenidos por numerosos autores contradicen este supuesto. Por este motivo, en este estudio se ensayaron probetas, tanto *p*CT como SCB, de 38, 50 y 100 mm de diámetro para determinar el efecto del tamaño de muestra. Del mismo modo, también se tuvo en cuenta la influencia de la longitud de la entalla ensayando muestras con distintas longitudes. Todos los ensayos se realizaron a una velocidad de desplazamiento constante de 0.1 mm/min (la velocidad es baja para evitar efectos dinámicos) en condiciones ambientales de laboratorio. En este trabajo, sólo se ha considerado el Nivel I de ensayo (nivel básico). Aunque para poder calcular K_{IC} a este nivel sólo se necesita medir la carga máxima (P_{max}) durante el ensayo, para poder profundizar en el comportamiento del material se han registrado, además de la carga (P), las magnitudes de LPD y CMOD de manera continua. Desde la perspectiva de los balances de energía, la fractura se produce cuando la energía disponible para su crecimiento y propagación supera la resistencia del material. Por tanto, la tenacidad de fractura también puede verse como la tasa de liberación de energía necesaria para crear nuevas superficies de fractura en la muestra. En este estudio, las curvas carga-desplazamiento de cada ensayo se han usado para caracterizar el contenido energético del proceso de fracturación. En la metodología *p*CT, gracias al buen control del ensayo incluso después de P_{max}, la

energía total (E_{tot}) se pudo dividir en dos porciones: la energía pre-pico (E_{pre}, es decir, el trabajo realizado para inducir el inicio de la fractura en la probeta), y la energía post-pico (E_{post}, es decir, el trabajo realizado para propagar la fractura). Para poder calcular K_{IC} es necesario conocer no sólo la carga máxima (P_{max}) y la longitud de la entalla (a), sino la expresión del factor de intensidad de tensiones adimensional (Y') específico de cada geometría de muestra y condiciones de carga. Para el ensayo SCB, la expresión correspondiente (Y'_{SCB}) se puede encontrar en la literatura. Sin embargo, para nuestra configuración *p*CT, no fue posible encontrar una expresión adecuada, y fue necesario usar el método de los elementos finitos para obtener una función polinómica de cuarto grado para cada tamaño de muestra y para un rango de longitudes de entalla (Y'_{pCT}).

Para conseguir profundizar todavía más en los procesos de inicio, propagación y coalescencia de las fracturas, se empleó la técnica de emisión acústica (AE). AE es una técnica de ensayo no destructiva ampliamente usada para registrar la evolución de daño en rocas. Cuando una fractura crece, se libera energía en forma de ondas elásticas que viajan a través del material y que pueden ser registradas en tiempo real usando sensores situados sobre la superficie de la probeta. En el desarrollo de esta tesis y para algunos ensayos, la actividad acústica se registró usando hasta 8 sensores situados a distintas distancias de la entalla. La adquisición de datos se realizó con un sistema multicanal AMSY-6 de Vallen Systeme GmbH. Los sensores se colocaron sobre la probeta usando unos imanes adheridos a su superficie. En cada ensayo se registraron una serie de parámetros de AE (como cuentas, amplitud, duración o frecuencia pico) útiles para evaluar las distintas etapas y procesos, la proximidad de la rotura de la probeta, y los distintos modos de rotura (por ejemplo, usando el ratio AF:RA y el '*improved b-value*'). Además, gracias al sistema multicanal, se pudieron localizar los hipocentros de los eventos de AE a lo largo de la duración del ensayo, lo que fue útil para analizar la evolución y la propagación de las fracturas en la muestra. Usando la información de AE, también se exploró la relación entre la liberación de energía asociada a los procesos de fractura y la capturada por los sensores de AE (E_{AE}). Aunque ambas magnitudes son en líneas general diferentes (la AE puede tener dispersión y/o atenuación), aun así

podría ser posible identificar una relación formal entre las dos propiedades. De hecho, considerando que la actividad acústica es proporcional al número y magnitud de fracturas, es razonable asumir que debe haber alguna relación entre E_{AE} y la energía de fractura.

Con los datos obtenidos, se compararon los métodos *p*CT y SCB tanto desde el punto de vista de la evolución mecánica, como de la evolución de diversos parámetros de AE en distintas de etapas de ensayo. Nuestros resultados muestran que la combinación de pequeños desplazamientos (permitiendo tasas de deformación extremadamente pequeñas), elevada capacidad de carga y alta rigidez del dispositivo de ensayo hace que el ensayo *p*CT sea adecuado para el análisis de la tenacidad de fractura tanto en rocas frágiles como dúctiles. Además, la metodología de preparación de muestra más simple del *p*CT en comparación con otros métodos de ensayo lo convierte en un candidato interesante para la determinación de la tenacidad de fractura de manera rutinaria. Para las rocas ensayadas, el crecimiento de la fractura fue lento durante la duración total de los ensayos *p*CT. De hecho, para incrementar su extensión era necesario el movimiento continuo de la mordaza. Por tanto, el proceso de propagación de la fractura fue controlado en todo momento, incluso después de alcanzar la fuerza máxima, y las curvas carga-desplazamiento (*P*-*d*) se pudieron registrar de manera precisa incluso más allá de P_{max}, proporcionando una gran información sobre el comportamiento post-pico. En general, el proceso de carga se divide en tres etapas diferenciadas: (1) un periodo de crecimiento lineal de la curva (comportamiento elástico); (2) un periodo no-lineal de formación de nuevas microfisuras en el que la pendiente de la curva gradualmente decrece hasta P_{max}; y (3) un periodo de bajada durante el cual la carga disminuye mientras la fractura macroscópica se propaga a lo largo del plano del ligamento. Al contrario, y con la excepción de algunas muestras de arenisca de Corvio (una roca blanda), las curvas de carga para los ensayos SCB muestran un crecimiento casi lineal hasta la rotura repentina de la probeta a la carga pico (P_{max}). Este comportamiento evidencia que la metodología SCB no permite un buen control de ensayo más allá de (P_{max}) y que la fractura, una vez iniciada, se propaga rápidamente hacia la parte superior de la muestra. Podría

discutirse si mejorando el control electrónico y la rigidez del sistema (para evitar el almacenamiento de energía elástica en el equipo de ensayo) se podría mejorar la calidad de los resultados para el método SCB. Sin embargo, en nuestra opinión, el factor clave que determinaría su menor eficacia en la región post-pico sería el almacenamiento de energía en la muestra, que tiene lugar en un volumen significativamente más grande que el que rodea la punta de la entalla (por ejemplo, en el punto de contacto de los cilindros y a lo largo de todo el ligamento). Cuando la carga alcanza su valor máximo, toda esta energía almacenada en la muestra se libera instantáneamente y la fractura se propaga de manera incontrolada. Sin embargo, en el caso del ensayo *p*CT, la carga se transfiere a la muestra a lo largo de las líneas de contacto con las mordazas y desde ahí directamente a la entalla.

Tomando como referencia los resultados de 146 ensayos (81 *p*CT y 65 SCB), se ha comprobado la consistencia mutua de los valores de K_{IC} obtenidos usando ambas metodologías. Del mismo modo, se ha evaluado la influencia de características como el tamaño de muestra o la longitud de la entalla. Con una perspectiva amplia, se observa que, para los dos métodos de ensayo, los resultados son compatibles para cada uno de los tipos de roca. La tenacidad de fractura en modo I obtenida para los ensayos *p*CT para las areniscas de Corvio (~0.06-0.12 MPa $m^{1/2}$) y Arcera (~0.24-0.60 MPa $m^{1/2}$) es baja, lo que es consistente con su condición de rocas blandas. Sin embargo, los valores de $K_{IC,}$ tanto para la arenisca de Pinacas como para el granito Blanco Mera, son apreciablemente más altos (~1.05-1.4 MPa $m^{1/2}$). Para las mismas rocas, los resultados de los ensayos SCB son ligeramente superiores para la arenisca de Corvio (~0.07-0.18 MPa $m^{1/2}$), pero más bajos para la de Arcera (~0.26-0.46 MPa $m^{1/2}$). En el caso de la arenisca de Pinacas y el granito Blanco Mera, la dispersión en los resultados de K_{IC} es más alta que para los ensayos *p*CT (~0.69-1.64 y ~0.72-1.51 MPa $m^{1/2}$, respectivamente). La zona de procesos de fractura (FPZ, que se corresponde con el volumen microfisurado alrededor de la punta de la entalla) es teóricamente menor en las muestras SCB, lo que debería implicar una menor dispersión en los resultados. Sin embargo se observa lo contrario, lo que sugiere que la FPZ no estaría jugando un papel determinante en los ensayos

*p*CT. Una explicación a este comportamiento podría ser la mayor longitud de ligamento (~3 veces) de las muestras *p*CT en comparación con las SCB.

Para los ensayos *p*CT, se encontró una fuerte relación entre la resistencia a tracción y K_{IC}. Aunque los valores obtenidos son internamente consistentes (es decir, el rango de variación es pequeño), se observa que K_{IC} aumenta con el tamaño de la muestra y disminuye con la longitud de entalla. Es interesante destacar que la litología parece magnificar la influencia de estas dos características geométricas sobre K_{IC}, siendo un factor determinante para los materiales más duros (fuertemente cementados), como la arenisca de Pinacas y el granito Blanco Mera. En nuestra opinión, a parte de los factores geométricos, deberían tenerse en cuenta las características de la roca ensayada para fijar los requerimientos mínimos desde el punto de vista dimensional en los ensayos de tenacidad de fractura. Aun así, según nuestros resultados experimentales, se recomendaría usar muestras *p*CT de tamaño medio (diámetro = 50 mm) y con una longitud de entalla normalizada relativamente grande (a/b > 0.25) para obtener valores de K_{IC} más consistentes. En cuanto a la metodología de ensayo, la influencia del tamaño de muestra es menor en los ensayos *p*CT, mientras que los SCB proporcionan una información menos consistente y menos sensible con respecto a la dependencia de la longitud de la entalla.

En los ensayos *p*CT, gracias a la buena correlación observada entre LPD y CMOD, sería posible determinar de manera directa CMOD sin utilizar transductores de contacto directo como extensómetros de clip, lo que es especialmente ventajoso en muestras de pequeño tamaño. Por el contrario, esto no es posible con el SCB. Las relaciones entre E_{pre} y E_{post} con E_{tot} sugieren que, independientemente de la litología, tamaño de muestra y longitud de entalla, se necesita el mismo nivel de energía para generar la fractura que para propagarla de manera controlada posteriormente. Los balances de energía obtenidos también apoyan la hipótesis de que la energía de fractura depende del tamaño de la muestra para un valor de longitud de entalla determinado. Sin embargo, nuestros resultados indican una dependencia más compleja, en la que la litología jugaría un papel importante.

En general, la evolución cualitativa de E_{AE} ilustra de manera adecuada los procesos mecánicos que tienen lugar en las muestras ensayadas, con unas tasas de cambio netas (aceleración/desaceleración) coincidentes con las transiciones mecánicas. Sin embargo, con los datos disponibles no fue posible obtener una relación funcional entre la energía de fractura y $E_{AE..}$ Aun así, no se descarta que se pueda obtener una relación en un futuro con una base de datos de AE más completa.

La localización de los hipocentros de AE fue útil para analizar la evolución y propagación de la fractura a lo largo del plano del ligamento. Como se esperaba, los eventos se ubicaron alrededor de la punta de la entalla en ambos métodos de ensayo cuando la carga alcanzó su valor máximo. En la región post-pico de los ensayos *p*CT, la distribución de los eventos conforma una fractura vertical, que ligeramente se desvía o aumenta la dispersión lateral (en función del material) a la vez que la roca pierde cohesión, siendo consistente con las fracturas observadas en las muestras tras los ensayos.
La tomografía computarizada de micro rayos X realizada sobre algunas muestras *p*CT reveló que la fractura no siempre se inicia en la punta de la entalla, y que el punto de generación varía a lo largo del espesor de la probeta. La forma semicircular de la punta de la entalla permitiría que la fractura se iniciase en cualquier punto de su geometría circular. Este factor, junto con la disposición de partículas en el interior de la roca, podría determinar que la fractura se desvíe de la trayectoria vertical esperada, tanto hacia la izquierda como hacia la derecha. En los ensayos SCB y para el material más duro (arenisca de Pinacas), la localización de los hipocentros de AE evidencia una migración de los eventos acústicos desde la punta de la entalla hacia el cilindro de carga superior en el momento en que se produce la rotura de la muestra. Sin embargo, para un material más blando (arenisca de Arcera), se observa un daño progresivo en el área próxima al punto de aplicación de la carga, lo que finalmente origina una fractura oblicua. Estas observaciones ponen en evidencia el potencial de la técnica de AE para mejorar el conocimiento de los procesos de fractura asociados con los ensayos de tenacidad. Además, la localización de los eventos también permitió determinar de manera aproximada las dimensiones de la FPZ.

El análisis de las frecuencias pico (f_{peak}) revela inconsistencias aparentes con el comportamiento generalmente aceptado (es decir, valores altos relacionados con la aparición de microfisuras, y valores más bajos con fracturación). Sin embargo, si se tiene en cuenta el efecto de la atenuación acústica, es posible relacionar la aparición/desaparición de señales con valores específicos de f_{peak} y de amplitud normalizada con los procesos que ocurren a distintos niveles de tensión. Además, los mayores niveles de dispersión a ciertos rangos de frecuencias podrían estar relacionados con el tamaño de los defectos.

En los ensayos *p*CT, la tracción es el modo de rotura predominante tanto en la región pre-pico como en las últimas etapas de la post-pico, según el análisis paramétrico realizado en base a los ratios AF vs. RA. Sólo en los primeros instantes de la etapa post-pico, donde la fractura macroscópica crece como resultado de la convergencia de mico y meso-fisuras, se produce, aunque de manera limitada, un modo mixto (tracción/cortante). La aparición de un modo de rotura distinto a la tracción podría explicarse por el tipo de roca y sus propiedades (es decir, mineralogía, tamaño de grano, cementación u homogeneidad) que determinarían la orientación de la fractura. Según esto, si se necesita menos energía para que la fractura avance a través del cemento que a través de los granos de la roca, el plano de fractura puede no ser perpendicular a la carga de tracción, resultando en un esfuerzo cortante localizado debido a la mayor tortuosidad. Esta hipótesis se refuerza con las características geométricas (desviación y ramificación) observadas tanto en la localización de los eventos de AE como en la tomografía de rayos X. Finalmente, el análisis del '*improved b-value*' permite identificar un potencial relevante para discernir entre propagación de fractura estable e inestable. De todos modos, se necesitarían unas técnicas de filtrado más específicas para llevar a cabo un análisis detallado.

En resumen, y considerando las conclusiones de este trabajo, el ensayo *p*CT presenta ciertas ventajas sobre otros métodos de ensayo de tenacidad de fractura, entre las que se incluirían: a) pequeña cantidad de material requerido (probetas con forma de disco con un ratio diámetro-espesor de 2); b) proceso de preparación de muestra sencillo (muesca en U y entalla fina); c) control de

propagación de fractura mejorado, especialmente después de la carga pico; d) rotura a tracción pura; y e) gracias a la posibilidad de capturar el comportamiento post-pico, resultados más detallados y más completos tanto desde el punto de vista mecánico (por ejemplo, evolución de la energía de fractura) como de información de AE. Además, la configuración de ensayo permite mantener las muestras sumergidas en fluido, y por tanto saturadas, durante la total duración de los ensayos. Este aspecto hace que el *p*CT sea apropiado para el estudio del impacto potencial de los fluidos sobre K_{IC}.

Desde el punto de vista metodológico, se advierte de la importancia en el método SCB de garantizar un buen alineamiento de la muestra para evitar modos mixtos (I/II), así como de la tendencia de esta configuración al deslizamiento lateral cuando se aplica una fuerza distribuida en una superficie circular. Ninguno de estos problemas es relevante con la técnica *p*CT.

A2. Resumo estendido

Tódolos materiais conteñen defectos como poros ou gretas, que se poden desenvolver durante a súa vida útil ou incluso ser inherentes á súa natureza. Os criterios de rotura máis simples asumen que tódolos materiais son perfectamente homoxéneos, isótropos e libres de defectos. De acordo con isto, unha mostra romperase cando a tensión supere a resistencia última do material. Sen embargo, isto non adoita ocorrer na realidade, xa que a inevitable presenza de descontinuidades ou defectos que poden xerar concentración de tensións de xeito localizado, reducindo a resistencia xeral do material e conducindo a unha rotura prematura e inesperada. A necesidade de coñecer estes procesos con maior profundidade orixinou o desenvolvemento da mecánica da fractura. Ó contrario que os enfoques máis tradicionais, a mecánica da fractura ten en conta o tamaño dos defectos na avaliación da resistencia á rotura. O obxectivo principal desta rama é, polo tanto, cuantificar a relación crítica que existe entre a tensión aplicada e o tamaño do defecto que producirá a rotura antes de que se alcance a resistencia última do material. A propiedade que une estes dous parámetros

(tensión e tamaño del defecto) e polo tanto mide a resistencia dun material á propagación dunha fisura coñécese como tenacidade de fractura (K_C). A mecánica de fractura distingue tres modos básicos de carga: a) modo I, ou modo de apertura/tracción; b) modo II, ou modo de cortante no plano/escorredura; e c) modo II, ou modo de cortante fóra do plano/cizalla.

En mecánica de rochas, predicir a rotura é unha das maiores preocupacións. Sen embargo, é básico considerar que as rochas son materiais descontinuos a tódalas escalas. Por exemplo, a escala microscópica, contén descontinuidades como poros, grans ou microfisuras, que poden producir altas concentracións de tensión baixo carga. En rochas, a resistencia a tracción é comparativamente máis baixa que a resistencia a compresión ou cortante. Polo tanto, a tenacidade de fractura en modo I (K_{IC}) é un dos parámetros máis importantes e máis estudados na mecánica de fractura aplicada a rochas: cuanto máis alto sexa o valor de K_{IC}, máis alta será a resistencia á propagación de fracturas a tracción. A tenacidade de fractura pode ter unha importancia crucial nos proxectos que involucren materiais rochosos, como en enxeñería térmica (por exemplo, a enerxía xeotérmica ou a xestión de residuos radioactivos), mecánica (por exemplo, a estabilidade de estruturas mineiras), hidráulica/química (por exemplo, a fracturación hidráulica, o almacenamento xeolóxico de CO_2 ou a gasificación subterránea do carbón), ou de procesos (por exemplo, a perforación e corte de rochas, ou a trituración de minerais). Nos últimos anos, a investigación dos procesos de inicio e propagación de fracturas en materiais xeolóxicos gañou importancia debido á necesidade de resolver problemas de fracturación en xeofísica. En particular, a crecente demanda de hidrocarburos favoreceu a investigación dos procesos de fracturación en certas litoloxías (por exemplo, arenitas compactas ou lousas). Por este motivo, é esencial desenvolver métodos de ensaio apropiados que axuden a mellorar a precisión nos valores de tenacidade de fractura. A Sociedade Internacional para la Mecánica de Rochas (ISRM) propuxo catro métodos de ensaio para determinar K_{IC} usando mostras cilíndricas, chamados '*short rod*' (SR), '*chevron bend*' (CB), '*cracked chevron notched Brazilian disc*' (CCNBD) e '*semi-circular bend*' (SCB). Sen embargo, estes métodos poden ser difíciles de aplicar de xeito

rutineiro debido a aspectos coma: a) as baixas cargas ás que se produce a rotura, que obrigan a ter un excelente control de ensaio; b) o tamaño de mostra que requiren é relativamente grande (CB); c) a preparación das mostras é difícil e problemática (SR, CB y CCNBD); d) o cálculo do factor de intensidade de tensións é impreciso (CCNBD); e) a xeración de cargas de tracción realizase de xeito indirecto a través da compresión da mostra (especialmente en SCB y CCNBD); e f) a propagación da fractura prodúcese moi rapidamente unha vez alcánzase a resistencia pico.

Para superar estas limitacións, o obxectivo principal desta tese é desenvolver un método de ensaio alternativo e simple, denominado '*pseudo-compact tensión*' (*p*CT), que permita medir K_{IC} en rochas usando mostras cilíndricas baixo condicións de tracción pura. El *p*CT baséase nunha modificación da probeta '*compact tensión*' (CT) descrita no método estandarizado E399-90 de la ASTM (1997) para metais. A mostra *p*CT é un disco (cunha relación diámetro-espesor de ~2) que se pode obter a partir de cilindros de rocha. Os dous buratos que se usan na mostra CT para aplicar a carga substitúense no ensaio *p*CT por un corte en forma de U. Ademais tamén se introduce unha entalla fina que actúa como concentrador de tensións, forzando a que ése sexa o punto de inicio da fractura. A xeometría da probeta *p*CT presenta vantaxes sobre as que se utilizan noutros métodos debido á súa simplicidade, pequena cantidade de material necesario e mínima preparación. Unha vez a mostra está lista, o procedemento de ensaio é simple e directo: a probeta sitúase nunha plataforma e se pon en contacto cun par de mordazas de aceiro de alta resistencia e rixidez que encaixan no corte en U e transmiten a forza de tracción á mostra. Mentres que unha das mordazas permanece inmóbil, a outra afástase cun ritmo de desprazamento constante. A tracción que se xera na entalla provoca que a probeta se rompa en dúas metades simétricas. A fractura orixínase na punta da entalla e se propaga ó longo do diámetro vertical da mostra, é dicir, no plano do ligamento.

Os valores de K_{IC} medidos có ensaio *p*CT valídanse comparándoos cos obtidos cun dos métodos suxeridos pola ISRM, o ensaio SCB. A probeta SCB é

un semi-cilindro cunha entalla recta cortada no centro da súa cara plana. Entre os métodos dispoñibles, optouse polo SCB como estándar de comparación debido á súa popularidade, simplicidade (dende o punto de vista de preparación da mostra) e configuración de ensaio directa. Neste traballo usáronse catro tipos de rocha distintos (arenitas de Corvio, Arcera y Pinacas, y granito Branco Mera) para avaliar a súa correspondente K_{IC} usando os dous métodos de ensaio. Todas estas rochas son practicamente isótropas pero difiren unhas das outras na súa resistencia e comportamento mecánico. As arenitas de Corvio e Arcera teñen unha resistencia relativamente baixa, un tamaño de gran pequeno (< 1 mm), elevada porosidade y baixo módulo elástico. Sen embargo, a arenita de Pinacas, a pesar de ter un tamaño de gran similar, é considerablemente máis dura, ten unha porosidade máis baixa e un módulo elástico maior. O granito Branco Mera é unha rocha homoxénea de tamaño de gran medio (1-6 mm), baixa porosidade e resistencia moderada.

Os cilindros de rocha necesarios para preparar as mostras obtivéronse de bloques homoxéneos usando unha perforadora con coroa de diamante. Despois, os cilindros cortáronse en discos cunha relación diámetro-espesor de 2 usando un disco de diamante circular. Para as mostras SCB, os discos cortáronse diametralmente en dúas metades usando unha serra para cortar azulexos modificada. No caso das mostras *p*CT, o corte en U introduciuse con esta mesma serra usando un disco de diamante de 2 mm de espesor, facendo varios cortes mentres se desprazaba a mostra de xeito horizontal despois de cada pasada. A posición vertical do disco, que determina a profundidade da entalla, fíxase cun parafuso vertical. Coa axuda duns elementos de referencia (nivel láser, regra) e un agarre horizontal móbil asegúrase o correcto aliñamento da mostra con respecto ó disco da serra. Para cortar a entalla fina nos dous tipos de mostra (*p*CT e SCB) seguiuse un procedemento similar, aínda que neste caso a entalla se cortou cun disco de diamante máis fino (1 mm de espesor) nunha única pasada. Unha vez preparadas, as mostras secáronse nunha estufa a 60ºC por un mínimo de 24 horas.

Para levar a cabo os ensaios *p*CT construíuse un dispositivo de ensaio especialmente deseñado para tal fin. Entre os requisitos que se tiveron en conta no seu deseño incluíronse a mobilidade da máquina (o que supuxo importantes restricións de tamaño, peso e robustez), posibilidade de colocación de mostras de distintos tamaños garantindo a estabilidade mecánica durante os ensaios, facilidade de instalación dos dispositivos de medida e substitución dos elementos danados, e a rapidez das operacións complementarias (colocación da probeta, limpeza, etc.). O dispositivo de ensaio está formado por un marco de aceiro de alta rixidez equipado cunha célula de carga de tracción/compresión de 50 kN, dous transdutores diferenciais de variación lineal (LVDTs) e dous extensómetros de medición de apertura de fisura (COD). As sinais eléctricas de tódolos dispositivos de medida intégranse nun sistema destinado á adquisición de datos. O movemento da mordaza de aceiro consíguese a través dun parafuso que converte en desprazamento lineal o movemento de rotación dun motor eléctrico paso a paso cun ángulo de paso de 1.8º (equivalente a 200 pasos por revolución). Para mellorar o seu rendemento, o motor conéctase a unha redutora planetaria cun rato de redución de 1:100. Esta configuración, aínda que simple, proporciona un elevado nivel de precisión no desprazamento (0.018º/paso), equivalente a 0.25 µm/paso desde el punto de vista do desprazamento lineal do parafuso, que se pode manter desde 0 a 50 kN. Os dous LVDTs, situados simetricamente a ambos lados da probeta, miden o desprazamento do punto de carga (LPD), que en este caso se corresponde co desprazamento da mordaza móbil. Ó mesmo tempo, e de xeito redundante, un extensómetro de clip montado sobre un par de coitelas unidas ás propias mordazas mide a mesma magnitude. Adicionalmente, es posible montar outro extensómetro directamente na superficie da mostra (tamén a través dunhas coitelas) para medir o desprazamento de apertura da punta da fractura (CMOD). Mentres que as curvas carga-desprazamento (*P*-LPD) se rexistraron en tódolos ensaios *p*CT, CMOD mediuse só en 11 deles.

As probetas SCB ensaiáronse a flexión con tres puntos de apoio nunha prensa servo-controlada equipada cunha célula de carga de 4.448,22 N. Con esta configuración, a carga transfírese á parte superior da mostra a través dun

cilindro de aceiro. Outros dous cilindros adicionais, colocados na parte inferior, serven para soportar a probeta. Neste caso, o LPD correspóndese co desprazamento vertical do cilindro de carga superior. Co obxectivo de evitar os problemas inherentes a usar extensómetros de clip en mostras de pequeno tamaño, CMOD mediuse usando dous LVDTs enfrontados colocados perpendicularmente á entalla no plano diametral da mostra. Hai que ter en conta que a xeometría curva da mostra magnifica os errores de contacto asociados coa rotación da superficie superior durante o ensaio. Por isto, e para garantir o contacto dos LVDTs coa mostra en todo momento, se adheriron unhas pezas en forma de T creadas cunha impresora 3D nos dous extremos da probeta. Con este método de ensaio se rexistraron para tódolos ensaios tanto as curvas *P*-LPD como as *P*-CMOD.

Os resultados dos dous métodos de ensaio (*p*CT e SCB) analizáronse tendo en conta unha serie de parámetros relevantes, todos eles con algunha influencia potencial sobre K_{IC}. Aínda que a tenacidade de fractura se considera unha propiedade intrínseca do material e polo tanto debería ser razoablemente independente da xeometría das mostras e a configuración do ensaio, os valores experimentais de K_{IC} obtidos por numerosos autores contradín este suposto. Por este motivo, neste estudo ensaiáronse probetas, tanto *p*CT como SCB, de 38, 50 e 100 mm de diámetro para determinar o efecto do tamaño de mostra. Del mesmo modo, tamén se tivo en conta a influencia da lonxitude da entalla ensaiando mostras con distintas lonxitudes. Tódolos ensaios realizáronse a unha velocidade de desprazamento constante de 0.1 mm/min (a velocidade é baixa para evitar efectos dinámicos) en condiciones ambientais de laboratorio. Neste traballo, só se considerou o Nivel I de ensaio (nivel básico). Aínda que para poder calcular K_{IC} a este nivel só se necesita medir a carga máxima (P_{max}) durante o ensaio, para poder profundar no comportamento do material se rexistraron, ademais da carga (P), as magnitudes de LPD e CMOD de xeito continuo. Desde a perspectiva dos balances de enerxía, a fractura prodúcese cando a enerxía dispoñible para o seu crecemento e propagación supera a resistencia do material. Polo tanto, a tenacidade de fractura tamén se pode ve como a taxa de liberación de enerxía necesaria para crear novas superficies de fractura na

mostra. Neste estudo, as curvas carga-desprazamento de cada ensaio usáronse para caracterizar o contido enerxético do proceso de fracturación. Na metodoloxía *p*CT, grazas ó bo control do ensaio incluso despois de P_{max}, a enerxía total (E_{tot}) púidose dividir en dúas porcións: a enerxía pre-pico (E_{pre}, é dicir, o traballo realizado para inducir o inicio da fractura na probeta), e a enerxía post-pico (E_{post}, é dicir, o traballo realizado para propagar a fractura). Para poder calcular K_{IC} é necesario coñecer non só a carga máxima (P_{max}) e a lonxitude da entalla (a), senón a expresión do factor de intensidade de tensións adimensional (Y') específico de cada xeometría de mostra e condiciones de carga. Para o ensaio SCB, a expresión correspondente (Y'_{SCB}) pódese atopar na literatura. Sen embargo, para a nosa configuración *p*CT, non foi posible atopar unha expresión adecuada, e foi necesario usar o método dos elementos finitos para obter unha función polinómica de cuarto grado para cada tamaño de mostra e para un rango de lonxitudes de entalla (Y'_{pCT}).

Para conseguir profundar aínda máis nos procesos de inicio, propagación e coalescencia das fracturas, empregouse a técnica de emisión acústica (AE). AE é unha técnica de ensaio non destrutiva amplamente usada para rexistrar a evolución de dano en rochas. Cando unha fractura crece, se libera enerxía en forma de ondas elásticas que viaxan a través do material e que poden ser rexistradas en tempo real usando sensores situados sobre a superficie da probeta. No desenvolvemento desta tese e para algúns ensaios, a actividade acústica rexistrouse usando ata 8 sensores situados a distintas distancias da entalla. A adquisición de datos realizouse cun sistema multicanal AMSY-6 de Vallen Systeme GmbH. Os sensores colocáronse sobre a probeta usando uns imáns adheridos á súa superficie. En cada ensaio rexistráronse unha serie de parámetros de AE (como contas, amplitude, duración ou frecuencia pico) útiles para avaliar as distintas etapas e procesos, a proximidade da rotura da probeta, e os distintos modos de rotura (por exemplo, usando a relación AF:RA e o ‘i*mproved b-value*’). Ademais, grazas ó sistema multicanal, se puideron localizar os hipocentros dos eventos de AE ó longo da duración do ensaio, o que foi útil para analizar a evolución e a propagación das fracturas na mostra. Usando a información de AE, tamén se explorou a relación entre a liberación de enerxía

asociada ós procesos de fractura e a capturada polos sensores de AE (E_{AE}). Aínda que ambas magnitudes son en liñas xerais diferentes (a AE pode ter dispersión e/ou atenuación), aínda así podería ser posible identificar unha relación formal entre as dúas propiedades. De feito, considerando que a actividade acústica é proporcional ó número e magnitude de fracturas, é razoable asumir que debe existir algunha relación entre E_{AE} y a enerxía de fractura.

Cos datos obtidos, comparáronse os métodos *p*CT y SCB tanto desde o punto de vista da evolución mecánica, como da evolución de diversos parámetros de AE en distintas de etapas de ensaio. Os nosos resultados amosan que a combinación de pequenos desprazamentos (permitindo taxas de deformación extremadamente pequenas), elevada capacidade de carga e alta rixidez do dispositivo de ensaio fai que o ensaio *p*CT sexa adecuado para a análise da tenacidade de fractura tanto en rochas fráxiles como dúctiles. Ademais, a metodoloxía de preparación de mostra máis simple do *p*CT en comparación con outros métodos de ensaio convérteo nun candidato interesante para la determinación da tenacidade de fractura de xeito rutineiro. Para as rochas ensaiadas, o crecemento da fractura foi lento durante a duración total dos ensaios *p*CT. De feito, para incrementar a súa extensión era necesario o movemento continuo da mordaza. Polo tanto, o proceso de propagación de la fractura foi controlado en todo momento, incluso despois de alcanzar a forza máxima, e as curvas carga-desprazamento (*P-d*) se puideron rexistrar de xeito preciso incluso máis alá de P_{max}, proporcionando unha gran información sobre o comportamento post-pico. En xeral, o proceso de carga divídese en tres etapas diferenciadas: (1) un período de crecemento lineal da curva (comportamento elástico); (2) un período non-lineal de formación de novas microfisuras no que a pendente da curva gradualmente decrece ata P_{max}; e (3) un período de baixada durante o cal a carga diminúe mentres a fractura macroscópica se propaga ó longo do plano do ligamento. Ó contrario, e coa excepción de algunhas mostras de arenita de Corvio (unha rocha branda), as curvas de carga para os ensaios SCB mostran un crecemento case lineal ata a rotura repentina da probeta á carga pico (P_{max}). Este comportamento evidencia que a metodoloxía SCB non permite un bo control de ensaio máis alá de (P_{max}) e que a fractura, unha vez

iniciada, se propaga rapidamente ata a parte superior da mostra. Poderíase discutir se mellorando o control electrónico e a rixidez do sistema (para evitar el almacenamento de enerxía elástica no equipo de ensaio) se podería mellorar a calidade dos resultados para o método SCB. Sen embargo, na nosa opinión, o factor clave que determinaría a súa menor eficacia na rexión post-pico sería o almacenamento de enerxía na mostra, que ten lugar un volume considerablemente máis grande que o que rodea a punta da entalla (por exemplo, no punto de contacto dos cilindros e ó longo de todo o ligamento). Cando a carga alcanza o seu valor máximo, toda esta enerxía almacenada na mostra libérase instantaneamente e a fractura se propaga de xeito incontrolado. Sen embargo, no caso do ensaio *p*CT, a carga se transfire á mostra ó longo das liñas de contacto coas mordazas e desde alí directamente á entalla.

Tomando como referencia os resultados de 146 ensaios (81 *p*CT e 65 SCB), comprobouse a consistencia mutua dos valores de K_{IC} obtidos usando ambas metodoloxías. Do mesmo modo, avaliouse a influencia de características como o tamaño de mostra ou a lonxitude da entalla. Cunha perspectiva ampla, obsérvase que, para os dous métodos de ensaio, os resultados son compatibles para cada un dos tipos de rocha. A tenacidade de fractura en modo I obtida para os ensaios *p*CT para las arenitas de Corvio (~0.06-0.12 MPa $m^{1/2}$) e Arcera (~0.24-0.60 MPa $m^{1/2}$) é baixa, o que é consistente coa súa condición de rochas brandas. Sen embargo, os valores de $K_{IC,}$ tanto para a arenita de Pinacas como para o granito Branco Mera, son apreciablemente máis altos (~1.05-1.4 MPa $m^{1/2}$). Para as mesmas rochas, os resultados dos ensaios SCB son lixeiramente superiores para a arenita de Corvio (~0.07-0.18 MPa $m^{1/2}$), pero máis baixos para a de Arcera (~0.26-0.46 MPa $m^{1/2}$). No caso da arenita de Pinacas e o granito Branco Mera, a dispersión nos resultados de K_{IC} é máis alta que para os ensaios *p*CT (~0.69-1.64 e ~0.72-1.51 MPa $m^{1/2}$, respectivamente). A zona de procesos de fractura (FPZ, que se corresponde co volume microfisurado ó redor da punta da entalla) é teoricamente menor nas mostras SCB, o que debería implicar unha menor dispersión nos resultados. Sen embargo se observa o contrario, o que suxire que a FPZ non estaría xogando un papel determinante nos ensaios *p*CT.

Unha explicación a este comportamento podería ser a maior lonxitude de ligamento (~3 veces) das mostras *p*CT en comparación coas SCB.

Para os ensaios *p*CT, atopouse unha forte relación entre a resistencia a tracción e K_{IC}. Aínda que os valores obtidos son internamente consistentes (é dicir, o rango de variación é pequeno), se observa que K_{IC} aumenta co tamaño da mostra e diminúe coa lonxitude de entalla. É interesante destacar que a litoloxía parece magnificar a influencia destas dúas características xeométricas sobre K_{IC}, sendo un factor determinante para os materiais máis duros (fortemente cementados), como a arenita de Pinacas e el granito Branco Mera. Na nosa opinión, a parte dos factores xeométricos, deberían terse en conta as características da rocha ensaiada para fixar os requirimentos mínimos desde o punto de vista dimensional nos ensaios de tenacidade de fractura. Aínda así, segundo os nosos resultados experimentais, se recomendaría usar mostras *p*CT de tamaño medio (diámetro = 50 mm) e con unha lonxitude de entalla normalizada relativamente grande (a/b > 0.25) para obter valores de K_{IC} máis consistentes. En canto á metodoloxía de ensaio, a influencia do tamaño de mostra é menor nos ensaios *p*CT, mentres que os SCB proporcionan unha información menos consistente e menos sensible con respecto á dependencia da lonxitude da entalla.

Nos ensaios *p*CT, grazas á boa correlación observada entre LPD e CMOD, sería posible determinar de xeito directo CMOD sen utilizar transdutores de contacto directo como extensómetros de clip, o que é especialmente vantaxoso en mostras de pequeno tamaño. Polo contrario, isto non é posible co SCB. As relacións entre E_{pre} e E_{post} con E_{tot} suxiren que, independentemente da litoloxía, tamaño de mostra e lonxitude de entalla, se necesita o mesmo nivel de enerxía para xerar a fractura que para propagala de xeito controlado posteriormente. Os balances de enerxía obtidos tamén apoian a hipótese de que a enerxía de fractura depende do tamaño da mostra para un valor de lonxitude de entalla determinado. Sen embargo, os nosos resultados indican unha dependencia máis complexa, na que a litoloxía xogaría un papel importante.

En xeral, a evolución cualitativa de E_{AE} ilustra de xeito adecuado os procesos mecánicos que teñen lugar nas mostras ensaiadas, cunhas taxas de cambio netas (aceleración/desaceleración) coincidentes coas transicións mecánicas. Sen embargo, cos datos dispoñibles non foi posible obter unha relación funcional entre a enerxía de fractura e $E_{AE..}$ Aínda así, non se descarta que se poida obter unha relación nun futuro cunha base de datos de AE máis completa.

A localización dos hipocentros de AE foi útil para analizar a evolución e propagación da fractura ó longo do plano do ligamento. Como se esperaba, os eventos se localizaron ó redor da punta da entalla en ambos métodos de ensaio cando a carga alcanzou o seu valor máximo. Na rexión post-pico dos ensaios *p*CT, a distribución dos eventos conforma unha fractura vertical, que lixeiramente se desvía ou aumenta a dispersión lateral (en función do material) á vez que a rocha perde cohesión, sendo consistente coas fracturas observadas nas mostras tras os ensaios. A tomografía computarizada de micro raios X realizada sobre algunhas mostras *p*CT revelou que a fractura non sempre se inicia na punta da entalla, e que o punto de xeración varía ó longo do espesor da probeta. A forma semicircular da punta da entalla permitiría que a fractura se iniciase en calquera punto da súa xeometría circular. Este factor, xunto coa disposición de partículas no interior da rocha, podería determinar que a fractura se desvíe da traxectoria vertical esperada, tanto á esquerda como á dereita. Nos ensaios SCB e para o material máis duro (arenita de Pinacas), a localización dos hipocentros de AE evidencia unha migración dos eventos acústicos desde a punta da entalla ata o cilindro de carga superior no momento en que se produce a rotura da mostra. Sen embargo, para un material máis brando (arenita de Arcera), se observa un dano progresivo na área próxima ó punto de aplicación da carga, o que finalmente orixina unha fractura oblicua. Estas observacións poñen en evidencia o potencial da técnica de AE para mellorar o coñecemento dos procesos de fractura asociados cos ensaios de tenacidade. Ademais, a localización dos eventos tamén permitiu determinar de xeito aproximado as dimensións da FPZ.

A análise das frecuencias pico (f_{peak}) revela inconsistencias aparentes co comportamento xeralmente aceptado (é dicir, valores altos relacionados coa aparición de microfisuras, e valores máis baixos con fracturación). Sen embargo, si se ten en conta o efecto da atenuación acústica, é posible relacionar a aparición/desaparición de sinais con valores específicos de f_{peak} e de amplitude normalizada cos procesos que ocorren a distintos niveles de tensión. Ademais, os maiores niveles de dispersión a certos rangos de frecuencias poderían estar relacionados co tamaño dos defectos.

Nos ensaios *p*CT, a tracción é o modo de rotura predominante tanto na rexión pre-pico como nas últimas etapas da post-pico, segundo a análise paramétrica realizada en base ás relacións AF vs. RA. Só nos primeiros instantes da etapa post-pico, onde a fractura macroscópica crece como resultado da converxencia de mico e meso-fisuras, se produce, aínda que de xeito limitado, un modo mixto (tracción/cortante). A aparición dun modo de rotura distinto á tracción podería explicarse polo tipo de rocha e as súas propiedades (é dicir, mineraloxía, tamaño de gran, cementación ou homoxeneidade) que determinarían a orientación da fractura. Segundo isto, se se necesita menos enerxía para que a fractura avance a través do cemento que a través dos grans da rocha, o plano de fractura pode non ser perpendicular á carga de tracción, resultando nun esforzo cortante localizado debido á maior tortuosidade. Esta hipótese se reforza coas características xeométricas (desviación e ramificación) observadas tanto na localización dos eventos de AE como na tomografía de raios X. Finalmente, a análise do '*improved b-value*' permite identificar un potencial relevante para discernir entre propagación de fractura estable e inestable. De todos modos, precisaríanse unhas técnicas de filtrado máis específicas para levar a cabo unha análise detallada.

En resumen, e considerando as conclusións deste traballo, o ensaio *p*CT presenta certas vantaxes sobre outros métodos de ensaio de tenacidade de fractura, entre as que se incluirían: a) pequena cantidade de material requirido (probetas con forma de disco cunha relación diámetro-espesor de 2); b) proceso de preparación de mostra sinxelo (corte en U e entalla fina); c) control de

propagación de fractura mellorado, especialmente despois da carga pico; d) rotura a tracción pura; e e) grazas á posibilidade de capturar o comportamento post-pico, resultados máis detallados e máis completos tanto desde o punto de vista mecánico (por exemplo, evolución da enerxía de fractura) como de información de AE. Ademais, a configuración de ensaio permite manter as mostras somerxidas en fluído, e polo tanto saturadas, durante a total duración dos ensaios. Este aspecto fai que o *p*CT sexa apropiado para o estudo do impacto potencial dos fluídos sobre K_{IC}.

Desde o punto de vista metodolóxico, advírtese da importancia no método SCB de garantir un bo aliñamento da mostra para evitar modos mixtos (I/II), así como da tendencia desta configuración á escorredura lateral cando se aplica unha forza distribuída nunha superficie circular. Ningún destes problemas é relevante coa técnica *p*CT.

APPENDIX B: Testing device for pseudo-compact tension tests

B1. Components

B1.1. Stepper motor

The bipolar stepper motor selected (DST56EL61A, Teco Electro Devices Co; Figure B.1) provides precise positioning control and high torque within the low/mid-speed range. The motor has the following characteristics: a) step angle ($S_{a\text{-}motor}$): 1.8º; b) steps per revolution: 200; c) current: 2A/phase; d) shaft diameter ($D_{s\text{-}motor}$): 6.35 mm; e) holding torque: 1.35 Nm; f) format: NEMA 23. A full turn of the shaft represents a displacement of 19.95 mm ($L_{turn\text{-}motor} = \pi * D_{s\text{-}motor}$), so the corresponding step angle increment is 0.1 mm/step ($L_{turn\text{-}motor}$ / nº steps).

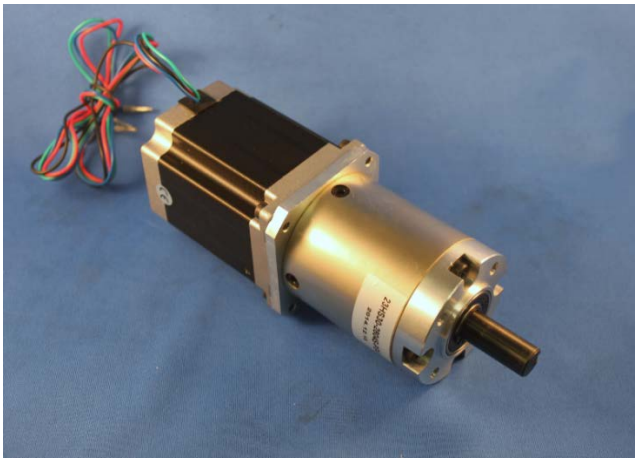

Figure B.1: Assembly of motor and gearhead.

B1.2. Gearhead

A planetary gearhead (IP57-M2-100, McLennan Servo Supplies; Figure B.1) with a reduction ratio of 1:100 was chosen to multiply the torque provided by

the motor. This gearhead has a shaft diameter ($D_{s\text{-}gearhead}$) of 12.69 mm, and can deliver a peak torque ($T_{p\text{-}gearhead}$) of 24 Nm. Once assembled to the motor, it provides a turn accuracy of 0.018º ($S_{a\text{-}motor}$ / reduction ratio) per step.

B1.3. Ball screw

The rotatory motion of the motor is converted into linear displacement using a ball screw (VFU 40005 DIN 69051 FORM B, NBS) suitable for operating at medium load, low speed, and short distance. The main components of the ball screw are the shaft, the nut, and the bearing (Figure B.2). Dimensions and properties of these elements are listed in Table B.1. The turn accuracy of the motor/gearhead assembly (i.e. 0.018º per step) is equivalent to 0.25 µm in terms of linear movement of the shaft.

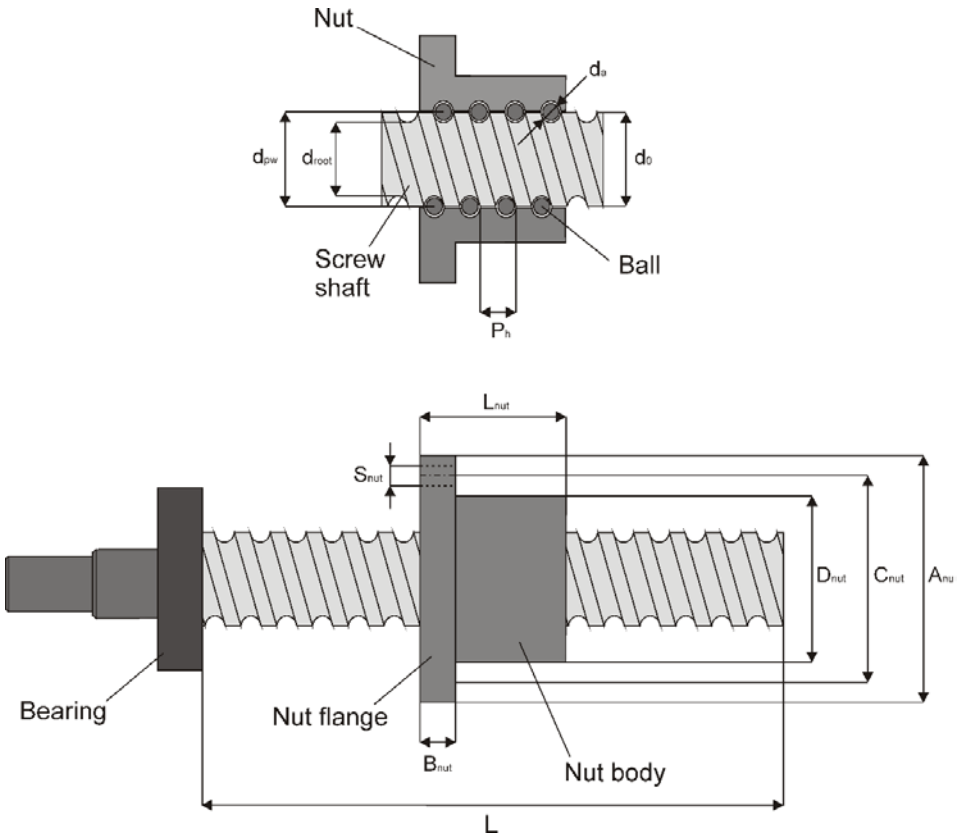

Figure B.2: Ball screw (d_0 = nominal diameter, d_{root} = shaft root diameter; P_h = lead; L = bar length; d_{pw} = primitive ball circle diameter; d_a = ball diameter) and nut (L_{nut} = length; D_{nut} = diameter; A_{nut} = flange diameter; B_{nut} = flange thickness; C_{nut} = flange diameter at fixing points; S_{nut} = through hole diameter) components and dimensions.

In order to dimension a ball screw, a number of loads and torques have to be considered (see Table B.2 for equations). A preload ($F_{preload}$) is usually required to eliminate the axial play between the screw shaft and the balls, to minimize the elastic deformation under axial load, to enhance stiffness, and to gain accuracy in positioning. The driving torque ($T_{driving}$) and reverse torque ($T_{reverse}$) convert the rotatory motion into linear displacement and vice versa, respectively. The motor drive torque (T_{motor}) is the torque necessary to drive the ball screw at constant speed against an external load. This torque is maximized by a factor of two to ensure safety (T_{max}). The maximum axial compressive ($F_{buckling}$) and tensile ($F_{tensile}$) loads are also limited to avoid large deflections of the screw and to ensure operating below the yield stress, respectively. In addition, it is recommended to operate below the critical speed (rpm_{max}) to reduce vibrations and bending of the screw. Values for these loads and torques are presented in Table B.3. A ball screw support bearing fixed-side round type (FK30-C5, Hiwin) was chosen to provide axial and rotational support for the ball screw.

B1.4. Coupling

A stainless steel bellow coupling with clamping hub (WK4/60-89-SX 49/15, StS Coupling) is used to connect the motor and the ball screw (Figure B.3). It provides with a torque of 60 Nm, and has an overall length of 89 mm.

B1.5. Measuring devices

A 50 kN load cell (TC4-AMP 5 ton, AEP Transducers) was mounted between the sample and the motor (Figure B.3). In order to measure the displacement of the steel jaw, two LVDTs (VG/10/S, Solartron Metrology) were symmetrically placed on both sides of the specimen, and a clip-on gauge (3541-020M-040M-ST, Epsilon Technology Corp.) was mounted on a pair of bolt-on knife edges attached to the jaws (Figure B.4). An additional clip-on gage (632.03B-30, MTS) is mounted directly on the specimen at the level of the notch tip (Figure B.5) to measure crack mouth opening displacement (CMOD).

Table B.1.: Dimensions and properties of the ball screw.

Material characteristics		
Young's modulus (E)		205 GPa
Tensile strength (σ)		147 MPa
Specific weight (γ)	kg/m^3	7850
Screw (SR 4005) dimensions		
Nominal screw diameter (d_0)		40 mm
Screw lead (P_h)		5 mm
Ball diameter (d_a)	mm	3.175
Screw bar length ($L_{screw} = L$)		200 mm
Screw shaft root diameter ($d_{root} \approx d_0 - d_a/2.8$)	mm	38.413
Screw shaft cross sectional area at d_{root} ($A = \pi d_{root}^2/4$)	mm^2	1158.971
Primitive ball circle diameter ($d_{pw} \approx d_0$)		40 mm
Screw ball lead angle ($\varphi = \arctan(P_h/\pi d_{pw})$)		2.3º
Screw (SR 4005) mechanical properties		
Dynamic load capacity of the screw bar (C_a)		16100 N
Static load capacity of the screw bar (C_{0a})		53300 N
Screw axial stiffness (K)	N/µm	490
Friction coefficient (μ)		0.01
Friction angle ($\rho = \arctan \mu$)		57.3º
Mounting method factor for buckling (C_1)		0.25

Mounting method factor for rotational speed (C_2)	1.875
Nut (VFU 4005) dimensions	
Nut flange thickness (B_{nut})	14 mm
Nut length (L_{nut})	55 mm
Nut diameter (D_{nut})	63 mm
Nut flange diameter (A_{nut})	93 mm
Nut diameter at flange fixing points (C_{nut})	78 mm
Nut through hole diameter (S_{nut})	9 mm
Lubrication hole – ISO metric screw thread (P)	M8
Number of ball circuits (n)	4

Table B.2.: Equations for ball screw dimensioning.

Load	Equations	Parameters
Preload ($F_{preload}$)	$F_{preload} = \frac{F_{mean}}{2.8}$	F_{mean} = mean operation load
Axial load (F)	$F = F_{preload} + \mu \cdot W$	μ = friction coefficient W = work piece weight
Drag torque (T_{drag})	$T_{drag} = \frac{0{,}05}{\sqrt{tan\,(\varphi)}} x \frac{F_{preload} \cdot P_h}{2 \cdot \pi} x10^{-3}$	P_h = screw ball lead φ = screw ball lead angle
Driving torque ($T_{driving}$)	$T_{driving} = \frac{F \cdot P_h}{2 \cdot \pi \cdot \eta_1} x10^{-3}$	η_1 = system's forward efficiency to convert rotatory to linear motion
Forward efficiency (η_1)	$\eta_1 = \frac{\tan(\varphi)}{\tan(\varphi + \rho)}$	ρ = friction angle

Reverse torque ($T_{reverse}$)	$T_{reverse} = \frac{F \cdot P_h \cdot \eta_2}{2 \cdot \pi} x 10^{-3}$	η_2 = system's reverse efficiency to convert linear to rotatory motion
Reverse efficiency (η_2)	$\eta_2 = \frac{\tan(\varphi - \rho)}{\tan(\varphi)}$	
Motor drive torque (T_{motor})	$T_{motor} = (T_{driving} + T_{drag} + T_{bearing}) x \frac{G_{driver}}{G_{driven}}$	$T_{bearing}$ = friction torque of the supporting bearing G_{driver} = number of teeth in the driver gear (=100) G_{driven} = number of teeth of the driven gear (=1)
Maximum torque (T_{max})	$T_{max} = T_{motor}\ x\ FS$	FS = safety factor
Buckling load ($F_{bcuckling}$)	$F_{buckling} = \frac{C_1 \cdot \pi^2 \cdot E \cdot I}{L^2}$	C_1 = mounting method factor for buckling E = Young's modulus I = minimum secondary moment of inertia of the screw shaft L = distance between support points
Minimum secondary moment of inertia (I)	$I = \frac{\pi \cdot d_{root}^4}{64}$	d_{root} = screw shaft root diameter
Maximum tensile/compressive load ($F_{tensile}$)	$F_{tensile} = \frac{\sigma \cdot \pi \cdot d_{root}^2}{4}$	σ = tensile strength

Critical speed (rpm_{max})	$rpm_{max} = \frac{60 \cdot C_2^2}{2 \cdot \pi \cdot L^2} \sqrt{\frac{E \cdot 10^3 \cdot I}{\gamma \cdot A}} \cdot 0{,}8$	C_2 = mounting method factor for rotational speed γ = specific weigth A = screw shaft cross sectional area at d_{root}
Required drive power (P_{drive})	$P_{drive} = \frac{T_{driving} \cdot rpm_{max}}{9.55}$	

Table B.3.: Loads, torques and efficiency of the ball screw.

Load	
m	1 kg
W	9.81 N
F_{mean}	10 N
F	10.1 N
$F_{preload}$	3.6 N
Efficiency	
η_1	0.80
η_2	0.75
Torque	
$T_{driving}$	$1.01 \cdot 10^{-2}$ Nm
$T_{reverse}$	$6 \cdot 10^{-3}$ Nm
T_{drag}	$7 \cdot 10^{-4}$ Nm
$T_{bearing}$	0 Nm
T_{motor}	1.1 Nm
T_{max} (FS=2)	2.2 Nm

Maximum permissible loads	
$F_{buckling}$	1351.4 kN
F_{max} (FS=2)	675.7 kN
$F_{tensile}$	170.4 kN
P_{drive}	34.7 kW

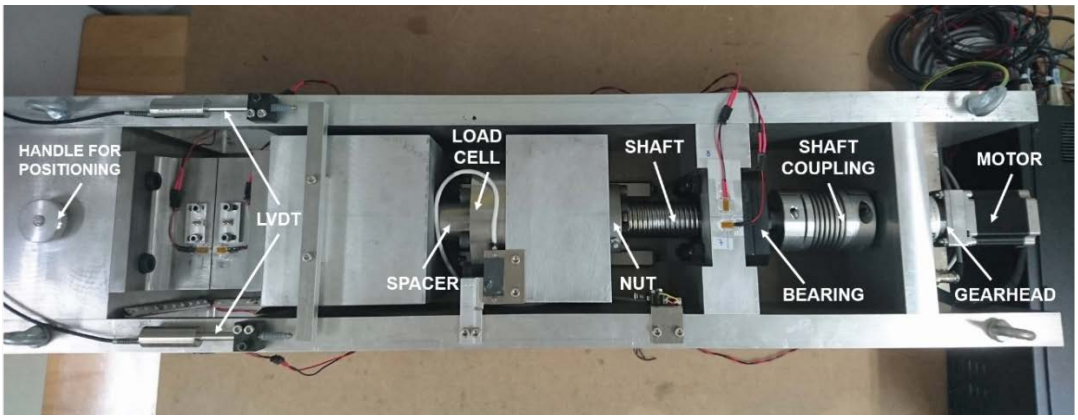

Figure B.3: Top view of the experimental device.

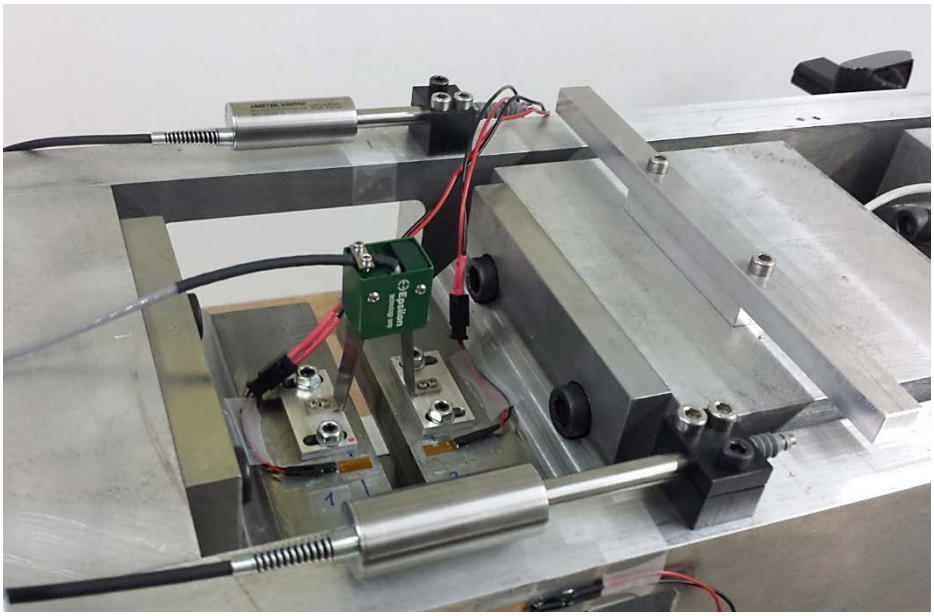

Figure B.4: LVDTs and clip-on gage for measuring load point displacement.

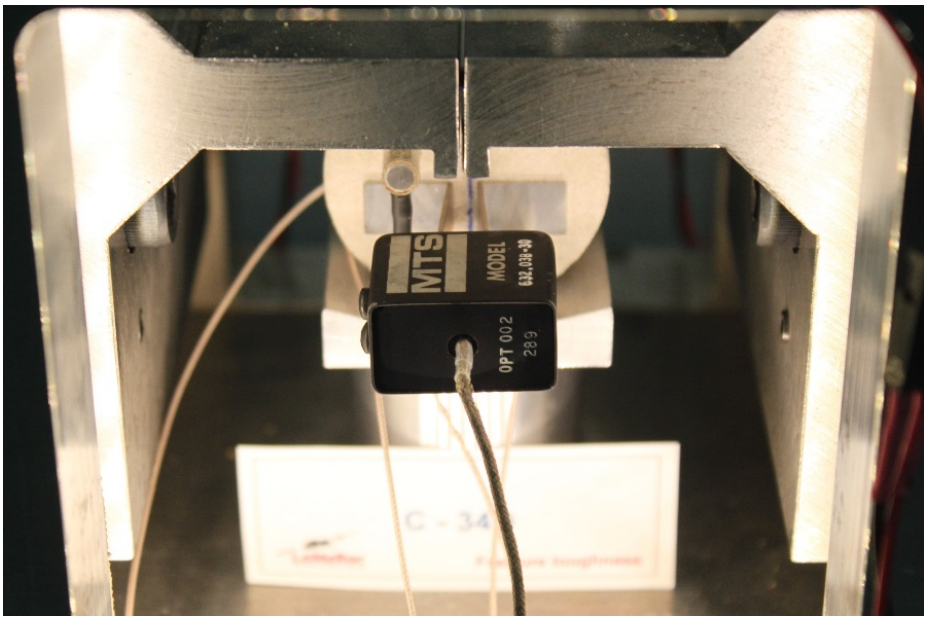

Figure B.5: Clip-on gage mounted on the specimen surface.

B1.6. Controlling and data acquisition systems

A computer is used to control the back and forth movement of the device. A simple preliminary firmware allowed to manually operating the motor by setting the speed (in revolutions per minute, rpm), the number of steps, and the sense of rotation. These features were implemented in a software interface using USB protocol communications (Figure B.6). Afterwards, this version was improved by adding new characteristics (Figure B.7). As before, the motor can be operated manually (left side of the screenshot), but now it is also possible to reset the step value at any time by adjusting a new virtual zero movement, and directly moving the steel jaw to this position (“go to zero”) or to the left limit (“go to start”). In addition, the displacement accuracy can be increased from 0.25 µm/step to 0.125 µm/step by performing “micro steps” and save the data into a file. However, the most remarkable novelty is the possibility of programming scheduled movements, i.e. setting a configuration of cycles to be automatically performed by the controller (center part of the screenshot). By defining four parameters (speed, magnitude of displacement in mm, sense of rotation, and delay time), the firmware allows performing load/unload cycles (for fatigue tests) or stepwise loading. In addition, there are additional safety elements, such as an emergency stop, or limit detectors (right side of the screenshot).

On the other hand, the computer is also used to acquire mechanical data during testing. To this aim, an instruNet data acquisition system (http://www.gwinst.com) records real-time values coming from the load cell, LVDTs, and clip-on gauges.

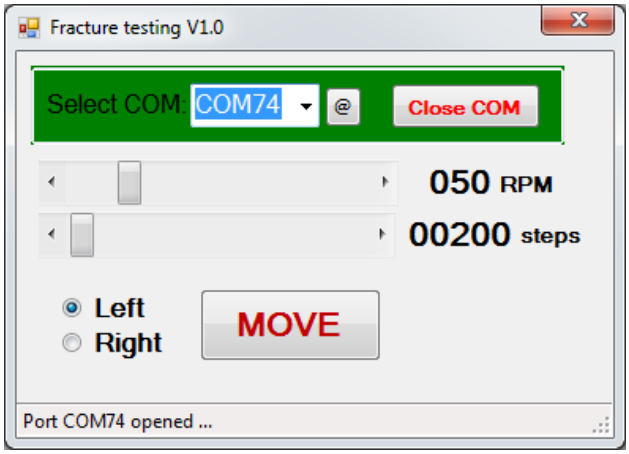

Figure B.6: Screenshot of the basic software interface.

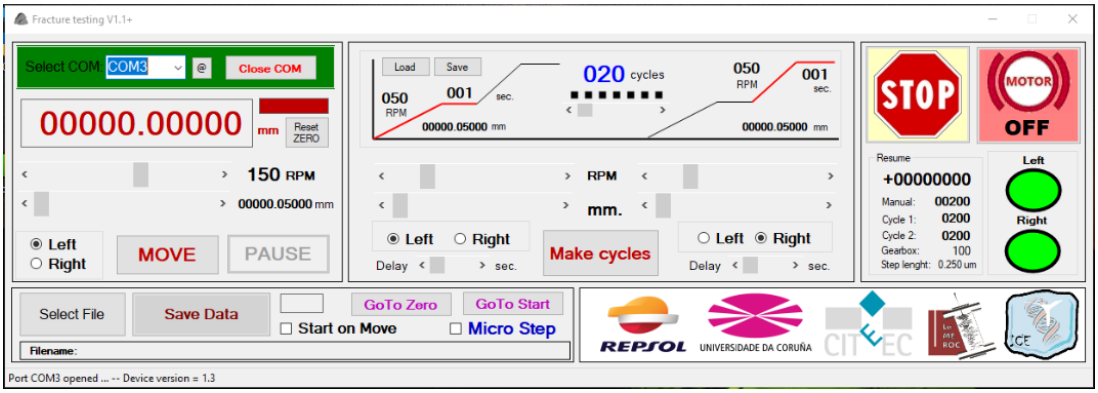

Figure B.7: Screenshot of the advanced software interface.

B2. Performance tests

B2.1. Motor performance

To carry out the first tests, the motor was controlled with a L298 dual-H bridge motor driver integrated circuit. With this configuration, the coils of the motor were tested by controlling the exposure time and its influence on the movement between phases. Since the constant load intensity is 2.5 A per coil and the point demand can reach to 5 A, a high-performance switching power supply of 12 V

and 12.5 A was used. In a preliminary approach, the motor was commanded using an AVR ATMEGA2560 series microcontroller, which was selected due to its versatility, available free software, and connectivity to an Arduino board. A number of preliminary tests were executed with the first version of the software (described in section B1.6) rendering satisfactory results: it was confirmed that the number of steps in a complete turn was 200, and that the maximum permissible speed was 150 rpm. Higher velocities resulted in overlapping pulses, loss of steps, and noisy behavior of the motor, which increased as more steps were skipped.

B2.2. Motor/gearhead performance

The performance of the motor/gearhead assembly was assessed under different loading conditions using the advanced version of the software (section B0). To this aim, the system was fixed to a steel frame and attached to a 9 cm radii pulley equipped with a steel wire (Figure B.8). This wire was used to hang a water tank that, filled with different water volumes, simulated different load conditions. The peak torque of the gearhead (24 Nm) limited the maximum load the system could lift under safe conditions (~22.07 Nm for a load of 25 kg and a 9 cm radii pulley). The effect of water oscillations (dynamic bouncing) was also considered since it could eventually increase the load value and exceed the allowable torque limit of the gearhead. By lifting and descending the tank, and repeating the movement back and forth, it was possible to check positioning reproducibility. For a speed limit of 150 rpm, the results were satisfactory for the masses considered (5, 10, 15, 20 and 25 kg), even in simulations of load/unload cycles. However, the metal casing of the motor started to overheat after 20 minutes of operation because the dual H-bridge configuration neither limits nor protects the motor coils, and neither controls the peak and proportional supplied intensity. For this reason, a stepping controller based on an A4983 integrated circuit was considered in later tests. This circuit, that includes a metal heat sink, can provide an intensity per phase of 2 A while controlling the operating limit and temperature. Although no overheating was detected on the motor coils with this new configuration, the controller, which was designed to work at lower intensity

values, started to overheat after 15 minutes and was unable to properly perform the required retention capacity. The problem was circumvented by incorporating an air-operated refrigeration system (fan).

Figure B.8: Elements used to perform preliminary load tests with the motor/gearhead assembly.

APPENDIX C: Impact of saturating fluids on mode I fracture toughness

C1. Introduction

Rock fracturing will occur when the stress conditions exceed the failure threshold (Fjaer et al. 2008). However, the presence of fluids in the rock matrix can reduce the energy needed to generate and propagate a fracture, resulting in failure at a stress level below the critical stress (Røyne et al. 2011; Ilgen et al. 2018). This phenomenon, known as subcritical crack growth, is relevant in a variety of engineering applications dealing with fluid flow and transport, such as geothermal energy extraction, oil recovery, fluid transport, CO_2 geosequestration, or radioactive waste management (Bergsaker et al. 2016). The physico-chemical processes arising from rock-fluid interaction will depend on the mineralogical composition and the microstructural properties of the rock (i.e. grain size, porosity, etc.), as well as on the fluid characteristics (Duda and Renner 2013). The chemical mechanisms controlling subcritical crack growth include stress corrosion (i.e. weakening of strained bonds at the crack tips produced by a chemical reaction) and dissolution (i.e. ionic bond breakage) (Atkinson 1984; Atkinson and Meredith 1987), while the physical processes are related to pore pressure increase, as well as capillary tension and surface energy reduction (Homand and Shao 2000; Cai et al. 2019; Maruvanchery and Kim 2019; Zhong et al. 2019).

The properties of geomaterials under saturating conditions are expected to differ from those in a dry state. A number of experimental evidences have revealed the impact of fluids over relevant rock properties, such as uniaxial compressive strength or brittleness (Kim and Changani 2016; Anne Perera et al. 2018). However, the effect over fracture toughness has not received much

attention so far. In this study, we have performed a series of mode I fracture toughness (K_{IC}) tests on saturated rock specimens using the pseudo-compact tension test (*pCT*) approach. The *pCT* test configuration is advantageous to this respect because it allows the insertion of the sample into a fluid bath that keeps the sample saturated all along the experiment. Two rock types, a porous siliceous sandstone (Corvio), and a high-strength, low porosity granite (Blanco Mera), were selected to assess the influence of seven different fluids on K_{IC} and related properties. Taking as reference the results obtained in dry tests, specimens of the two lithologies were tested under identical experimental conditions (diameter, thickness, depth of starter notch, temperature, loading rate, etc.). Here we present the experimental results obtained from the rock-fluid interplay and discuss the associated implications.

C2. Materials and methods

C2.1. Materials

Two different rock types, namely Corvio sandstone (C) and Blanco Mera granite (GR), were used in this study. While quartz (~ 94 wt. %) with subordinated kaolinite (~ 3.5 wt. %) and K-feldspar (~ 1.7 wt. %) dominate in the mineralogical composition of Corvio sandstone (Falcon-Suarez et al. 2017), Blanco Mera granite is mainly composed of plagioclase (~ 35 wt. %), alkaline feldspar (~ 27 wt. %), and quartz (~ 20 wt. %) (Arzúa 2015). Dry properties of these rocks have been reported previously in Muñoz-Ibáñez et al. (2020). Due to its relevance in the present study, we emphasize the large effective porosity (n_e) difference between both lithologies (n_e~18-24% for Corvio sandstone, n_e ~1% for Blanco Mera granite).

We saturated the rock samples using seven different wetting and non-wetting fluids with geological and/or oil industry related applications: 1) deionized water; 2) NaCl-saturated water; 3) HF95Y mineral oil; 4) B7 diesel fuel; 5) methanol; 6) 10% wt. HCl solution; and 7) 0.2M NaOH solution.

C2.2. Sample preparation

Specimens were cut using a customized tile saw. Dimensions of the prepared specimens are listed in Table C.1. After preparation, all the samples were dried at 60ºC for 24 hours, and then immersed in the corresponding fluid during one week before testing. To do this, each sample was placed vertically on the bottom of a beaker, and fluid was added beyond the height of the notch tip (Figure C.1). Special care was taken to ensure that the ligament plane was permanently submerged in fluid, and so two measures were taken: (1) in order to avoid excessive fluid evaporation, each beaker was covered with a plastic film; and (2) when it was observed that the fluid level decreased below the height of the notch tip due to rock absorption, the beakers were refilled until the original level.

In a second test series, four additional samples of slightly smaller size (see Table 5.1 for dimensions) were prepared and immersed in NaOH solution for a week. Two of them, one of each rock type, were later introduced into a second bath of HCl solution during an additional week before testing.

Figure C.1: *p*CT specimens of Blanco Mera granite (left) and Corvio sandstone (right) immersed in diesel fuel and HCl solution, respectively.

Table C.1: Specimen dimensions: D = diameter; B = thickness; G_d = groove depth; G_w = groove width; a/b = notch length ratio.

Testing series	D (mm)	B (mm)	G_d (mm)	G_w (mm)	a/b
1	53.8±0.2	27.7±0.2	5	10	0.34±0.01
2	49.2±0.3	24.9±1.5	5	10	0.4

C2.3. Experimental setup and procedure

Specimens were loaded using the testing equipment specially designed to perform *p*CT tests, which allows measuring the energy associated with crack propagation. Tests were performed at room temperature at a constant displacement rate of 0.1 mm/min. The testing procedure is similar to that previously described for dry samples in Muñoz-Ibáñez et al. (2020), with the difference that the specimens were kept inside the fluid bath during testing. To perform the experiments, the saturated samples were moved to a shorter glass container filled with the corresponding fluid (Figure C.2). A custom-made 3D-printed platform placed inside the container was used to provide stability to the sample during the experiment, and to lift it to a position such that the steel jaws could fit into the U-shaped groove while keeping the ligament plane submerged in the fluid at all times. In order to place the container in a suitable position for testing, it was necessary to replace the positioning cradle originally used to hold the dry samples with a flat thin platform. The modified experimental setup is shown in Figure C.3.

Load (P) and load point displacement (d) were recorded continuously using a 50 kN load cell and two linear variable differential transformers (LVDT), respectively. Since the samples were immersed in a fluid bath during testing, it was no possible to measure the crack mouth opening displacement (CMOD).

Figure C.2: Prepared specimen of Blanco Mera granite immersed in diesel fuel before testing.

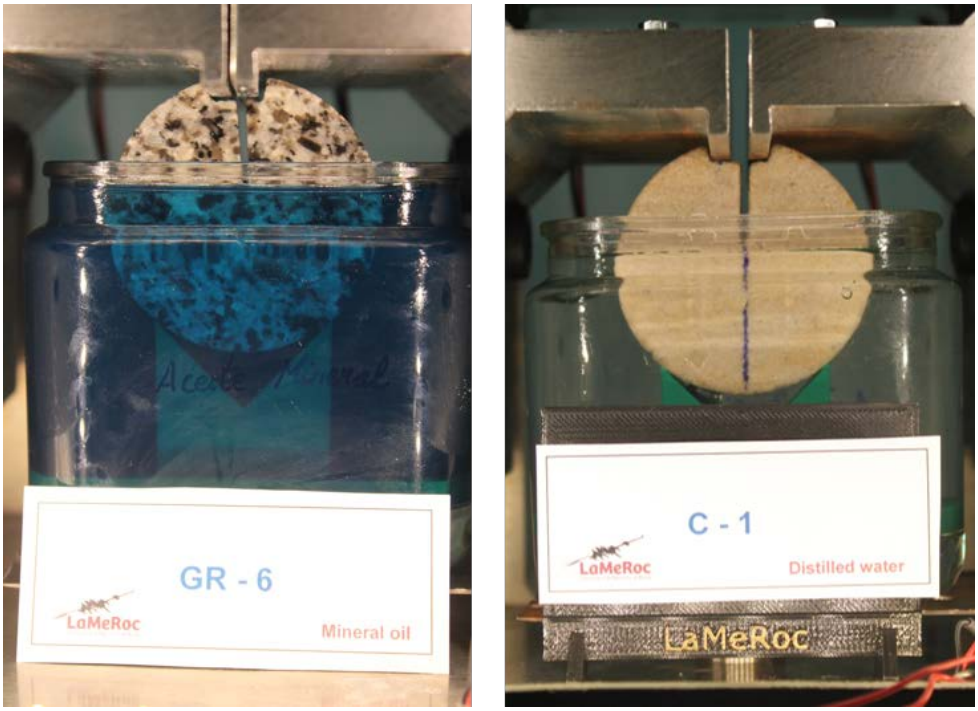

Figure C.3: Experimental setup for immersed *p*CT test: Blanco Mera granite specimen immersed in mineral oil (left); and Corvio sandstone specimen immersed in deionized water (right).

C3. Results

C3.1. Mode I fracture toughness (K_{IC})

K_{IC} was computed for each specimen using Equation (2.1), where P_{max} is the peak load, B is the specimen thickness, a is the notch length, and b is the distance from the base of the U-shaped groove to the bottom of the specimen.

$$K_{IC} = Y' \frac{P_{max}}{bB} \sqrt{\pi a} \tag{2.1}$$

The dimensionless stress intensity factor (Y') was calculated from the expression proposed by Muñoz-Ibáñez et al. (2020) for 50 mm-diameter *p*CT specimens:

$$Y' = 12.651 - 47.054\left(\frac{a}{b}\right) + 157.72\left(\frac{a}{b}\right)^2 - 247.17\left(\frac{a}{b}\right)^3 + 296.33\left(\frac{a}{b}\right)^4$$

K_{IC} values obtained for each rock type and saturating fluid are displayed in Figure C.4. Although in a first approach we performed one test of each type (i.e. for each combination of rock/saturating fluid), we considered necessary to repeat a few of them to confirm the validity of results (this situation is indicated in the figure as n=2). We observe a general trend for fracture toughness to decrease in the presence of fluids. Experimental results also illustrate an enhanced sensitivity of K_{IC} to fluid immersion in the case of the sandstone than in the granite. Regarding the type of fluid, we observe that the largest reductions on K_{IC} are found for deionized water and HCl solution. On the other hand, we observe that the presence of non-wetting fluids (mineral oil and diesel fuel) in the rock matrix, far from weakening the specimen, may even have a strengthening effect (i.e. K_{IC} increases with respect to dry tests) in the case of granite. The results obtained from the second test series are also plotted in Figure C.4. Interestingly, the reduction in K_{IC} after NaOH immersion is partially recovered after the subsequent saturation in HCl. What is more, the value of fracture toughness obtained for the granite specimen is within the range of values expected for dry specimens.

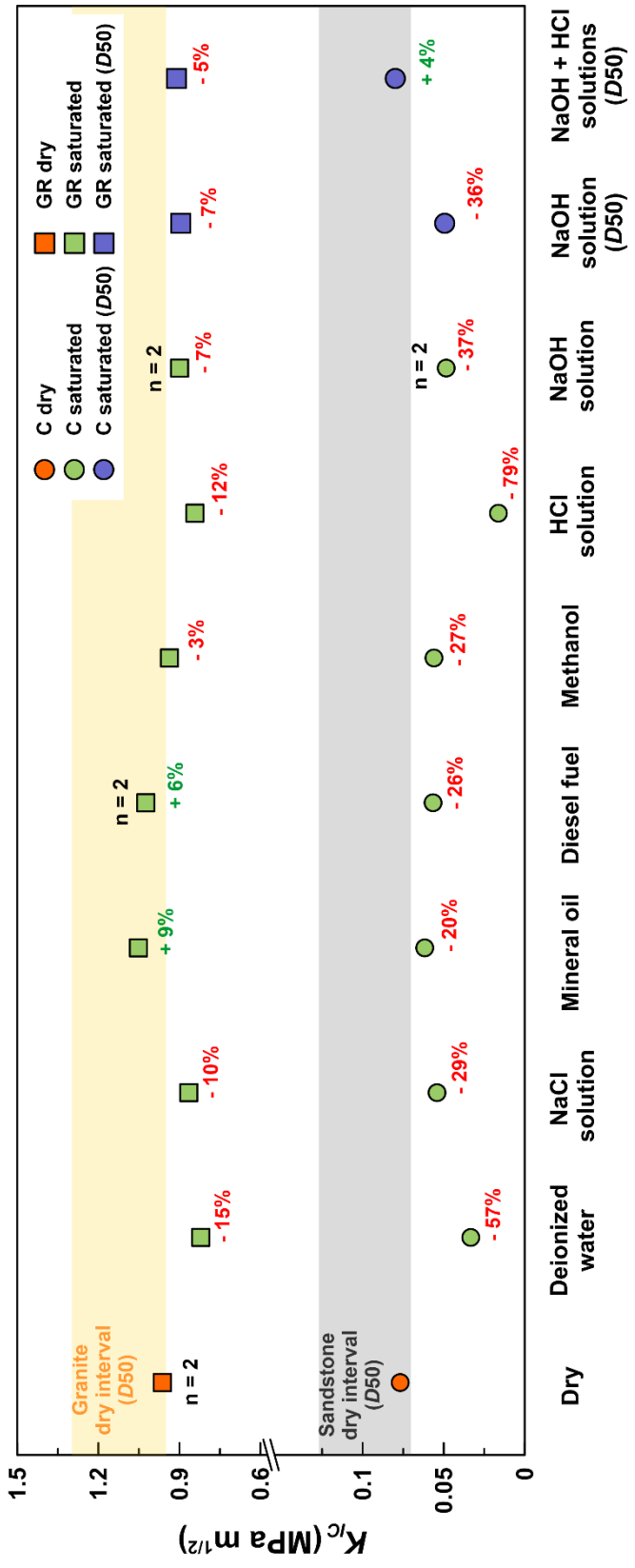

Figure C.4: Mode I fracture toughness (K_{IC}) obtained from 54 mm- and 50 mm- diameter *p*CT specimens immersed in different saturating fluids. Values for dry samples are also given in first place as a reference. Average K_{IC} is represented for tests performed twice (n = 2). Shaded areas indicate the K_{IC} intervals previously obtained from 50-mm diameter dry *p*CT specimens of each rock type (Muñoz-Ibáñez et al. 2020).

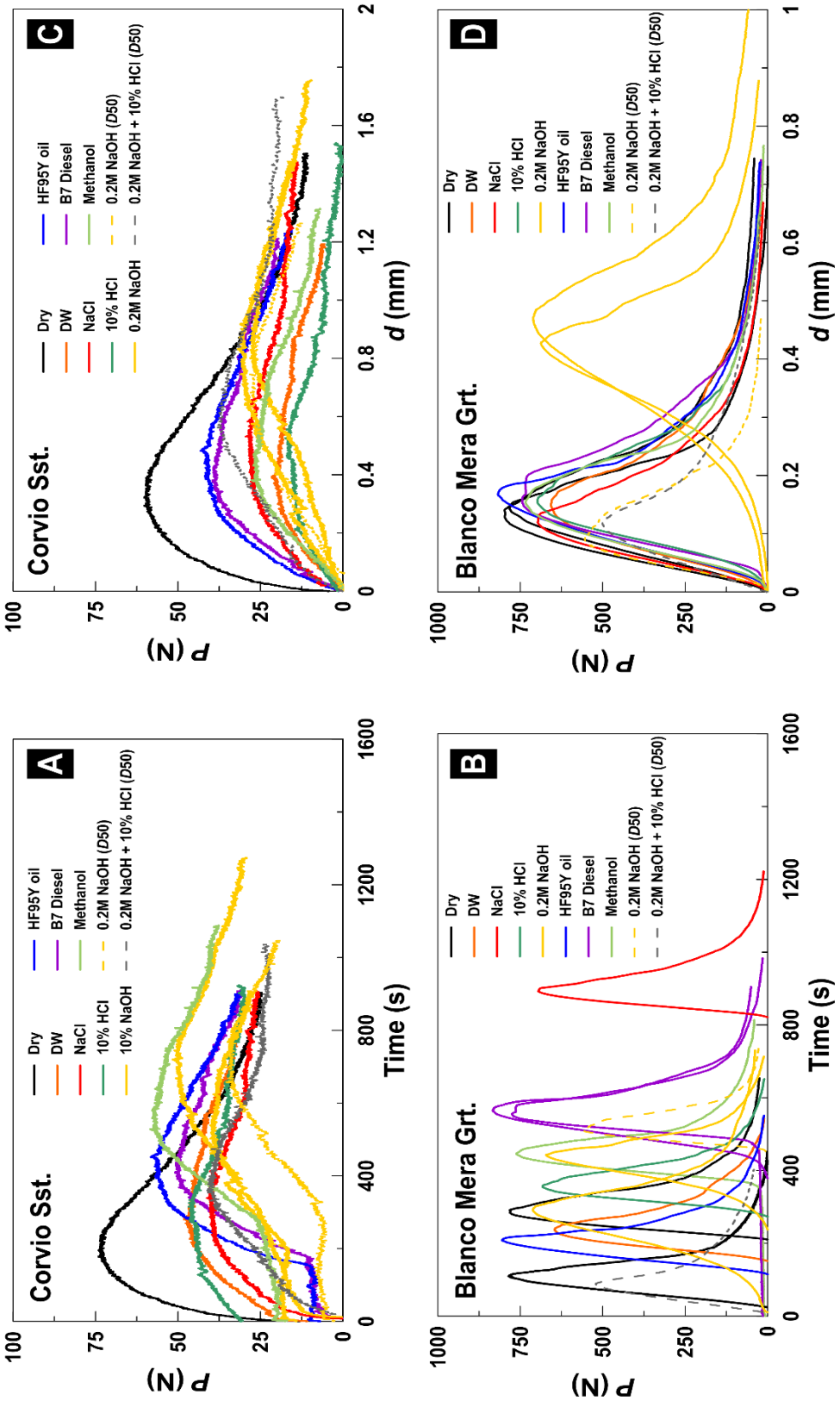

Figure C.5: Raw (A&B) and processed (C&D) experimental curves

C3.2. Load-displacement curves

In order to identify the onset of loading for each experiment, an Akaike Information Criterion (AIC) algorithm was applied to the average-normalized load vs time raw data. Figure C.5 illustrates raw (i.e. *P* vs time curves) and processed (i.e. *P* vs *d* curves) experimental results from *p*CT tests. At first glance, we observe that fluid effects are more prominent in the sandstone: while for this rock type the stiffness (i.e. the slope in the *P-d* curve) becomes reduced for the seven saturating fluids considered, this is not the case of granite. The only exception is for a highly alkaline fluid (NaOH solution), which makes even the granite less stiff.

C3.3. Energy

In a second-order approach, we considered the relative contribution of the subcritical crack growth and the stable crack propagation stages in the total energy balance of a single test. This is to split the initiation (E_{pre}) and propagation (E_{post}) energies at the point of maximum load (P_{max}) from the total fracture energy (E_{tot}), as displayed in Figure C.6. Although for saturated samples we could not measure CMOD, we have previously observed a good agreement between the energy computed from *P-d* curves (E_{tot}) and that from *P*-CMOD ($E_{tot\text{-}CMOD}$) for dry *pCT* tests (Figure C.7).

There is a significant correlation between P_{max} and E_{tot} in the sandstone but not so clear in the granite (Figure C.8). Interestingly, for the sandstone the correlation is better with respect to E_{post} than for E_{pre}. For all the samples (dry and saturated specimens of either sandstone or granite), we also observe that E_{tot} is strongly correlated to E_{pre} and E_{post} (Figure C.9). However, the slope is larger for the relation between E_{tot} and E_{post} than between E_{tot} and E_{pre}. Regarding the type of fluid, we observe that the energy needed to generate the fracture (E_{pre}) in both rock types is lower for the samples immersed in deionized water, methanol, and HCl solution compared with dry specimens (Figure C.10). This is also true for sandstone samples saturated in diesel fuel and NaOH solution, and the granite samples immersed in NaCl solution. Curiously, the energy needed to propagate the fracture (E_{post}) is reduced in all cases in comparison with dry conditions, with the only exception of the combination of granite with non-wetting fluids (Figure

C.11). We also observe a partial recovery in both E_{pre} and E_{post} for the 50 mm-diameter specimens saturated in HCl solution that were firstly immersed in NaOH.

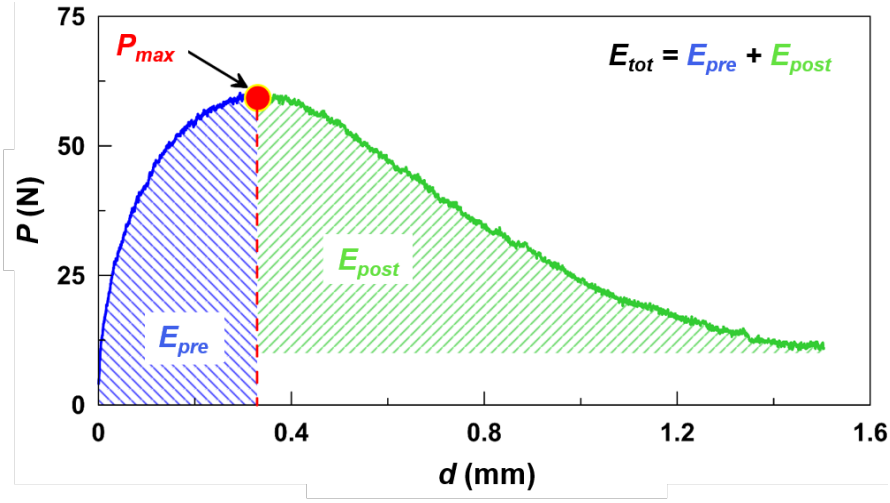

Figure C.6: Initiation (E_{pre}) and propagation (E_{post}) energies obtained from load versus displacement (P-d) curves. The maximum load (P_{max}) marks the transition from from E_{pre} to E_{post}.

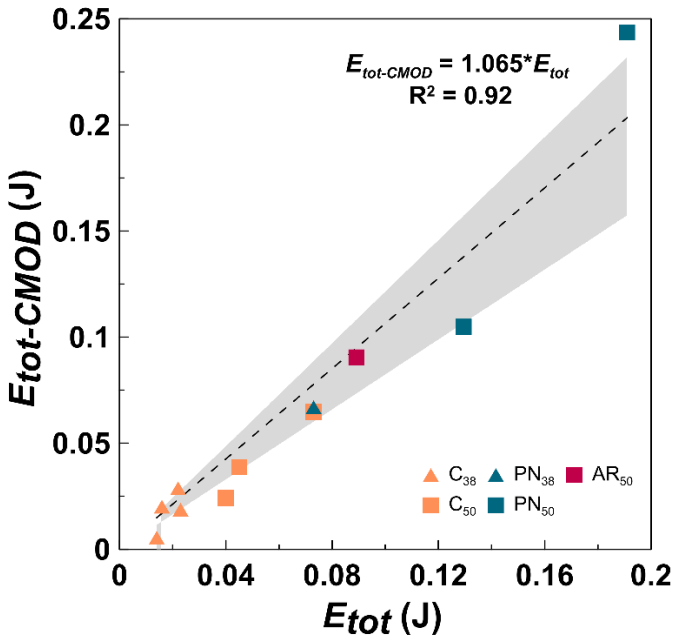

Figure C.7: Total energy obtained from load-CMOD curves ($E_{tot\text{-}CMOD}$) versus total energy obtained from load-displacements curves (E_{tot}) for *p*CT testing. The shaded region represents the confidence interval.

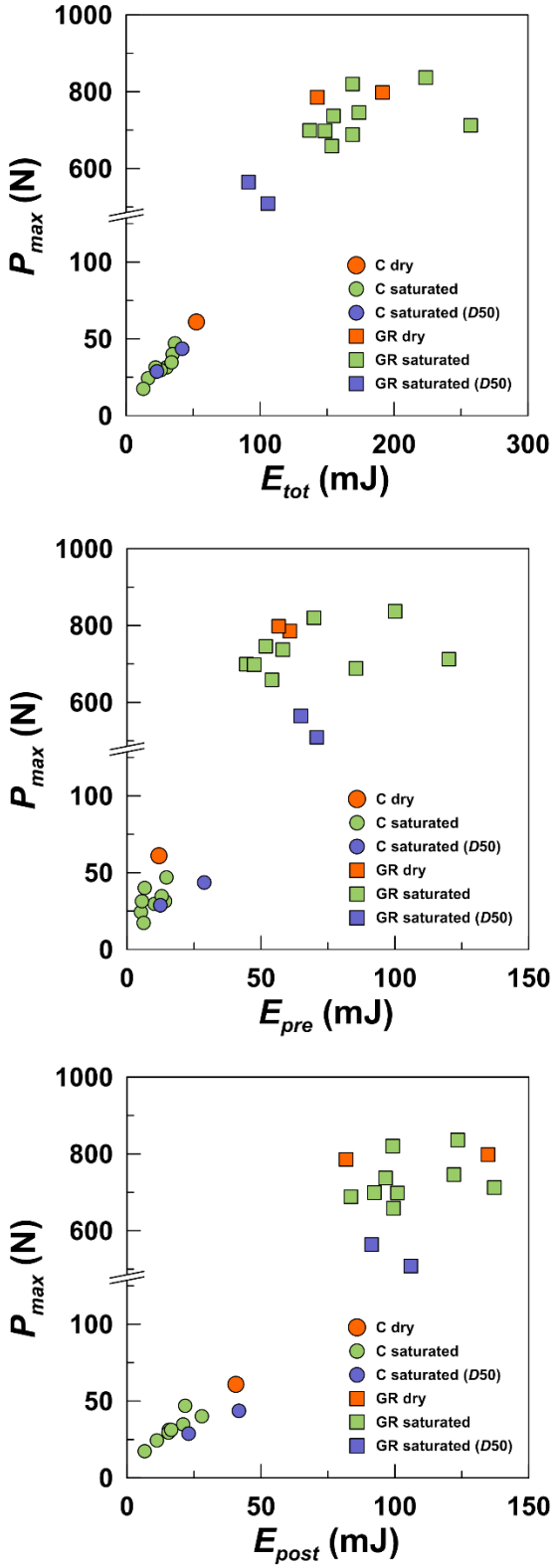

Figure C.8: Maximum load (P_{max}) versus total energy (E_{tot}; top), initiation energy (E_{pre}; middle), and propagation energy (E_{post}; bottom).

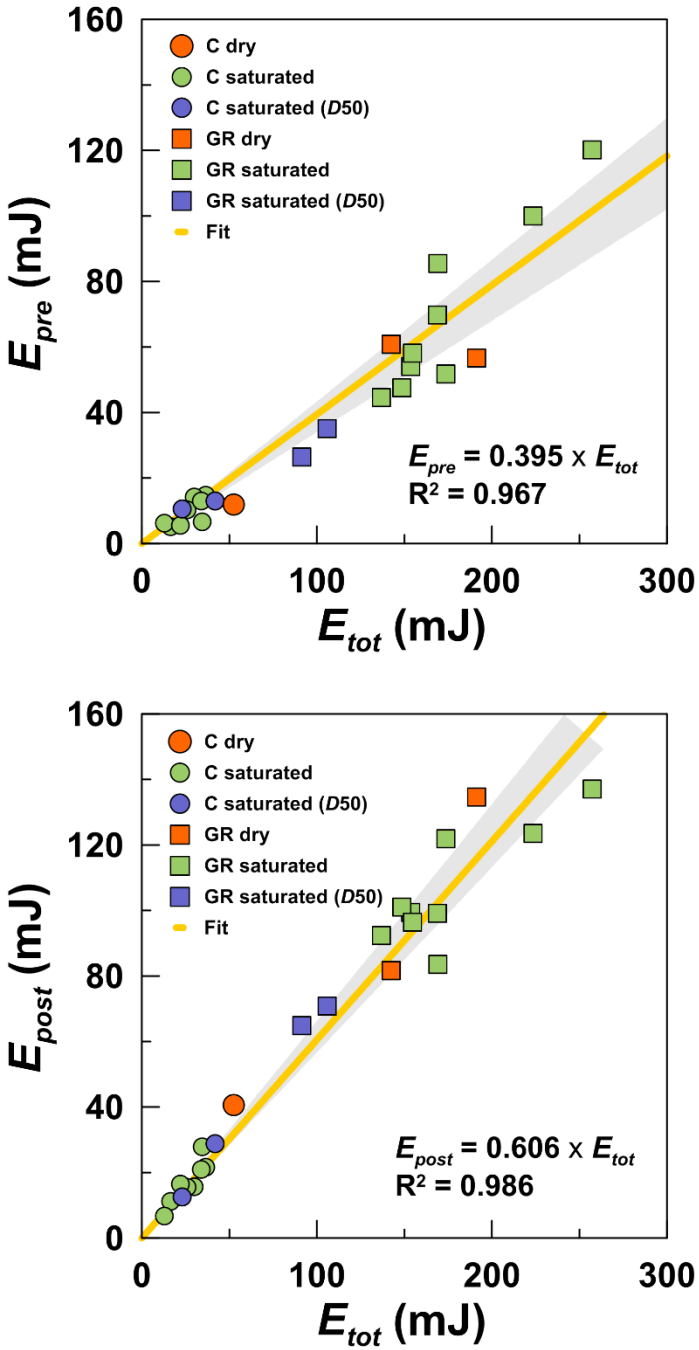

Figure C.9: Initiation energy (E_{pre}; top) and propagation energy (E_{post}; bottom) versus total energy (E_{tot}).

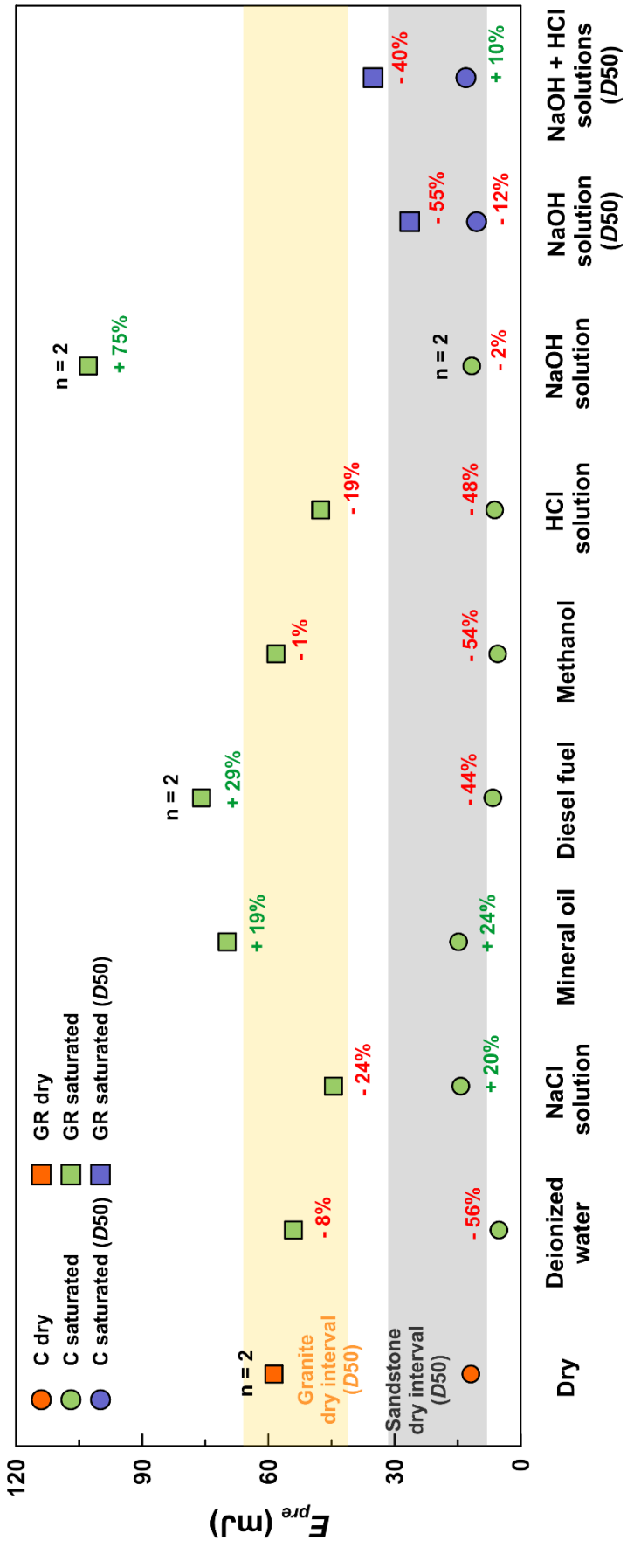

Figure C.10: Initiation energy (E_{pre}) for each combination of rock type and saturating fluid. Values for dry samples are also given as a reference. Average E_{pre} is represented for tests performed twice (n = 2). Shaded areas indicate the E_{pre} intervals previously obtained from 50-mm diameter dry *p*CT specimens of each rock type (Muñoz-Ibáñez and Delgado-Martín 2020).

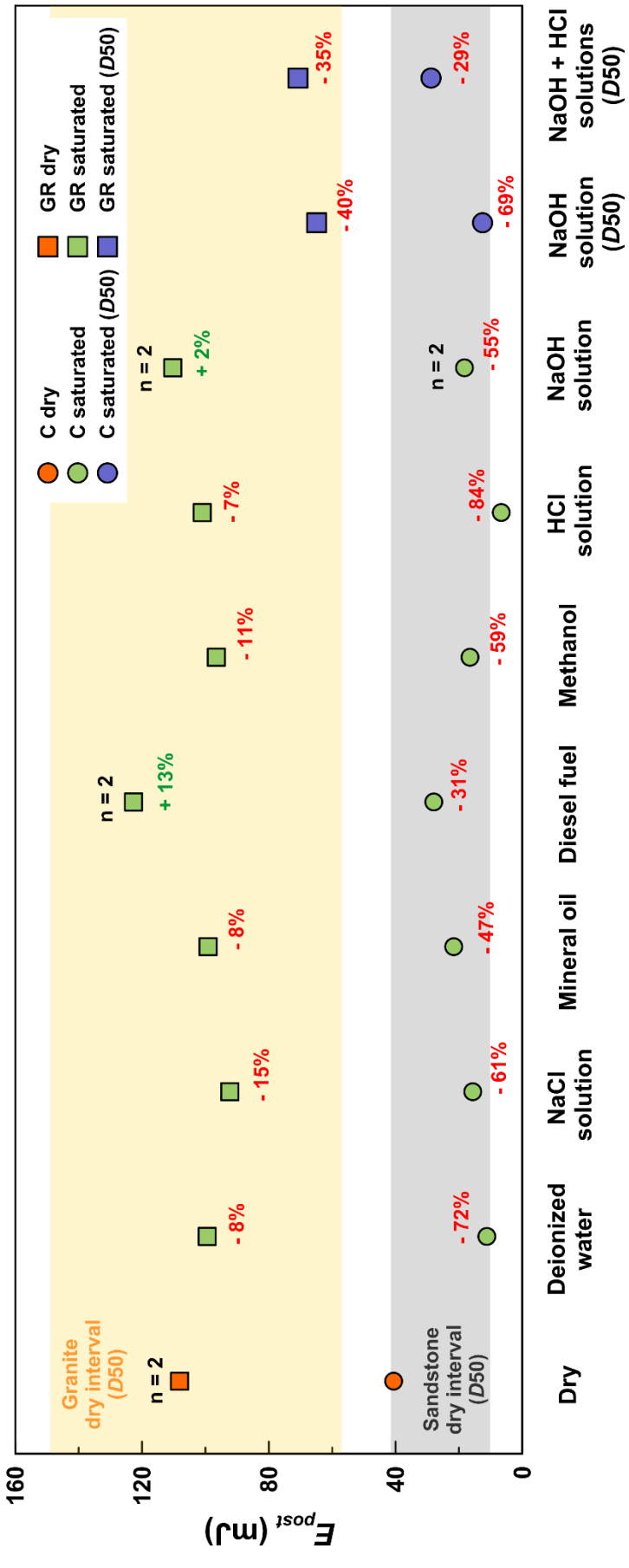

Figure C.11: Propagation energy (E_{post}) for each combination of rock type and saturating fluid. Values for dry samples are also given as a reference. Average E_{post} is represented for tests performed twice (n = 2). Shaded areas indicate the E_{post} intervals previously obtained from 50-mm diameter dry *p*CT specimens of each rock type (Muñoz-Ibáñez and Delgado-Martín 2020).

C4. Discussion

Mechanical properties of rock (e.g. compressive or tensile strength) usually decrease in the presence of fluids. A water-weakening effect on rock strength has been previously reported for different rock types, including both porous sandstones (Rutter and Mainprice 1978) and low porosity granites (Lajtai et al. 1987). The rock-fluid interaction produces a microstructural damage in the cementing or rock matrix that would explain the strength loss (Maruvanchery and Kim 2019). Ojo and Brook (1990) found that the tensile strength of sandstone samples saturated in water was half of the value obtained in dry conditions. In three-point bending experiments performed on saturated granite specimens, Zhao (2018) reported a strength reduction in the presence of water (25%) but also of other fluids such as 10% w.t. HCl (32%), 10% w.t. NaOH (27%), and kerosene (24%). Han et al. (2016) also observed an overall weakening trend (in compression and tensile strengths, as well as in K_{IC}) for granite specimens saturated in four different fluids, including 0.01 mol/L of NaOH solution and distilled water. Although they also reported the lowest resistance for samples immersed in acid solutions (0.01 mol/L Na_2SO_4, and 0.01 mol/L $NaHCO_3$), they found that the degree of chemical deterioration was diminished under strong alkaline conditions (NaOH). Their results are in agreement with those reported here for *p*CT testing, in which the lowest fracture toughness is found for rock specimens saturated in an acid HCl solution. Although our experimental results also suggest a lower impact of NaOH on K_{IC} when compared with other fluids such as distilled water, the effect is stronger in comparison with other fluids such as mineral oil, diesel fuel, or methanol. Curiously, the alkaline NaOH solution produces the most significant reduction in stiffness for both rock types, seeming to be the only fluid affecting the granite in this sense. In fact, fluid effects (K_{IC} and stiffness reduction) are more notable in Corvio sandstone than in Blanco Mera granite. Under water saturated conditions, Cai et al. (2019) also reported a stronger reduction in the compressive strength for sandstone than for granite or marble. This behaviour is likely effect of the porosity and the source of strength in each lithology. The cohesion of mineral grains arises from different processes

for each rock type: while in sandstones the grains are bonded together by means of cement (silica and carbonates), the texture of granite is formed by intergrowth (i.e. grain interlocking due to crystallization). The easy access of fluids to the porous and highly pervious sandstone makes possible a more efficient fluid/cement interaction, which is dominated by dissolution processes. In this regard, the non-wetting fluids are not expected to contribute to dissolution although significant lowering of the stiffness and the fracture energy in the sandstone is still observed.

Quartz (SiO_2) is one of the most common minerals of the continental crust (Fjaer et al. 2008). While quartz is the main component (~94 wt. %) of Corvio sandstone, the proportion of this mineral is lower in the case of Blanco Mera granite (~20 wt. %). Initially, in the absence of load and fluids, the starter notch of the rock specimen is in stable equilibrium with the residual stress field around the crack tip (Lawn and Cook 2012). If the sample is immersed in fluid and loaded afterwards, subcritical crack growth will occur due to the breakage of chemical bonds at the fracture tip under tension (Ilgen et al. 2018). For the rock types considered here, this process would be related to the chemical reaction between the broken siloxane bonds (Si-O-Si) at the notch and the fluid under consideration (Nara et al. 2011). Under water saturated conditions, the strong silica-oxygen bonds in silicates would be replaced by much weaker hydrogen bonds, which would explain the reduction in the stress needed for rock fracturing in the presence of water (Dyke and Dobereiner 1991). Nevertheless, the effect would be less remarkable in the case of granite due to its significantly lower porosity (Cai et al. 2019). Rimsza et al. (2018) performed atomistic simulations to investigate the weakening effect of silica in the presence of water. They found that the aqueous solution decreased the mechanical/energetic requirement for Si-O bond breakage, favouring fracture propagation and lowering $K_{IC.}$ In a more recent contribution, Rimsza et al. (2019) carried out similar simulations considering four different environmental conditions, including water, 1M NaCl solution, and 1M NaOH solution. Although they found that any of these aqueous solutions weakened silica, the effect was more remarkable for the alkaline NaOH solution, which was attributed to increased interactions between Na^+ ions and the

broken siloxane bonds at the crack surface. In our experiments, the enhanced sorption of Na at the crack tips due to deprotonation and breaking of siloxane bonds would explain the significant stiffness reduction observed for NaOH. However, the partial recovery of K_{IC} and fracture energy after subsequent immersion of NaOH saturated samples in HCl solution suggests that this could be a reversible process. In a basic environment, the siloxane bonds of the crack surface attract the Na^+ ions present in the solution. Then the later immersion in an acid solution with considerably larger H^+ concentration (10^{-1} for a 0.1 M HCl solution; 10^{-13} for a 0.1 M NaOH solution) would induce the replacement of Na^+ ions at the chemical bonds by H^+.

The surface energy needed to develop a crack may be reduced due to fluid adsorption on crack surfaces (Hudson 1993). The presence of a water layer would induce changes in the cohesion and friction of the grains, stabilising the heterogeneous mineral surfaces and decreasing the surface free energy (Arsalan et al. 2015). Ilgen et al. (2018) related the lower K_{IC} obtained in cracks exposed to liquids to a reduction in: (i) the elastic potential energy of chemical bonds at the crack tip; or (ii) the energy from the added surface area of the fracture. In our tests, we also reported a decrease in the crack propagation energy for the two rock types tested here under saturating conditions (except for the granite samples immersed in non-wetting fluids), which may be related to reactions at the fluid-mineral interfaces.

C5. Conclusions

The effect of fluid saturation on the initiation and propagation of tensile cracks in rocks was analysed. A series of pseudo-compact tension (*p*CT) experiments were carried out using an experimental device that allows the measurement of the energy associated with crack propagation. Specimens of two types of reference rocks (Corvio sandstone and Blanco Mera granite) were saturated prior to testing and kept immersed in the selected fluid during the experiments. The experimental conditions (temperature, loading rate, etc.) were identical to those used for dry tests in order to ensure that fluid saturation was the only factor affecting the results. We observed significant effects associated

with rock-fluid interaction. The saturating fluids have a more pronounced impact on the mode I fracture toughness (K_{IC}) and the energy content (E_{pre} and E_{post}) in the case of sandstone than in the granite. Although the stiffness is less affected in the case of granite, both types of rocks show significant stiffness reduction when the contact fluid is NaOH. However, the weakening effect produced by this alkaline solution could be recovered partially after subsequent immersion in HCl solution. For all the tests, we observe that the ratio of energy between crack initiation and propagation is constant but with a higher storage (~60% of total energy) during propagation.

C6. References

Anne Perera MS, Suresh Madushan Sampath KH, Ranjith PG, Rathnaweera TD (2018) Effects of pore fluid chemistry and saturation degree on the fracability of Australian warwick siltstone. *Energies* 11:

Arsalan N, Buiting JJ, Nguyen QP (2015) Surface energy and wetting behavior of reservoir rocks. *Colloids and Surfaces A: Physicochemical and Engineering Aspects* 467:107–112

Arzúa J (2015) Study of the mechanical behavior of intact and jointed rocks in laboratory with particular emphasis on dilatancy. PhD thesis; University of Vigo, Vigo, Spain

Atkinson BK (1984) Subcritical crack growth in geological materials. *Journal of Geophysical Research: Solid Earth* 89:4077–4114

Atkinson BK, Meredith PG (1987) The theory of Sub-Critical Crack Growth with Applications to Minerals and Rocks. In: Atkinson BK (ed) Fracture Mechanics of Rock. Academic Press, pp 111–166

Bergsaker AS, Røyne A, Ougier-simonin A, Aubry J, Renard F (2016) The effect of fluid composition, salinity, and acidity on subcritical crack growth in calcite crystals. *Journal of Geophysical Research: So* 121:1631–1651

Cai X, Zhou Z, Liu K, Du X, Zang H (2019) Water-Weakening Effects on the Mechanical Behavior of Different Rock Types: Phenomena and

Mechanisms. *Applied Sciences* 9:

Duda M, Renner J (2013) The weakening effect of water on the brittle failure strength of sandstone. *Geophysical Journal International* 192:1091–1108

Dyke CG, Dobereiner L (1991) Evaluating the strength and deformability of sandstones. *Quarterly Journal of Engineering Geology* 24:123–134

Falcon-Suarez I, Canal-Vila J, Delgado-Martin J, North L, Best A (2017) Characterisation and multifaceted anisotropy assessment of Corvio sandstone for geological CO_2 storage studies. *Geophysical Prospecting* 65:1293–1311

Fjaer E, Holt RM, Horsrud P, Raaen AM, Risnes R (2008) Petroleum related rock mechanics. 2nd edition. Elsevier

Han T, Shi J, Chen Y, Li Z (2016) Effect of Chemical Corrosion on the Mechanical Characteristics of Parent Rocks for Nuclear Waste Storage

Homand S, Shao JF (2000) Mechanical behaviour of a porous chalk and effect of saturating fluid. *Mechanics of Cohesive-Frictional Materials* 5:583–606

Hudson JA (1993) Comprehensive Rock Engineering. Principles, Practice and Projects. Volume 3: Rock Testing and Site Characterization. Pergamon Press

Ilgen AG, Mook WM, Tigges AB, Choens RC, Artyushkova K (2018) Chemical controls on the propagation rate of fracture in calcite. *Scientific Reports* 1–13

Kim E, Changani H (2016) Effect of water saturation and loading rate on the mechanical properties of Red and Buff Sandstones. *International Journal of Rock Mechanics and Mining Sciences* 88:23–28

Lajtai EZ, Schmidtke RH, Bielus LP (1987) The effect of water on the time-dependent deformation and fracture of a granite. *International Journal of Rock Mechanics and Mining Sciences & Geomechanics Abstracts* 24:247–255

Lawn BR, Cook RF (2012) Probing material properties with sharp indenters : a retrospective. *Journal of Materials Science* 47:1–22

Maruvanchery V, Kim E (2019) Effects of water on rock fracture properties: Studies of mode I fracture toughness, crack propagation velocity, and consumed energy in calcite-cemented sandstone. *Geomechanics and Engineering* 1:57–67

Muñoz-Ibáñez A, Delgado-Martín J, Costas M, Rabuñal-Dopico J, Alvarellos-Iglesias J, Canal-Vila J (2020) Pure mode I fracture toughness determination in rocks using a pseudo-compact tension (*p*CT) test approach. *Rock Mechanics and Rock Engineering* 53: 3267-3285

Muñoz-Ibáñez A, Delgado-Martín J, Juncosa-Rivera R Experimental investigation on the size and other effects on mode I fracture toughness in selected rock types using the *p*CT and SCB testing methods. *International Journal of Rock Mechanics and Mining Sciences.*

Nara Y, Morimoto K, Yoneda T, Hiroyoshi N, Kaneko K (2011) Effects of humidity and temperature on subcritical crack growth in sandstone. *International Journal of Solids and Structures* 48:1130–1140

Ojo O, Brook N (1990) The effect of moisture on some mechanical properties of rock. 10:145–156

Rimsza JM, Jones RE, Criscenti LJ (2018) Chemical Effects on Subcritical Fracture in Silica From Molecular Dynamics Simulations. *Journal of Geophysical Research: Solid Earth* 123:9341–9354

Rimsza JM, Jones RE, Criscenti LJ (2019) Mechanisms of Silica Fracture in Aqueous Electrolyte Solutions. *Frontiers in Materials* 6:

Røyne A, Bisschop J, Dysthe DK (2011) Experimental investigation of surface energy and subcritical crack growth in calcite. 116:1–10

Rutter EH, Mainprice DH (1978) The effect of water on stress relaxation of faulted and unfaulted sandstone. *Pure and Applied Geophysics* 116:634–654

Zhao W (2018) Strength of granite saturated in various fluids. Master Thesis; University of Pittsburgh, Pennsylvania, USA

Zhong C, Zhang Z, Ranjith PG, Lu Y, Choi X (2019) The role of pore water plays

in coal under uniaxial cyclic loading. *Engineering Geology* 257:105125